# Towards a Photo-Driven Artificial Hydrogenase Using the Biotin-Streptavidin Technology

**Inauguraldissertation**

zur

Erlangung der Würde eines Doktors der Philosophie

vorgelegt der

Philosophisch-Naturwissenschaftlichen Fakultät

der Universität Basel

von

**Sascha Georg Keller**

aus Deutschland

Basel, 2019

Genehmigt von der Philosophisch-Naturwissenschaftlichen Fakultät

auf Antrag von

Prof. Dr. Thomas R. Ward

Prof. Dr. Oliver S. Wenger

Basel, den 12. Dezember 2017

Prof. Dr. Martin Spiess

Dekan

*(…) water will one day be employed as a fuel, that hydrogen and oxygen that constitute it, used singly or together, will furnish an inexhaustible source of heat and light, of an intensity of which coal is not capable. Someday the coal rooms of steamers and the tenders of locomotives will, instead of coal, be stored with these two condensed gases, which will burn in the furnaces with enormous caloric power (…). I believe, that when the deposits of coal are exhausted, we shall heat and warm ourselves with water. (…) Water will be the coal of the future (…).*

*Jules Verne (1828 – 1905), "L'Ile Mystérieuse" 1874*

*Für meine Familie*

# Abstract

It is estimated that the world's population will reach 11 billion by 2100 and thus the energy need will increase. Already today this is a delicate topic since the use of finite energy sources as coal and oil are depleting. Furthermore, the $CO_2$ released is negatively effecting the climate.

Artificial photosynthesis to produce hydrogen as a clean fuel is one possibility that caught much attention. The reaction product of hydrogen and oxygen is solely water.

Many small molecule catalysts have already been reported that produce hydrogen, but they are not as active as natural hydrogenases. Natural enzymes have a highly evolved and sophisticated coordination sphere around the catalytic center, as well as hydrogen, proton and electron channels. These features are hardly added by synthetic modification of a ligand of a small molecule catalyst. Incorporation of those catalysts into a protein scaffold would add a second coordination sphere that mimics natural enzymes.

In this context, this thesis explores the biocompatibility of some molecular catalysts that produce hydrogen from formic acid for future *in vivo* or protein incorporation applications. Here, we could show that certain complexes show good turnovers and high recyclability rates, as well as oxygen tolerance under bio-compatible reaction conditions.

To address the matter of electron transfer in proteins and their surface we explored the electron transfer properties of a dyad of an electron donating triarylamine and a bio-conjugated ruthenium photosensitizer. Different distances of the dyad were tested and the best system was further improved. Not only was an electron acceptor also bio-conjugated to the proteins *N*-terminus, but also a negative patch of three negatively charged amino acids was introduced in close proximity to the

photosensitizer. This negative patch increased the local concentration of the electron acceptor, even when not tethered to the protein. We could show that the protein can successively be bio-conjugated in three different ways: i) biotin-binding, ii) nucleophilic substitution on a cysteine residue and iii) *N*-terminal modification. The compatibility of these biorthogonal bio-conjugation procedures may open a new possibility of assembling catalytic systems on a protein surface.

The thesis further discusses the use of the biotin-streptavidin technology to assemble an artificial hydrogenase to perform hydrogen evolution. A small molecule pentapyridin ligated Co catalyst was incorporated into different mutants of streptavidin and photocatalytic hydrogen evolution was measured. It could be shown that a lysine that was incorporated *via* mutagenesis has a beneficial influence on turnover numbers and rates. We also found that it decreased the initial lag-phase, often seen in small molecule hydrogen evolution catalysts, significantly. These findings support the idea that basic residues in close proximity to a hydrogen reducing or oxidizing catalyst have a positive impact, giving insights into its mechanism. The fact that the biotin-streptavidin provides a catalyst incorporated into a protein binding pocket also enables to exclude a heterolytic hydrogen evolution mechanism often proposed, since the Co-centers are too far away to react with each other, at least in our system.

We envision that these findings will help to develop artificial hydrogenases that are at least as active as natural hydrogenases.

# Self-Citations

## Self-Citations

During the course of my PhD at the University of Basel, four manuscripts were published. The preprints and the corresponding supporting information of these four manuscripts are integrated in this thesis.

**Chapter 3**

This chapter is an adapted version of *„Evaluation of Formate Dehydrogenase Activity of Three-Legged Pianostool Complexes in Dilute Aqueous Solution"*, Sascha G. Keller, Mark R. Ringenberg, Daniel Häussinger and Thomas R. Ward, *Eur. J. Inorg. Chem.* **2014**, *34*, 5860–5864.

**Chapter 4**

This chapter is an adapted version of *„Light-Driven Electron Injection from a Biotinylated Triarylamine Donor to $[Ru(diimine)_3]^{2+}$-Labeled Streptavidin"*, Sascha G. Keller, Andrea Pannwitz, Fabian Schwizer, Juliane Klehr, Oliver S. Wenger and Thomas R. Ward, *Org. Biomol. Chem.* **2016**, *14*, 7197-7201.

**Chapter 5**

This chapter is an adapted version of *„Streptavidin as a Scaffold for Light-Induced Long-Lived Charge Separation"*, Sascha G. Keller, Andrea Pannwitz, Hendrik Mallin, Oliver S. Wenger and Thomas R. Ward, *Chem. Eur. J.* **2017**, *23*, 18019-18024.

**Chapter 6**

This chapter is an adapted version of *„Photo-Driven Hydrogen Evolution by an Artificial Hydrogenase Utilizing the Biotin-Streptavidin Technology“*, Sascha G. Keller, Benjamin Probst, Tillmann Heinisch, Roger Alberto and Thomas R. Ward, *Helv. Chim. Acta.* **2018**, *101*, e1800036.

# Table of Content

# Abbreviations

| | |
|---|---|
| A | acceptor |
| α | alpha |
| Ac | acetyl |
| ADP | adenosine diphosphate |
| ArM | artificial metalloenzyme |
| AscOH | ascorbic acid |
| ATP | adenosine triphosphate |
| β | beta |
| biot | biotin |
| bpy | 2,2'-bipyridine |
| $CH_2Cl_2$ | dichloromethane |
| CHOOH | formic acid |
| CO | carbon monoxide |
| $CO_2$ | carbon dioxide |
| Cp* | cyclopentadienyl |
| δ | chemical shift |
| D | donor |
| Da | Dalton |
| DAF | deazaflavin |
| DHA | dehydroascorbic acid |
| DMSO | dimethyl sulfoxide |
| DMF | dimethylformamide |
| $e^-$ | electron |
| ELISA | enzyme-linked immunosorbent assay |
| ESI | electron spray ionisation |
| EtOH | ethanol |
| g | gram |
| GP | guanylyl pyridinol |
| h | hour |
| $H^+$ | proton |

| | |
|---|---|
| $H_2$ | dihydrogen |
| $H_4$MPT | tetrahydromethanopterin |
| HCl | hydrochloric acid |
| HABA | 4'-hydroxyazobenzene-2-carboxylic acid |
| HmuO | *Corynebacterium diphteriae* heme oxygenase |
| HO1 | rat oxygenase 1 |
| HRMS | high resolution mass spectrometry |
| Hz | hertz |
| *J* | coupling constant [Hz] |
| J | Joule |
| K | Kelvin |
| M | molar [mol/l] |
| Mb | sperm whale myoglobin |
| MeOH | methanol |
| MLCT | metal-to-ligand charge transfer |
| MS | mass spectrometry |
| MV | methyl viologen |
| NADH | nicotinamide adenine dinucleotide (reduced form) |
| NAD | nicotinamide adenine dinucleotide |
| NADP | nicotinamide adenine dinucleotide phosphate |
| NaOH | sodium hydroxide |
| NMR | nuclear magnetic resonance |
| NOE | Nuclear Overhauser Effect |
| $O_2$ | dioxygen |
| OEC | oxygen evolving complex |
| OTEC | ocean thermal energy conversion |
| pH | proton concentration |
| pI | isoelectric point |
| $PPh_3$ | triphenylphosphine |
| ppm | parts per million |
| PS | photosensitizer |
| PSI | photosystem I |
| PSII | photosystem II |
| s | second |
| Sav | streptavidin |
| SDS | sodium dodecyl sulfate |
| SED | sacrificial electron donor |
| TAA | triarylamine |
| TCEP | tris(2-carboxyethyl)phosphine |
| TEOA | triethanolamine |
| TOF | turnover frequency |
| TON | turnover number |
| Twy | terawatt years |
| V | volts |
| WOC | water oxidation catalyst |
| WRC | water reduction catalyst |
| WT | wild-type |

# 1

# General Introduction

When the industrial revolution started in the late 18th century in Great Britain, mankind was not aware of the negative impacts that an improved quality of life might bring for future generations 150 years later (Figure 1.1).[1,2] There is no doubt that the increase in productivity, efficiency, mobility and a secure production of food changed the world as mankind knew it until then. Little was known about the consequences that continuous burning of fossil fuels might have on climate. Nowadays, the effects of greenhouse gases as $CO_2$ or methane are well understood and tremendous efforts on finding a solution to said problems are undertaken by scientists worldwide.[3,4] Their aim is to find sustainable and renewable ways to produce carbon-free or carbon neutral energy.

The world's energy consumption has increased by a factor of 200 since 1850, with coal, oil and gas being by far the most used sources of energy (Figure 1.1). Burning fossil fuels produces $CO_2$ which is released into the atmosphere. The rise of the $CO_2$-level can be linked to the growth of the world population and its accompanying need for more energy (Figure 1.2). While there are currently about 7.6 billion people on earth, it is estimated that by 2050, there will be 9 billion inhabitants and by 2100, 11.2 billion people. This calls for a radical change in energy production habits.[1]

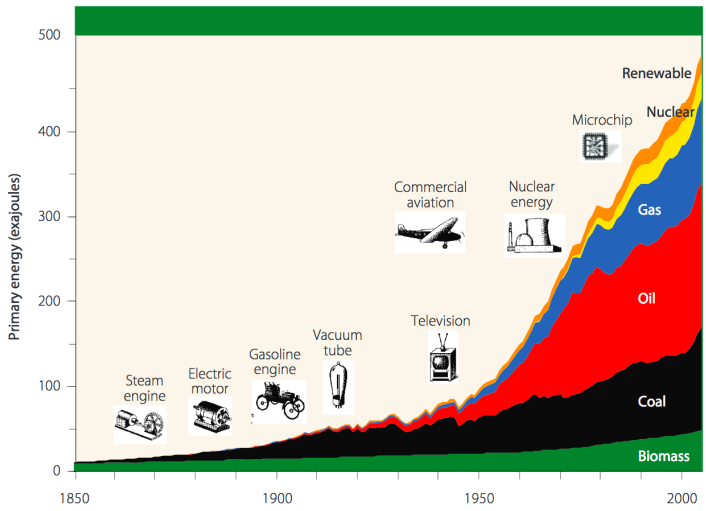


**Figure 1.1:** Rise in energy consumption since the first industrial revolution from 1850 till today. The Figure is reproduced from reference[1].

Not only climate change is a reason to address the energy problem, but also the finite nature of our primary source of fuels. The world's finite resources of natural gas, petroleum, uranium and coal sum up to around 1.570 Twy (terawatt-year), which means, that they will only last for another 85 years, given the annual world energy consumption of 18.5 Twy (Figure 1.3). Yet, it Is expected that this number will increase by 2050 to 28 Twy.[5]

Renewable resources on the other hand offer a different picture. While tidal, geothermal, wave, hydro, biomass or OTEC (Ocean Thermal Energy Conversion) only show relatively small amounts of potential annual energy, wind energy could easily fuel the whole world if harvested accordingly. Solar energy on the other hand is the major energy source we could utilize on our planet. Annually, the sun shines 1250 times more energy on earth than we need to sustain worldwide energy needs.

Harvesting that energy is one problem, storing that energy is another.[6] In Winter time, most energy is utilized for heating or illumination purposes but since there is less sunshine for example and the days are shorter, the energy should to be stored while there is sun or to be transported from areas of the world where there is more sunshine duration.

Transporting energy directly *via* landlines is a problem, since there is a huge loss because of resistance and produced heat. A common way to store energy is by pumping water uphill into a reservoir and, when needed, the water runs downhill to produce energy by passing through turbines.[7] A drawback is that mountains are not omnipresent, allowing to implement such a system and even if, it comes along with a huge amount of construction and cost. Another possibility are batteries: they

could be charged at a certain location and transported to a location of interest.[8] A major disadvantage is that such batteries are often very heavy and thus their transportation is difficult and energy intensive.

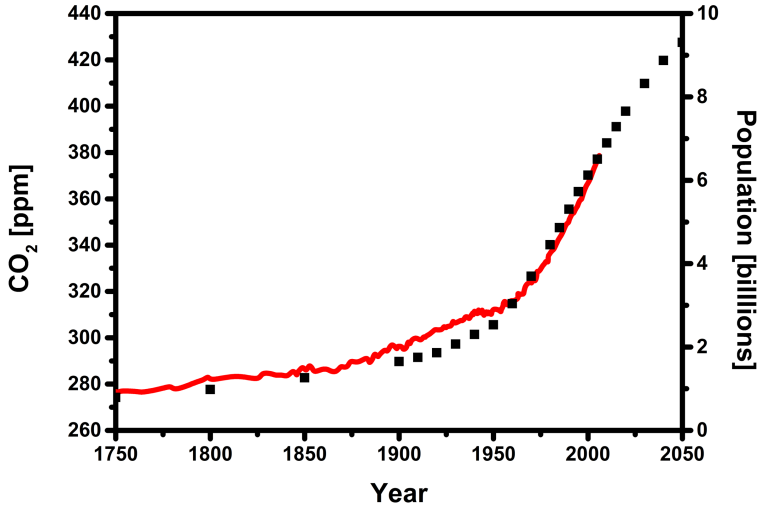


**Figure 1.2:** (a) Exponential growth of the world population from 1750 to 2050 (black squares),[9,10] (b) Exponential increase in greenhouse gas emissions from 1750 to 2006 (red trace).[11]

A more economical way to store energy would be using the smallest batteries known to man: chemical bonds. The energy produced can be stored between two atoms to form a stable molecule and that energy could be released at any desired location when needed. The produced molecule should be easily transportable, light and no waste products as $CO_2$ or other greenhouse gases should be released upon combustion.

A molecule that caught much attention that partially fulfills these criteria is molecular hydrogen.[12,13] But unlike fossil fuels, hydrogen is not readily available in nature. However, it can be produced from many energy sources and be used as a fuel, either for direct combustion or in a fuel cell, only producing water as byproduct.[14] Hydrogen possesses the highest energy content compared to any known fuel and is globally accepted as an environmentally benign secondary form of renewable energy. It can be stored as compressed gas, cryogenic liquid, solid hydride or in hydrogen carriers as formic acid for example.[15]

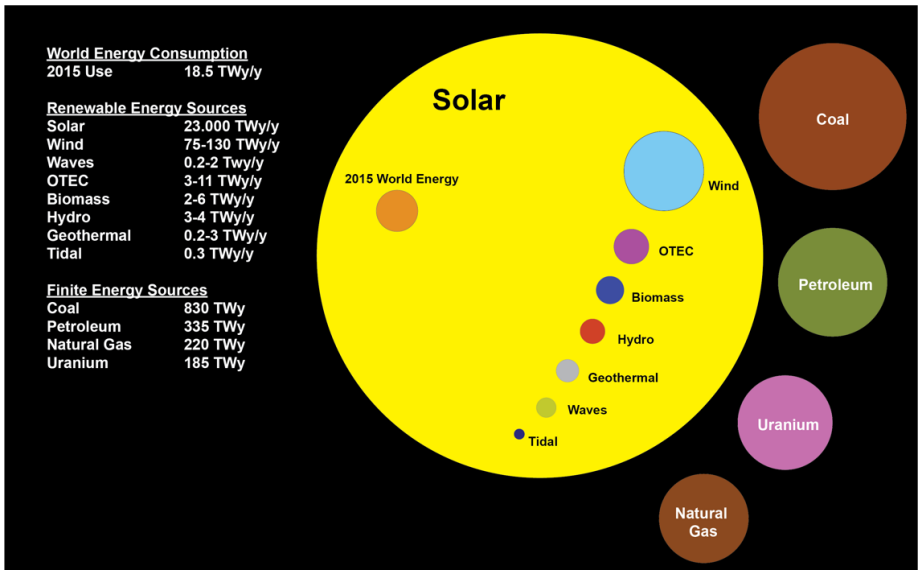


**Figure 1.3:** Totally estimated, recoverable finite (outside the solar circle) and the yearly potential energy of renewable (inside the solar circle) planetary energy reserves in Terawatt-years by 2015. The annual potential energy of the sun is 1250 times higher than the annual energy use of the whole planet. The energy values were transferred into a volume of a sphere, yet, the representation is only two-dimensional, so the real difference of the different values is much higher. The figure is adapted from reference [5].

Molecular hydrogen can be produced from fossil fuels by steam reforming, partial oxidation, autothermal reforming or hydrocarbon pyrolysis.[16] When renewable sources are used instead, $H_2$ can be produced by biomass, thermochemical or biological processes. One more interesting way is water splitting either by thermolysis or photo-electrolysis. When the required energy is provided by renewable energy sources, the hydrogen produced is the unarguably the cleanest fuel available.

Nature uses the sun's radiant energy in a process called photosynthesis, storing energy in chemical bonds.[17] Mimicking that process is one of the biggest challenges of current research and accomplishing a so called artificial photosynthesis would be a big leap for mankind to overcome our addiction for ever-increasing energy.[18–22]

# 2

# Theoretical Background

## 2.1 Hydrogen

### 2.1.1 What is Hydrogen?

There are at the moment 118 elements known in chemistry of which over 90 occur naturally. Hydrogen is the lightest element and it exists as $H_2$. Dihydrogen consists of two protons and two electrons. After its discovery in 1766 by the British chemist and physicist Henry Cavendish, its name "hydro-gène" ("water producer") was first introduced by the French chemist Antoine Laurent de Lavoisier in 1787, from the Greek words "hydor" (water) and "genes" (producing).[23] It was the first element created in the Universe after the Big Bang and it is the first element in the periodic table.[12] After hydrogen was discovered in the 18$^{th}$ century as a flammable gas, important technologies for the production and the use of hydrogen were developed in the 19$^{th}$ and early 20$^{th}$ century.[24] Its potential for the energy industry was then recognized and it was already early envisioned,[13] that hydrogen could play a big role as an energy source in the future, given its very high energy content (120 MJ/kg for hydrogen versus 44 MJ/kg for gasoline, Figure 2.1).[25] This is one reason why it has been used as a fuel for space travel since the 60s.[26] Hydrogen is a clean and sustainable energy option, because its combustion product with oxygen is only pure water[14]. Yet, so far, the energy sources used mostly still rely on fossil fuels.

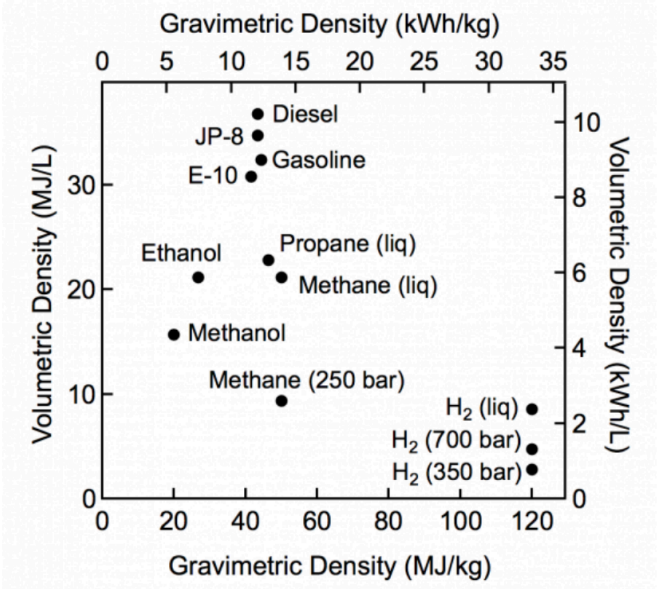


**Figure 2.1:** Comparison of the volumetric versus gravimetric energy density of a group of materials and technologies. Hydrogen can be found on the bottom-right corner. The figure is reproduced from reference [27].

### 2.1.2 Where can hydrogen be found?

Hydrogen is the first and most abundant element in the universe and its mass fraction is estimated in the order of 75% and more than 90% by the number of atoms.[12] Even though space is filled with highly diluted hydrogen, gigantic gas clouds that consist of hydrogen and suns that release their radiant energy by "hydrogen burning", the proportion of hydrogen on Earth is much smaller. The part of the Earth that is accessible to humans makes up only less than 1% of the Earth's mass. The proportion of molecular hydrogen in the Earth's atmosphere is only 0.5 parts per million (ppm). Furthermore, hydrogen on Earth exists only very rarely in its molecular form; it is commonly found in chemical compounds as hydrocarbons or water. In fact, the largest proportion of hydrogen on Earth can be found in the form of water.

### 2.1.3 How can hydrogen be produced?

Since hydrogen is only rarely found in its pure form, technologies were developed to produce chemically larger amounts of molecular hydrogen.[28–31] Most ways of producing hydrogen still rely on fossil fuels. The most widespread procedure is steam-reforming of natural gas, whereby methane and water react at high temperatures (1000-1400 K) to yield carbon monoxide and three equivalents of dihydrogen ($CH_4 + H_2O \rightarrow CO + 3\ H_2$).[32] Not only are hydrocarbons used as a hydrogen source, energy is needed to sustain the required high temperatures and CO is produced as a byproduct.

Electrolysis of water is another way of producing clean hydrogen, hence two molecules of water are reassembled into one molecule of oxygen at the anode and two molecules of hydrogen at the cathode.[33] When the electric energy is gained by renewable energies (i.e. solar energy), this process is the cleanest way of producing molecular hydrogen. However, the electrodes required for electrolysis are made from noble metals as platinum and are thus expensive.

Homogeneous catalysts that can produce molecular hydrogen either electrochemically or photochemically have been developed within the last decades (see below). They are very attractive since their chemical and photochemical properties can be scrutinized and tuned on a molecular level. Moreover, in homogeneous systems, catalysts may be covalently bound to photosensitizers, which could lead to more efficient electron transfer. Thus, molecular devices for water splitting based on such systems are of great interest, especially those relying on Earth-abundant metals.

Nature itself utilizes a more sophisticated system to store the sun's energy in chemical bonds. A process known as photosynthesis splits water and stores solar energy in chemical bonds.

## 2.2 Natural Photosynthesis

Photosynthesis is nature's way to transform solar energy into storable chemical energy. This process is the foundation for higher life-forms. Photosynthesis takes place in plants, algae and cyanobacteria, where sunlight is used to produce high-energy chemicals as proteins and sugars from carbon dioxide and water. Not only 100 billion tons of biomass are produced by photosynthesis annually, but its "waste product" dioxygen is what most living aerobic organisms rely on for respiration.[34] Also, fossil fuels, such as oil, natural gas, and coal originate from photosynthetic activity.[35] The success of natural photosynthesis can be traced back to the fact that sunlight, water, and carbon dioxide are available in abundant quantities on Earth. The process of photosynthesis can be divided into two separate processes, the light-dependent reaction and the light-independent reaction, where carbon dioxide is fixed. The light-dependent reaction takes place in the thylakoid membrane of chloroplasts. The absorbed solar energy is used to drive an electron transport chain to oxidize water to dioxygen and to afford reducing equivalents NADPH, which can be viewed as the biological equivalent of molecular hydrogen. Since the oxidation of water at the oxygen evolving complex (OEC) requires strong oxidants, and the reduction of $NADP^+$ to NADPH requires a relatively strong reductant, the light-driven reaction is split into photosystem I (PSI) and photosystem II (PSII). Both systems contain a central pair of chlorophyll molecules (P700 for PS I and P680 for PS II) in close van der Waals distance. This dimer of chlorophyll molecules is often referred to as the

"special pair" and it is enclosed by several well-organized chromophores. These chromophores harvest as much light as possible and transfer their energy to the embedded reaction center.[36] The so-called Z-scheme (Figure 2.2) provides a schematic overview on the spatial separation and the energy levels in PS I and PS II.[22,37] Once photo-excited, either by direct light absorption or by transduction of singlet excited state energy from antenna pigments, the reaction center injects an electron to a neighboring pheophytin.[38] Electron-transfer processes tend to be rather slow over large distances and, thus, have to be non-competitive with other energy-consuming reactions. To overcome this challenge, photosynthetic organisms have developed sequences of short-range electron transfer events, which eventually generate long-lived transmembrane charge-separated states. The initial electron transfer from the special pair of PSII to a neighboring pheophytin for instance occurs within 3 ps.

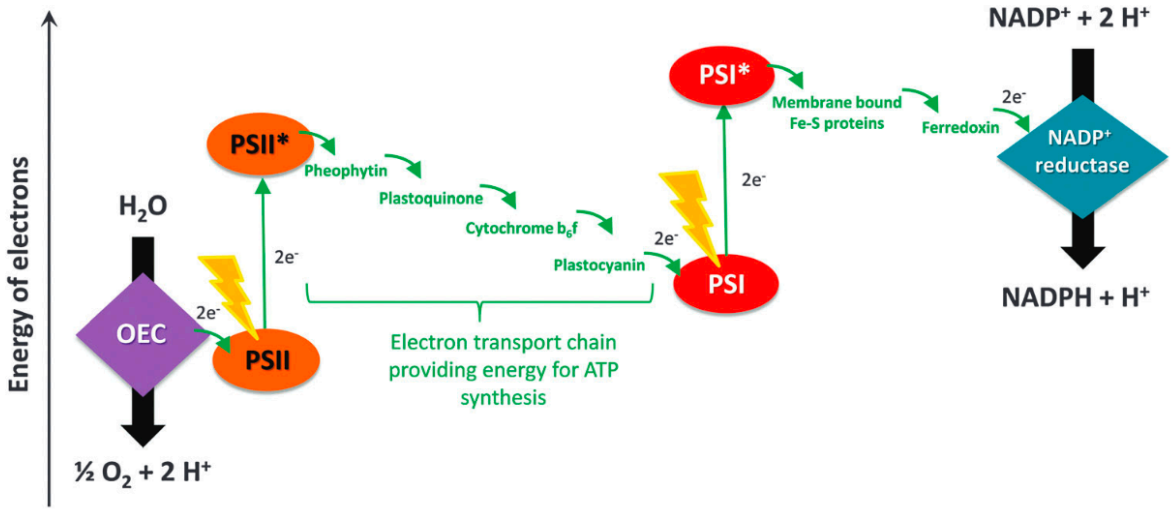


**Figure 2.2:** The Z-scheme illustrating electron transport in photosynthesis. The scheme shows the light absorbing units PSI and PSII, the electron transport chain, the oxygen evolving centre (OEC) and the $NADP^+$ reductase. The figure is reproduced from reference [19].

The reduced pheophytin transfers its electron to an electron-accepting plastoquinone Q within a few hundred picoseconds. Plastoquinone accepts two electrons and two protons to yield plastoquinol $QH_2$ in the micro- to millisecond time scale.[37] Afterwards, it diffuses from the reaction center to the cytochrome $b_6f$ complex. As the electrons are shuttled through the electron transport chain this complex, together with a plastocyanin, releases energy to produce a chemiosmotic potential by pumping protons across the membrane and into the thylakoid space. An ATP synthase enzyme uses that chemiosmotic potential to produce ATP from ADP during photophosphorylation.[39] ATP

is required, along with NADPH, to convert $CO_2$ into energy-rich carbohydrates.[40] The oxidized special pair is re-reduced to its neutral form *via* a redox-active tyrosine, which channels electrons from the oxygen evolving complex.[41,42] Oxygen evolution is triggered by four sequential photon absorption events at a nearby antenna array.[43] Each photon that is absorbed and delivered to the reaction center results in 1 $e^-$ oxidation of the OEC. Following buildup of four oxidative equivalents at the OEC leads to $O_2$ evolution. The oxidation is accompanied by proton loss and release from the OEC through a proton exit channel that avoids local charge buildup. The gained electrons, are then transferred to a chlorophyll molecule in Photosystem I. There, it is further excited by the light absorbed by that photosystem. The electron is then passed along a chain of FeS-clusters functioning as electron acceptors. During this process, some of the energy is used to move hydrogen ions across the thylakoid membrane into the lumen. The electron is eventually used to reduce the co-enzyme $NADP^+$ with a $H^+$ to NADPH, which has functions in the light-independent reaction.

Since decades, the goal of research groups worldwide is to understand and mimic this sophisticated machinery. The key concepts, which are typically borrowed from natural photosynthesis in order to achieve efficient artificial solar to chemical energy conversion, are: i) light harvesting, ii) energy transfer, and iii) electron transfer.

## 2.3 Artificial Photosynthesis

### 2.3.1 Photocatalytic water splitting

Photocatalytic water splitting is a very attractive method to store solar energy in chemical bonds.[44–47] This and related approaches are often referred to as artificial photosynthesis.[18–20] A full functioning water splitting system consists of a photosensitizer (PS) which acts as a photo-activated "electron pump", a water oxidation catalysts (WOC) which oxidizes $H_2O$ to $O_2$ and protons and a water reducing catalyst (WRC) which reduces protons to $H_2$ (Scheme 2.1). It turned out to be highly challenging to drive both half reactions of this highly complex process with artificial molecular catalysts simultaneously. Molecular approaches are often supported by the use of materials.[48–52] A completely homogeneous molecular water splitting system will most probably not work since back-electron transfer between the $O_2$ and $H_2$ evolving half reactions will short-ciruit the whole system.[19] Light-driven, full water splitting was mainly achieved photo-electrochemically with heterogeneous semiconductors or dye-sensitized materials.[53] This is why, especially for homogeneous, molecular-based water splitting, both half-reactions are investigated separately by replacing the WOC by a

sacrificial electron donor (SED) for water reduction and the WRC by a sacrificial electron acceptor (SEA) for water oxidation.[54–59]

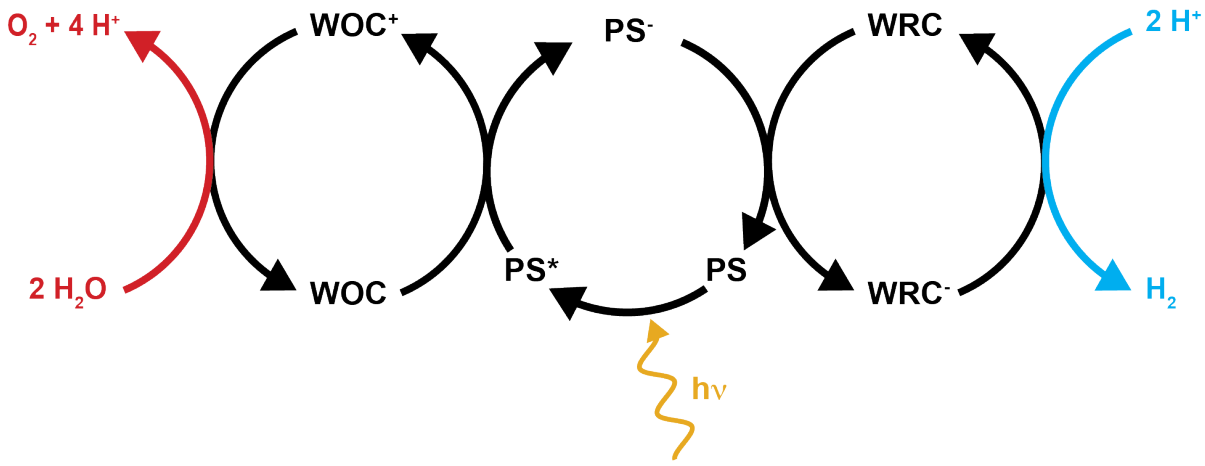


**Scheme 2.1:** Schematic representation of a complete water splitting system: (i) when the photosensitizer (PS) is excited by light (PS*) it oxidizes a water oxidation catalyst (WOC) after excitation, (ii) the oxidized WOC itself oxidizes water to yield oxygen and four protons, (iii) the reduced PS reduces a water reduction catalyst (WRC) and (iv) the reduced WRC is then reducing protons to eventually form dihydrogen. The Scheme was adapted from reference [60].

### 2.3.2 Photocatalytic water oxidation

Photocatalytic water oxidation is a highly complex process, since four electrons have to be transferred. Two water molecules are transformed into one oxygen molecule and four protons as well as four electrons ($2\ H_2O \rightarrow O_2 + 4\ H^+ + 4\ e^-$). This process is more difficult to achieve than the two-electron proton reduction (see below) and is considered to be the bottleneck to obtain a full water-splitting device. Water oxidation catalysts are often investigated electrochemically or using ceric ammonium nitrate [$(NH_4)_2Ce(NO_3)_6$]-driven chemical water oxidation at low pH values. Photocatalytic oxygen evolution is most often performed with [$Ru(bpy)_3$]$Cl_2$ **1** as a photosensitizer (PS, see below) and sodium peroxodisulfate ($Na_2S_2O_8$) as sacrificial electron donor. Up to now, the most efficient and stable molecular WOCs are ruthenium-based complexes.[61] Catalysts based on earth abundant metals such as manganese, cobalt and copper have also been reported.[19]

### 2.3.3 Photocatalytic water reduction

Photocatalytic water or proton reduction is a two-electron process in which the protons are reduced to molecular hydrogen ($2\ H^+ + 2\ e^- \rightarrow H_2$). In the last decade, aqueous photo-catalytic hydrogen production was thoroughly scrutinized. Various PS and WRC have been investigated and

the performance of this half reaction was constantly improved. However, only a few SEDs have been discovered so far; mainly ascorbate ($AscO^-$) **2**, triethanolamine (TEOA) **3** or trialkylamines are used (Figure 2.3).[62] Under slightly basic conditions, amines are used for photo-catalysis and are irreversibly oxidized to products that do not interfere with the catalytic cycle. For acidic pH-values, ascorbic acid (AscOH), also known as vitamin C, is mainly used as SED.[63,64] When ascorbate is oxidized, it forms dehydroascorbic acid (DHA) **4** which can again be reduced, thus regenerating ascorbic acid (i.e. TCEP (tris(2-carboxyethyl)phosphine) **5**).[60]

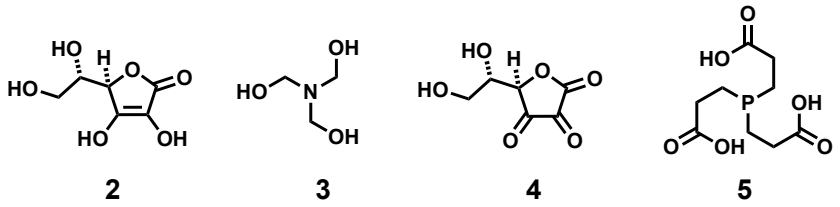


**Figure 2.3:** Some commonly used sacrificial electron donors (ascorbic acid **2**, triethanolamine **3** and TCEP **5**) and the oxidized form of ascorbic acid **4**.

The AscOH-DHA pair is a quasi-reversible $e^-$-donor and can cause undesired back electron-transfer from reduced PS or WRC to DHA which inhibits catalysis.[65] WRCs have been widely explored over the last years and for photo- and electrocatalysis various complexes based on earth-abundant metals including cobalt, nickel, iron or molybdenum have been reported (see below). Three key parameters are crucial for a good catalytic performance: i) long term stability of the WRC, which is characterized by the turnover number (TON, $H_2$/WRC), ii) the amount of hydrogen molecules produced per WRC over time (turnover frequency or TOF, in $s^{-1}$ or $h^{-1}$) and iii) a catalyst that only requires a low overpotential to produce molecular hydrogen. The overpotential describes the potential at which the WRC reduces protons compared to the thermodynamic potential of $H^+$ reduction. Artero and Savéant could show, that the TOF and the overpotential are interdependent: the higher the applied overpotential, the higher the TOF.[66]

### 2.3.4 Photosensitizers

The first step of an artificial photosynthetic system is light-harvesting by a chromophore. Such a light-absorbing component is analogous to the photosynthetic pigments. This chromophore should efficiently absorb and convert the incoming solar energy into a long-lived excited state that can transfer an electron to an acceptor for the creation of a charge-separated state, thus generating the required thermodynamic driving force for the desired chemical reactions. Both, photo-active molecular dyes

and semiconductors can favor electron transfer and may be used as light-harvesting chromophores in a future artificial device for $H_2O$ splitting. Molecular photosensitizers are mainly based on precious metals, including: ruthenium **1**, rhenium **6**, iridium **7**, rhodium or platinum, but also organic dyes such as Eosin Y **8** or Rose Bengal **9** have been investigated (Figure 2.4).[67–70] In the last few years, also homo- and heteroleptic Cu(I) complexes as **10** were used as noble metal-free molecular PS.[71–75]

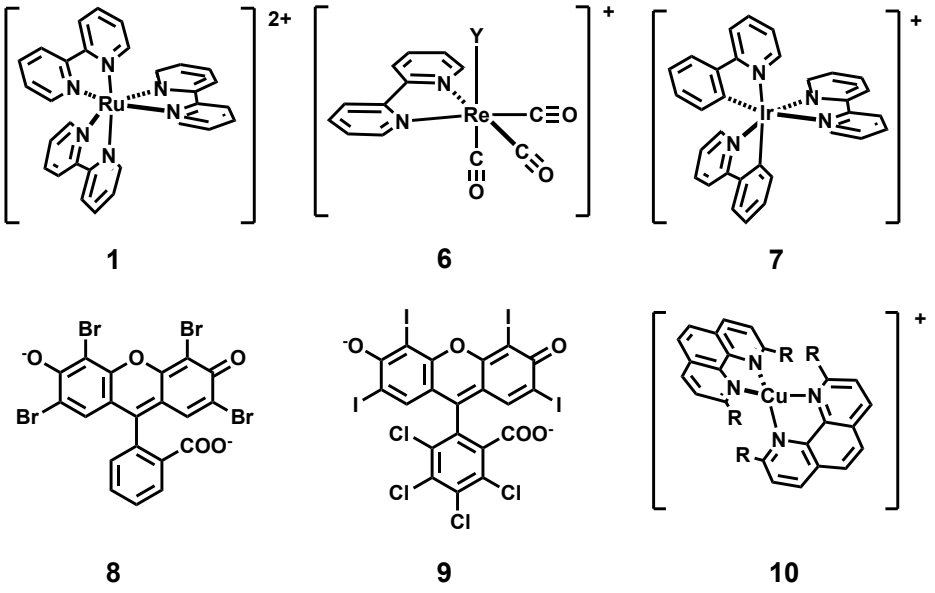


**Figure 2.4:** Structures of some commonly used noble metal-based photosensitizers (top), organic photosensitizers Eosin Y and Rose Bengal, as well as a homoleptic copper-based photosensitizer (R = *s*-butyl) used for solar hydrogen production. The well-known $[Ru(bpy)_3]Cl_2$ **1** was used as a photosensitizer in the course of this work

Yet, the most well-studied molecular photosensitizers for electron-transfer processes are the ruthenium(II) polypyridyl, $[Ru(bpy)_3]^{2+}$-type complexes (bpy = 2,2′-bipyridine).[67,76–78] These complexes have been studied since the early 1970s when it was discovered that they could undergo electron transfer from their excited states to a sacrificial electron acceptor.[79,80] This opened new possibilities and these complexes have been used in various applications ever since, also in the field of photo-redox catalysis.[81–85] These photosensitizers have a distinct absorption in the visible region ($\lambda_{max}$ ≈ 450 nm), and upon illumination, one electron in a metal-centered $t_{2g}$-orbital is excited to a ligand-centered $\pi^*$-orbital. In this metal-to-ligand charge transfer state (MLCT), the ruthenium center has formally been photo-oxidized to Ru(III), while the bipyridyl ligand has undergone a single electron reduction.

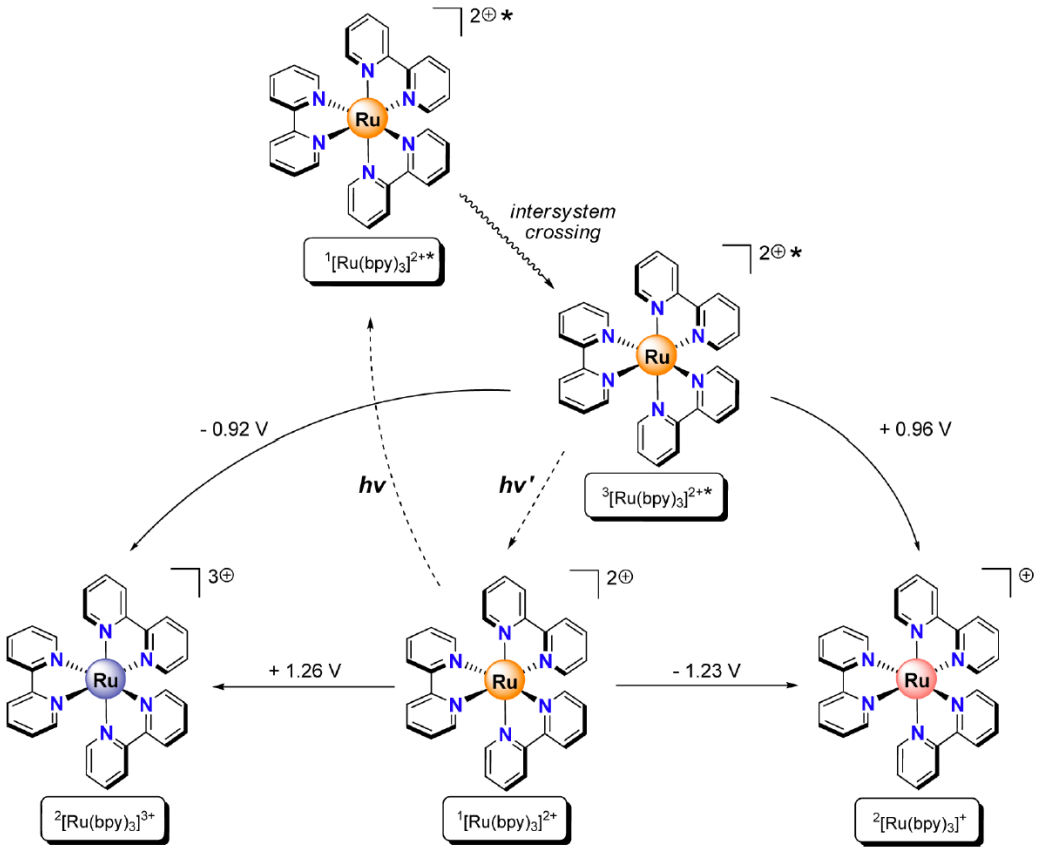


**Scheme 2.2:** Schematic overview of the photochemistry of $[Ru(bpy)_3]^{2+}$. Excited $[Ru(bpy)_3]2+$ The figure is reproduced from reference [21].

The initial photo-generated state, the lowest excited singlet state ($^1[Ru(bpy)_3]^{2+*}$), is short-lived and undergoes a rapid intersystem crossing to yield a long-lived triplet state, $^3[Ru(bpy)_3]^{2+*}$, that has the potential to take part in a single-electron transfer.[70] The electronic configuration of this excited state has almost only triplet character and can be described as a $^3[(d_\pi)^5(\pi_{bpy}^*)^1]$-state. Since the conversion back to the singlet state is spin-forbidden and decays to the ground state on the microsecond timescale, the lifetime of the excited triplet state is long. It is sufficiently long to engage in bimolecular electron-transfer reactions. The photo-excited state is more oxidizing and more reducing than the ground state of $[Ru(bpy)_3]^{2+}$. This dual nature of the excited state makes it serve either as a single-electron oxidant or reductant, as can be seen in Scheme 2.2.[21,86–89] This unique property of $[Ru(bpy)_3]^{2+}$-type complexes coupled with their redox properties, chemical stability, excited-state reactivity, excited-state lifetime and synthetic flexibility makes them highly versatile and attractive for both photo-oxidation and photo-reduction.

## 2.4 Natural Hydrogenases

Hydrogenases are a group of natural occurring metalloenzymes than can catalyze one of the simplest molecular reactions: the conversion of two protons and two electrons into molecular hydrogen and the reverse reaction (Eq. I).[90–92]

$$2\,H^+ + 2\,e^- \rightleftharpoons H_2 \qquad \text{(Eq. I)}$$

This reaction occurs at a specialized metal cluster that increases the acidity of $H_2$ dramatically and is strongly accelerated by a nearby base. Dihydrogen formation involves the coupling of $H^-$ and $H^+$ and its heterolytic mechanism has been confirmed by H/D isotope exchange experiments.[93] Hydrogenases can be found in archaea, bacteria and some eukarya and can be divided into three classes, depending on the metal ion composition of their active site, hence [Fe], [FeFe] and [NiFe] hydrogenases.[90–92,94–98]

[Fe] hydrogenases are found in methanogenic archaea only. They also contain four different [NiFe] hydrogenases, but [Fe] hydrogenases are upregulated under conditions with low nickel concentrations.[99] The enzyme catalyzes one of the reaction steps in the methanogenic energy conversion pathway from carbon dioxide with $H_2$ to methane.[94] The reaction is the reversible reduction of the substrate methenyltetrahydromethanopterin (methenyl-$H_4$MPT$^+$) with $H_2$ to methylene-$H_4$MPT and a proton (Figure 2.5 and Scheme 2.3).[100] Therefore, [Fe] hydrogenases are also referred to as: "$H_2$-forming methylenetetrahydromethanopterin (methylene-$H_4$MPT) dehydrogenase" (Hmd). The enzyme harbors a unique Fe-cofactor (Fe-guanylylpyrodinol, Fe-GP) and does not contain any iron–sulfur clusters. The iron atom in [Fe] hydrogenases has CO ligands bound and displays an unusual coordination sphere.[101–103]

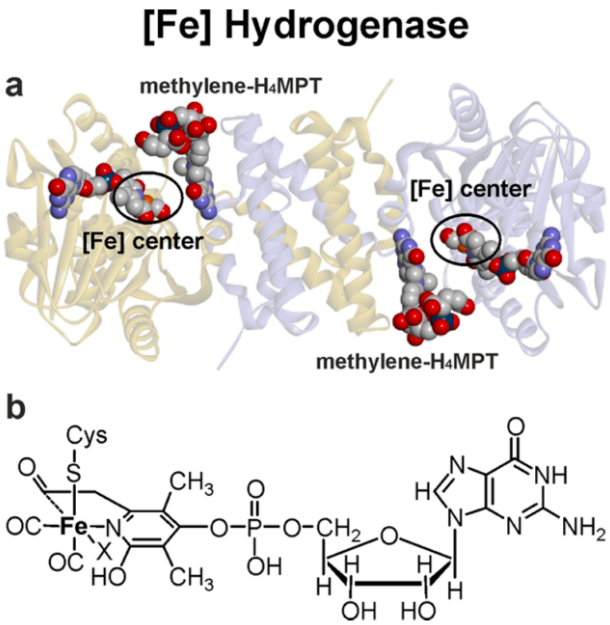


**Figure 2.5:** (a) X-ray structure of the dimeric *Methanocaldococcus jannaschii* (*Mj*) [Fe] hydrogenase (C176A) with the substrate (methylene-$H_4$MPT) in its open form (PDB 3H65).[104] The Fe-GP cofactor and the substrate are shown by sphere representation. (b) The chemical structure of the Fe-GP cofactor. The possible $H_2$-binding site is indicated as "X". The figure was taken from reference [92].

Its structure and catalytic reaction mechanism differ from that of [NiFe] or [FeFe] hydrogenases,[105] and its activity is dependent on the substrate, methenyl-$H_4$MPT$^+$. The enzyme does not reduce electron acceptors like artificial dyes and the $H_2$ activation occurs only in the presence of the substrate.[101].

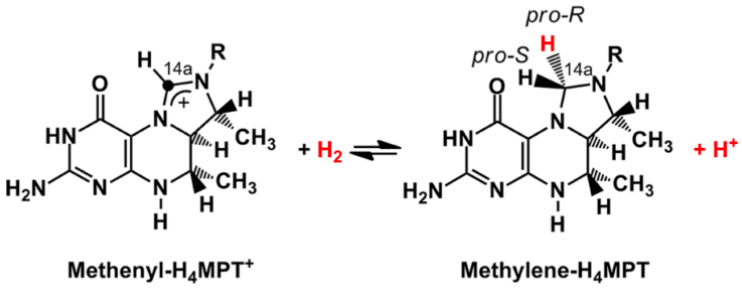


**Scheme 2.3:** Reaction of methenyl-$H_4$MPT$^+$ with $H_2$. The [Fe] hydrogenase catalyzes the reversible reduction of the substrate methenyltetrahydromethanopterin (methenyl-$H_4$MPT$^+$) with $H_2$ to methylene-$H_4$MPT and a proton by transferring a hydride ion to the *pro*R position of the C14a-carbon of methylene-$H_4$MPT. The figure was taken from reference [92].

The iron atoms in [FeFe] and [NiFe] hydrogenases are ligated by $CN^-$ and CO and the metal centers are bridged by sulfur atoms (Figure 2.6).[106–108] The ligands help to tune the metal centers for

optimal interaction with $H_2$ and to bind the heterolytically generated $H^-$ terminally to Fe. The resulting proton on the other hand is transferred to a pendant amine base in the azadithiolate ligand. $CN^-$ and CO are strong-field ligands which lead to low-spin Fe complexes.[108–111] Simultaneously, they provide empty acceptor orbitals for the two extra electrons of the forming hydride. The hydride acceptor ability of the metal is adjusted by fine-tuning the energies of the orbitals by either a charged $CN^-$ ligand or a CO ligand serving as a σ-donor and π-acceptor.

The pendant amine in close proximity of the metal center, whose basicity is fine-tuned by the binding geometry and the surrounding of the nitrogen, acts as a base. The secrets of the high hydrogen splitting and formation efficiency of those hydrogenases are the geometrical arrangement of the base as well as the electronic fine-tuning of the metal site and the base.[112] Even small changes in this highly-evolved system can lead to drastic reduction in activity and stability.

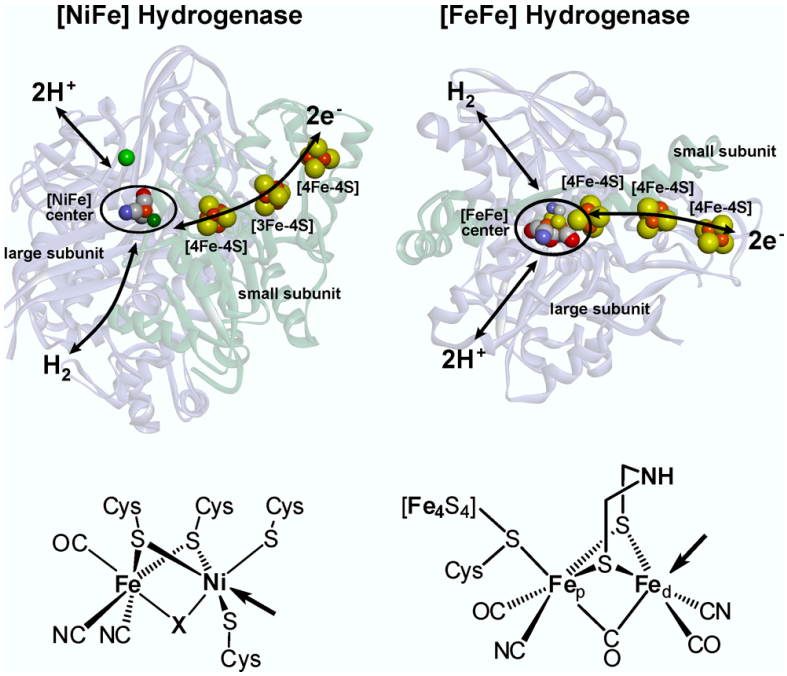


**Figure 2.6:** Structures of the [NiFe] hydrogenase from *Dv*MF[113] and of the [FeFe][114] hydrogenase from *Dd*. The electron transfer chain (*via* iron–sulfur centers) is schematically indicated as well as pathways for dihydrogen and the $H^+$ transfer. The chemical structures of the active sites of the two classes of hydrogenases; arrows indicate the open metal coordination site for hydrogen to bind. The figure is reproduced from reference [92].

Hydrogenases can be found in the cytoplasm or periplasm, membrane-bound or in soluble form.[115] The primary functions of hydrogenases are to balance the redox potential of a cell and to provide energy for the organism by the oxidation of molecular hydrogen. They can split $H_2$ and provide electrons or they can remove reducing equivalents by the production of molecular hydrogen.

Hydrogenases can be tuned either for hydrogen oxidation or hydrogen reduction, depending on the location in the cell. Most purified hydrogenases that show catalytic activity are catalyzing the reaction in both ways, depending on the physiological context in the cell.

While [NiFe] hydrogenases are usually more active in $H_2$ oxidation [FeFe] hydrogenases are better in producing dihydrogen.[90,115] Some [FeFe] hydrogenases show extremely high turn-over frequencies of ~$10^4$ molecules of $H_2$ per second at room temperature.[116,117] Their catalytic center is oriented in a highly-optimized protein environment that not only provides ligands for the metals but also orthogonal channels for electron transfer, proton transfer and dihydrogen transfer. Efficient electron delivery to or from the active site in [FeFe] hydrogenases is achieved by a directly bound [4Fe-4S] center which acts as an electron wire. Even though there are certain hydrogenase species that are oxygen-tolerant, most hydrogenases are inhibited by traces of molecular oxygen, especially the [FeFe] hydrogenases.[118,119] Most [NiFe] hydrogenases are reversibly inhibited by molecular oxygen and can be restored in a reducing atmosphere. Furthermore, these enzymes are prone to denaturation if not used at certain pH values or temperatures. All this, and the fact that their synthesis and purification is not trivial, encouraged scientists try to mimic their unique reactivity.

## 2.5 Bioinspired Hydrogenase Model Systems

When the crystal structures of the [FeFe] and [NiFe] hydrogenases in the late nineties and of the [Fe] hydrogenase in 2008 were published, chemists started to mimic the active sites of the enzymes.[120–122] Due to the complex arrangement around the metal core, it was challenging to synthesize functional models. The active site of all hydrogenases is deeply buried in the protein scaffold and provides a hydrophobic pocket. The hydrogenase itself, is perfectly tailored for the reaction to occur by providing channels for hydrogen, acidic and basic residues and $H_2O$ molecules for the proton transfer and a pathway for electrons through FeS clusters. It seems contra intuitive to assume that a hydrogenase mimic would thus be working in aqueous solution. The key features of a [FeFe] hydrogenase mimic, which should be prone to hydrogen evolution, should have are i) stabilization of an open coordination site where $H_2$ can bind, ii) a base in close proximity to shuttle protons and iii) a contact site for external redox partners. A bridging amine had a beneficial impact in many cases.

Despite the hundreds of structural models developed to date, only a few have shown electrocatalytic activity related to proton reduction or hydrogen oxidation.[123,124] Yet, many [FeFe] hydrogenase analogs have been reported that actually do undergo electrocatalytic hydrogen

evolution.[125,126] Rauchfuss and coworkers reported in 2001 the first di-iron dithiolate system, $[Fe_2[\mu\text{-}S_2(CH_2)_3](CN)(CO)_4(PMe_3)]$ **11**, which evolved hydrogen catalytically (Figure 2.7).[127]

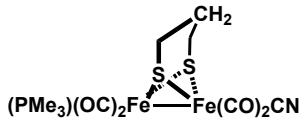


**11**

**Figure 2.7:** The first di-iron dithiolate system $[Fe_2[\mu\text{-}S_2(CH_2)_3](CN)(CO)_4(PMe_3)]$ **11**, mimicking the active site of [FeFe] hydrogenases with catalytic activity, reported by Rauchfuss.

However, the efficiency of this system is far below that of the natural hydrogenase. Following this work, many related systems have been reported that display electrocatalytic activity. Mostly, however, they operate with relatively large overpotentials.[124,128] Nevertheless, these models have helped to understand the roles of bridging thiolate ligands and the hydride-binding modes associated with their catalytic function.[123]

More than 50 structural mimics of [NiFe] hydrogenases have been reported. In the beginning, mostly biomimetic complexes that differed significantly from the enzyme structure showed electrocatalytic behavior.[129–138] More recently, two competent Ni–Fe catalysts were reported that mimic both the structure and function of active [NiFe] hydrogenase.[139,140] A nickel–iron dithiolato hydride $[(CO)_3Fe(pdt)(\mu\text{-}H)Ni(dppe)]^+$ **12** (pdt = 1,3-propandithiolate, dppe = $1,2\text{-}C_2H_4(PPh_2)_2$) from the Rauchfuss lab is an active catalyst for the reduction of trifluoroacetic acid in $CH_2Cl_2$ (Figure 2.8).[139] Catalytic activity of another nickel–iron dithiolato complex $[Ni(xbsms)FeCp(CO)]^+$ **13** ($H_2$xbsms = 1,2-bis(4-mercapto-3,3-dimethyl-2-thiabutyl)benzene, Figure 2.8) with a chelating $S_4$-ligand was reported by Fontecave and Artero, with catalysis observed with trifluoroacetic acid in dimethylformamide (DMF).[140]

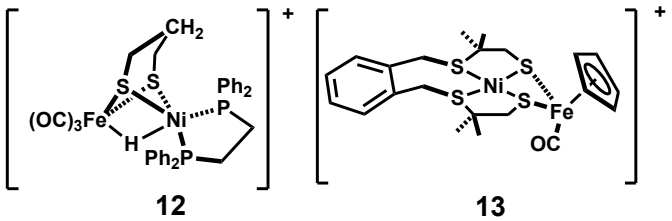


**12** **13**

**Figure 2.8:** [NiFe] hydrogenase active site mimics (left) $[(CO)_3Fe(pdt)(\mu\text{-}H)Ni(dppe)]^+$ **12** shows electrocatalytic activity towards hydrogen evolution from trifluoracetic acid in $CH_2Cl_2$; (right) $[Ni(xbsms)FeCp(CO)]^+$ **13**, an active iron-nickel containing electrocatalyst for hydrogen evolution from trifluoracetic acid in DMF.

Several non-biomimetic systems display high efficiencies for $H_2$ evolution. The most successful molecular and noble-metal free ones are Co-[55,59,141–145], Ni-[143,146–148] and Mo-[149,150] based systems (Figure 2.9). The mononuclear nickel complex $[Ni(PPh_2NPh_2)_2]^{2+}$ **19**, with non-coordinating pendant amines incorporated into the backbone of cyclic diphosphane ligands is highly active for catalytic hydrogen evolution, with a reported turnover frequency of 350 $s^{-1}$under optimal conditions.[151–153] This is comparable to those of natural [NiFe] hydrogenase enzymes. Mechanistic studies suggest that the pendant amines act as a proton relay to the metal site, stabilize dihydrogen binding, and lower the barrier for heterolytic formation and cleavage of dihydrogen. This functionality in the second coordination sphere leads to much higher turnover rates and lower overpotentials than with complexes lacking those pendant bases.[153–157]

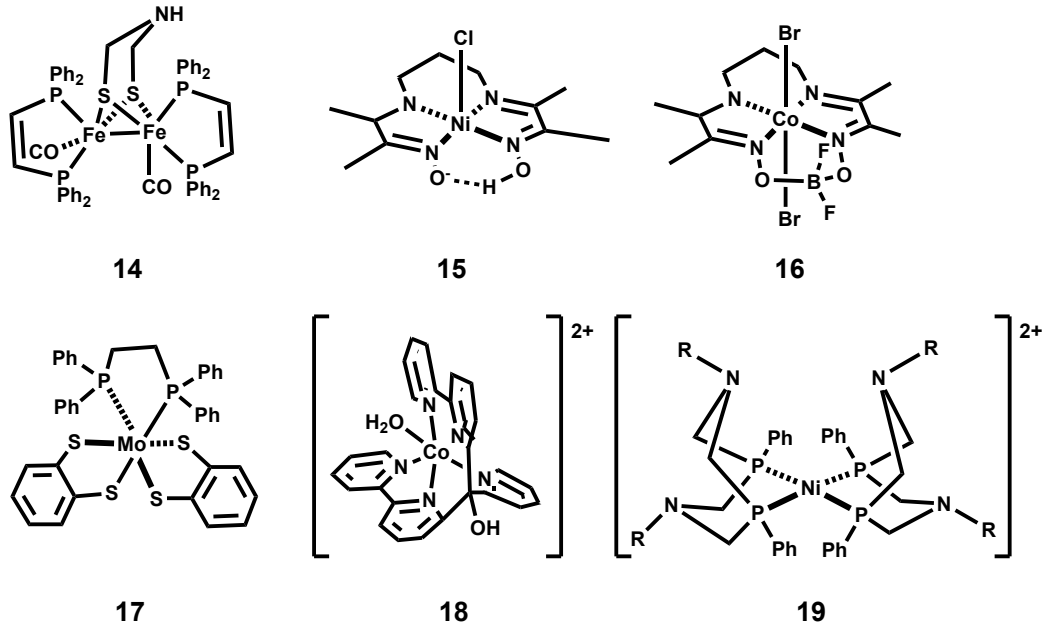


**Figure 2.9:** Structures of selected noble metal-free water reduction catalysts. Top (from left to right): iron- based hydrogenase mimic **14** and nickel/cobalt diimine-dioxime (for cobalt: Cobaloxime) type complexes **15** and **16**. Bottom: Molybdenum dithiolato complex **17**, polypyridine based cobalt WRC **18** and DuBois-type nickel complex **19**.

Other mimics rely on cobalt with nitrogen-based ligands and have been reported to be active hydrogen-evolution catalysts. These complexes usually involve imine, oxime, glyoxime or polypyridin ligands. Cobalt diglyoxime, also known as cobaloximes, and polypiridyl complexes are promising molecules that evolve hydrogen in both aqueous and organic media (Figure 2.9).[142,144] They are not only electrocatalytically active but also photo-catalytically. Catalyst **17** for instance displays turnover

numbers exceeding 30.000 when TCEP is used in combination with ascorbic acid acting as an electron relay.[158]

While good progress was made by mimicking the [FeFe] and [NiFe] active site, there are still difficulties to adapt to the protein scaffold responsible for the transport of substrates, products and electrons. One possibility would be to assemble a synthetic hydrogen evolving complex within a protein scaffold and thus enhance its reactivity. The result of incorporating a metallocofactor into a protein scaffold is commonly referred to artificial metalloenzymes (ArM).[159]

## 2.6 Towards artificial hydrogenase enzymes

### 2.6.1 Artificial Metalloenzymes

Pioneering work in 1976 by Kaiser as well as Whitesides and Wilson resulted in a blooming new strategy to create artificial enzymes.[160,161] The resulting second coordination sphere resulting from incorporation can interact with the metal catalyst, substrates, intermediates or products to facilitate reactions or to discriminate similarly reactive moieties on substrates.[162] Furthermore, since the homogenous small molecule catalyst is incorporated into a genetically-encoded protein matrix, the performance of the ArM can be improved by mutagenesis.[163–166] Relying on this technique, ArMs can lead to systems suitable for practical application and provide insights in how a second coordination sphere influences the performance of organometallic catalysts.

There are four complementary strategies commonly used to integrate a metallic cofactor within a well-defined second coordination sphere environment provided by a host protein (Figure 2.10):

(i) **Covalent anchoring** involves an irreversible and high-yielding reaction between a cofactor bearing a reactive functional group and an amino acid on the protein scaffold.[167] Some commonly used reactions used to form an ArM are a) nucleophilic attack of a cysteine or another activated residue on the protein on an electrophilic moiety on the cofactor, b) disulfide bond formation of a protein bound cysteine and a nucleophilic sulfur containing cofactor and c) “click”-reaction between an unnatural amino acid bearing a terminal azide (or alkyne) with an alkyne (or azide) bearing cofactor.[168–170]

(ii) **Supramolecular anchoring** makes use of the high affinity some proteins (host) display for certain non-covalent inhibitors, substrates or natural cofactors (guest). Covalent modification of these with a cofactor may retain the affinity for the protein, ensuring a quantitative incorporation of the cofactor within the host protein. Since no chemical modification step is required after the incorporation of the cofactor the integrity of the

organometallic species is retained. A perfect example of this supramolecular anchoring is represented by the biotin-streptavidin technology.[168]

(iii) **Dative anchoring** stands for the coordination of a coordinately unsaturated metal center to one or more nucleophilic amino acid residues (Asp, Cys, Glu, His, Ser, etc.). This strategy is often complemented by either supramolecular or covalent strategies.[161,171]

(iv) **Metal substitution** refers to a unique activity a non-native metal combined with a uniquely tailored active site of a natural metalloenzyme. The substitution of the metal center can catalyze new-to-nature reactions.[172–175]

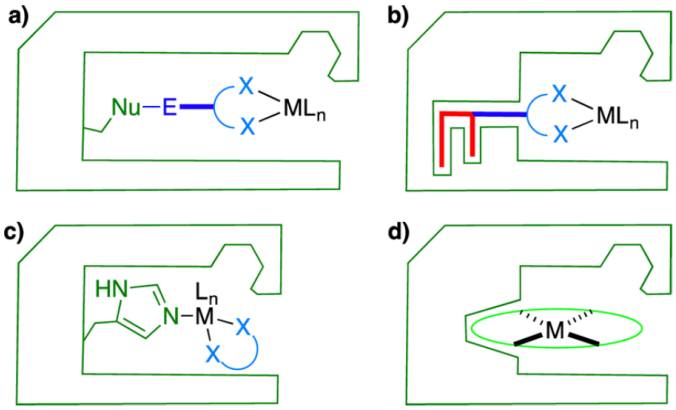


**Figure 2.10:** The four anchoring strategies to introduce an abiotic cofactor within a protein scaffold: (a) covalent, (b) supramolecular, (c) dative, and (d) metal substitution. Color codes: protein and natural cofactor (green), supramolecular anchor (red), variable spacer and ligand (blue), and abiotic metal (black). The figure is reproduced from reference [159].

### 2.6.2 Biotin-Streptavidin Technology

As mentioned before, the supramolecular anchoring strategy involves strong and specific interactions between the tetrameric protein streptavidin and its substrate biotin **20** (Figure 2.11). It turned out that the biotin-(strept)avidin system is a perfect couple to assemble artificial metalloenzymes. In the late 80s Whitesides and Wilson used this technology to create the first artificial metalloenzyme.[160] They converted avidin into an enantioselective catalyst by incorporating a biotinylated achiral rhodium-diphosphine complex into the biotin-binding pocket. Due to the fact that due to the following reasons:

i) The affinity of (strept)avidin for biotin is the strongest non-covalent biological interaction known, with a supramolecular binding affinity of $K_A$ = ca. $10^{15}$ $M^{-1}$ for avidin and $K_A$ = ca. $10^{13}$ $M^{-1}$ for streptavidin.[176–178] Derivatization of the valeric chain of biotin by the

introduction of linkers or by the modulation of the chelating residues does not alter its affinity dramatically.[179]

ii) The protein shows exceptional tolerance towards environment changes, which allows to utilize the technology on a large variation of different reactions. A biotin-loaded streptavidin survives temperatures up to 110°C for several minutes, and is not completely denatured under extreme pH conditions (6 M guanidinium chloride at pH 1.5) and can tolerate high concentrations of organic solvents (up to 50% EtOH) and the presence of surfactants (i.e. sodium dodecyl sulphate, SDS).[176,177,180,181]

iii) The modular approach of the biotin-streptavidin technology allows for a fairly straightforward way to optimize the system, since the cofactor can be modified separately and the protein can be mutated by genetic means and bioconjugation.

iv) The access to the protein is an important parameter in the creation of metalloenzymes. Streptavidin, which is naturally secreted by *Streptomyces avidinii* bacteria, can be readily expressed from *E. coli* cultures and produced as recombinant protein with high yields (up to 8.3 grams per liter of *E. coli* culture).[182,183] Avidin, naturally available from egg white,[177] on the other hand is difficult to produce in bacteria, but reasonable yields can be obtained in yeast cells as *Pichia pastoris*.[184] Because of their stability, they are easy to purify by affinity chromatography using immobilized iminobiotin.

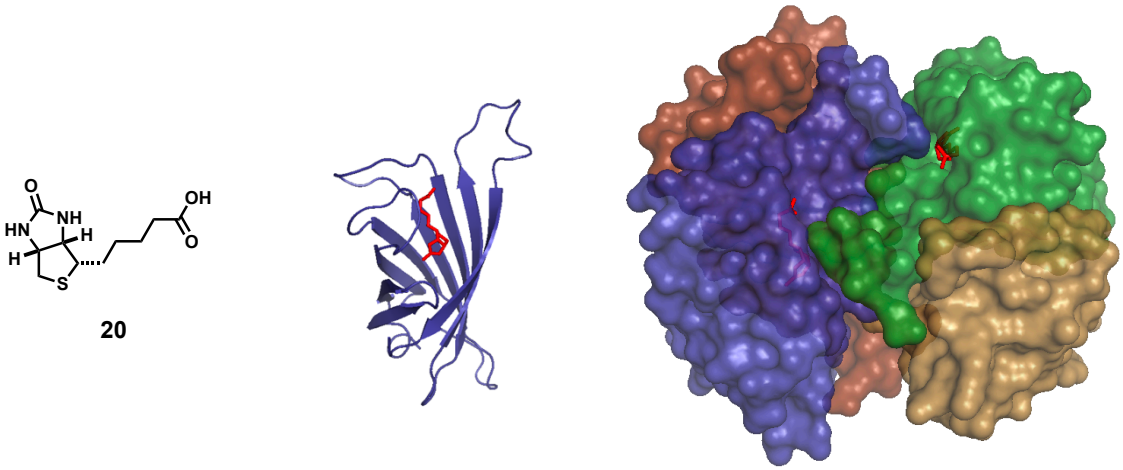


**Figure 2.11:** The biotin-streptavidin technology: (left) the biotin molecule (also known as vitamin H) that can be bound to abiotic cofactors *via* its carboxylic acid moiety; (middle cartoon representation of a streptavidin monomer with an incorporated biotin molecule (red stick representation); (right) surface representation of tetrameric streptavidin with an incorporporated biotin molecule (red stick representation); (pdb code: 3PK2).[185]

Avidin and streptavidin share an amino acid similarity of only 41% but have almost identical secondary, tertiary and quaternary structures.[176,186,187] Both fold in an eight-stranded antiparallel beta-barrel and their quaternary structure is composed of four identical barrels. Each subunit has a single biotin-binding site placed near one end of the barrel. The binding site provides a perfect fit for the biotin molecule (also known as vitamin $B_7$, vitamin H or coenzyme R).[188] Even when no biotin is bound the involved amino acids are already pre-organized to accommodate the biotin molecule. Following biotin-binding, a flexible loop located between the strands 3 and 4 becomes ordered, locking the biotin molecule in the binding site. Given the fact that the isoelectric points (pI) differ in both proteins streptavidin (pI = 6.2) is preferred over avidin (pI = 10.4) for many biological applications.[189] ArMs based on the biotin-streptavidin technology have been developed to catalyze a wide variety of water compatible reactions including: hydrogenation,[190] olefin metathesis,[191] sulfoxidation,[192] dihydroxylation,[193] asymmetric allylic alkylation,[194] Suzuki-coupling,[195] C–H activation[196] and transfer hydrogenation.[185,197]

### 2.6.3 Artificial Hydrogenase mimics

The concept of artificially assembling a small molecule cofactor into a protein scaffold to produce hydrogen has been explored so far.[198–203]

One possibility is the artificial synthesis of natural hydrogenases. Promising results were achieved by Fontecave and co-workers with the [FeFe]-hydrogenase HydA. The formation of its di-iron catalytic site (or H-cluster) requires a complete maturation machinery of many different enzymes, involving at least HydE, HydG, and HydF. The exogenous ligands (CO, $CN^-$, aza-propanedithiol) are introduced by HydE and HydG. HydF serves as the host protein in which the di-iron complex is finally assembled. In the last step, the nearly mature di-iron complex is transferred to apo-HydA. Fontecave and co-workers showed that a hydrogenase could be maturated *in vitro*, without the maturation machinery involved. By loading an inactive artificial di-iron cofactor into apo-HydF, they could transfer the synthetic complex into the apo form of the hydrogenase HydA, reconstituting a fully active HydA (Scheme 2.4a).[204] Those results also show, that the central atom of the bridging dithiolate ligand must be a nitrogen, since only then catalytic activity was detected (X in Scheme 2.4a). Fontecave and Happe could even show that the use of HydF could be avoided. They demonstrated that a direct loading of a synthetic complex into apo-HydA is possible (Scheme 2.4b).[205] Hu and co-workers built on this strategy and reported the direct formation of an [Fe]-hydrogenase by loading its apo-form with a synthetic complex (Scheme 2.4c).[206]

These findings show that it is indeed possible to generate an active hydrogenase without the need of its complex enzymatic maturation machinery. This opens the possibility of expressing hydrogenases in a heterologous organism and opening the possibility of introducing a fully synthetic cofactor within an apo-hydrogenase. This will allow for large screening libraries of hydrogenases (i.e. by directed evolution) resulting in variants with higher activity and/or oxygen-tolerance. Hu and Lubitz could already demonstrate, that small variations of the cofactor lead, in most cases, to inactive hydrogenases.[207] This will help to understand the complexity of these systems and lead eventually to more active artificial hydrogenases.

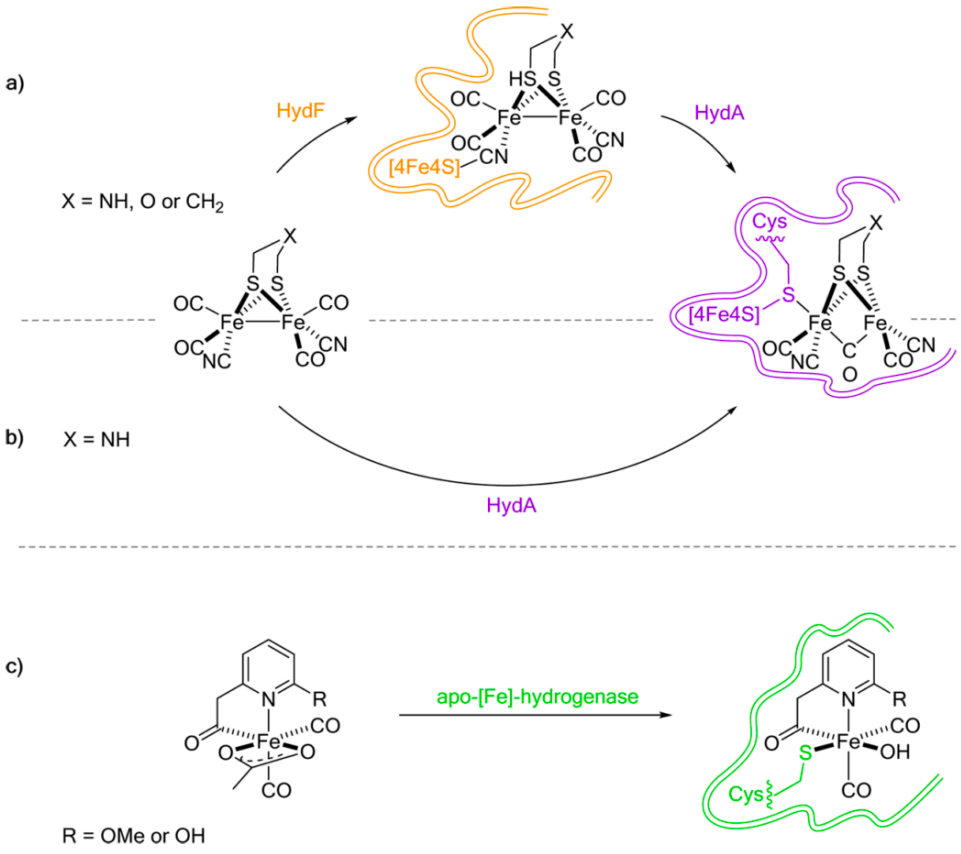


**Scheme 2.4:** Reconstitution of apo-hydrogenases with synthetic cofactors affords functional hydrogenases, demonstrated either by (a) the use of less maturation enzymes, (b) direct loading of a synthetic complex into apo-HydA or by (c) direct formation of an [Fe]-hydrogenase by loading its apo-form with a synthetic complex. This scheme was taken from reference [159].

This strategy seems promising, yet the complexity and the size of the scaffold are limiting. A scaffold that is reduced to its minimum size would be favorable for industrial applications, especially systems that are stable over a wide range of conditions. Other groups explored the possibility of

assembling synthetic complexes within various protein scaffolds to produce hydrogen. Yet, only a limited amount of catalysts and protein scaffolds have been investigated until now.[159]

The group of Hayashi *et al.* for example inserted active site [FeFe] hydrogenase mimics into various host proteins.[203] By datively anchoring a di-iron complex into the active site of apo-cytochrome *c*, they were able to afford an active hydrogenase containing a $[(\mu\text{-S})_2Fe_2(CO)_6]$-moiety (Scheme 2.5). The protein contains a Fe-protoporphyrin(IX) cofactor that is covalently attached to the protein *via* a thioether linkage at a Cys-$X_2$-Cys motif, where X are other amino acids. Catalytically inactive $[Fe_2(CO)_9]$ **21** was bound to the Cys-$X_2$-Cys motif of the apo-cytochrome *c* after removal of the heme. When $[Ru(bpy)_3]^{2+}$ **1** was added as a PS and ascorbic acid **2** as sacrificial electron donor, the ArM produced hydrogen (82 TON after 2 h) with a maximal TOF of 0.035 $s^{-1}$. When, on the other hand, a synthetic heptapeptide containing the Cys-$X_2$-Cys motif and a His residue to mimic the active site of cytochrome *c* was utilized, lower activities were achieved (4-fold lower TOF and 8-fold lower TON). This demonstrates the protective role of the protein scaffold.

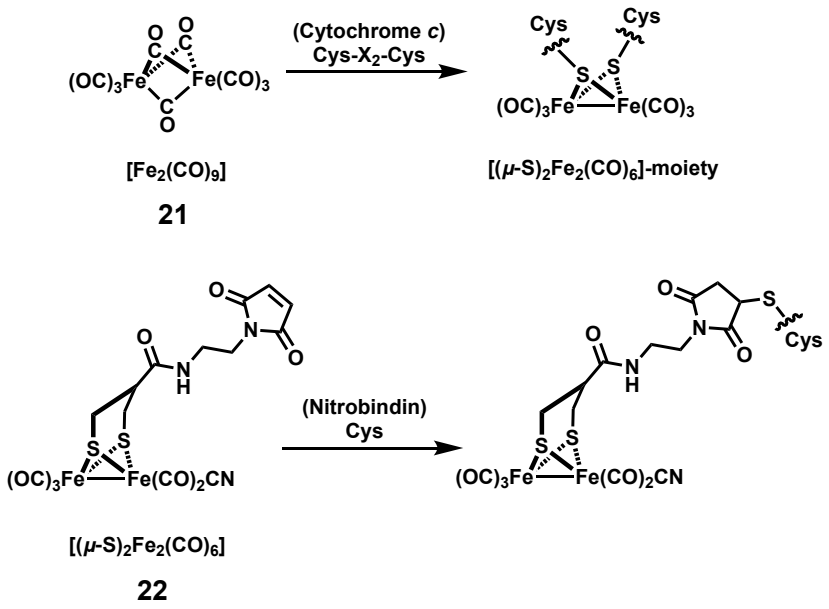


**Scheme 2.5:** Dative and covalent anchoring of **21** and **22** afford photo-catalytically active [FeFe] hydrogenase mimics.

When a more rigid scaffold was used to create an artificial hydrogenase, hence anchoring the di-iron cofactor **22** *via* a maleimide linker to an artificially introduced cysteine of aponitrobidin Q96C, showed a TON of 120 after 2 h (130 after 6 h) and a maximum TOF of 0.038 $s^{-1}$ upon irradiation.[208] However, when the free cofactor was irradiated under similar conditions, it performed three times faster and catalysis ceased after 2 h with a TON of 130. The decreased accessibility of the cofactor inside the protein probably reduces the rate of electron transfer from the PS. Even though there is a

clear decrease in rate, the protein matrix provides a stabilizing environment, making the catalyst last three times as long.

Bren and coworkers substituted iron by cobalt in enzymes containing iron-protoporphyrin(IX) which afforded active hydrogenases.[209] Eventually, the catalysts showed a longer catalyst lifetime inside the protein (24 h against 4 h) and 10-fold higher TON (11.000 against 1.000) in electrocatalysis experiments. However, the incorporation into a protein scaffold did not lower the high overpotential required (830 mV against 850 mV).

A cobalt-substituted myoglobin was used by Ghirlanda *et al.*. They could show that, upon irradiation at pH 7.0 in the presence of ascorbate and a photosensitizer, the host protein increased the TON compared to the free cofactor by the factor of 4.3, hence 518 in 12 h.[209]

Artero *et al.* explored a similar strategy in incorporating cobaloximes **23** and **24** into the apo form of sperm whale myoglobin.[210] They could show that the catalysts occupied the heme-site to form **23**·Mb and **24**·Mb. When photochemical hydrogen production was performed using deazaflavin (DAF hereafter) and tris-buffer (pH 7) as electron donor **24**·Mb performed up to 5 TON in 15 min. However, the free cofactor **24** outperformed the artificial hydrogenase (TON 8.3). Other heme-binding proteins were also investigated, hence rat heme oxygenase 1 (HO1 hereafter) and *Corynebacterium diphteriae* heme oxygenase (HmuO hereafter).[210] The resulting artificial hydrogenases **24**·HO1 (6.3 TON) and **24**·HmuO (15.3 TON) were more active than **24**·Mb (5.0 TON) under photochemical conditions. However, the free catalyst **24** afforded 20 TON. The reason for this could be that the protein shields the catalyst and disturbs the interaction between the PS and the incorporated catalyst. Furthermore, the catalyst was deactivated rapidly. The authors hypothesize that the Co(III)–H intermediate could reduce the oxime ligand itself. The lifetime of this intermediate could be shortened if the electron transfer to the catalyst could be accelerated and thus preventing ligand degradation. One way to achieve this would be to keep the catalyst and the PS in close proximity to enable fast electron transfer.

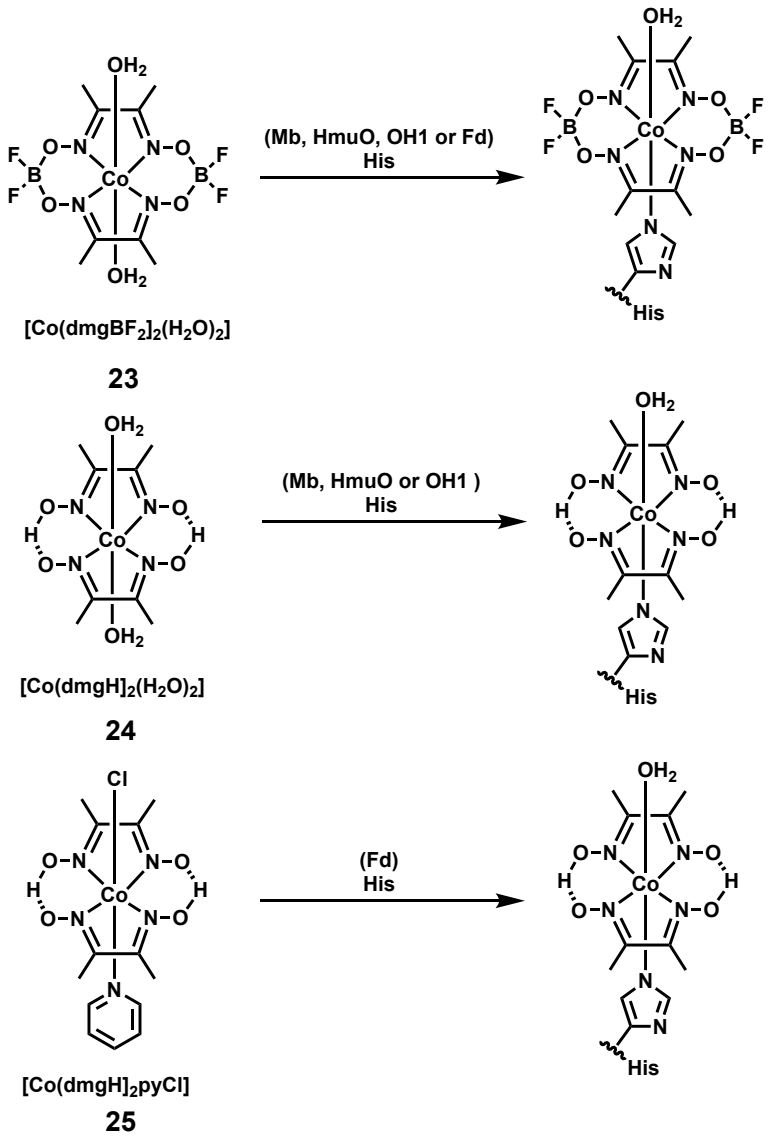


**Scheme 2.6:** Cobaloximes are highly active hydrogen production catalyst. They can be anchored *via* a histidine or a methionine residue of the apo-heme protein.

This strategy was addressed by Utschig *et al.* making use of the affinity of **25** (Scheme 2.6) and **26** (Figure 2.12) towards the photosystem I (PSI hereafter).[211,212] PSI, a component of the naturally occurring photosynthetic electron transport chain, contains a light-harvesting center and a series of electron relays, incorporated within a large protein matrix. The authors hypothesize that the interaction of the two catalysts and the PSI is non-covalent and hydrophobic patches of the PSI are involved. Upon irradiation of **25**·PSI (which was obtained by incubation of PSI with **25**), ascorbate **2** (pH 6) and cytochrome $c_6$ as electron transport, hydrogen evolution could be measured. This system performed 2080 TON in 1.5 h, with a maximum TOF of 1.13 $s^{-1}$ and under similar conditions, **26**·PSI performed 1870 TON in 3 h, relative to cobalt. In both cases however, analysis of the catalytic mixture upon completion of the reaction revealed that approximately 90% of the metal dissociated from the

protein. This is probably due to the poorly defined and weak interactions between PSI and those catalysts and catalytic degradation processes.

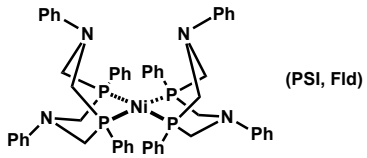


$[Ni(P_2^{Ph}N_2^{Ph})_2]^{2+}$

**26**

**Figure 2.12:** Nickel Phosphines are synthetic complexes with high hydrogen production catalytic activity. They can be bound to PSI or Fld.

In general, the artificial hydrogenases reported to date show that incorporating a proton-reduction catalyst within a protein scaffold can, in some cases, increase TOF and TON in aqueous media at neutral pH. However, sometimes the artificial hydrogenases are less efficient than the cofactor alone. Especially for photocatalytic systems where the interactions between the PS and the catalyst are hindered, eventually leading to slow catalytic rates or catalyst degradation. Some advantageous issues of artificial hydrogenases need to be systematically explored. For instance, very few examples of random mutagenesis or directed evolution are reported.[213] Only few modifications in the immediate proximity of the metal center have been tested either by mutating residues or by testing different scaffolds from a same family (e.g. heme-binding proteins). Most importantly, none of these examples led to a dramatic improvement of catalytic activity. In a biomimetic spirit, artificial hydrogenases could be improved by engineering facilitated pathways for proton or electron delivery or removal at the metal center and gas release pathways, resembling the channels and electron relays present in natural hydrogenases. So far, no efforts have been undertaken to utilize the biotin-(strept)avidin technology as a scaffold for artificial hydrogenases.

## 2.7 Aim of this thesis

Climate change is the ultimate proof that mankind has to change its way of producing energy. To use the suns radiant energy and store it in chemical bonds between hydrogen molecules has become a fashionable and sustainable way of doing so. Artificial photosynthesis or photocatalytic water splitting, and mimicking nature is one way of overcoming that problem. Synthetic hydrogen evolving mimics of the catalytic center of hydrogen producing enzymes were developed, yet they lack the second coordination sphere of those enzymes. This second coordination sphere provides gas and proton channels as well as electron relays and electron transporting pathways. They are the reason for their incredible activity. The goals of this thesis are:

(i) Exploring the biocompatibility of hydrogen evolution catalysts from formic acid in under biological friendly conditions.

(ii) Exploring electron transfer pathways of bio-conjugated assemblies of electron acceptors, electron donors and photosensitizers on the surface of streptavidin.

(iii) Exploring the impact of a secondary coordination sphere of streptavidin on photocatalytic hydrogen evolution of an incorporated metalorganic catalyst.

The findings should help to improve the progress in synthesizing and assembling nature-like hydrogenases to eventually solve the world energy problem.

# 3

# Evaluation of Formate Dehydrogenase Activity of Three-Legged Pianostool Complexes in Dilute Aqueous Solution

*The following section has been published in:*

*Eur. J. Inorg. Chem.* **2014**, *34*, 5860–5864.

http://dx.doi.org/10.1002/ejic.201402348

## Evaluation of Formate Dehydrogenase Activity of Three-Legged Pianostool Complexes in Dilute Aqueous Solution

Sascha G. Keller,[a] Mark R. Ringenberg,[a,b] Daniel Häussinger[a] and Thomas R. Ward[*,a]

[a] Department of Chemistry, University of Basel, Spitalstrasse 51, CH-4056 Basel, Switzerland,

[b] Department of Chemistry, University of Stuttgart, Pfaffenwaldring 55, 70569 Stuttgart, Germany

[*] Correspondence: thomas.ward@unibas.ch

Keywords: Formic acid, Pianostool Complexes, Dehydrogenation, Iridium, Hydrogen

## 3.1 Abstract

Formic acid is an attractive means to reversibly store dihydrogen. In this context, $d^6$-pianostool complexes rank among the most effective formate dehydrogenase catalysts. With biologically produced formic acid in mind, we evaluated the performance of iridium-based pianostool complexes bearing a cooperative ligand, known to catalyze formate decomposition. Interestingly, the phenyl-pyrazine derived catalyst $[Cp^*Ir(phenpz)(OH_2)]^+$ **7** compares favorably with the very best systems $[Cp^*Ir(phenpz(CO_2H))H_2O]^+$ **8** and $[Cp^*Ir(imim)H_2O]^{2+}$ **11**. These catalysts display remarkable air tolerance, recyclability and activity under dilute aqueous conditions.

## 3.2 Introduction

Hydrogen is an attractive, clean and renewable energy vector. In this context, formic acid has been identified as a promising, safe and easy to handle hydrogen storage medium.[214–220] The reversible catalytic decomposition of formic acid yields dihydrogen and carbon dioxide and is mediated by organometallic catalysts. In particular, $d^6$-pianostool complexes have demonstrated their versatility as formate dehydrogenases.[221–229] These studies are, however, typically performed using high formic acid concentrations.

In a biological context, formic acid can be produced metabolically from glucose via a pyruvate lyase mechanism.[230–232] With the long-term goal of producing bio-hydrogen *in vivo* via a chemoenzymatic cascade,[233] we set out to compare and evaluate the performance of $d^6$-pianostool complexes at low formate, potentially biologically relevant concentrations.

## 3.3 Results and Discussion

Scrutiny of the literature revealed that many of the most promising organometallic formate dehydrogenase catalysts possess ligands that contain a basic functionality (B:). In a biomimetic spirit, dihydrogen is reversibly mobilized as a metal hydride and a protonated ligand.[116,234] The ligands selected for this study and their corresponding complexes **1**-**12** are displayed in Scheme 3.1.

In order to evaluate the involvement of the cooperative ligand, complexes lacking the basic appendage (B:) were synthesized and evaluated as well: $[Cp^*Ir(\mathbf{bpy})(OH_2)]^{2+}$ **2**, $[Cp^*Ir(\mathbf{phenpy})(OH_2)]^{+}$ **4** and $[Cp^*Ir(\mathbf{phenpz})(OH_2)]^{+}$ **7**. Complexes **1**-**12** were prepared according to literature protocols (see Appendix A for further information). For comparison purposes, all complexes **1**-**12** were isolated as aquo complexes with (hydrogen)sulfate as counteranion.

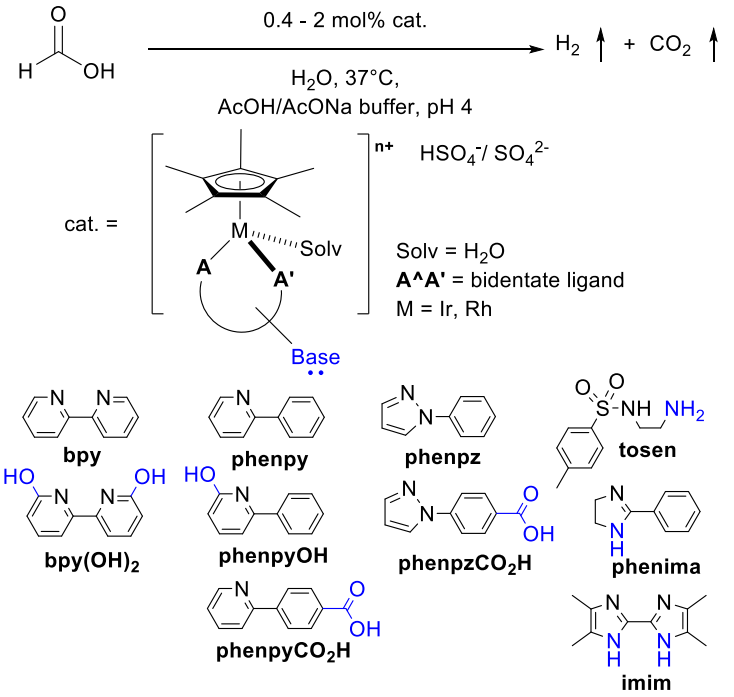


| | | | |
|---|---|---|---|
| $[Cp^*Ir(H_2O)_3]^{2+}$ | **(1)** | $[Cp^*Ir(\mathbf{phenpz})(H_2O)]^{+}$ | **(7)** |
| $[Cp^*Ir(\mathbf{bpy})(H_2O)]^{2+}$ | **(2)** | $[Cp^*Ir(\mathbf{phenpzCO_2H})(H_2O)]^{+}$ | **(8)** |
| $[Cp^*Ir(\mathbf{bpy(OH)_2}(H_2O)]^{2+}$ | **(3)** | $[Cp^*Ir(\mathbf{tosen})(H_2O)]^{+}$ | **(9)** |
| $[Cp^*Ir(\mathbf{phenpy})(H_2O)]^{+}$ | **(4)** | $[Cp^*Ir(\mathbf{phenima})(H_2O)]^{+}$ | **(10)** |
| $[Cp^*Ir(\mathbf{phenpyOH})(H_2O)]^{+}$ | **(5)** | $[Cp^*Ir(\mathbf{imim})(H_2O)]^{2+}$ | **(11)** |
| $[Cp^*Ir(\mathbf{phenpyCO_2H})(H_2O)]^{+}$ | **(6)** | $[Cp^*Rh(\mathbf{phenpzCO_2H})(H_2O)]^{+}$ | **(12)** |

**Scheme 3.1:** Catalytic decomposition of formate to dihydrogen and carbon dioxide is catalyzed by $d^6$-pianostool complexes. Ligands and corresponding complexes screened in this study.

Most studies to date are performed in pure formic acid or high concentration of formate solutions. In order to mimic *in vivo* formate decomposition, biocompatible reaction conditions were selected: buffered solutions (pH 4.0), 37 °C, and either 230 mM or 45 mM formate (Appendix A). Screening complexes **1**-**12** for their formate dehydrogenase was achieved by determining the gas evolution[235] revealed the following trends (Figure 3.1):

i) The presence of a bidentate ligand is indispensable to ensure activity for the $d^6$ Ir-pianostool moiety, as reflected by the poor performance of $[Cp^*Ir(OH_2)_3]^{2+}$. In the presence of a bidentate ligand, the {Cp*Ir(III)} derived catalysts **1**-**11** clearly outperform the {Cp*Rh(III)} congener (compare $[Cp^*Ir(\mathbf{phenpzCO_2H})H_2O]^{+}$ **8** with $[Cp^*Rh(\mathbf{phenpzCO_2H})H_2O]^{+}$ **12**).

ii) Using 45.5 mM formate, complexes $[Cp^*Ir(\mathbf{bpy(OH)_2})H_2O]^{2+}$ **3**, $[Cp^*Ir(\mathbf{phenpy(CO_2H})H_2O]^{+}$ **6**, $[Cp^*Ir(\mathbf{phenpz})H_2O]^{+}$ **7**, $[Cp^*Ir(\mathbf{phenpz(CO_2H)})H_2O]^{+}$ **8** and $[Cp^*Ir(\mathbf{imim})H_2O]^{2+}$ **11** yield similar turnover numbers (i.e. > 40 TON) after 180 minutes in the

presence of 0.9 mM catalyst (2.0 % loading). It is interesting to note that complex [Cp*Ir(**phenpz**)$H_2O$]$^+$ **7** which lacks a basic moiety on the ligand ranks among the best catalysts after three hours.

iii) Increasing the concentration to 230 mM formate in the presence of 0.9 mM catalyst further highlights the superiority of [Cp*Ir(**phenpz(CO$_2$H)**)$H_2O$]$^+$ **8** and [Cp*Ir(**imim**)$H_2O$]$^{2+}$ **11** over all other catalysts tested. Again here, [Cp*Ir(**phenpz**)$H_2O$]$^+$ **7**, which lacks a basic appendage, is the third best catalyst.

iv) Comparing conversions after 30 minutes reveal marked differences among complexes [Cp*Ir(**bpy(OH)$_2$**)$H_2O$]$^{2+}$ **3**, [Cp*Ir(**phenpy(CO$_2$H)**$H_2O$]$^+$ **6**, [Cp*Ir(**phenpz**)$H_2O$]$^+$ **7**, [Cp*Ir(**phenpz(CO$_2$H)**)$H_2O$]$^+$ **8** and [Cp*Ir(**tosen**) )$H_2O$]$^+$ **9** and [Cp*Ir(**imim**)$H_2O$]$^{2+}$ **11** suggesting that complex [Cp*Ir(**phenpz(CO$_2$H)**)$H_2O$]$^+$ **8** displays the highest reaction rates.

Next, we selected the most promising catalysts [Cp*Ir(**bpy(OH)$_2$**)$H_2O$]$^{2+}$ **3**, [Cp*Ir(**phenpz**)$H_2O$]$^+$ **7**, [Cp*Ir(**phenpz(CO$_2$H)**)$H_2O$]$^+$ **8** and [Cp*Ir(**tosen**) )$H_2O$]$^+$ **9** and [Cp*Ir(**imim**)$H_2O$]$^{2+}$ **11** and determined their first-order rate constants for the decomposition of formic acid, Figure 3.2 and Table 3.1 (See Appendix A for details). Although complex [Cp*Ir(**tosen**)$H_2O$]$^+$ **9** has the highest initial activity, it rapidly levels off after ca. 35 turnovers. Complexes [Cp*Ir(**phenpz(CO$_2$H)**)$H_2O$]$^+$ **8** and [Cp*Ir(**imim**)$H_2O$]$^{2+}$ **11** display similar rates and higher turnover numbers.

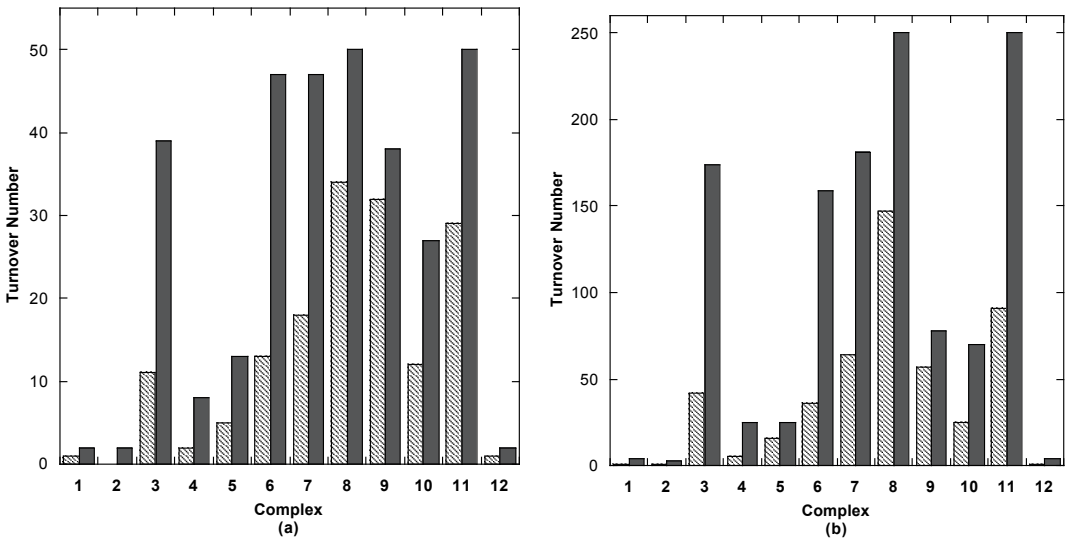


**Figure 3.1**: Formate dehydrogenase properties of complexes **1**-**12**. The TONs were determined after 30 min (hatched bars) and 180 min (solid bars) using 0.0455 M formic acid and 2 mol % catalyst at pH 4 and 37 °C (a); and 0.23 M formic acid and 0.4 mol % catalyst at pH 4 and 37 °C (b).

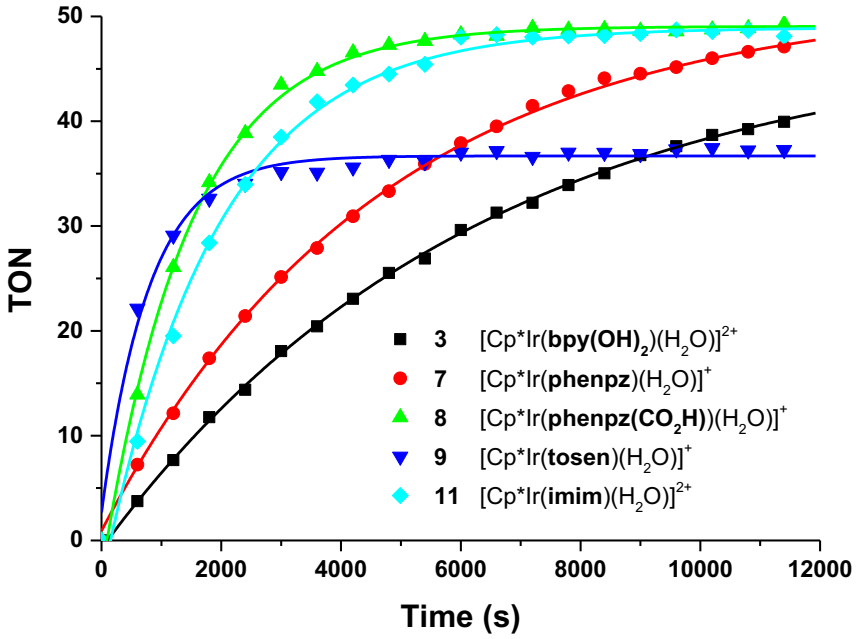


**Figure 3.2:** Formate dehydrogenase activity catalysed by $[Cp^*Ir(\mathbf{bpy(OH)_2})H_2O]^{2+}$ **3** (black), $[Cp^*Ir(\mathbf{phenpz})H_2O]^{+}$ **7** (red), $[Cp^*Ir(\mathbf{phenpz(CO_2H)})H_2O]^{+}$ **8** (green) and $[Cp^*Ir(\mathbf{tosen})H_2O]^{+}$ **9** (blue) and $[Cp^*Ir(\mathbf{imim})H_2O]^{2+}$ **11** (turquoise). The solid lines were obtained by fitting the gas evolution using a first-order rate equation in OriginPro 9 (see Appendix A for details). Reaction conditions: 45.5 mM formic acid and 0.9 mM catalyst in a 2.5 M acetic acid/sodium acetate buffer at pH 4 and 37°C.

Having identified $[Cp^*Ir(\mathbf{phenpz(CO_2H)})H_2O]^{+}$ **8** and $[Cp^*Ir(\mathbf{imim})H_2O]^{2+}$ **11** as the most active catalysts, their recyclability was evaluated, Figure 3.3. For this purpose, a reaction vessel was charged with 45.5 mM formic acid (0.1 mmol) and 0.9 mM catalyst **8** (2% catalyst loading) in a 2.5 M acetic acid/sodium acetate buffer at pH 4 and 37 °C. After gas evolution had ceased, the vessel was recharged with 0.1 mmol formate. The reaction was run to completion for each four recycling experiments. As can be appreciated, $[Cp^*Ir(\mathbf{imim})H_2O]^{2+}$ **11** outperforms $[Cp^*Ir(\mathbf{phenpz(CO_2H)})H_2O]^{+}$ **8** as its decomposition rate does not erode over time, Figure 3.3.

**Table 3.1:** First-order rate constants for the catalytic decomposition of formic acid[a]

| Complex | Rate constants ($s^{-1}$) |
|---|---|
| $[Cp^*Ir(\mathbf{bpy(OH)_2})H_2O]^{2+}$ **3** | $k = 1.60 \cdot 10^{-4} \pm 1.56 \cdot 10^{-7}$ |
| $[Cp^*Ir(\mathbf{phenpz})H_2O]^{+}$ **7** | $k = 2.16 \cdot 10^{-4} \pm 2.28 \cdot 10^{-7}$ |
| $[Cp^*Ir(\mathbf{phenpz(CO_2H)})H_2O]^{+}$ **8** | $k = 6.85 \cdot 10^{-4} \pm 6.01 \cdot 10^{-7}$ |
| $[Cp^*Ir(\mathbf{tosen}))H_2O]^{+}$ **9** | $k = 8.7 \cdot 10^{-4}$ [b] |
| $[Cp^*Ir(\mathbf{imim})H_2O]^{2+}$ **11** | $k = 5.28 \cdot 10^{-4} \pm 6.06 \cdot 10^{-7}$ |

[a] Reaction conditions: 45.5 mM formic acid and 0.9 mM catalyst in a 2.5 M acetic acid/sodium acetate buffer at pH 4 and 37°C; [b] The catalyst deactivates after ca. 35 TONs, the rate was thus estimated from the half life by $k = \ln 2 / t_{1/2}$

In order to evaluate the air-tolerance of catalysts $[Cp^*Ir(\mathbf{phenpzCO_2H})H_2O]^{+}$ **8** and $[Cp^*Ir(\mathbf{imim})H_2O]^{2+}$ **11**, reactions were carried out i) under nitrogen atmosphere, ii) under air, iii) in an air-saturated solution and iv) using catalyst solution allowed to stand on the bench for three weeks. All tolerance tests resulted in similar results, the TON after thirty minutes varied by less than ten percent, highlighting the robustness of $[Cp^*Ir(\mathbf{phenpzCO_2H})H_2O]^{+}$ **8** and $[Cp^*Ir(\mathbf{imim})H_2O]^{2+}$ **11**. Upon reducing the catalyst concentration from 910 μM to 2.3 μM (i.e. 0.4% to 0.001%), the TON after thirty minutes increased from 159 to 710 in both cases. Using 9 μM $[Cp^*Ir(\mathbf{phenpzCO_2H})H_2O]^{+}$ **8** and $[Cp^*Ir(\mathbf{imim})H_2O]^{2+}$ **11,** > 3650 and > 8700 turnovers were achieved respectively within 48 hours. With biological applications in mind, we evaluated the activity of $[Cp^*Ir(\mathbf{phenpzCO_2H})H_2O]^{+}$ **8** in pure water. Upon increasing the pH, the TON after three hours decreased from 250 (pH 4.0), 204 (pH 5.0) to 147 (pure water). Repeating the experiment with $[Cp^*Ir(\mathbf{imim})H_2O]^{2+}$ **11**, the TON after three hours displayed a different trend, namely from 250 (pH 4.0), 47 (pH 5.0) to 250 (pure water), highlighting its versatility under non-buffered conditions.

Further insight into the mechanism of the catalysis and the stability of the catalysts was obtained by monitoring the formate conversion by NMR. $[Cp^*Ir(\mathbf{phenpzCO_2H})H_2O]^{+}$ **8** and $[Cp^*Ir(\mathbf{imim})H_2O]^{2+}$ **11** were allowed to react at room temperature at a concentration of 910 μM with sodium formate 45.5 mM in pure water (95% $H_2O$ + 5% $D_2O$) or in acetic acid-d4 buffered water (pH 4.0). In all cases a pronounced shift of the $^1H$ resonances of the complex were observed after the addition of formate and within several minutes a low intensity resonance at –11.51 ppm indicated the formation of an iridium hydride species. The attachment of the ligands to the iridium Cp* moiety was deduced by NOE contacts of the ligand with the Cp* methyl protons. In the time course of 24 hours

the resonances of the complexes and the hydride signal remained virtually unchanged while the formate signal at 8.34 ppm steadily decreased (Figure A.3). Using deuterium labeled NaDCOO nevertheless yielded the hydride signal at –11.51 ppm and, in addition, the HCOO resonance appeared after 1 hour, indicating an iridium catalyzed H-D-exchange of the formate. In order to follow the formate conversion also by $^{13}$C-NMR, $^{13}$C-labeled sodium formate was used for the reaction.

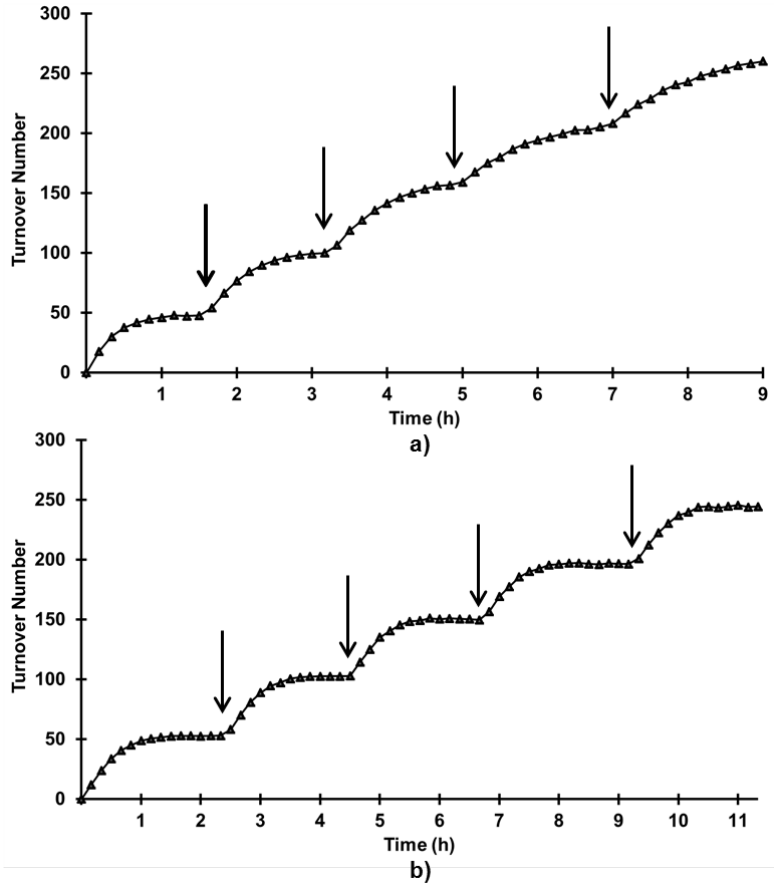


**Figure 3.3:** Recyclability of [Cp*Ir(**phenpzCO$_2$H**)H$_2$O]$^+$ **8** a); and [Cp*Ir(**imim**)H$_2$O]$^{2+}$ **11** b) towards formate dehydrogenase (0.1 mmol formate added at each recharging step). The arrows indicate the recharging of the flask with 0.1 mmol formate in 200 µL water.

The formate resonance at 170.5 ppm slowly disappeared while a new resonance at 124.7 ppm was observed which is conclusive for the formation of carbon dioxide. No trace of carbon monoxide (181.3 ppm) was observed during the reaction. To independently determine whether CO is produced under the chosen reaction conditions a modified spot test with phosphomolybdic acid and $PdCl_2$ was performed but showed no CO evolution of complexes **8** and **11** (Appendix A). These findings are consistent with previous reports.[226,236]

## 3.4 Conclusions

With the aim of identifying the most effective $d^6$ pianostool complex for formate dehydrogenase in dilute formic acid, we evaluated the performance of twelve different catalysts. Both $[Cp^*Ir(\mathbf{phenpzCO_2H})H_2O]^+$ **8** and $[Cp^*Ir(\mathbf{imim})H_2O]^{2+}$ **11** performed very well yielding up to > 3650 TON and > 8700 TON respectively. With biological applications in mind, these catalysts were shown to be air tolerant and display activity under near physiological conditions. Current efforts are aimed at evaluating these catalyst's performance in the presence of engineered cells producing formic acid.

## 3.5 Experimental Section

All syntheses were conducted under nitrogen. All chemicals were used as purchased. Complexes **1**, **2**, **3**, **4**, **5**, **7**, **8**, **9**, **10** and **11** were synthesized according to literature procedures (Supporting Information).

### 3.5.1 Synthesis of $[Cp^*Ir(\mathbf{phenpyCO_2H})(\mathbf{H_2O})]^+$ (6)

To $N_2$ sparged water (12 ml), was added a solution of $[Cp^*IrCl_2]_2$ (0.292 mmol) in acetonitrile (5 ml) and the ligand (0.584 mmol). $Ag_2SO_4$ (0.584 mmol) was added and the reaction mixture was heated to reflux overnight. The reaction solution was allowed to cool to room temperature and centrifuged for 6 min at 4400 rpm. The supernatant was decanted and filtered through a 0.45 micron filter. The organic solvent was removed under reduced pressure and the water was removed by lyophylization. The resulting yellow solid was collected (286 mg, 97.6 %).

**$^1$H NMR** (400 MHz, DMSO-$d_6$): δ = 1.69 (s, 15H), 2.07 (s, 3H), 7.58 (t, J = 6.4 Hz, 1 H), 7.81 (d, J = 8.0 Hz, 1 H), 8.14 (d, J = 8.2 Hz, 1 H), 8.20 (t, J = 7.8 Hz, 1 H), 8.23 (s, 1 H), 8.44 (d, J = 8.2 Hz, 1 H), 8.82 (d, J = 5.6 Hz, 1 H), 11.35 (br, 1 H); **$^{13}$C NMR** (101 MHz, DMSO-$d_6$): δ = 167.20, 165.13, 154.05, 152.31, 149.13, 140.85, 135.96, 132.36, 126.20, 125.62, 125.32, 121.90, 118.04, 96.25 (5C), 8.19 (5C), 1.14; **EA** found: C, 40.46; H, 4.37; N, 3.61. Calc. for $C_{24}H_{27}IrN_2O_6S$ + 3 $H_2O$: C, 40.16; H, 4.63; N, 3.90%; **HRMS** ($ESI^+$) calcd. for $C_{22}H_{23}IrNO_2$, 526.1358; found, 526.1353.

### 3.5.2 Synthesis of $[Cp^*Rh(\mathbf{phenpzCO_2H})(\mathbf{H_2O})]^+$ (12)

To $N_2$ sparged water (12 ml) was added a solution of $[Cp^*RhCl_2]_2$ (0.292 mmol) in acetonitrile (5 ml) and the ligand (0.584 mmol). $Ag_2SO_4$ (0.584 mmol) was added and the reaction

mixture was heated to reflux overnight. The reaction solution was allowed to cool to room temperature and afterwards centrifuged for 6 min at 4400 rpm. The supernatant was decanted and filtered through a 0.45 micron filter. The organic solvent was removed under reduced pressure and the water was removed by lyophylization. The resulting orange solid was collected (218 mg, 66.3 %).

**$^1$H NMR** (400 MHz, Methanol-$d_4$) δ = 1.74 (s, 15 H), 2.05 (s, 3 H), 6.83 (s, 1 H), 7.62 (d, J = 8.3 Hz, 1 H), 7.91 (d, J = 8.3 Hz, 1 H), 8.20-8.62 (br, 2 H), 8.65 (d, J = 2.8 Hz, 1 H); **$^{13}$C NMR** (101 MHz, Methanol-$d_4$) δ = 169.01, 153.20 (d, $J$ = 31.8 Hz), 146.34, 144.88, 139.69, 131.13, 131.03, 129.55 , 118.29, 114.03 , 112.22 , 103.96 (d, $J$ = 5.7 Hz, 5 C), 9.09 (5 C), 0.88; **EA** found: C, 43.48; H, 5.34; N, 6.73. Calc. for $C_{22}H_{26}N_3O_6RhS$ + 2 $H_2O$: C, 44.08; H, 5.34; N, 6.73%; **HRMS** ($ESI^+$) calcd. for $C_{20}H_{22}NO_2Rh$, 425.0733; found, 425.0731.

## 3.6 Acknowledgements

We thank the Swiss Nanoscience Institute for a PhD award to S. K., the Swiss National Science Foundation for generous support (grant SNF 2012 200020_144354) and Umicore for the gift of $[Cp^*IrCl_2]_2$ and $[Cp^*RhCl_2]_2$.

## 3.7 Supporting Information

The full supporting information can be found in the Appendix A.

# 4

# Light-Driven Electron Injection from a Biotinylated Triarylamine Donor to $[Ru(diimine)_3]^{2+}$-Labeled Streptavidin

*The following section has been published in:*

*Org. Biomol. Chem.* **2016**, *14*, 7197-7201

http://dx.doi.org/10.1039/c6ob01273f

## Light-Driven Electron Injection from a Biotinylated Triarylamine Donor to $[Ru(diimine)_3]^{2+}$-Labeled Streptavidin

*Sascha G. Keller,[a] Andrea Pannwitz,[b] Fabian Schwizer,[a] Juliane Klehr,[a] Oliver S. Wenger[*,b] and Thomas R. Ward[*,a]*

[a] Department of Chemistry, University of Basel, Spitalstrasse 51, CH-4056 Basel, Switzerland,

[b] Department of Chemistry, University of Basel, St. Johanns-Ring 19, CH-4056 Basel, Switzerland

[*] Correspondence: thomas.ward@unibas.ch, oliver.wenger@unibas.ch

## 4.1 Abstract

Electron transfer from a biotinylated electron donor to photochemically generated Ru(III) complexes covalently anchored to streptavidin is demonstrated by means of time-resolved laser spectroscopy. Through site-selective mutagenesis, a single cysteine residue was engineered at four different positions on streptavidin, and a Ru(II) tris-diimine complex was then bioconjugated to the exposed cysteines. A biotinylated triarylamine electron donor was added to the Ru(II)-modified streptavidins to afford dyads localized within a streptavidin host. The resulting systems were subjected to electron transfer studies. In some of the explored mutants, the phototriggered electron transfer between triarylamine and Ru(III) is complete within 10 ns, thus highlighting the potential of such artificial metalloenzymes to perform photoredox catalysis.

## 4.2 Introduction

Streptavidin (hereafter Sav) is an exquisitely robust protein of ca. 64 kDa comprised of four homologous sub-units, each of which can bind a biotin molecule with an association constant of ~$10^{14}$ $M^{-1}$ under physiological conditions.[237] Sav can readily be over-expressed and purified from the bacterium *Escherichia coli*. Owing to this combination of favorable properties, biotin-streptavidin systems have been exploited in various contexts where host-guest recognition is desirable, ranging from targeted drug delivery, to live cell imaging and new applications in catalysis.[238]

By biotinylation of small metal catalysts, novel catalytic functions can be conferred to the resulting biotin-streptavidin assemblies, resulting in artificial metalloenzymes.[239–241] Their function can be tailored either chemically, i. e., through variation of the biotin-linker-catalyst moiety, or genetically through site-specific mutagenesis of Sav. In the best case, such chemogenetic optimization can lead to catalytic performance which is superior to that observed for the related small metal catalyst outside the protected environment of the biotin binding pockets of Sav, manifesting for example in unusually high enantioselectivity.[156,242]

In principle, such artificial metalloenzymes should also be amenable to the emerging field of redox photocatalysis,[82,84,243] and for this purpose it would be desirable to equip the biotin-streptavidin systems with redox photosensitizers. Complexes of $d^6$ metal ions such as ruthenium(II) and iridium(III) are good candidates in this regard.

There have been several studies of the luminescence properties of biotinylated $d^6$ metal complexes, including ruthenium(II) polypyridines,[244–247] rhenium(I) tricarbonyl diimines,[248–252] and cyclometalated iridium(III) complexes.[253–258] In most cases, binding to streptavidin leads to enhanced luminescence properties, and this is important for example for cell imaging purposes.[259,260] The above mentioned classes of metal complexes are well suited for photosensitization of electron transfer reactions,[261] but, to the best of our knowledge, this has not yet been realized within the context of the biotin-streptavidin technology.[262] However, ruthenium(II) and rhenium(I) complexes have been employed frequently for investigation of phototriggered electron-transfer in other proteins (e. g., azurin, cytochrome c, or plastocyanin), mostly for distance-dependence studies and for elucidating electron tunneling pathways.[263–268] The ruthenium(II) and rhenium(I) metal centers were commonly ligated to histidine ligands for this purpose, and the natural redox-active groups of these proteins (e. g., blue copper centers or heme groups) served as electron-transfer reaction partners.

Typical photoredox systems usually require a photosensitizer combined with a distinct catalytic moiety. As the binding of biotinylated probes to Sav is non-cooperative, introducing two distinct dyads within a streptavidin tetramer remains an unmet challenge.[179] To assemble such dyads using a Sav scaffold, we thus opted to bioconjugate the photosensitizer to an engineered cysteine residue, thus leaving the four biotin-binding sites of Sav free to introduce either a catalytic or an electron-donor moiety.

As Sav possesses no cysteine residue, site-directed mutagenesis was used to engineer this highly nucleophilic residue at selected positions. The resulting single-point mutants were subsequently bioconjugated with a $[Ru(bpy)_2(phen)]^{2+}$-photosensitizer **1** (Figure 4.1, bpy = 2,2'-bipyridine, phen = 1,10-phenanthroline). The triarylamine (TAA) unit was equipped with a biotin group to yield **Biot-TAA** (see Appendix B for details, **2** displayed in Figure 4.1). The resulting **Biot-TAA** / Ru(II)-streptavidin adducts are donor-acceptor systems in which photo-triggered electron transfer can be investigated. The goal of this work was to explore whether photo-triggered electron injection from a biotinylated donor to ruthenium(II)-labeled streptavidin is possible and if so, what position on the surface of Sav is most suitable for the covalent anchoring of the photosensitizer.

## 4.3 Results and Discussion

### 4.3.1 Structural and synthetic aspects

The ruthenium(II) complex (*rac*-**1** displayed in Figure 4.1) was covalently tethered to streptavidin through nucleophilic attack by a cysteine residue with concomitant elimination of HBr.[269] Single cysteine residues were introduced by site directed mutagenesis on each of the four homologous units of streptavidin, leading to a fourfold Ru(II)-labeling of each streptavidin tetramer. The biotinylated triarylamine unit **Biot-TAA** was synthesized as a binding partner. The acetyl-substituted triarylamine (**TAA-Ac**) **3** served as a reference compound (Figure 4.1). Syntheses and mutagenesis procedures are presented in the Appendix B.

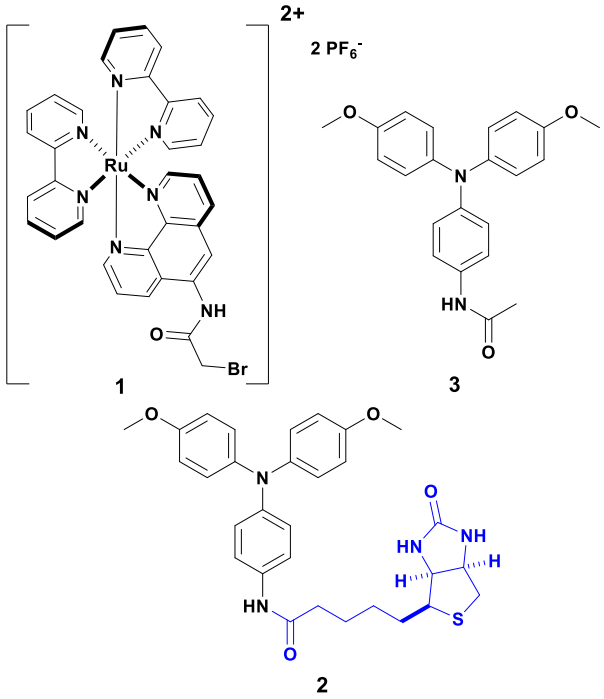


**Figure 4.1:** Chemical structures of the ruthenium(II)-label for streptavidin **1**, the **Biot-TAA** moiety **2** (biotin is displayed in blue) and the **TAA-Ac** reference molecule **3**. See Appendix B for syntheses.

Inspection of the X-ray structure of S112A Sav (pdb code: 3PK2)[185] led us to select four positions for the introduction of a cysteine residue by site-directed mutagenesis. The following four mutants were produced using a previously published method and purified by affinity chromatography[270] and characterized by ESI-MS: Sav T66C, R84C, S112C, and K121C (Figure 4.2).

Subsequent bioconjugation was achieved by mixing the mutant protein overnight with an eightfold excess of Ru-complex **1** at 4°C in phosphate buffer (50 mM, pH 7) in the dark. The excess of the unbound Ru-complex **1** was removed by dialysis and the resulting $Ru_4$Sav bioconjugates ($Ru_4$Sav T66C, $Ru_4$Sav R84C, $Ru_4$Sav S112C, and $Ru_4$Sav K121C respectively) were characterized by ESI-MS, revealing a quantitative conversion to the Ru-containing proteins (see Appendix B for details). The biotin-binding capacity of the $Ru_4$Sav bioconjugates was assessed relying on a displacement titration using HABA (2-(4-hydroxyphenylazo)benzoic acid). Upon incorporation within Sav, HABA displays an absorption at $\lambda_{max}$ 506 nm. Upon addition of biotinylated probes, the HABA is displaced, leading to a disappearance of the absorption at 506 nm.[187,242] This simple procedure revealed that all four biotin-binding sites can accommodate the biotinylated cofactor **Biot-TAA**, and the affinity is similar to that of pure unmodified biotin (see Figure 4.3, more details in the Appendix B).

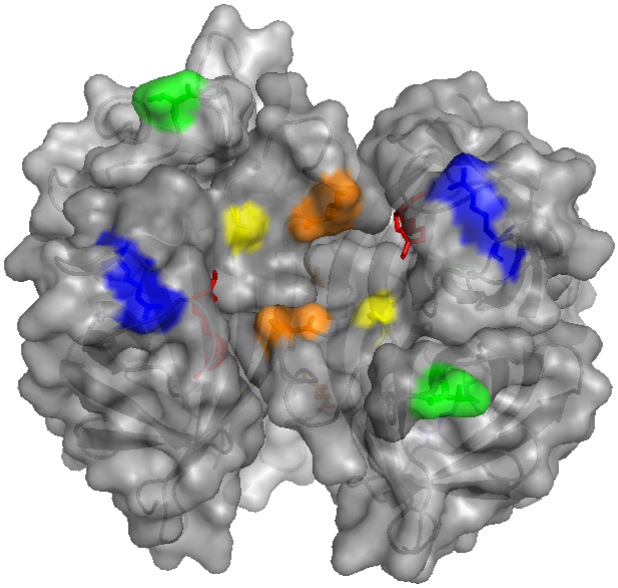

**Figure 4.2:** Surface display representation of homotetrameric streptavidin, highlighting the symmetry related positions selected for introducing cysteine residues: K121 (orange), S112 (yellow), R84 (blue), T66 (green) and biotin (red stick representation); (pdb code: 3PK2).[185]

This confirms that the bulky **Biot-TAA** moieties bind to $Ru_4$Sav isoforms, despite the presence of the bulky $Ru(bpy)_2(phenNHCOCH_2)$ moieties which, in the S112C and K121C mutants, lie in the proximity of the biotin-binding vestibule.

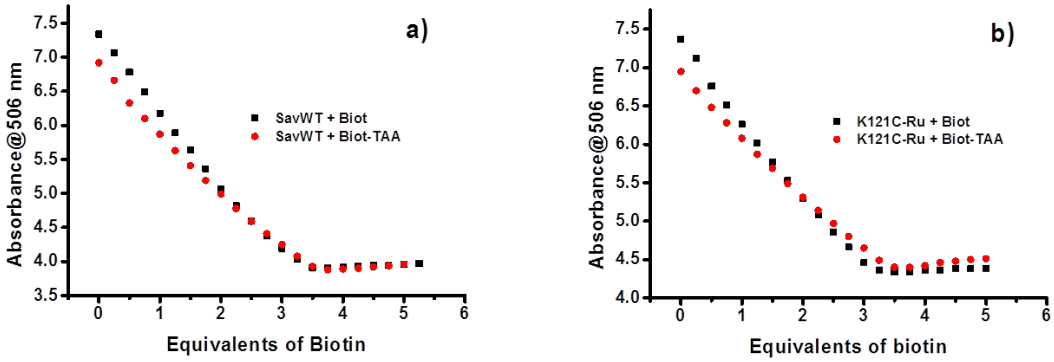


**Figure 4.3:** HABA displacement titrations of biotin (black symbols) and the biotinylated triarylamine **Biot-TAA** (red symbols) for a) WT streptavidin and b) K121C-Ru (see Appendix B for experimental details).

Since no crystal structure could be obtained so far, through-space distances were estimated based on a previously published crystal structure of an Ir-loaded streptavidin mutant (pdb code: 3PK2).[185] The arylated biotin moiety bearing a *para*-sulfur atom was used for distance estimation. This latter sulfur atom was selected as a surrogate for the nitrogen atom of the **Biot-TAA** moiety (Figure B.16). The shortest through-space distances from the sulfur atom to the -carbon of the amino

acids targeted for mutagenesis ranges from 7.1 to 22.1 Å (Table 4.1). As, by symmetry four cysteine residues result from a single point mutation, the mean value of the two closest residues was also determined: it increases from K121 (7.9 Å) < S112 (9.5 Å) < R84 (18.3 Å) < T66 (20.0 Å).

**Table 4.1.** Estimated through-space distances between α-carbon atom of the targeted mutagenesis positions and the sulfur atom of a biotinylated cofactor based on the crystal structure of streptavidin (pdb code: 3PK2)[185]. The two closest Cα are listed as well as their mean values (Figure B.16-B.20 in the Appendix B for details).

| mutant | $R_1$ [Å] | $R_2$ [Å] | mean [Å] |
|---|---|---|---|
| K121C | 7.1 | 8.6 | 7.9 |
| S112C | 6.9 | 12.1 | 9.5 |
| R84C | 14.8 | 21.7 | 18.3 |
| T66C | 17.8 | 22.1 | 20.0 |

### 4.3.2 Electron transfer studies

To explore the electron transfer in the **Biot-TAA** / Ru(II)-streptavidin dyads a flash quench technique was applied (Figure 4.4).[271–273]

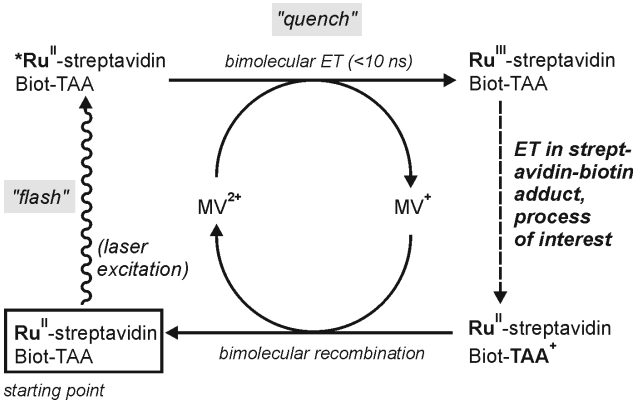


**Figure 4.4:** Illustration of the flash-quench procedure used for studying electron transfer in the **Biot-TAA** / Ru(II)-streptavidin adducts.[263–268] $MV^{2+}$ stands for methylviologene.

Therefore, the ruthenium(II) photosensitizer was excited selectively at 532 nm with laser pulses of ~10 ns duration. In the presence of 120 mM methylviologen dichloride ($MV^{2+}$) added to the aqueous solution, the luminescent $^3$MLCT excited state of the photosensitizer *Ru(II) is quenched oxidatively with diffusion-limited kinetics, i. e., initial excitation ("flash") is followed by oxidation of *Ru(II) to Ru(III) ("quench") within the ~10 ns duration of the laser pulse.

In a sample containing 50 µM Ru(II)-streptavidin (K121C mutant) and 120 mM $MV^{2+}$ but no **Biot-TAA** in MilliQ water at 25 °C, one observes the typical spectroscopic signatures of the $MV^{\bullet+}$ radical (green trace in Figure 4.5a).[274] Specifically, there is a sharp and intense absorption at 393 nm and a broader, less intense band with a maximum at 605 nm which can be attributed unambiguously to $MV^{\bullet+}$.[274,275] The oxidation product Ru(III) manifests as a bleach at ~450 nm. When adding 25 µM **Biot-TAA** to the same solution, an additional band at ~760 nm becomes observable (black trace in Figure 4.5a) in addition to the $MV^{\bullet+}$ bands.

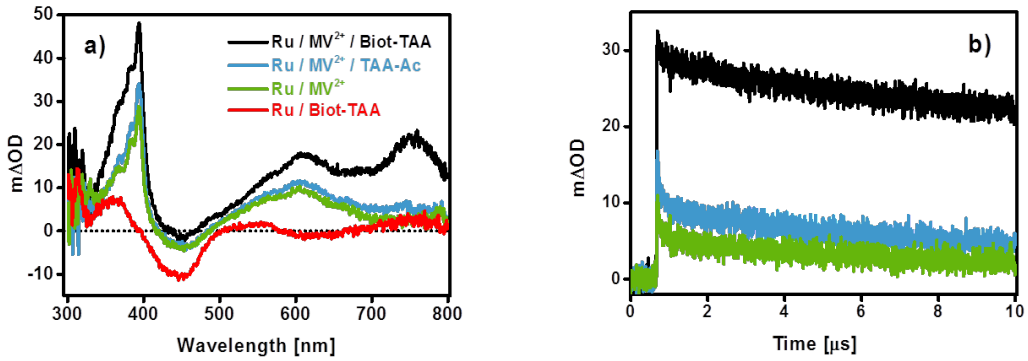


**Figure 4.5:** (a) Transient absorption spectra of K121C-Ru measured after excitation at 532 nm with laser pulses of ~10 ns duration. The spectra were time-integrated over 200 ns immediately after excitation. Sample concentrations were: 50 µM Ru(II)-streptavidin, 120 mM $MV^{2+}$, 25 µM **Biot-TAA** or **TAA-Ac**, where applicable. The solvent was MilliQ water at 25 °C. (b) Temporal evolution of the transient absorption signal at 760 nm for 3 of the 4 samples from (a).

The band at 760 nm is typical for $TAA^{+}$,[21] and hence this is clear evidence for electron transfer from TAA to Ru(III), which (based on the relevant redox potentials)[276–282] is expected to be associated with a reaction free energy ($\Delta G_{ET}^{0}$) of ca. -0.5 eV. In the reference experiment in which 50 µM Ru(II)-streptavidin and 120 mM $MV^{2+}$ were measured in the presence of 25 µM **TAA-Ac**, the band at 760 nm does not appear (blue trace in Figure 4.5a), confirming that in the Ru(II)-streptavidin (K121C mutant) / TAA-biotin system, the photo-triggered electron transfer from TAA to Ru(III) does indeed rely on the tight association between the streptavidin host and the **Biot-TAA** guest.

The $TAA^{+}$ signal at 760 nm rises with instrumentally limited kinetics (black trace in Figure 5b), indicating that phototriggered electron transfer from TAA-biotin to Ru(III)-streptavidin (K121C mutant) occurs with a rate constant $k_{ET} \geq 10^{8}\ s^{-1}$. The signal then decays on a timescale > 10 µs, due to bimolecular electron transfer between **Biot-TAA**$^{+}$ and $MV^{\bullet+}$ (Figure 4.5b). $MV^{\bullet+}$ has non-negligible

absorbance at 760 nm hence the observation of small signals even in absence of **Biot-TAA** (blue and green traces in Figure 4.5b).

For the S112C mutant, qualitatively similar results are obtained (Supporting Information). There is clear indication for rapid ($k_{ET} \geq 10^8\ s^{-1}$) electron transfer from **Biot-TAA** to Ru(III)-streptavidin, and the resulting photoproduct is again very long-lived (> 10 μs). However, for the R84C and T66C mutants, no such evidence was obtained. We conclude that these two ruthenium(II)-labeled mutants are not well suited for electron transfer with biotinylated triarylamine guests. These findings correlate with the increasing distances between the photosensitizer and the electron donating triarylamine. It is possible that electron transfer between photo-excited Ru(II) and $MV^{2+}$ is less efficient in these cases even though they seem to be even better exposed as the Ru(II) complexes in the other two mutants.

## 4.4 Summary and Conclusions

Rapid photo-triggered electron transfer from biotinylated guests to ruthenium photosensitizers which are covalently attached to cysteine residues of streptavidin is possible in carefully selected mutants. This is an important finding in view of photo-redox catalysis which makes use of catalysts which are embedded in the protected environment of a biotin binding pocket of streptavidin and photosensitizers which are bound to the surface of streptavidin. Catalysts in the biotin binding pocket can exhibit markedly better performance than outside streptavidin,[156,239] and our study paves the way to photo-redox catalysis in specifically engineered artificial metalloenzymes.

## 4.5 Acknowledgements

This work was supported by the Swiss National Science Foundation as part of the NCCR Molecular Systems Engineering as well as the SNI (PhD scholarship awarded to Sascha Keller).

## 4.6 Supporting Information

The full supporting information can be found in the Appendix B.

# 5

# Streptavidin as a Scaffold for Light-Induced Long-Lived Charge Separation

*The following section has been published in:*

*Chem. Eur. J.* **2017**, *23*, 18019-18024.

http://dx.doi.org/10.1002/chem.201703885

## Streptavidin as a Scaffold for Light-Induced Long-Lived Charge Separation

*Sascha G. Keller,[a] Andrea Pannwitz,[b] Hendrik Mallin,[a] Oliver S. Wenger[*,b] and Thomas R. Ward[*,a]*

[a] Department of Chemistry, University of Basel, Spitalstrasse 51, CH-4056 Basel, Switzerland,

[b] Department of Chemistry, University of Basel, St. Johanns-Ring 19, CH-4056 Basel, Switzerland

[*] Correspondence: thomas.ward@unibas.ch, oliver.wenger@unibas.ch

Keywords: Charge Separation, Photosensitizer, Streptavidin, Triad, Triarylamine

## 5.1 Abstract

Long-lived photo-driven charge separation is demonstrated by assembling a triad on a protein scaffold. For this purpose, a biotinylated triarylamine was added to a Ru(II)- streptavidin conjugate bearing a methyl viologen electron acceptor covalently linked to the *N*-terminus of streptavidin. To improve the rate and lifetime of the electron transfer a negative patch consisting of up to three additional negatively charged amino acids was engineered *via* mutagenesis close to the biotin-binding pocket of streptavidin. Time-resolved laser spectroscopy revealed that the covalent attachment and the negative patch were beneficial for charge separation within the streptavidin hosted triad: the charge separated state was generated within the duration of the excitation laser pulse, and lifetimes up to 3120 ns could be achieved with the optimized supramolecular triad.

## 5.2 Introduction

In nature, the multicomponent photosystems II and I (PS II, PS I) harvest the energy provided by the sun and convert it into cellular fuel NADH. In plant photosynthesis, the electrons for the reduction of $NAD^+$ to NADH are provided by the oxidation of water, on the other side of the enzyme complex.[283] Upon light absorption, water is oxidized and the electrons are transferred via a cascade to the catalytic reduction site. All redox and electron transfer processes take place in specific and specialized protein environments. In a biomimetic spirit, artificial photosynthesis aims at: i) mimicking the performance and functionality of natural photosynthesis, ii) converting visible light into electrochemical energy and iii) storing the extracted energy as chemical fuels. To achieve this ambitious goal, the generation of long-lived charge-separated states is essential. If the resulting electron-hole pair recombination is slow, the produced generated potential can be valorized to drive chemical reactions. In the past forty years, significant effort has been invested by chemists to mimic the exquisitely complex photosynthetic reaction center.[284–287] For this purpose, covalent or supramolecular assembly of an electron acceptor (A), an electron donor (D) and a photosensitizer (PS) affords an artificial triad A–PS–D.[288,289] Upon photochemical irradiation, the excited state A–PS*–D can react to afford the corresponding (transient) charge-separated species $A^-$–PS–$D^+$. In a biomimetic spirit, we set out to exploit a protein scaffold to position all three components of an artificial triad. There are few examples of artificial dyads embedded within proteins or peptides;[201,211,283,290–295] but artificial intramolecular triads relying on a protein scaffold seem unexplored to the best of our knowledge.

We selected streptavidin (Sav hereafter) as a scaffold for the assembly of such a triad. Sav is a remarkably stable and versatile homotetrameric protein (4 X 159 aminoacids, ca. 65 kDa). Each of the four identical monomers can bind one equivalent of biotin with a supramolecular binding affinity of $K_A$ = ca. $10^{13}$ $M^{-1}$.[296] The biotin-(strept)avidin technology, commonly referred to as molecular velcro, draws its versatility from the remarkable affinity between biotinylated probes and (strept)avidin. Importantly, derivatization of the carboxylate of biotin by large probes does not affect significantly this remarkable affinity. Since its introduction by Bayer and Wilchek half a century ago, it has found numerous applications in live cell imaging, drug delivery, ELISA and pull-down assays.[237] Additionally, this technology was used in the past decade to anchor abiotic cofactors within a protein environment to create artificial metalloenzymes.[238,297–306]

This effort was inspired by a visionary publication by Whitesides.[303,307–311] In a related context, several studies on the luminescence properties of (strept)avidin-embedded biotinylated $d^6$-metal

complexes, including ruthenium(II) polypyridines,[247,312–314] rhenium(I) tricarbonyl diimines[249–251,315,316] and cyclometalated iridium(III) complexes[256,258,317–320] suggest that such protein-based systems are well-suited for the generation of photo-induced charge separation.[321]

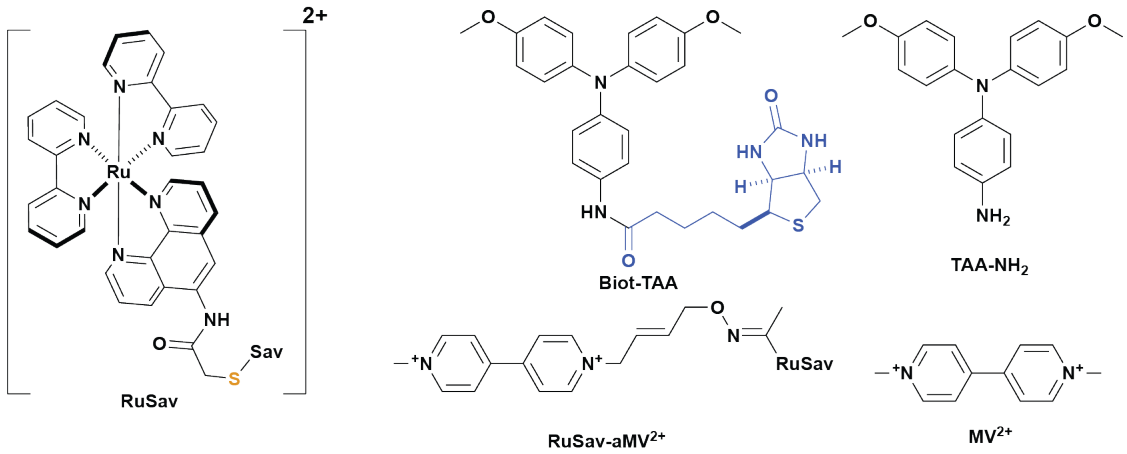


**Figure 5.1:** Structures of the photosensitizer, the donor and the acceptor used with cysteine-bearing Sav mutants to create Sav-embedded triads. Cysteine-bound ruthenium(II) photosensitizer, (**RuSav**); biotinylated triarylamine **Biot-TAA** (biotin in blue), the **TAA-NH$_2$** used as reference, methyl viologen **MV$^{2+}$** and the methyl viologen analogue **aMV$^{2+}$** that was covalently bound to the *N*-terminus of Sav to afford **RuSav**–**aMV$^{2+}$** (see SI for synthesis and characterization).

In a recent study,[322] we covalently anchored **[Ru(bpy)$_2$(phenNHCOCH$_2$Br)](PF$_6$)$_2$** to four different Sav isoforms bearing a single cysteine residue per monomer (Figure 5.1). Upon addition of a biotinylated triarylamine **Biot-TAA**, acting as electron donor, and excess methyl viologen **MV$^{2+}$** as external electron acceptor, we could characterize, by transient absorption spectroscopy, the formation of charge-separated species by photo-induced electron transfer.

By varying the position of the **[Ru(diimine)$_3$]$^{2+}$** photosensitizer on the Sav scaffold (i. e. by testing four different cysteine-bearing Sav mutants), we could identify the most suitable Sav mutant that favored an efficient electron transfer, as detected by the photoproduct of the oxidized electron donor. To ensure efficient electron transfer however, the terminal acceptor **MV$^{2+}$** was added in a large excess to the solution containing the Sav-embedded dyad.[322]

Building on these results, we report herein on our efforts to assemble and optimize a supramolecular triad embedded within a streptavidin scaffold.

## 5.3 Results and Discussion

### 5.3.1 Synthesis and structural aspects

In order to improve the rate of the electron transfer as well as the lifetime of the charge-separated species, we hypothesized that we may be able to combine both chemical- and genetic optimization strategies to assemble within streptavidin a triad.[297] With this goal in mind, we set out to covalently anchor **aMV$^{2+}$** to the *N*-terminus of Sav. We speculated that this strategy would increase the effective molarity of the terminal **aMV$^{2+}$** acceptor in the proximity of the biotinylated donor **Biot-TAA** embedded within the Sav bearing a covalently bound photosensitizer. The resulting Sav-embedded triad, abbreviated **Biot-TAA · RuSav–aMV$^{2+}$**, was further optimized by genetic means. We hypothesized that engineering an anionic patch in the proximity of the biotin-binding vestibule (hosting both, the **Biot-TAA** and the **[Ru(diimine)$_3$]$^{2+}$**-moiety) may contribute to further increase the effective molarity of the terminal electron acceptor in the proximity of both photosensitizer and electron donor. This concept has been used by nature, where an accumulation of negatively charged amino acids (negative patch) on plastocyanin are proposed to be involved in recognition of physiological reaction partners as cytochrome f and Photosystem I.[323–325] The effect of both chemical and genetic optimizations of the triad was evaluated relying on time-resolved photo-excitation experiments.

The ruthenium(II) complex **[Ru(bpy)$_2$(phenNHCOCH$_2$Br)](PF$_6$)$_2$**, the biotinylated supramolecular binding partner triarylamine **Biot-TAA** and the reference triarylamine **TAA-NH$_2$** were synthesized as previously described (Figure 5.1).[322] The alkoxy-amine containing methyl viologen analogue **aMV$^{2+}$** was synthesized in 4 steps as detailed in the Appendix C (Scheme C.1 and Figures C.1-C.7). As previously demonstrated,[322] the dyad bearing the ruthenium photosensitizer covalently anchored at position K121C of Sav displayed the highest quantum yield of the oxidized **Biot-TAA**. We thus selected K121C Sav as a starting scaffold for all mutagenesis studies reported herein. Inspection of the X-ray structure of the mature S112A Sav (pdb code: 3PK2)[185] revealed a disordered *N*-terminus (i.e. residues 2-12, ASMTGGQQMGR). These residues were modelled using Yasara[326] and possessed an α-helical structure. To flexibilize this *N*-terminus, thus increasing the probability bringing the **aMV$^{2+}$** closer to the **PS,** we substituted the -QQMGRD- motif (residues 9-14) by a -SGGGGS- sequence (*N*-flex hereafter).

In a second step, to evaluate the effectiveness of a negative patch to bring the positively charged **aMV$^{2+}$** in the proximity of the biotin-binding vestibule, we engineered additional glutamate and aspartate residues at positions N82-Y83-R84 (Figure 5.2 and Figure C.8). These three residues

were identified using Yasara[326] as suitably positioned to allow the **aMV$^{2+}$** to reach the negative patch generated upon incremental introduction of Glu or Asp residues at these positions (Figure 5.2).

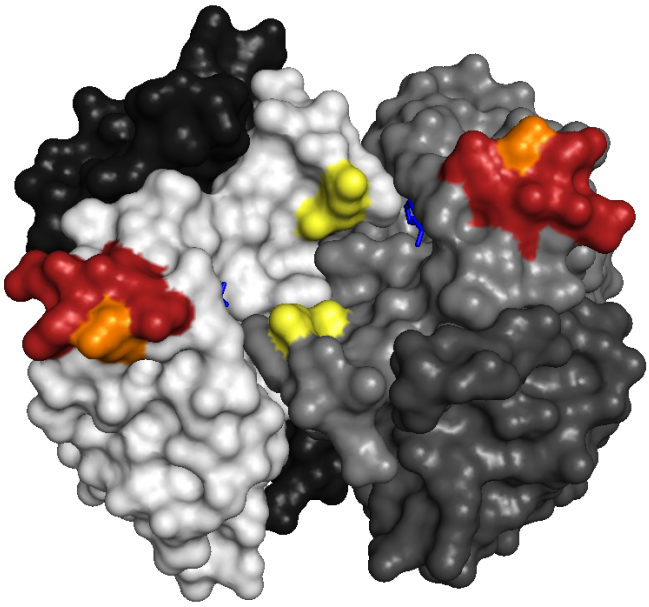

**Figure 5.2:** Engineering a negative patch in the proximity of the biotin binding vestibule. Surface representation of homotetrameric streptavidin, highlighting the selected amino acids (N82-Y83-R84, red) for the introduction of a negative patch; the K121C position (yellow) for the introduction of the Ru(II) photosensitizer, the naturally occurring E51 (orange) as well as biotin (blue, stick representation) (S112A mutant, the organometallic cofactor bound to the biotin was removed due to clarity, pdb: 3PK2).[185]

We mutated, expressed and purified four different mutants using *N*-flex K121C Sav as template with either no (**Sav$^{0}$** hereafter), one (**Sav$^{1}$** hereafter, R84E), two (**Sav$^{2}$** hereafter, N82D-R84E) or three (**Sav$^{3}$** hereafter, N82D-Y83E-R84E) additional carboxylate side chains (Figure 2). As the WT Sav contains a glutamate E51 in the proximity of the engineered negative patch, up to four negative charges may be present in the case of the *N*-flex-**Sav$^{3}$** mutant (highlighted in orange and red in Figure 5.2). The mutants were expressed using ZYP-5052 media, purified by affinity chromatography using iminobiotin-sepharose matrix and characterized by ESI-MS (details collected in the Appendix C, Figures C.10-C.17).[270,327] SDS-PAGE analysis using biotin-4-fluorescein demonstrated the biotin binding capability of the engineered Sav tetramers and highlighted a marked change in its isoelectric point p*I* as evidenced by the significant difference in electrophoretic mobility (Figure C.9).

To covalently link the methyl viologen analogue **aMV$^{2+}$** to Sav's *N*–terminus, the versatile procedure developed by Francis *et al.* was slightly modified, Figure 5.3.[328] The procedure tolerated

the use of pyridoxal-5-phosphate **PLP** which, added in excess to a phosphate-buffered solution (50 mM, pH 6.5) of the **RuSav**, resulted in the oxidation and hydrolysis of the *N*-terminal amine group to a ketone (Figure 5.3).

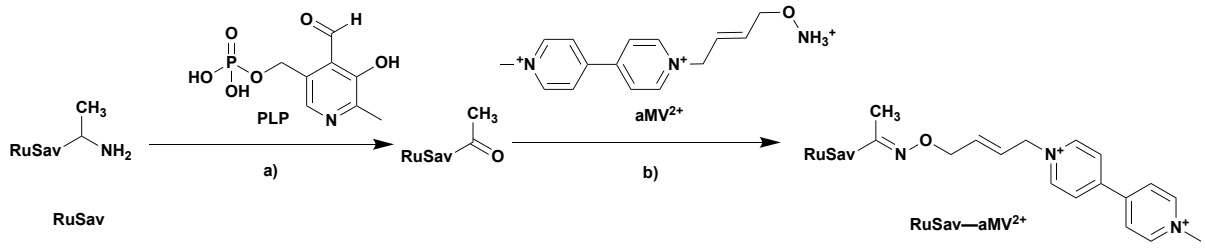


**Figure 5.3:** Coupling a modified activated methyl viologen **aMV**$^{2+}$ to the *N*-terminus of **RuSav** *via* a pyridoxal-5-phosphate-mediated transformation to yield the methyl viologen containing conjugate **RuSav**–**aMV**$^{2+}$. (a) 0.2 M PLP, 50 mM $PO_4^{3-}$ buffer, pH 6.5, 37°C, 1 h (b) 250 mM **aMV**$^{2+}$, 50 mM $PO_4^{3-}$ buffer, pH 2.2, 37°C, 1.5 h.

After removal of excess **PLP** by ultrafiltration dialysis (10 kDa cut off), the resulting Sav bearing a single ketone functionality readily reacted with the alkoxyamine-bearing **aMV**$^{2+}$, added in excess to a phosphate-buffered solution (50 mM, pH 2.2). The resulting oxime linkage is stable towards hydrolysis. The reaction was performed for one hour at 37°C and the resulting bioconjugates were purified via dialysis. Hereafter, we refer to the engineered Sav bioconjugates bearing the covalently attached [**Ru**(**diimine**)$_3$]$^{2+}$-photosensitizer as **RuSav**$^{n}$ and the covalently modified **aMV**$^{2+}$ as **RuSav**$^{n}$–**aMV**$^{2+}$ (where n = 0, 1, 2 or 3).

Since no crystal structure could be obtained so far, through-space distances were estimated based on a previously published crystal structure of an Ir-loaded streptavidin mutant (pdb code: 3PK2).[54] In a similar fashion to our previous study,[50] the arylated biotin moiety bearing a *para*-sulfur atom was used for distance estimation (Figure C.18 and Table C.1). This latter sulfur atom was selected as a surrogate for the nitrogen atom of the **Biot-TAA** moiety. The through-space distances from the sulfur atom to the α-carbons of the K121 residues can be estimated to 7.1 Å and 8.6 Å respectively. The through space distances of the α-carbons of the K121 residues and the α-carbons of the closest negatively charged R84 residues were determined to be 18.7 Å and 22.0 Å respectively. Furthermore, the distances of the **Biot-TAA** itself and the negative patches are 14.8 Å and 21.7 Å respectively. Given the flexibility of the system those are rough estimates.

The biotin-binding capacity of the **RuSav**$^{n}$ and the **RuSav**$^{n}$–**aMV**$^{2+}$ bioconjugates was evaluated relying on a displacement titration using 2-(4-hydroxyphenylazo)benzoic acid (HABA).[302,327,329] Upon incorporation within Sav, HABA displays an absorption at $\lambda_{max}$ = 506 nm.

Addition of a biotinylated probe displaces HABA, thus leading to the disappearance of the absorption band at 506 nm. This straightforward procedure revealed that each of the four biotin-binding sites of the homotetrameric Sav bioconjugates can accommodate one biotinylated cofactor **Biot-TAA** (Figure C.19 and C.20). Moreover, the affinity of **Biot-TAA** for **RuSav$^{n}$** or **RuSav$^{n}$–aMV$^{2+}$** (where n = 0 - 3) is comparable to that of biotin for WT Sav. This confirms that the bulky **Biot-TAA** moieties tightly bind to **RuSav$^{n}$** and **RuSav$^{n}$–aMV$^{2+}$** isoforms, despite the presence of the bulky **[Ru(diimine)$_3$]$^{2+}$** moiety which lies in the immediate proximity of the biotin-binding vestibule.

### 5.3.2 Optical spectroscopic studies

UV/Vis transient absorption spectroscopy was used to explore photo-induced electron transfer in the streptavidin-based donor-photosensitizer-acceptor systems. Selective photoexcitation of the Ru(II) chromophore of the **RuSav$^{n}$–aMV$^{2+}$ · Biot-TAA** systems at 450 nm with laser pulses of ~10 ns duration under deaerated conditions in milliQ water lead to the transient absorption spectra displayed in Figure 5.4.

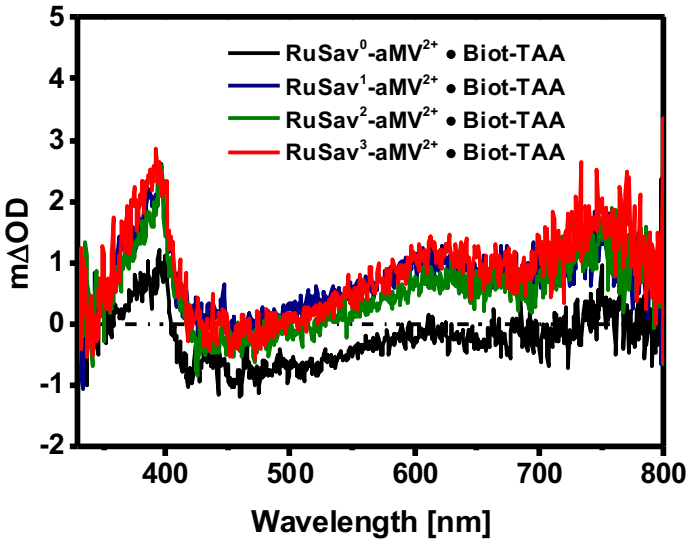


**Figure 5.4:** Transient absorption spectra of 50 µM of **RuSav$^{0}$–aMV$^{2+}$** (black trace), **RuSav$^{1}$–aMV$^{2+}$** (blue trace), **RuSav$^{2}$–aMV$^{2+}$** (green trace) and **RuSav$^{3}$–aMV$^{2+}$** (red trace) in milliQ water at 25 °C, 10 µs after excitation at 450 nm in presence of 50 µM **Biot-TAA**. Spectra were time-integrated over 4 µs.

The red trace in Figure 5.4, recorded with a time delay of 10 µs for the **RuSav$^{3}$–aMV$^{2+}$ · Biot-TAA** system, exhibits the spectroscopic signatures expected for electron transfer between the TAA / $MV^{2+}$ couple. In particular, the narrow intense band at around 400 nm as well as the weaker (broad) absorption around 605 nm are diagnostic for $MV^{+}$,[330,331] while the band at 750 nm is characteristic for

$TAA^+$.[332,333] Nearly identical transient absorption spectra are obtained for **RuSav$^2$–aMV$^{2+}$ · Biot-TAA** (green trace) and **RuSav$^1$–aMV$^{2+}$ · Biot-TAA** (blue trace), i. e., the systems having only two or one single point mutations (instead of three) to introduce additional negative charge on the protein surface. Only the **RuSav$^0$–aMV$^{2+}$ · Biot-TAA** system (black trace) without any mutations produces weaker $TAA^+$ and $MV^+$ signals. The clear message extracted from these experiments is that long-lived charge-separation is readily achievable based on this design principle. Importantly, point mutations that increase the negative charge on the streptavidin surface are beneficial for formation of the desired photoproducts comprised of $TAA^+$ / $MV^+$ pairs.

The quaternary structure of Sav consists of four sub-units that all harbour one $[\mathbf{Ru(diimine)_3}]^{2+}$ photosensitizer, one TAA donor, and one methyl viologen acceptor. Thus, all our **RuSav$^n$–aMV$^{2+}$ · Biot-TAA** systems are conformationally flexible tetrads of triads, and this complicates the kinetic analysis for two obvious reasons: (i) conformational flexibility leads to multiple donor-sensitizer, sensitizer-acceptor, and donor-acceptor distances in different proteins and its sub-units; (ii) electron transfer can also occur between redox-active units attached to different sub-units of Sav. Consequently, given the uncontrollable multitude of electron transfer distances and pathways, multi-exponential kinetics for formation and decay of the photoproducts are generally observed, unlike in rigid rod-like donor-sensitizer-acceptor compounds. It is thus not possible to extract rate constants for every individual photo-initiated processes in our streptavidin-based scaffolds in a meaningful manner.

The general observation for the **RuSav$^n$–aMV$^{2+}$ · Biot-TAA** systems is that a substantial amount of $TAA^+$ photoproduct (absorbing at 750 nm) is formed within the 10 ns duration of the laser pulse (Figure C.21), indicating that in a subset of triads electron transfer from TAA to the photo-excited $[\mathbf{Ru(diimine)_3}]^{2+}$ complex takes place with rate constants (k) exceeding $10^8$ $s^{-1}$. However, transient absorption spectra recorded immediately after photoexcitation are dominated by the signature of the $^3$MLCT state of the photosensitizer (Figure C.22), and based on this observation, we estimate that the subset undergoing photo-induced electron transfer amounts to roughly 10% at most under the conditions used for our experiments. Time-resolved luminescence data (Figure C.23) monitoring $[\mathbf{Ru(diimine)_3}]^{2+}$ emission at 630 nm confirm that the $^3$MLCT excited-state is only partially quenched in the **RuSav$^n$–aMV$^{2+}$ · Biot-TAA** systems. The disappointingly low yield for $TAA^+$ / $MV^+$ photoproduct formation likely has the following reasons: Electrostatic repulsion between the $[\mathbf{Ru(diimine)_3}]^{2+}$ complex and the $MV^{2+}$ unit in the conformationally flexible scaffolds is expected to lead to large $[\mathbf{Ru(diimine)_3}]^{2+}$-$MV^{2+}$ distances, disfavouring oxidative $[\mathbf{Ru(diimine)_3}]^{2+}$ $^3$MLCT

excited-state quenching. Most of the $^3$MLCT quenching therefore likely occurs via a reductive pathway, i. e., electron donation from TAA. Within the subset of scaffolds undergoing primary electron transfer from TAA to photo-excited $[\mathbf{Ru(diimine)_3}]^{2+}$, onward electron transfer from $[\mathbf{Ru(diimine)_3}]^{+}$ to $MV^{2+}$ is exergonic by -0.9 eV, but reverse electron transfer from $[\mathbf{Ru(diimine)_3}]^{+}$ to $TAA^{+}$ is thermodynamically even more favoured.[332,333] Indeed, the transient absorption kinetics in Figure C.24 suggest that 58-71% of the $TAA^{+}$ signal at 750 nm decay very rapidly after the laser pulse ($\tau \approx 20$ ns; Table 5.1 and Appendix C Figures C.21, C.22, C.24 and-C.25), and this is attributed to thermal reverse electron transfer between $[\mathbf{Ru(diimine)_3}]^{+}$ and $TAA^{+}$. Time-resolved luminescence data are compatible with this interpretation (Figure C.26 and Table C.2).

**Table 1:** Decay time constants ($t_1$, $t_2$, $t_3$) of the charge-separated state **RuSav$^n$–MV$^+$ · Biot-TAA$^+$** (n = 0, 1, 2, 3) extracted from triexponential fits. In each case, there was an initial rapid decay with a time constant ($t_1$) of ca. 20 ns, which leads to a rate constant of $5*10^7$ s$^{-1}$ for $TAA^{+}$ to $Ru(bpy)_3^{+}$ (reverse) electron transfer as mentioned in the main text. The time constants $t_2$ and $t_3$ reflect the decay of the $TAA^{+}$ / $MV^{+}$ charge-separated state.

| | $t_1$ [ns] | $t_2$ [ns] | $t_3$ [ns] |
|---|---|---|---|
| **RuSav$^0$–aMV$^+$ · Biot-TAA$^+$** | 25 (71%) | 287 (21%) | 2375 (8%) |
| **RuSav$^1$–aMV$^+$ · Biot-TAA$^+$** | 20 (62%) | 261 (25%) | 2380 (13%) |
| **RuSav$^2$–aMV$^+$ · Biot-TAA$^+$** | 20 (58%) | 225 (25%) | 1766 (17%) |
| **RuSav$^3$–aMV$^+$ · Biot-TAA$^+$** | 23 (60%) | 274 (26%) | 3120 (14%) |

Thus, in order to detect the $TAA^{+}$ / $MV^{+}$ photoproducts resulting from complete electron transfer as cleanly as possible, transient absorption spectra were generally recorded with a long delay time (10 μs) using long integration times (4 μs). After 10 μ s, unreacted $^3$MLCT excited states have decayed through common radiative and non-radiative pathways and do no longer contribute to the transient difference spectra, and simple $[\mathbf{Ru(diimine)_3}]^{+}$ to $TAA^{+}$ pairs have either recombined or undergone onward reaction to the desired $TAA^{+}$ / $MV^{+}$ products. Unfortunately, this leads to low signal to noise ratios (Figure 5.4).

Once the $TAA^{+}$ / $MV^{+}$ pairs have been formed, this charge-separated state decays on a microsecond time scale. The respective transient absorption data monitoring the decay of $TAA^{+}$ at 750 nm (Figure C.21) and the decay of $MV^{+}$ at 400 nm (Figure C.24) can be fitted in bi-exponential fashion for all four **RuSav$^n$–aMV$^{2+}$ · Biot-TAA** systems, with one time constant in the range of 225-

287 ns and a second time constant between 1766 and 3120 ns (Table 5.1).

The tethered triads **RuSav$^n$–aMV$^{2+}$ · Biot-TAA**, whereby the **MV$^{2+}$** is covalently linked to RuSav, affords instantly after photoexcitation an electron transfer to afford the corresponding TAA$^+$ / MV$^+$ (Figure C.24) in a subset of scaffolds. The charge separate state for the untethered triad on the other hand only builds over time (Figure C.25). In this case, **MV$^{2+}$** reduction is likely occurring from the long-lived $^3$MLCT excited-state via a diffusion controlled oxidative quenching pathway.

In control experiments, we found that **Biot-TAA** is of key importance for the successful photo-generation of TAA$^+$ / MV$^+$ pairs. When instead **TAA-NH$_2$** is used (i. e., a triarylamine compound lacking the biotin unit, Figure 5.1), no TAA$^+$ is formed (FigureC.S27). Conversely, covalent attachment of **MV$^{2+}$** was not essential for a photoproduct to form eventually, as long as a negative patch is engineered through point mutations in the proximity of the biotin-binding vestibule. Specifically, in the **RuSav$^n$** systems with n = 1 – 3, MV$^+$ formation is readily observable in presence of only 1 equivalent of ordinary (untethered) **MV$^{2+}$** (Figure C.28).

This nicely illustrates the effectiveness of the engineered negative patch in attracting a cationic electron acceptor. In the **RuSav$^n$** system with n = 0, i. e., the native Ru(II)-bioconjugated protein without negative patch, 15 equivalents of untethered **MV$^{2+}$** must be added in order to photo-generate a comparable amount of MV$^+$ as in the **RuSav$^n$** mutants with n = 1 – 3 in presence of only 1 equivalent of MV$^{2+}$ (Figure C.29). This again illustrates the effectiveness of the negative patch in triggering charge transfer.

Consequently, when adding 1 equivalent of **Biot-TAA** to the **RuSav$^n$** systems with n = 1 – 3, addition of one equivalent of untethered MV$^{2+}$ is sufficient for the photo-production of long-lived TAA$^+$ / MV$^+$ pairs (Figure C.30) similar to what was observed above for the **RuSav$^n$–aMV$^{2+}$ · Biot-TAA** systems in which MV$^{2+}$ was covalently tethered (Figure 5.4).Yet the combination of tethering the MV$^{2+}$-moiety and implementing the negative patch is crucial to enable instant electron transfer within the triad. When methyl viologen is added in solution and a negative patch (**RuSav$^3$**) is present, the temporal evolution of the transient absorption spectrum at 400 nm shows that the MV$^+$ signal builds up rather slowly over time (Figure 5.5a). In contrast when no negative patch is present and the methyl viologen is tethered (**RuSav$^0$–aMV$^{2+}$**) a signal is instantly observable (Figure 5.5b). In the optimized system (**RuSav$^3$–aMV$^{2+}$**) where the methyl viologen is tethered and a negative patch is present, however, the signal intensity of the instantly appearing signal at 400 nm is more intense (Figure 5.5c). This highlights that a combination of tethering an oxidant and engineering a negative patch to increase the local concentration facilitates electron transfer on a protein scaffold.

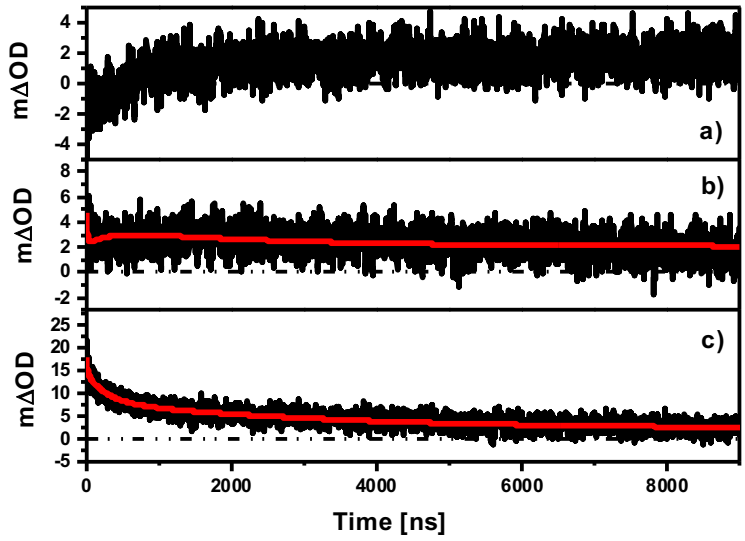


**Figure 5.5:** Temporal evolution of the transient absorption signal at 400 nm of (a) **RuSav$^{3}$ · Biot-TAA** with 1 equivalent of $MV^{2+}$ in solution (b) **RuSav$^{0}$–aMV$^{2+}$ · Biot-TAA** and (c) **RuSav$^{3}$–aMV$^{2+}$ · Biot-TAA** (black traces correspond to the recorded data and red traces represent the fitted functions).

## 5.4 Summary and Conclusions

Streptavidin was used as a scaffold for donor-photosensitizer-acceptor triad assemblies that lead to the formation of long-lived charge-separated states after photoexcitation in the visible spectral range. This is more commonly achieved in rigid rod-like compounds requiring multi-step syntheses and tedious purification procedures.[292] Our study highlights that streptavidin can serve as a platform for the straightforward assembly of suitable donors, photosensitizers, and acceptors. The effectiveness of the biotin anchor group for anchoring of a triarylamine donor is no surprise given its known affinity for (strept)avidin, but the influence of the genetically engineered negative patch for binding of the cationic methyl viologen acceptor, as well at the covalent attachment of the electron acceptor onto the protein is remarkable. Exploitation of this electrostatic effect could become a general design principle for attachment of artificial redox cofactors or small-molecule catalysts to enzymes. Furthermore, with these anionic patches, addition of 1 equivalent of untethered methyl viologen is nearly as effective as addition of 15 equivalents of methyl viologen to Ru(II)-modified streptavidin without any negative patch. At present, the quantum yield for formation of electron transfer photoproducts is low, but this could potentially be improved by optimizing the driving-forces for the individual (energy-storing) electron transfer steps through donor, sensitizer, and acceptor variation.

## 5.5 Acknowledgement

S.G.K. thanks the SNI for a PhD scholarship, T.R.W. and O.S.W. thank the NCCR "Molecular Systems Engineering", the Swiss National Science Foundation (grant 200020 162348 to TRW) and the EU (ERC, the DrEAM to TRW) for funding.

## 5.6 Supporting Information

The full supporting information can be found in the Appendix C.

# 6

# Photo-Driven Hydrogen Evolution by an Artificial Hydrogenase Utilizing the Biotin-Streptavidin

*The following section has been published in:*

*Helv. Chim. Acta.* **2018**, *101*, e1800036.

https://doi.org/10.1002/hlca.201800036

## Photo-Driven Hydrogen Evolution by an Artificial Hydrogenase Utilizing the Biotin-Streptavidin Technology

*Sascha G. Keller,[a] Benjamin Probst,[b] Tillmann Heinisch,[a] Roger Alberto[*,b] and Thomas R. Ward[*,a]*

[a] Department of Chemistry, University of Basel, Mattenstrasse 24a, CH-4002 Basel, Switzerland

[b] Department of Chemistry, University of Zürich, Winterthurerstrasse 190, CH-8057 Zürich, Switzerland

[*] Correspondence: thomas.ward@unibas.ch, ariel@chem.uzh.ch

Keywords: Hydrogen Evolution, Artificial Hydrogenase, Streptavidin, Photo-Catalysis, Biotin

## 6.1 Abstract

Photocatalytic hydrogen evolution by an artificial hydrogenase basted on the biotin-streptavidin technology is reported. A biotinylated cobalt pentapyridyl-based water reducing catalyst (WRC) was incorporated into different mutants of streptavidin. Catalysis with $[Ru(bpy)_3]Cl_2$ as a photosensitizer (PS) and ascorbate as sacrificial electron donor (SED) at different pH values highlighted the impact of close lying amino acids that may act as a proton relay under the reaction conditions (Asp, Arg, Lys). In the presence of a close-lying lysine residue, both the turnover numbers were improved and the lag-phase of the catalyst was reduced by up to 50%. The X-ray crystal structure of the artificial hydrogenase reveals a distance of 8.8 Å between the closest lying Co-moieties, we suggest that the hydrogen evolution mechanism is catalyzed via a single Co centre. Our findings highlight that streptavidin is a versatile host protein for the assembly of artificial hydrogenases and their activity can be fine-tuned via mutagenesis.

## 6.2 Introduction

Splitting water into $O_2$ and $H_2$ using sunlight as energy source offers an attractive means to address the World's growing energy needs.[334–337] Clean energies including solar, tidal, wind- or hydroelectric-power plants are widely used, but generate electricity which is challenging to store. Storing the energy within chemical bonds and producing an energy carrier that can be liquefied or transported as a gas is desirable. There are multiple ways of producing hydrogen on an industrial scale, yet most of them rely on carbon sources, precious metal catalysts and are not energy efficient.[16,29,30] Hydrogenases are natural enzymes found in a variety of bacterial and archaeal organisms, where they generate reducing equivalents in the form of $H_2$ or oxidize $H_2$ in reactions that require a reductant.[92] Such enzymes display exquisite catalytic properties as they operate: i) without the need of a high overpotential, ii) at high reaction rates (1,500 – 20,000 turnovers per second (TOF), iii) under physiological conditions pH 7 and 37°C in water. To achieve such unrivalled characteristics, hydrogenases are highly evolved: specialized channels to deliver the substrates and extract the product: proton-, electron- and dihydrogen channels ensure that the reaction does not lead to the generation of side-products.[338] Importantly, natural hydrogenases rely on earth-abundant metals (i.e. Ni and Fe), but require complex maturation machineries to assemble and display modest stabilities under non-physiological conditions. Their oxygen sensitivity and production costs call for the development of artificial hydrogenases. Several artificial hydrogenases relying on the incorporation of artificial metal cofactors in host proteins (cytochrome *c*, rubredoxin, ferredoxin) or linking to a polypeptide.[201,208,291,339–343] In the past decade, the biotin-streptavidin technology has found widespread use for the assembly of artificial metalloenzymes (ArM).[156,159,160,239,344–346] Streptavidin (Sav) is a remarkably stable and versatile homotetrameric protein (4 x 159 amino acids, ca. 65 kDa). Each of the four monomers can bind one equivalent of biotin with a supramolecular binding affinity of ca. $10^{13}$ $M^{-1}$, thus representing one of the strongest non-covalent interactions in nature. This feature offers the possibility to anchor abiotic cofactors within a protein environment to create artificial metalloenzymes. ArMs based on the biotin-Sav technology have been developed to catalyze a wide variety of water compatible reactions including: olefin metathesis, Suzuki-coupling, C–H activation or transfer hydrogenation etc.[159,185,191,195,347] Herein we report on our efforts to engineer an artificial hydrogenase based on the biotin-streptavidin technology. In view of the versatility of homogeneous Co-based hydrogen-evolution catalysts, we selected this base metal for the development of ArMs, using $[Ru(bpy)_3]Cl_2$ as photosensitizer and ascorbate as reducing agent.

## 6.3 Results and Discussion

### 6.3.1 Synthesis and binding studies

The pentapyridine (appy) ligand and the corresponding Co-catalyst [**CoBr(appy)-OH**]**Br** was selected for derivatization with a biotin anchor, Scheme 6.1.[145] The biotinylated water reduction catalyst (WRC) [**CoBr(appy)-Biot**]**Br** was synthesized in 6-steps from commercial compounds, (Scheme 6.1, Figures C.1-C.6, see Appendix D for details). The hydroxyl-bearing pentapyridine **(appy)-OH (1)** was reacted with 1-iodo-3-azido-propane **(2)** to afford the corresponding azido ether **(appy)-N$_3$ (3)**. The azide group was reduced and the resulting amine **(appy)-NH$_2$ (4)** was coupled to activated biotin-pentafluorophenylester **5** to afford the biotinylated ligand **(appy)-Biot (6)**. Reaction with $CoBr_2$ in MeOH yielded [**CoBr(appy)-Biot**]**Br** as a light brown solid which was purified by recrystallization.

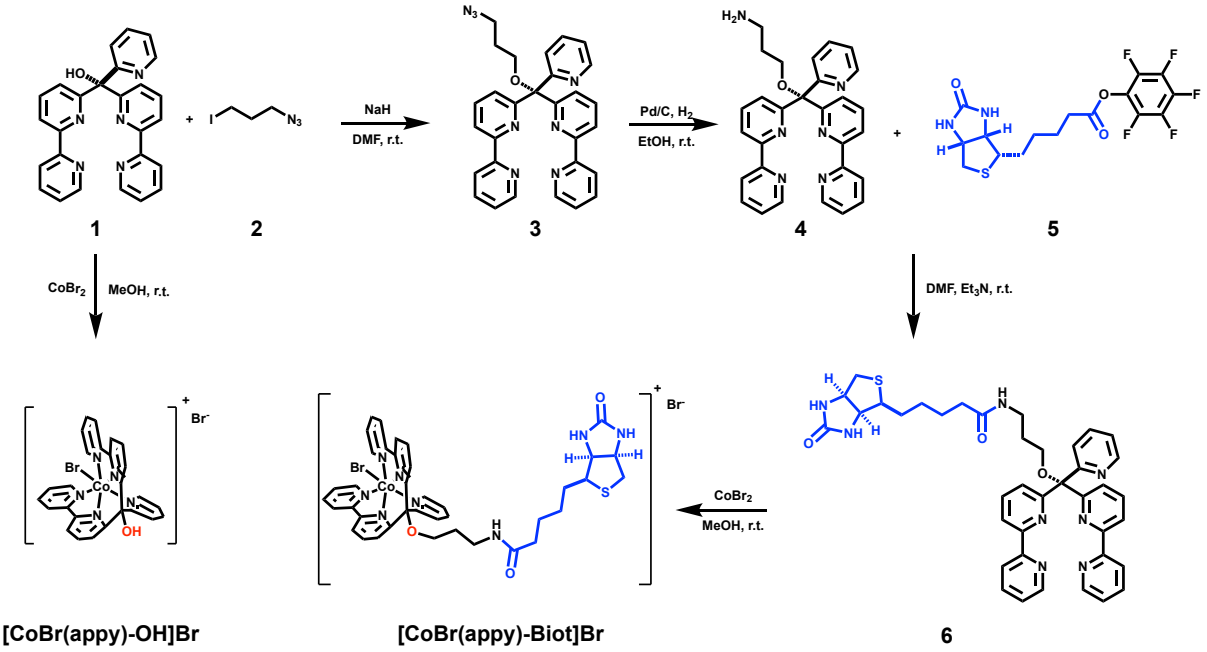


**Scheme 6.1**: Synthetic pathway of the water reduction catalyst [**CoBr(appy)-OH**]**Br** and its biotinylated counterpart [**CoBr(appy)-Biot**]**Br** (biotin depicted in blue, see the Appendix D for details).

The affinity of [**CoBr(appy)-Biot**]**Br** towards streptavidin was evaluated relying on a displacement titration using 2-(4-hydroxyphenylazo)benzoic acid (HABA).[237,242] The titration revealed that all four biotin-binding sites of the homotetrameric Sav could accommodate one biotinylated cofactor [**CoBr(appy)-Biot**]**Br** (Figure D.7). The linear segment profile of the displacement titration highlight that the affinity of [**CoBr(appy)-Biot**]**Br** for Sav WT is comparable

to that of biotin itself (i.e. > $10^{10}$ $M^{-1}$). This demonstrates that up to four equivalents of the bulky [**CoBr(appy)-Biot**]**Br** cofactor can bind quantitatively to the homotetrameric Sav host.

### 6.3.2 Photocatalysis and genetic optimization

To compare the activity of the Co-precursor [**CoBr(appy)-OH**]**Br** and its biotinylated analogue [**CoBr(appy)-Biot**]**Br**, argon-flushed, buffered (pH = 5) aqueous solutions were charged with 5 μM catalyst concentration, 1 M AscOH (sacrificial electron donor), 100 μM $[Ru(bpy)_3]Cl_2$ (photosensitizer) and were irradiated with a LED (453 nm and 1100 Lux). Hydrogen evolution was continuously monitored by an automated GC as described elsewhere.[348] With no Sav present, both [**CoBr(appy)-Biot**]**Br** and [**CoBr(appy)-OH**]**Br** display similar turnover numbers after 6.5 hours (TON = 1051 and TON = 1120 after 6 hours, black and blue traces for [**CoBr(appy)-Biot**]**Br** and [**CoBr(appy)-OH**]**Br** respectively, Figure 6.1a). Addition of Sav WT (10 μM free biotin binding sites, corresponding to 2.5 μM tetrameric Sav) did not impact on the activity of [**CoBr(appy)-OH**]**Br**, highlighting that there are no detrimental, non-specific interactions between the cofactor and Sav (grey trace, Figure 6.1a). In contrast, the biotinylated WRC displayed a marked decrease in activity (TON = 818 after 6 hours) highlighting the importance of second coordination sphere interactions on hydrogenase activity (green trace, Figure 6.1a). Next, we set out to explore the impact of the second coordination sphere of Sav. For this purpose, a focused library of Sav single point mutants was screened in combination with [**CoBr(appy)-OH**]**Br**. Building on previous studies, two close lying positions were selected: S112 and K121. Substitution of the serine residue S112 by either an Asp (Sav S112D, TON = 921 after 6 hours, light green trace, Figure 6.1b) or a Arg (Sav S112R, TON = 968 after 6 hours, turquoise trace, Figure 6.1b) lead to an increase in TON compared to Sav WT (green trace, Figure 6.1b). We speculate that this might be due to the presence of close lying amino acids capable of acting as a proton relay, potentially facilitating outer-sphere protonation of the Co-H species, as suggested in related studies.[148,158,349–353] This was confirmed by the improved activity of the S112K mutant which displays the highest activity (TON = 1069 after 6 hours, red trace, Figure 6.1b). To further investigate the critical role of acidic residues in the proximity of the Co–H moiety, the double mutant Sav S121AK121A, where the naturally occurring lysine at position K121 was mutated to an alanine, displays a marked decrease in activity (TON = 526, after 4.5 hours, yellow trace, Figure 6.1b). The Sav K121W shows an even higher erosion in activity (TON = 396 after 4.5 hours, orange trace, Figure 6.1b).

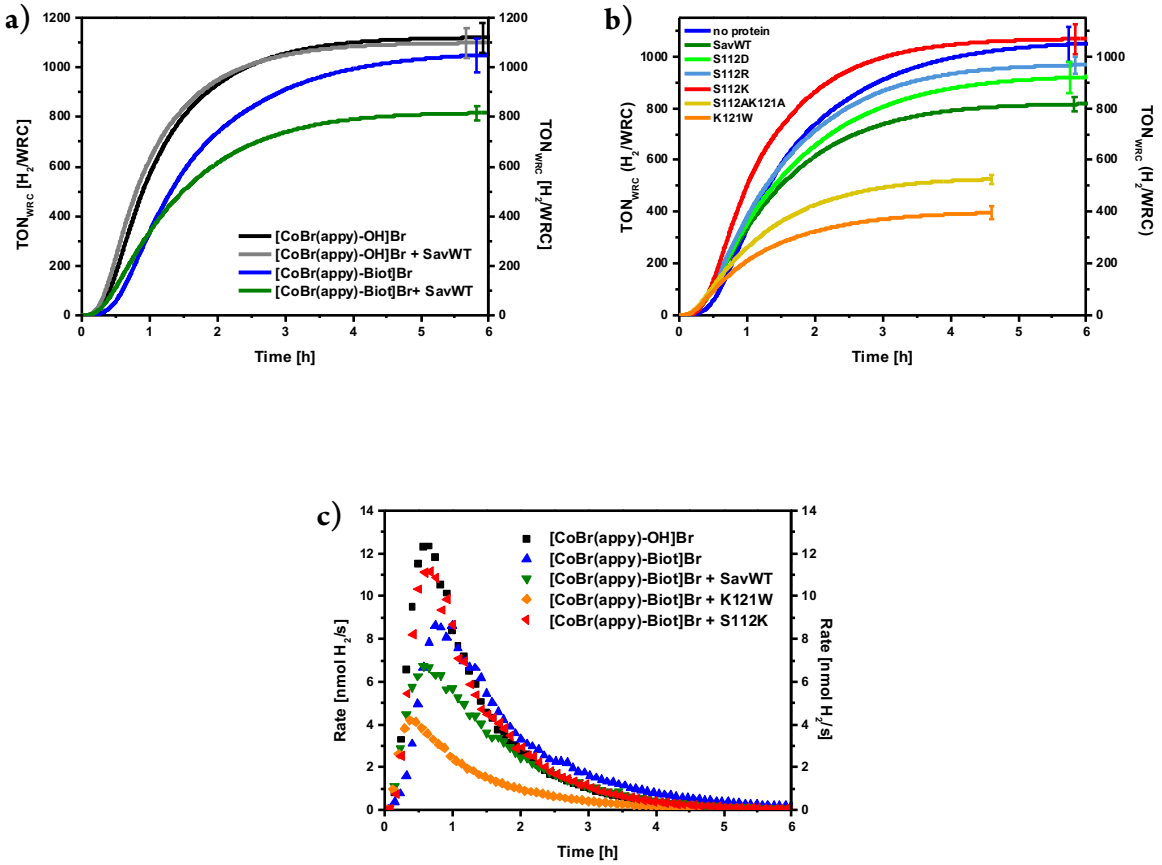


**Figure 6.1: Summary of turnover numbers and rates of artificial hydrogenases based on the biotin-streptavidin technology.** (a) hydrogen production profile of the parent and the biotinylated complex with and without Sav: [**CoBr(appy)-OH**]**Br** (black trace), [**CoBr(appy)-OH**]**Br** with Sav WT (grey trace), [**CoBr(appy)-Biot**]**Br** (blue trace) and [**CoBr(appy)-OH**]**Br** with Sav WT (green trace), (b) genetic optimization of the hydrogenase activity for [**CoBr(appy)-Biot**]**Br** in the presence of a variety of Sav mutants: no protein (blue trace), Sav WT (green trace), Sav S112D (light green trace) Sav S112R (turquoise trace), Sav S112K (red trace), Sav S112AK121A (yellow trace) and Sav K121W (orange trace), (c) Turnover frequencies of selected hydrogenases: [**CoBr(appy)-OH**]**Br** (black trace), [**CoBr(appy)-Biot**]**Br** (blue trace) with Sav WT (green trace), Sav K121W (orange trace) and Sav S112K (red trace). Experiments were performed using 5 μM WRC, 1 M ascorbate buffer (pH 5) and 100 μM $[Ru(bpy)_3]Cl_2$ and 10 μM free biotin binding sites (when Sav was present). See SI for details, irradiation

The reaction rates are also affected by incorporation of the cofactor into the protein. While the bare biotinylated cofactor [**CoBr(appy)-Biot**]**Br** has a maximum rate of 9 nmol $H_2$/s (blue triangles, Figure 6.1c), the non-biotinylated WRC [**CoBr(appy)-OH**]**Br** peaks at 13 nmol $H_2$/s (black squares, Figure 6.1c) and the incorporated cofactor [**CoBr(appy)-Biot**]**Br** · Sav S112K peaks at 12 nmol $H_2$/s (red triangles, Figure 6.1c). The presence of cationic residues in the immediate proximity of the {**Co(appy)**}-moiety affects both the TON and the corresponding the rates. The effect of the additional lysine is highlighted by the use of SavWT (green triangles, Figure 6.1c) and the

worst performing mutant K121W (orange squares, Figure 6.1c). In fact, since the binding pocket is symmetrical, not only two lysines are present within the binding pocket (S112K and K121) but four (2xS112K and 2xK121, Figure 6.5).

### 6.3.3 pH Dependence

Hydrogen evolution at neutral pH is desirable, since safety concerns of off-site hydrogen production can be overcome and the corrosion of materials can be prevented.[354] Furthermore, if a catalyst is active at a physiological pH an *in vivo* application may be possible.

Since the protein now provides a second coordination sphere around the catalytic centre and that lysines which lie in the close proximity of the cofactor were shown to have a positive effect on catalytic performance, we anticipated that the pH may influence catalysis. A pH screening of **[CoBr(appy)-OH]Br**, **[CoBr(appy)-Biot]Br** and **[CoBr(appy)-Biot]Br · Sav S112K** was performed (Figures D.8-D.14 and Tables D.1 and D.2). At pH 4 and pH 5 in 1 M AscOH buffer, **[CoBr(appy)-OH]Br** shows higher maximal rates than the biotinylated WRC **[CoBr(appy)-Biot]Br** either inside or outside the Sav S112K (Figure 6.2). Increasing the pH above 5.0, leads to an inversion in trend: at pH 5.7 (using 1 M acetate buffer with 0.1 M AscOH) the **[CoBr(appy)-Biot]Br · Sav S112K** displays the highest rates and turnover numbers. At pH values between 6 and 7.5 (using a 1 M phosphate buffer, with 0.1 M AscOH) the dihydrogen production rates follow the following order: **[CoBr(appy)-Biot]Br · Sav S112K** > **[CoBr(appy)-Biot]Br** ≈ **[CoBr(appy)-OH]Br** (Figure 6.2).

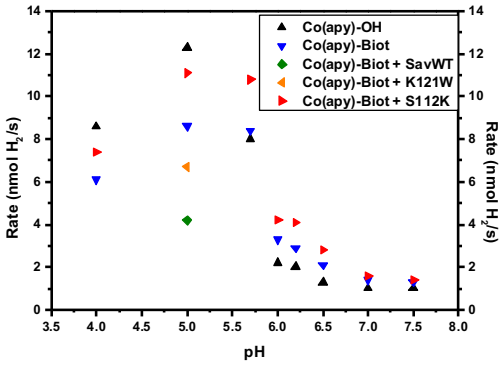


**Figure 6.2:** Maximum dihydrogen production rates determined as a function of pH for **[CoBr(appy)-OH]Br** (black squares) and **[CoBr(appy)-Biot]Br · Sav S112K** (red triangles), **[CoBr(appy)-Biot]Br · Sav WT** (green triangles), **[CoBr(appy)-Biot]Br · Sav K121W** (orange squares) and **[CoBr(appy)-Biot]Br** (blue triangle). The pH values were screened in buffered aqueous solutions (see Appendix D for details).

Incorporation of the biotinylated cofactor [**CoBr(appy)-Biot**]**Br** within **Sav S112K** affects both the reaction rate, as well as the time required to reach its maximal rate (Figure 6.3). As pH = 7.5, [**CoBr(appy)-Biot**]**Br** · **Sav S112K** requires 500 minutes to reach its maximum rate, whereas [**CoBr(appy)-OH**]**Br** requires 1100 minutes to react maximal rate.

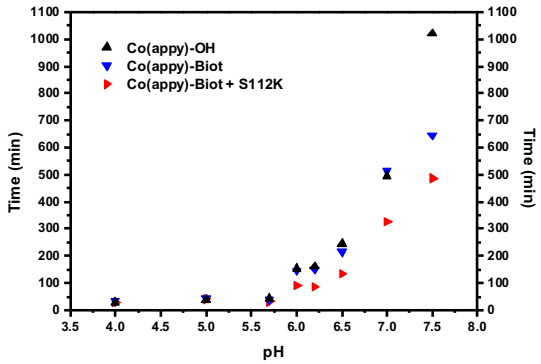


**Figure 6.3:** Summary of times required to reach the maximum rate of dihydrogen production as a function of pH. [**CoBr(appy)-OH**]**Br** (red squares), [**CoBr(appy)-Biot**]**Br** · **Sav S112K** (black triangle) and [**CoBr(appy)-Biot**]**Br** (blue triangle).

Upon monitoring both the rate and TON at pH = 7.0 reveals that [**CoBr(appy)-Biot**]**Br** · **Sav S112K** outperforms both [**CoBr(appy)-OH**]**Br and** [**CoBr(appy)-Biot**]**Br**, Figure 6.4. The most striking difference is the smaller latent/incubation time required until the onset of catalytic activity. Although such incubation times are often observed with small molecule hydrogen evolution catalysts, their origin and cause remains an unsolved puzzle.[349,355–357]

To rule out the possibility of spurious Co(II) species acting as catalyst, control experiments were conducted whereby some of the catalyst's ingredients were omitted (Figure D.15). Compared to [**CoBr(appy)-OH**]**Br** · **Sav S112K,** under otherwise identical reaction conditions, $Ru(bpy)_3^{2+}$ alone, Sav S112K, $CoBr_2$ or $CoBr_2$ · Sav S112K yielded only traces of dihydrogen. These observations suggest that the pentapyridine-coordinated Co(II) is indeed the species that generates the Co–H moiety, critical to the production of dihydrogen.

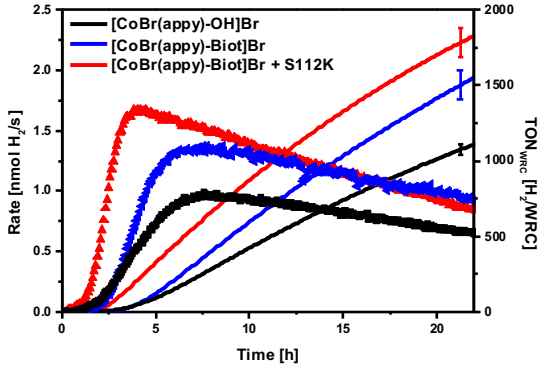


**Figure 6.4:** Comparison of the hydrogen production rate (left scale) and TON (right scale) for [**CoBr(appy)-OH**]**Br** (black trace), [**CoBr(appy)-Biot**]**Br** (blue trace) and [**CoBr(appy)-OH**]**Br** · **Sav S112K** (red trace) upon irradiation at 453 nm with 100 μM $[Ru(bpy)_3]Cl_2$ in 1 M $NaHPO_4$ buffer and 0.1 M AscOH present (See Appendix D for details).

### 6.3.4 Structural Insight

The localization of **CoBr(appy)-Biot**]**Br** within streptavidin was scrutinized by X-ray crystallography. A crystal of complex [**CoBr(appy)-Biot**]**Br** · Sav-K121A was obtained upon soaking apoprotein crystals with an excess of cofactor overnight. The X-ray structure of [**CoBr(appy)-Biot**]**Br** · **Sav S112A** was solved to 1.7 Å resolution (Figures 6.5 and D.16).

Upon solving the protein structure by molecular replacement residual electron density was visible in the biotin binding pocket. Complex [**CoH₂O(appy)-Biot**]$^{2+}$ was modelled in each of the four Sav monomers with full occupancy and in a single conformation. The first coordination sphere around cobalt is virtually identical to that found in the corresponding small molecule crystal structure (CCDC identifier: LILYAI).[145] The central metal is coordinated by the heteroaromatic groups in a distorted octahedral fashion. Axial bromide was replaced by water in the metalloenzyme. The bulky cobalt complex is accommodated within the biotin vestibule that is flanked from three side by loops 3,4; 5,6 and 7,8, the fourth site occupying a symmetry-related cofactor molecule. The axial water ligand is exposed to the solvent and is presumed to be the substrate binding site. The distance between two neighbouring Co-atoms is 8.8 Å. Considering the large distance between the catalytically competent metals, we can exclude a catalytic mechanism that would proceed via a bimetallic mechanism. This hypothesis is further supported by the fact that, under typical reaction conditions, only half of the biotin binding sites are occupied with [**CoBr(appy)-Biot**]**Br**, albeit with a statistical distribution.[179] Of the two postulated mechanisms put forward for Co-based hydrogenase mimics,[349,358,359] we suggest that the present system operates using a single Co-site. This is consistent

with the proposal by Fukuzumi and co-workers,[359] whereby a {Co(III)–H}-moiety is protonated to afford dihydrogen.

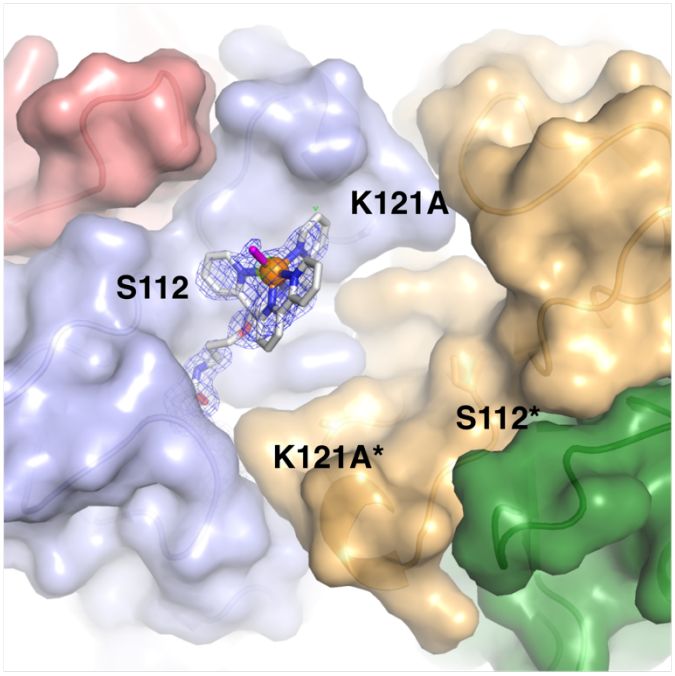


**Figure 6.5:** Close-up view of the active site in the crystal structure of complex **[CoH$_2$O(appy)-Biot] · Sav-K121A.** The protein is displayed as surface and cartoon model and the cofactor as stick model. The cofactor is contoured by a 2Fo-Fc electron density map (1.0 σ, blue colour) and an anomalous dispersion density map (3.0 σ, green colour). The orange sphere indicates a cobalt and the magenta stick a water molecule. For clarity only one cofactor molecule is displayed per Sav tetramer.

## 6.4 Conclusion and Outlook

In conclusion, we have demonstrated that incorporation of a biotinylated, molecular water reduction catalyst into streptavidin as a protein scaffold effects its activity in a positive way. The catalyst inside the protein not only showed higher turn overs at specific pH values but also higher maximum rates and a shorter period of reaching them in almost all cases. The genetically engineered additional basic amino acid S112K close to the catalyst is beneficial for the activity. We suggest that this close lying pendant base is protonated under the reaction conditions and can thus facilitate protonation of the Co–H species. This hypothesis is further supported by deletion of all close-lying lysine residues. Accordingly, S112AK121A and K121W derived hydrogenases display significantly reduced activities.

Furthermore, the incorporation of the catalyst into a protein cavity prevented two Co-centres to interact with another. Since the bound catalyst showed similar or in some cases better activity than the free catalyst, we suggest that the reaction mechanism proceeds *via* a single Co-center.

These findings suggest that such biohybrid catalysts may readily be optimized by genetic means. Future studies will focus on applying directed evolution optimization schemes to improve the hydrogenase activity. Finally, we hypothesize that the host protein may be immobilized on an electrode without perturbing the immediate environment around the metal cofactor.

## 6.5 Acknowledgements

SGK thanks the SNI for a PhD scholarship, TRW and TH thank the NCCR "Molecular Systems Engineering" and the Swiss National Science Foundation (grant 200020 162348 to TRW), as well as the ERC (the DrEAM) for generous funding.

## 6.6 Supporting Information

The full Supporting Information can be found in the Appendix D.

# 7

# Conclusion and Outlook

This thesis describes the efforts undertaken of assembling an artificial hydrogenase for photocatalytic hydrogen evolution from aqueous solutions at biological relevant conditions. Different aspects of a biocompatible hydrogen production system were examined.

First the hydrogen evolution activity of twelve different piano-stool complexes was tested. As hydrogen source served an aqueous solution of dilute formic acid which is split into one molecule of hydrogen and one molecule of carbon dioxide (Chapter 3). The catalysts $[Cp^*Ir(\mathbf{phenpzCO_2H})H_2O]^+$ **8** and $[Cp^*Ir(\mathbf{imim})H_2O]^{2+}$ **11** could be identified to perform very well, yielding up to >3650 TON and >8700 TON respectively. They furthermore displayed good oxygen tolerance and recyclability, what is important for industrial applications and potential *in vivo* systems

Next, the electron transfer on the surface of streptavidin was explored (Chapter 4). Four different streptavidin mutants were selected to study the rapid photo-triggered electron transfer from a biotinylated triarylamine to a ruthenium photosensitizer which was covalently attached to differently positioned cysteine residues. We could show that electron transfer occurred best, when the photosensitizer was attached to the K121C residue of streptavidin. This residue lies within the binding pocket and is thus in close proximity to an incorporated electron donor. This is an important finding in view of future photo-redox catalysis. This could make use of catalysts which are embedded in the protected environment of a biotin binding pocket of streptavidin and photosensitizers which are bound to the surface of streptavidin. In the case of this dyad the electron acceptor methylviologen was

added in high excess in solution. In a next step the electron acceptor was also covalently attached to the protein (Chapter 5). We chose to bind a methylviologen moiety to the *N*-terminus of the protein. The donor-photosensitizer-acceptor triad assembly lead to the formation of long-lived charge-separated states after photoexcitation in the visible spectral range. This is more commonly achieved in rigid rod-like compounds requiring multi-step syntheses and tedious purification procedures. This highlights that streptavidin can serve as a platform for the straightforward assembly of suitable donors, photosensitizers, and acceptors. Furthermore, we genetically implemented a negative patch consisting of three negatively charged amino acid residues to the protein. The patch was engineered to be in close proximity to the biotin binding pocket to exploit its electrostatic effect onto the cationic electron acceptor methylviologen. With the anionic patch, addition of 1 equivalent of untethered methyl viologen is nearly as effective as addition of 15 equivalents of methyl viologen to Ru(II)-modified streptavidin without any negative patch. This could become a general design principle for the attachment of artificial redox cofactors or small-molecule catalysts to enzymes.

This issue was addressed next, when a small molecule hydrogenase mimic was incorporated into streptavidin as a protein scaffold (Chapter 6). Depending on the explored mutants of streptavidin, higher turnover numbers and rates, as well as shorter lag-times were achieved. A genetically engineered additional lysine at position S112 close to the catalyst is beneficial for their activity since this pendant base is protonated under the tested conditions and can donate a proton. Pendant bases were already described to have a beneficial influence on hydrogen reduction and oxidation before, and we could support these findings. Interestingly, when the native lysine K121 was mutated to a tryptophan or alanine the reactivity dropped drastically. These findings show that these small molecule-protein agglomerates might be of great use in the future, since the protein provides a straightforwardly mutatable second coordination sphere, which is only hard to achieve by chemical means. Furthermore, the incorporation of the catalyst into the protein cavity prevented the two Co-centres to interact with another. The bound catalysts showed similar or in some cases better activity than the free catalyst in solution. This leads to the assumption that the proposed heterogeneous reaction mechanism, involving the reduction from Co(III)-H to Co(II)-H by another Co(I) seems unfeasible, at least in our system.

In the future, the combination of all tested approaches should be tested. For example, having the photosensitizer attached in close proximity to the protein binding could facilitate faster electron transfer from the photosensitizer to an incorporated catalyst. Furthermore, other photosensitizers, electron acceptors or electron donors can be assembled on the protein surface, eventually leading to

electron relays or proton or hydrogen channels, as found in natural hydrogenases. Other water reduction or water oxidation catalysts can be bound to biotin and brought into the binding pocket of streptavidin, since a beneficial effect of the assembly was found.

Also, different sacrificial electron donors should be tested and maybe the negative patch can improve their reactivity towards a bound photosensitizer. The assembled hydrogenase could further be immobilized on electrodes what would make recycling of the system possible.

Further mutagenesis of the protein, and utilization of two or more mutations simultaneously could eventually also add some of the features of real hydrogenase enzymes. Another approach would be the use of other enzymes (i.e. human carbonic anhydrase) with a different co-factor could yield in a higher activity.

# A

# Supplemental Information Chapter 3

## A.1 General Methods

### A.1.1 Solvents and reagents

Materials and reagents were purchased at the highest commercially available grade and used without further purification. Solvents used for reactions correspond to the quality "puriss".

### A.1.2 NMR Spectroscopy

$^{1}H$ and $^{13}C$ spectra were recorded (295 K) on Bruker Avance DRX-500 or DPX-400 MHz spectrometers. Solvents for NMR were obtained from Cambridge Isotope Laboratories, Inc. (Andover, MA, USA). Chemical shifts (δ) are reported in ppm using trimethylsilyane or the residual solvent peaks as a reference and coupling constants (J) are reported in Hertz (Hz).
The multiplicities are abbreviated as: s = singlet, d = doublet, t = triplet, m = multiplet and br= broad.

### A.1.3 Mass Spectroscopy

High resolution mass spectrometry (HRMS) was recorded on a Bruker FTMS 4.7T
BioAPEX II. The elemental analysis (EA) was measured on a Analysator 240 from Perkin-Elmer or a vario MICRO cube from Elementar.

### A.1.4 Spectrophotometry

Absorbance scans were recorded on a TECAN infinite M1000PRO.

## A.2 Synthesis

Complexes **1**[360], **2**[361], **3**[222], **4**[362] ($PF_6$), **5**[363] ($PF_6$), **7**[364] (Cl), **8**[365], **9**[366] (Cl), **10**[367] ($PF_6$) and **11**[236] were synthesized according to literature procedures.

**NMR-Spectra of $[Cp^*Ir(phenpyCO_2H)(H_2O)]^+$ (6)**

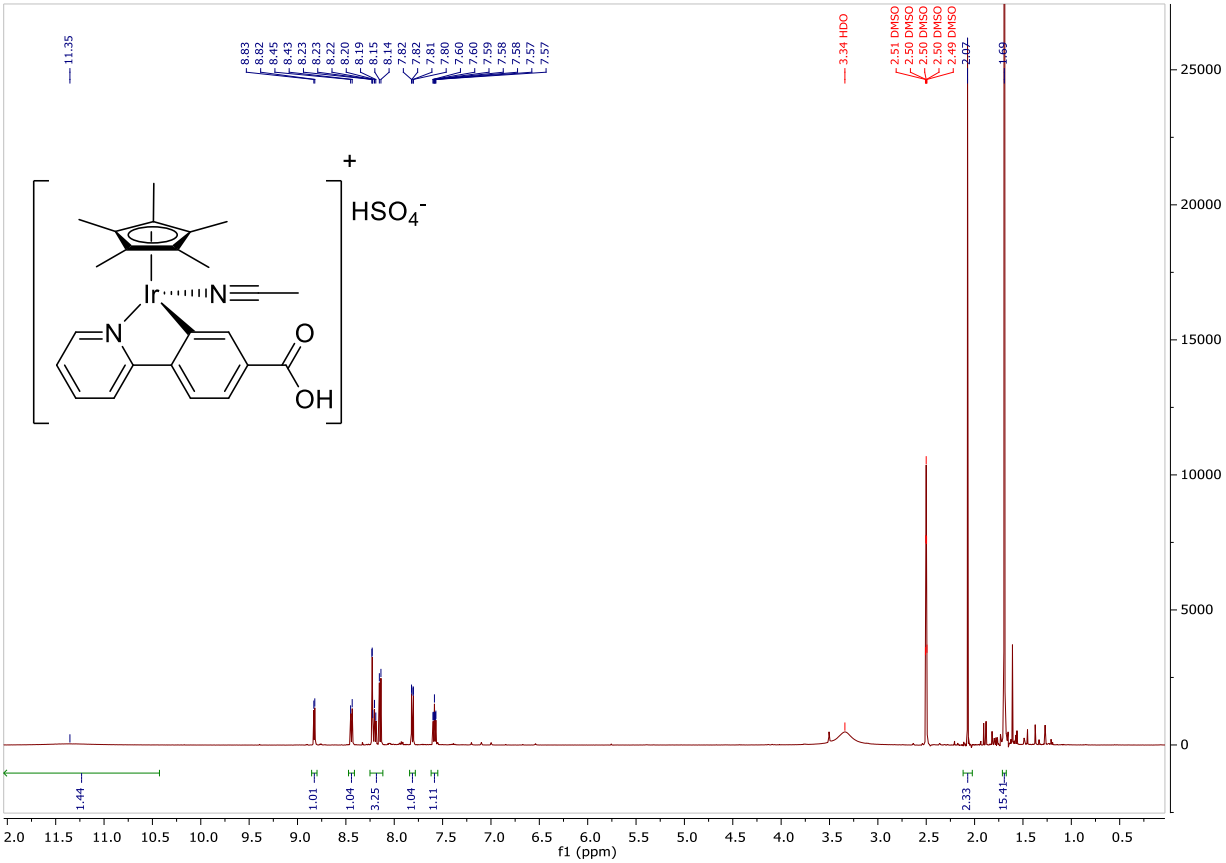

## NMR-Spectra of $[Cp^*Rh(phenpzCO_2H)(H_2O)]^+$ (12)

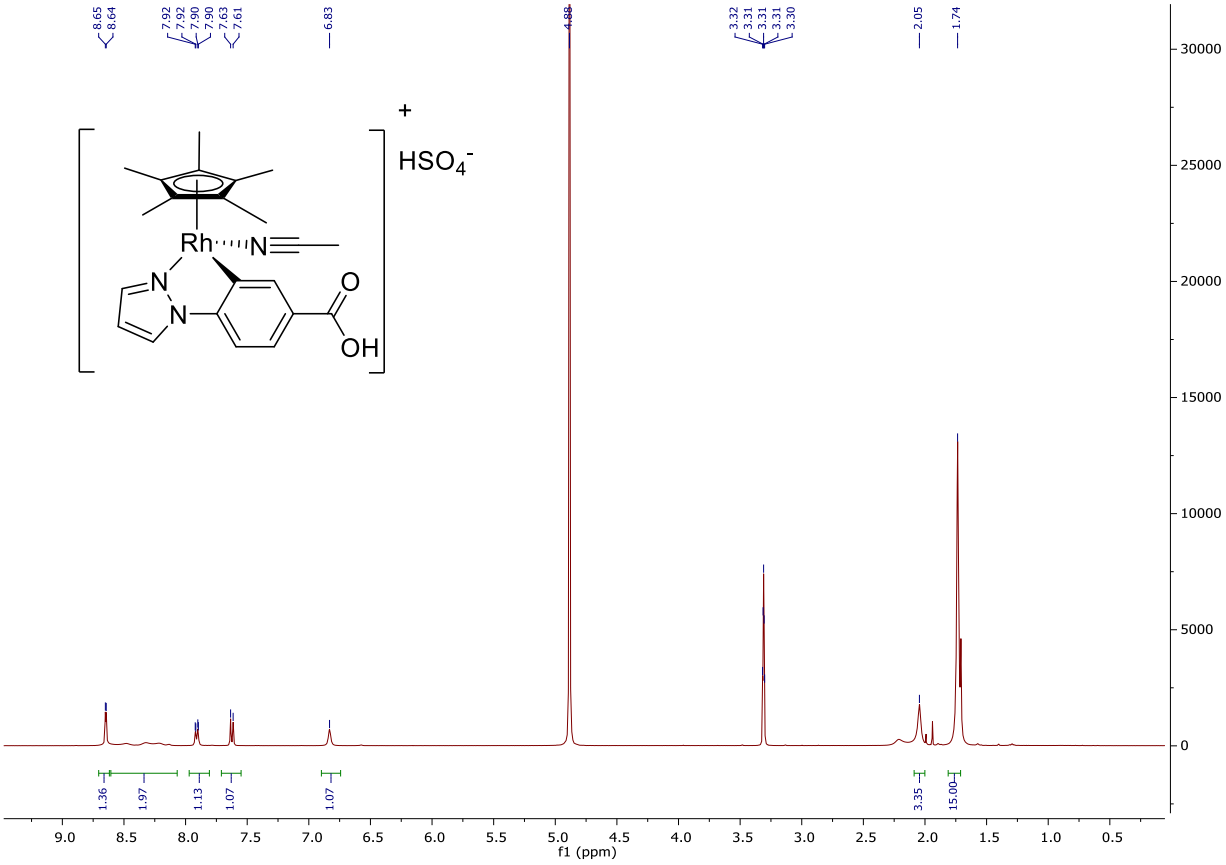


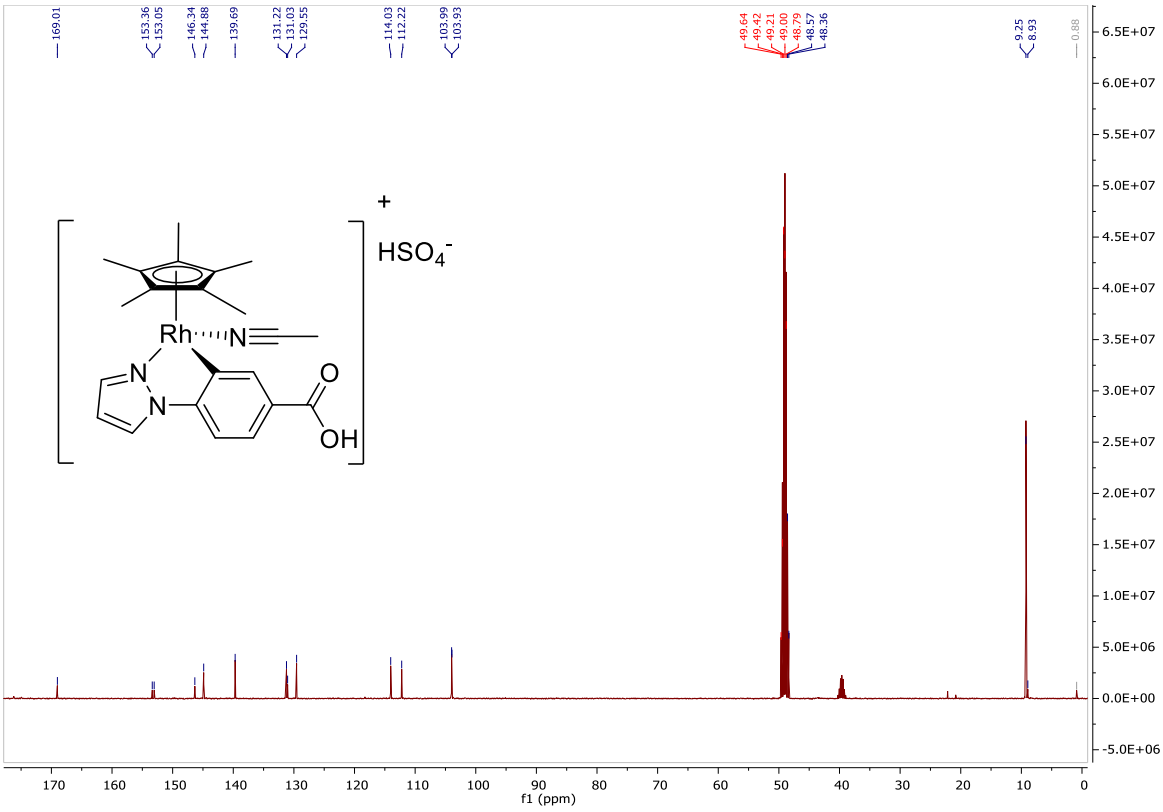

## A.3 Analytical Procedures

### A.3.1 Gas burette

The gas evolution was monitored by an automated gas burette.[235]

An acetic acid/sodium acetate buffer in water (2.0 ml of a 2.5 M stock solution) was charged with different concentrations of formic acid. The solution and the apparatus were degassed by sparging with $N_2$ for 10 minutes. The reaction vessel was heated to 37°C and the system was allowed to equilibrate for 20 minutes and the catalyst, dissolved in degassed water (200 µl), was injected. The instrument was then set to record at a rate of 0.8 Hz. The burette operates by bubbling the evolved gas through a low-density mineral oil measuring the change of pressure by the evolved gas with a headspace manometer.

For all further calculations, the composition of gas was assumed to be a 1:1 mixture of $H_2$ and $CO_2$ and the volume of 1 mole of gas was set to be 24.47 $dm^3$ at room temperature.

### A.3.2 Total turnover Number

An acetic acid/sodium acetate buffer (pH 4, 2.0 ml of a 2.5 M stock solution) in water was charged with 0.5 mmol formic acid yielding in a 0.23 M formic acid solution. The solution and the apparatus were degassed by sparging with $N_2$ for 10 minutes. Afterwards, the reaction vessel was heated to 37°C and the system was allowed to equilibrate for 20 minutes. The catalyst (0.02 µmol dissolved in 200 µl degassed water) was injected yielding a final 9 µM catalyst concentration. After injection, the gas evolution was monitored. As soon as gas evolution ceased, an additional formate (0.5 mmol) was added. This was repeated up to 3 times in 48 hours and resulted in the mentioned TTON.

### A.3.3 Air tolerance

An acetic acid/sodium acetate buffer (pH 4, 2.0 ml of a 2.5 M stock solution) in water was charged with 0.5 mmol formic acid yielding in a 0.23 M formic acid solution. The solution and the apparatus were not degassed by sparging with $N_2$ for 10 minutes.
Three different experiments were conducted:

i) Non-degassed solutions. No degassing was conducted.
ii) Sparging the solution with air. The solution, the apparatus and the catalyst were sparged for 2 minutes with air.

iii) Allowing the catalyst stand for 3 weeks on the lab bench in water under air. No degassing was conducted.

The reaction vessel was heated to 37°C and the system was allowed to equilibrate for 20 minutes. The catalyst (0.002 mmol dissolved in 200 µl water) was injected yielding a final 0.9 mM catalyst concentration. Following injection, the gas evolution was monitored.

### A.3.4 Dilution

An acetic acid/sodium acetate buffer (pH 4, 2.0 ml of a 2.5 M stock solution) in water was charged with 0.5 mmol formic acid yielding in a 0.23 M formic acid solution. The solution and the apparatus were degased by sparging with $N_2$ for 10 minutes. The reaction vessel was heated to 37°C and the system was allowed to equilibrate for 20 minutes. The catalyst (in 200 µl degassed water) was added to yield 45 µM, 23 µM and 2.3 µM final catalyst concentrations. After injection, the gas evolution was monitored.

### A.3.5 pH dependence

An acetic acid/sodium acetate buffer (pH 4, 2.0 ml of a 2.5 M stock solution) in water with pH set to 4.0 or 5.0 or pure water was charged with 0.5 mmol formic acid yielding a 0.23 M formic acid solution. The solution and the apparatus sparged with $N_2$ for 10 minutes. The reaction vessel was heated to 37°C and the system was allowed to equilibrate for 20 minutes. Then, the catalyst dissolved in degassed water (200 µl) was injected yielding a 0.9 mM catalyst concentration. After injection, the gas evolution was monitored.

### A.3.6 Calculations

To calculate the conversion of formic acid, the detected gas volume was correlated to the SATP molar gas volume at 25°C. Taking in account that 1 mole of gas has the volume of 24.47 liter, 1 mole of decomposed formic acid produces 48.94 liter of gas, since it is decomposed equally to $H_2$ and $CO_2$. Thus 0.1 mmol formic acid equals 4.94 ml of gas.

$$\left( \frac{evolved\ gas\ (l) / 24.47\ (l/mol)}{2} \right) = reacted\ substrate\ (mol)$$

Thus, for 2.1 ml gas collected after 30 minutes equals (2.1 ml / 24.47 ml/mmol) = 0.0858 mmol. Devided by two yields 0.0429 mmol, the amount of substance that has reacted. Taking in account that 0.002 mmol catalyst was present a turnover number of 21 after 30 minutes can be determined.

### A.3.7 Kinetic Calculations

The rate constants *k* and curves were calculated using OriginPro 9.0 by a first-order exponential fit function "ExpDec1".

$$y = A_1 \cdot \exp(-x/t_1) + y_0$$

**Complex 3:**

| | Value | | Standard Error | |
|---|---|---|---|---|
| $y_0$ | 0.00178 | mol/l | 1.89711E-5 | mol/l |
| $A_1$ | 0.04436 | mol/l | 1.55676E-5 | mol/l |
| $t_1$ | 6259.08607 | s | 6.11302 | s |
| *k* | 1.59768E-4 | $s^{-1}$ | 1.56039E-7 | $s^{-1}$ |
| tau | 4338.46786 | s | 4.23723 | s |

**Complex 7:**

| | Value | | Standard Error | |
|---|---|---|---|---|
| $y_0$ | -0.00147 | mol/l | 1.70508E-5 | mol/l |
| $A_1$ | 0.04609 | mol/l | 1.52203E-5 | mol/l |
| $t_1$ | 4638.20264 | s | 4.90027 | s |
| *k* | 2.15601E-4 | $s^{-1}$ | 2.27783E-7 | $s^{-1}$ |
| tau | 3214.95708 | s | 3.39661 | s |

**Complex 8:**

| | Value | | Standard Error | |
|---|---|---|---|---|
| $y_0$ | 8.59619E-4 | mol/l | 5.92873E-6 | mol/l |
| $A_1$ | 0.04746 | mol/l | 2.42519E-5 | mol/l |
| $t_1$ | 1459.67529 | s | 1.28076 | s |
| *k* | 6.85084E-4 | $s^{-1}$ | 6.0111E-7 | $s^{-1}$ |
| tau | 1011.76981 | s | 0.88775 | s |

**Complex 11**

| | Value | | Standard Error | |
|---|---|---|---|---|
| $y_0$ | 9.70201E-4 | mol/l | 9.40838E-6 | mol/l |
| $A_1$ | 0.04816 | mol/l | 2.91786E-5 | mol/l |
| $t_1$ | 1892.23489 | s | 2.17028 | s |
| $k$ | 5.28476E-4 | $s^{-1}$ | 6.0613E-7 | $s^{-1}$ |
| tau | 1311.59728 | s | 1.50432 | s |

Since catalyst **9** deactivated in the course of the reaction, no accurate $k$ value could be calculated. To estimate the rate constant, the dependence to the half time was used giving $k = \ln 2/t_{1/2}$ resulting in $k = 8.68 \cdot 10^{-4}\ s^{-1}$.

### A.3.8 CO detection

A modified spottest from the literature was used to detect possible CO evolution.[368]

A saturated aqueous solution of phosphomolybdic acid and a solution of 0.02 g $PdCl_2$ in 10 ml water were mixed in a 4:1 ratio. If CO is present a blue colour of molybdenum blue ($Mo_2O_5$) is detectable. A photospectrometer was used to measure the absorbance of the blue colour, if produced. For that purpose, different volumes of CO (10 µl, 20 µl, 50 µl and 100 µl) were injected to 200 µl of the mixed spot test solution. It was left sit for 1 h for the colour to build up. Then an absorbance scan measurement was conducted to determine the absorbance of the produced molybdenum blue (Figure S1, signal is increasing at around 760 nm). To measure whether the hydrogenases **8** and **11** also produced CO the evolved gas of the reaction with 0.23 M formate was passed through 200 µl of the spot test mixture. After the reaction was completed the absorbance was measured. Figure 2 shows that there is no difference between the reaction solution before and after the reaction.

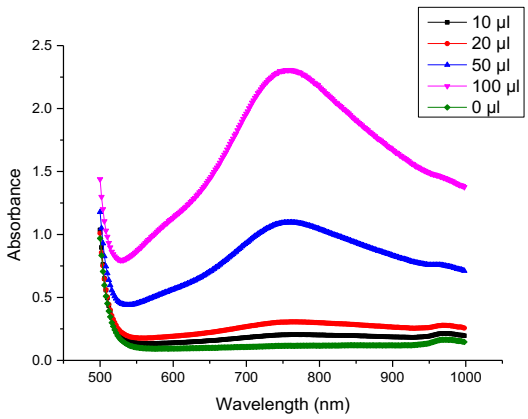


**Figure A.1:** Absorbance scan of different CO concentrations

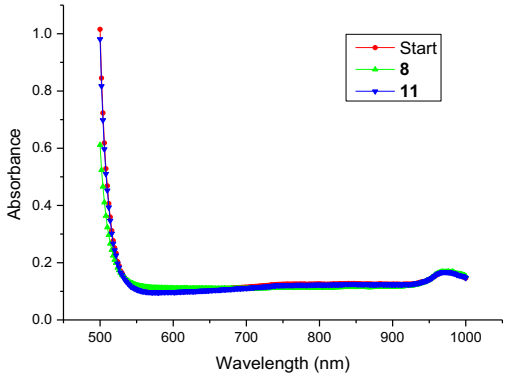


**Figure A.2:** Absorbance scan of the detecting solution at start and after the reaction of **8** and **11**

### A.3.9 NMR catalysis experiments

NMR experiments were performed on a 600 MHz Bruker Avance III instrument with a BBFO+ smart probe in $H_2O$ / $D_2O$ (95 / 5 %) with or without acetic acid d-4 buffer (pH 4.0). Catalyst concentrations were 910 µM, while 45.5 mM of formate were applied. $^1$H NMR spectra were recorded using an excitation sculpting pulse sequence for water suppression.[369]

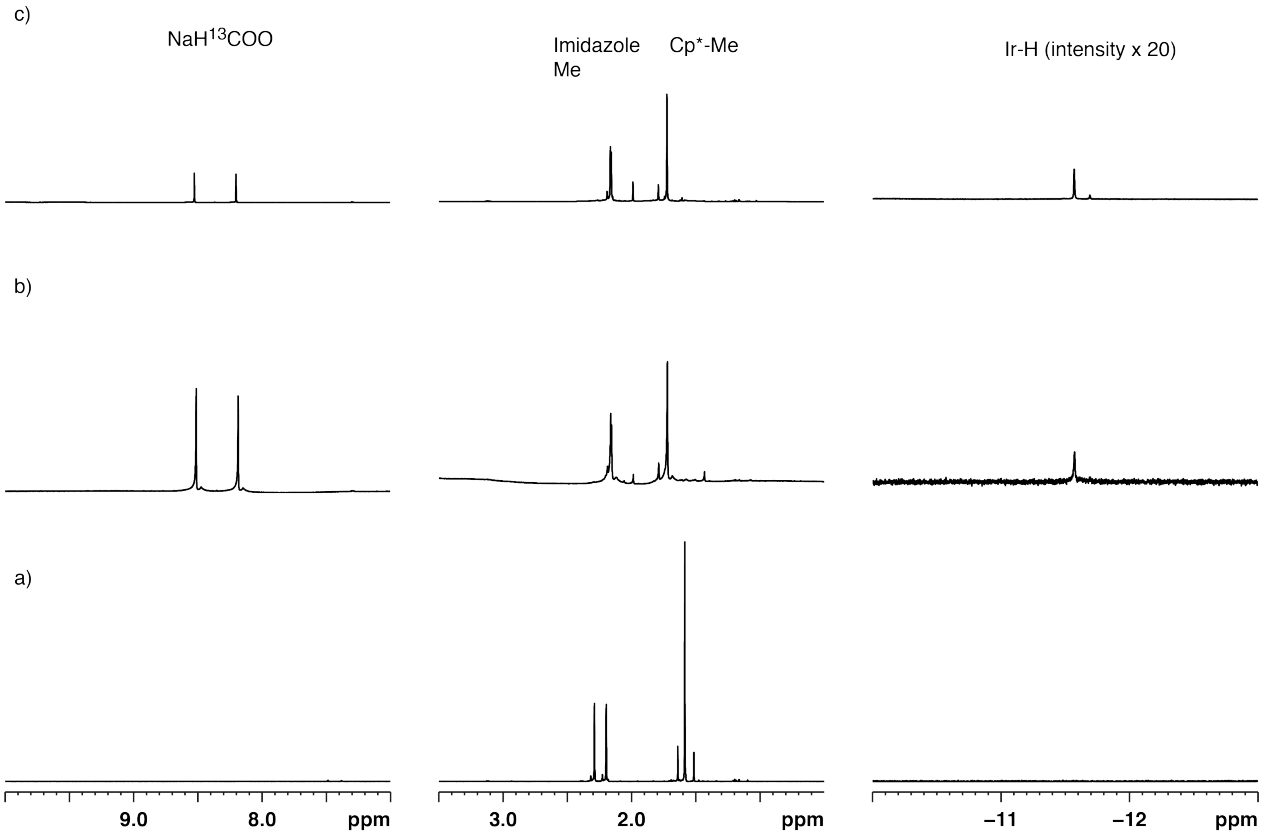


**Figure A.3:** NMR reaction of $[Cp^*Ir(imim)(H_2O)]^+$ (**11**) with $^{13}C$-labelled sodium formate at 298 K in $H_2O$: a) before formate addition, b) after 75 min reaction time, c) after 1.5 days reaction time

## A.4 TON determination

| Entry | Catalyst | Metal | Ligand | $TON_{30}$[a] | $TON_{180}$[a] | $TON_{30}$[b] | $TON_{180}$[b] |
|---|---|---|---|---|---|---|---|
| 1 | **1** | **Ir** | **$H_2O$** | 1 | 2 | 1 | 4 |
| 2 | **2** | **Ir** | **bpy** | 0 | 2 | 1 | 3 |
| 3 | **3** | **Ir** | **bpy(OH)$_2$** | 11 | 39 | 42 | 174 |
| 4[c] | **4** | **Ir** | **phenpy** | 2 | 8 | 5 | 25 |
| 5[c] | **5** | **Ir** | **phenpyOH** | 5 | 13 | 16 | 25 |
| 6[c] | **6** | **Ir** | **phenpy$CO_2H$** | 13 | 47 | 36 | 159 |
| 7 | **7** | **Ir** | **phenpz** | 18 | 47 | 64 | 181 |
| 8 | **8** | **Ir** | **phenpz$CO_2H$** | 34 | 50 | 147 | 250 |
| 9 | **9** | **Ir** | **tosen** | 32 | 38 | 57 | 78 |
| 10 | **10** | **Ir** | **phenima** | 12 | 27 | 25 | 70 |
| 11 | **11** | **Ir** | **imim** | 29 | 50 | 91 | 250 |
| 12 | **12** | **Rh** | **phenpz$CO_2H$** | 1 | 2 | 1 | 4 |
| 13[d] | – | – | – | 0 | 0 | 0 | 0 |

All experiments were conducted in 2.0 ml acetic acid/sodium acetate buffer (2.5 M, pH 4) containing the amount of tested substrate. That solution has been degassed for 10 minutes prior to the addition of catalyst by sparging with nitrogen gas. The temperature was set to 37 °C. After equilibration of the system 0.002 mmol catalyst dissolved in 0.2 ml of degassed water was added and the measurement was started.

[a] 0.1 mmol substrate, [b] 0.5 mmol substrate, [c] added 20% MeOH to the catalyst containing solution for better solubility, [d] 0.2 ml degased water without catalyst were added

# B

# Supplemental Information Chapter 4

## B.1 Materials and Instruments

Recombinant cysteine-containing streptavidin isoforms were engineered, expressed, purified and quantified as previously described.[270] Other reagents, substrates and materials were purchased from Sigma-Aldrich, TCI and Acros. $MV^{2+}$ was added as methylviologene dichloride hydrate purchased from Sigma-Aldrich and used as is. UV–Vis experiments were conducted on a Varian 50 Scan UV-Vis spectrophotometer. NMR experiments were performed on a Bruker Avance III NMR spectrometer operating at 400 MHz proton frequency and 101 MHz carbon frequency. Chemical shifts were referenced to residual $d_6$-DMSO (2.50 ppm) for $^{1}$H spectra or $d_6$-DMSO (39.52 ppm) for $^{13}$C spectra. Signals are quoted as s (singlet), d (doublet), t (triplet) and m (multiplet). Flash column purification was performed on a Biotage Isolera One. Mass spectra were acquired on Bruker esquire 3000 plus and Bruker maxis 4G QTOF EDI spectrometers. An LP920-KS instrument from Edinburgh Instruments was used for transient absorption spectroscopy. The frequency doubled output of a Quantel Brilliant b laser served as an excitation source. The laser pulse duration was 10 ns and the pulse frequency was 10 Hz. The typical pulse energy used for transient absorption studies was 15 mJ. Detection of transient absorption spectra occurred on an iCCD camera from Andor. All optical spectroscopic experiments were performed under aerated conditions in MilliQ water.

## B.2 Synthesis

The compounds TAA-$NO_2$,[370] TAA-$NH_2$,[371] $[Ru(bpy)_2(phenNH_2)](PF_6)_2$[372] and Biotin pentafluorophenyl ester[373] were synthesized as previously reported.

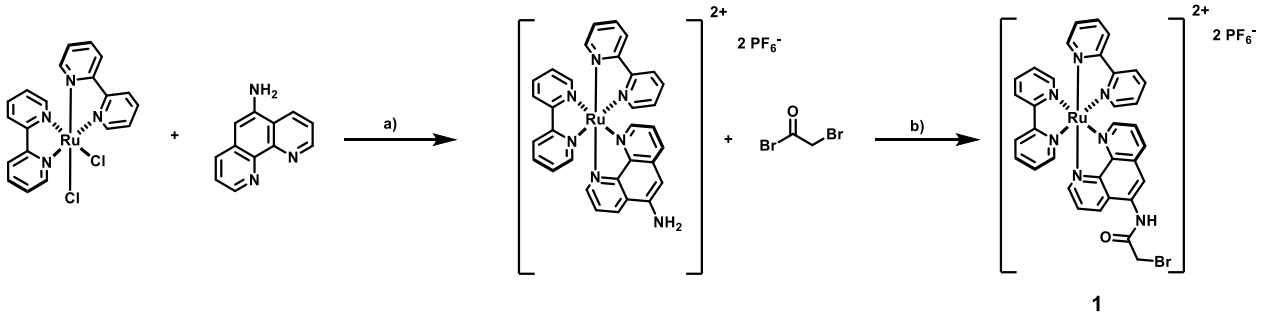


**Figure B.1:** Synthesis of $[Ru(bpy)_2(phenNHCOCH_2Br)](PF_6)_2$ **1**: a) $phenNH_2$, $[Ru(bpy)_2Cl_2]$, MeOH, reflux, overnight b) $[Ru(bpy)_2(phenNH_2)](PF_6)_2$, $BrCH_2COBr$, $CH_3CN$, r.t., overnight.

### B.2.1 Synthesis if $[Ru(bpy)_2(phenNHCOCH_2Br)](PF_6)_2$

Adapted from Fedorova *et al.*[374] Under $N_2$, $[Ru(bpy)_2(phenNH_2)](PF_6)_2$ (30.0 mg, 0.033 mmol) was dissolved in dry acetonitrile (2.0 ml). Bromoacetyl bromide (13.0 µl, 0.15 mmol) was added and the reaction mixture was stirred overnight at room temperature in the dark. The solvent was removed *in vacuo* and the residue was dissolved in a minimal amount of MeOH. A saturated aqueous solution of $NH_4PF_6$ was added and the precipitate was collected, washed with water followed by $Et_2O$ to yield the product as a red solid (0.027 mmol, 27.6 mg, 82%).

**$^1$H (400MHz, $d_6$-DMSO):** 10.87 (s, 1H), 8.93-8.76 (m, 6H), 8.64 (s, 1H), 8.21 (tt, *J* = 7.9, 1.5 Hz, 2H), 8.17 (dd, *J* = 5.3, 1.1 Hz, 1H), 8.11 (tdd, *J* = 7.8, 2.7, 1.5 Hz, 2H), 8.05 (dd, *J* = 5.2, 1.2 Hz, 1H), 7.94 (dd, *J* = 8.6, 5.2 Hz, 1H), 7.87-7.79 (m, 3H), 7.62-7.54 (m, 4H), 7.35 (ddt, *J* = 7.4, 5.8, 1.5 Hz, 2H), 4.34 (d, *J* = 1.3 Hz, 2H). **$^{13}$C (101 MHZ, $d_6$-DMSO):** 166.5, 156.8, 156.55, 156.52, 152.48, 151.5, 151.46, 147.24, 144.81, 137.97, 137.85, 136.47, 133.1, 132.28, 130.1, 127.84, 127.81, 127.74, 126.59, 126.3, 125.9, 124.47, 124.38, 29.89. **HRMS** ($ESI^+$) calcd. for $C_{34}H_{26}BrN_7ORu^{2+}$ 364.5207; found, 364.5213.

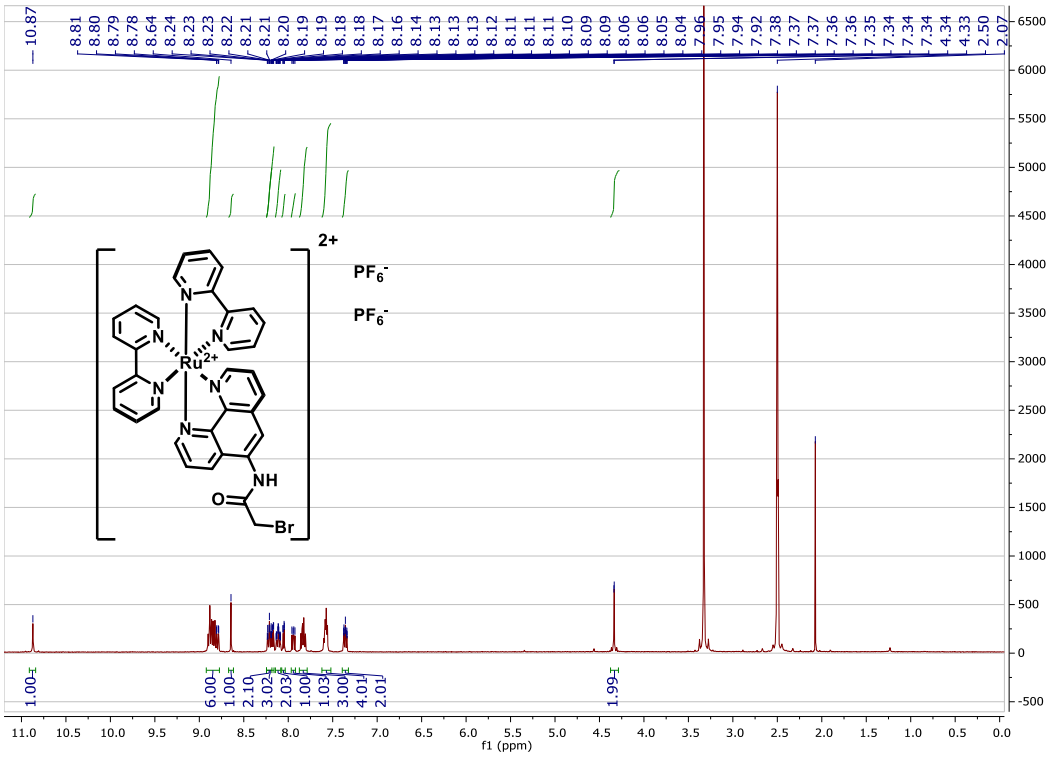


**Figure B.2:** [1]H-NMR spectrum of **1** in $d_6$-DMSO.

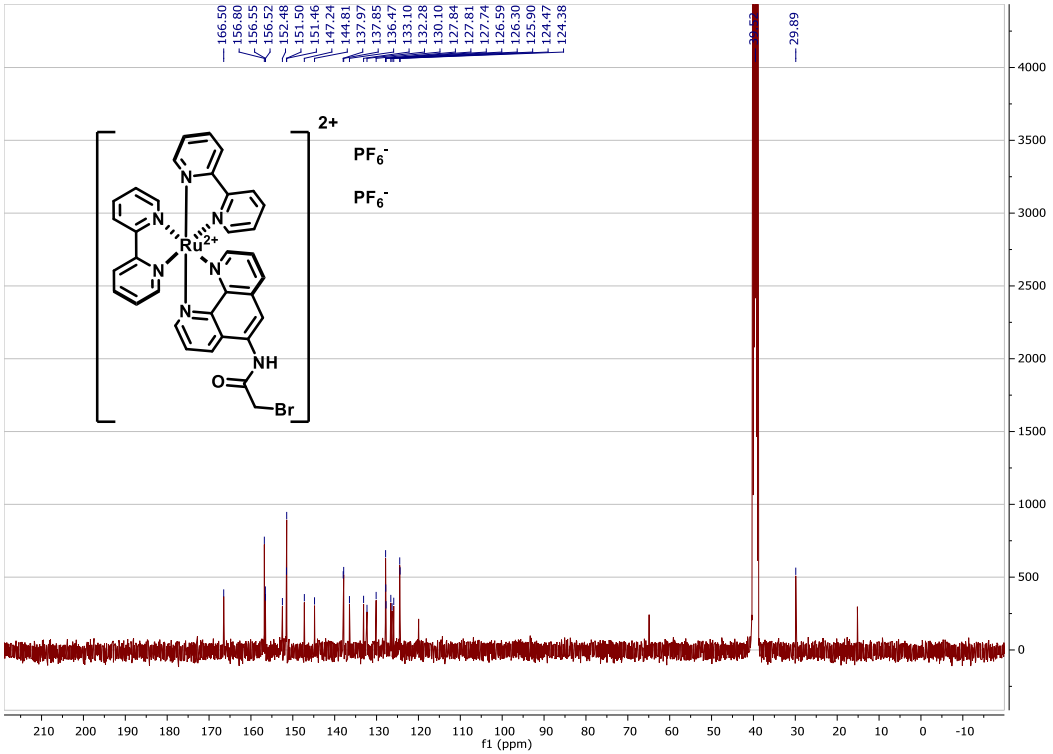


**Figure B.3:** [13]C-NMR spectrum of **1** in $d_6$-DMSO.

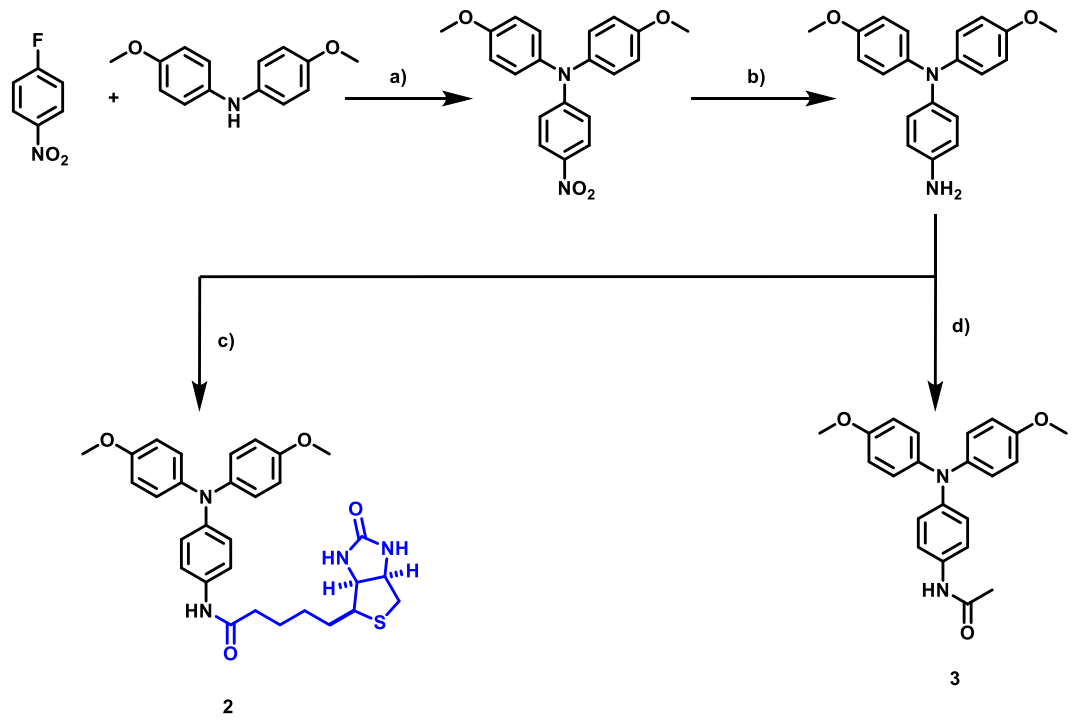


**Figure B.4:** Synthesis of **Biot-TAA 2** and **TAA-Ac 3**: a) *p*-fluoronitrobenzene, 4,4'-dimethoxydiphenylamine, NaH, DMAc, 100°C, 3 h b) $H_4N_2$, Pd/C, EtOH, 75°C, overnight. c) Biotin-PFP, TAA-$NH_2$, DMF, r.t., overnight d) AcOCl, $Et_3N$, TAA-$NH_2$, DCM, r.t., overnight.

### B.2.2 Synthesis of Biot-TAA

Biotin pentafluorophenyl ester (37.4 mg, 0.09 mmol) was dissolved in dry DMF (1.0 ml) under $N_2$. TAA-$NH_2$ (29.2 mg, 0.09 mmol), dissolved in dry DMF (1.0 ml), was added dropwise at 0°C. After addition, the reaction mixture was stirred overnight at room temperature. Dry DCM (3.0 ml) was added and the organic phase was washed with degassed $H_2O$ (3 x 10.0 ml). The combined organic phases were dried over $Na_2SO_4$ and the solvents were removed under reduced pressure. To remove residual DMF, the compound was dissolved in a minimal amount of dry DCM and precipitated with cold $Et_2O$ to yield the product as an off-white solid (0.06 mmol, 33.5 mg, 68%).

**$^1$H (400 MHz, $d_6$-DMSO):** 9.79 (s, 1H), 7.40 (d, $J$ = 9.0 Hz, 2H), 6.94-6.84 (m, 8H), 6.79 (d, $J$ = 8.9 Hz, 2H), 6.44 (s, 1H), 6.36 (s, 1H), 4.30 (ddt, $J$ = 7.6, 5.1, 1.1 Hz, 1H), 4.13 (ddd, $J$ = 7.8, 4.4, 1.8 Hz, 1H), 3.72 (s, 6H), 3.12 (ddd, $J$ = 8.5, 6.1, 4.4 Hz, 1H), 2.82 (dd, $J$ = 12.4, 5.1 Hz, 1H), 2.58 (d, $J$ = 12.5 Hz, 1H), 2.26 (t, $J$ = 7.3 Hz, 2H), 1.71-1.27 (m, 6H). **$^{13}$C (101 MHZ, $d_6$-DMSO):** 170.66, 162.68, 154.99, 143.54, 140.84, 133.24, 125.27, 121.85, 120.31, 114.79, 61.03, 59.18, 55.40, 55.21, 39,85, 36.10, 28.23, 28.09, 25.22. **HRMS** ($ESI^+$) calcd. for $C_{30}H_{34}N_4O_4S^+$ 546.2301; found, 546.2296.

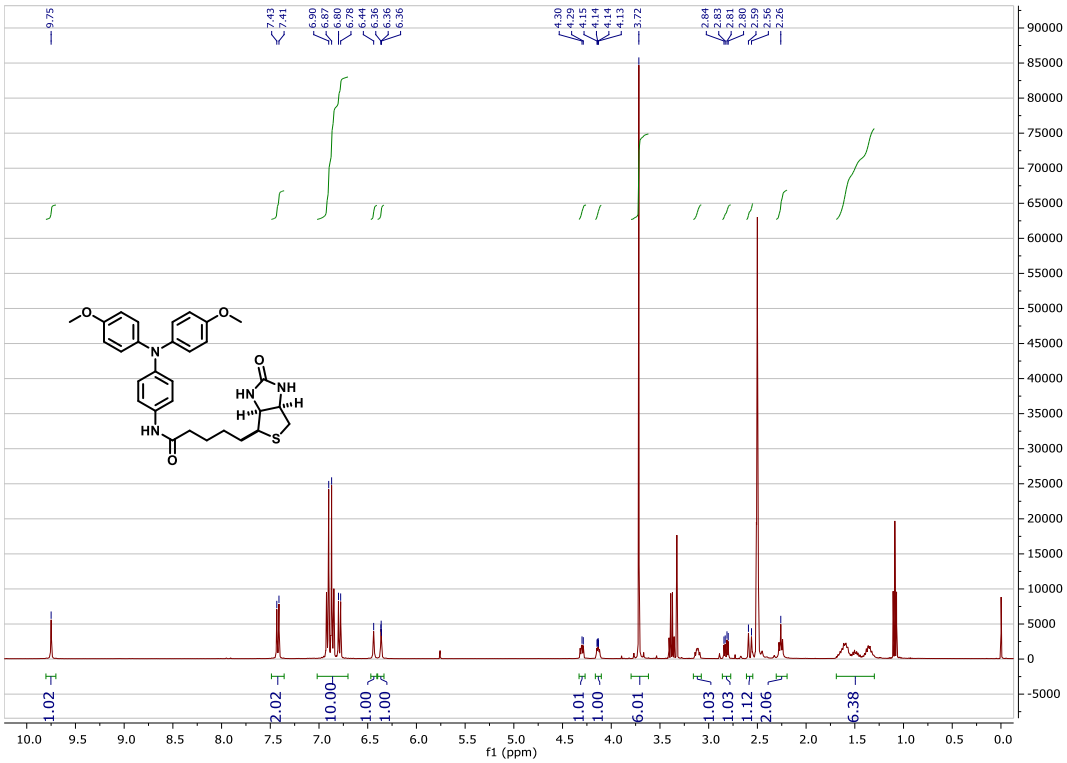


**Figure B.5:** $^{1}$H-NMR spectrum of **2** in $d_6$-DMSO.

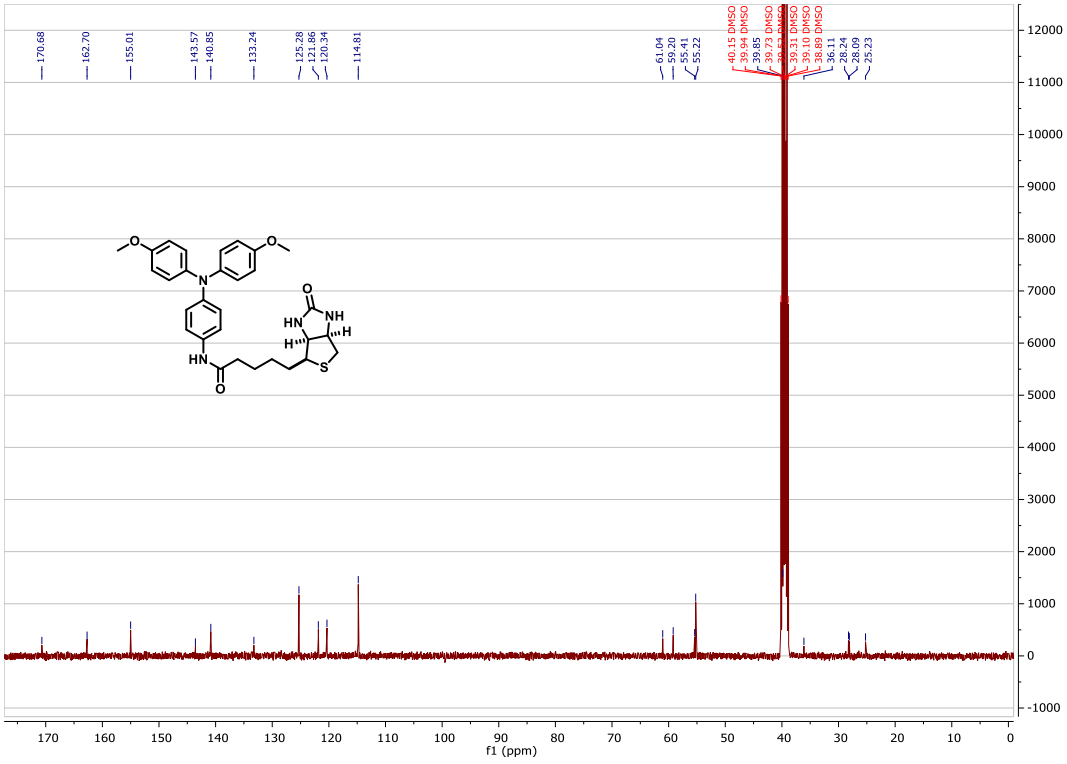


**Figure B.6:** $^{13}$C-NMR spectrum of **2** in $d_6$-DMSO.

### B.2.3 Synthesis of TAA-Ac

A solution containing of TAA-$NH_2$ (89.0 mg, 0.28 mmol) and $Et_3N$ (39 µl, 0.53 mmol) in dry DCM (4.0 ml) was added dropwise to a cooled solution of acetylchloride (20.0 µl, 0.28 mmol) in dry DCM (1.0 ml) at 0°C under an inert atmosphere. After addition, the reaction mixture and stirred overnight at room temperature. Dry diethyl ether (10.0 ml) was added and the reaction mixture was washed with $NH_4Cl$ sat. (2 x 10.0 ml) and brine (10.0 ml), dried over $Na_2SO_4$ and concentrated under reduced pressure. Further purification of the crude mixture by automated column chromatography (cyclohexane / EtOAc, 0%→50%) afforded the product as an off-white solid (0.14 mmol, 51 mg, 50%).

**$^1$H (400 MHz, $d_6$-DMSO):** 9.75 (s, 1H), 7.42 (d, $J$ = 8.9 Hz, 2H), 6.94-6.84 (m, 8H), 6.79 (d, $J$ = 8.9 Hz, 2H), 3.72 (s, 6H), 1.99 (s, 3H). **$^{13}$C (101 MHz, $d_6$-DMSO):** 167.72, 155.01, 143.56, 140.82, 133.23, 125.29, 121.75, 120.25, 114.79, 55.20, 23.80. **HRMS** (ESI$^+$) calcd. for $C_{22}H_{22}N_2O_3^+$ 362.1630; found, 362.1624.

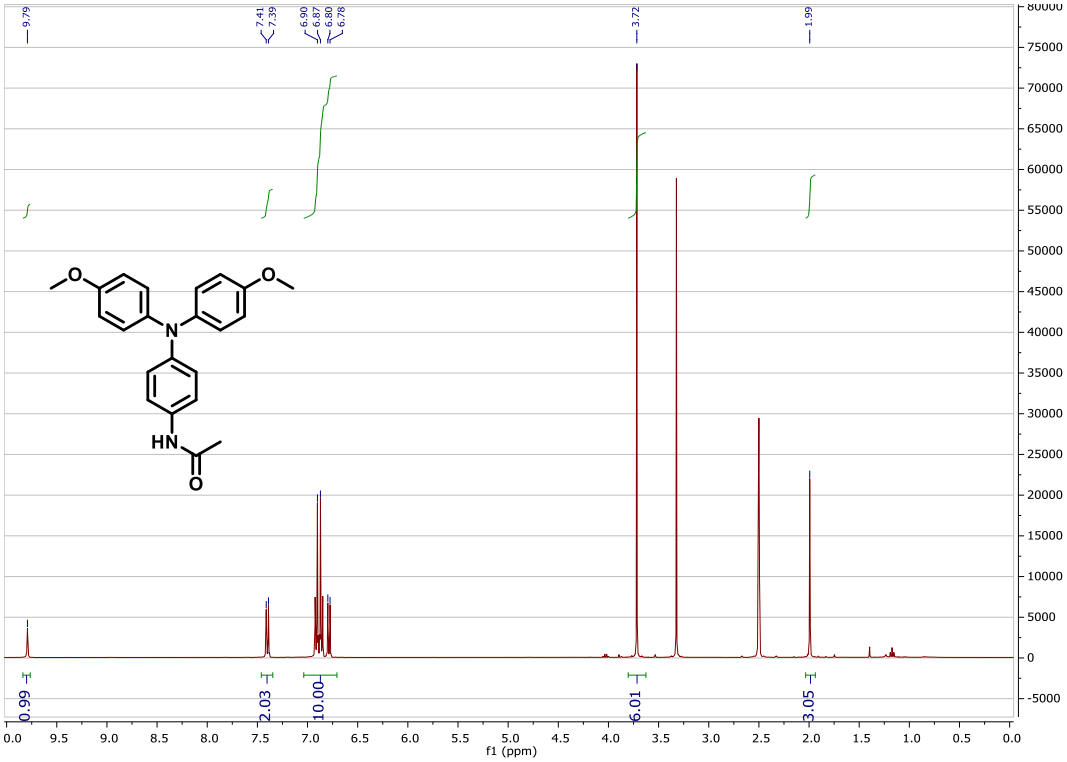


**Figure B.7:** $^1$H-NMR spectrum of **3** in $d_6$-DMSO.

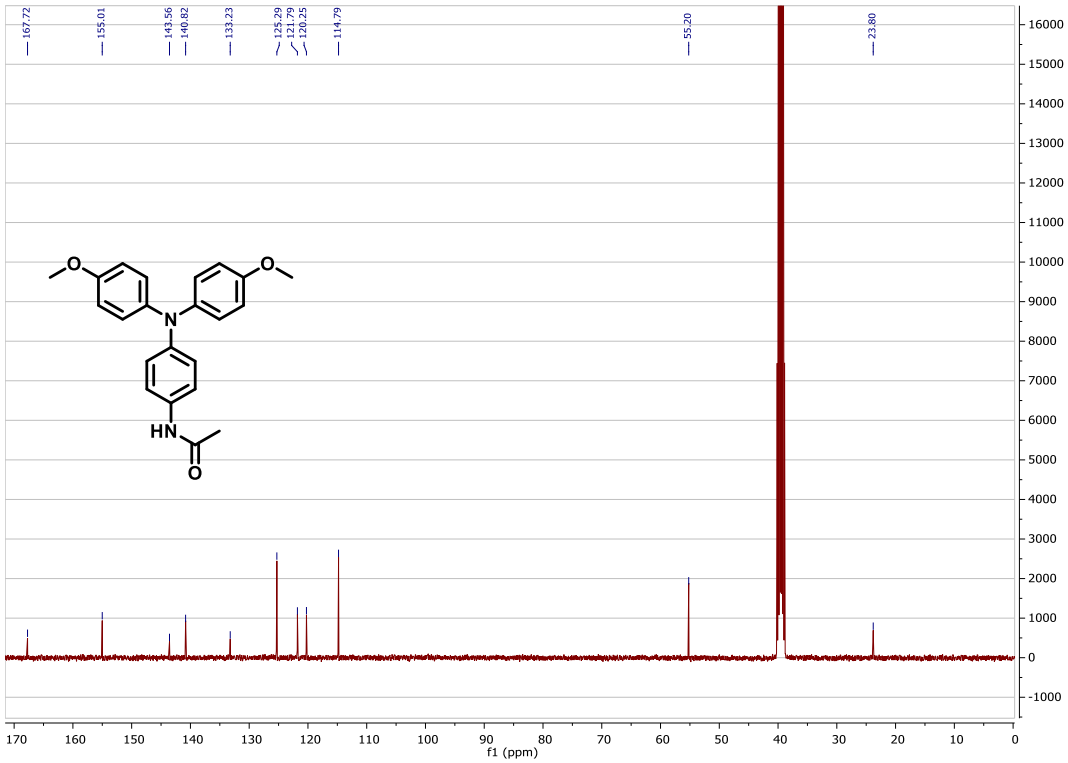


**Figure B.8:** $^{13}$C-NMR spectrum of **3** in $d_6$-DMSO.

## B.3 Manipulation of the streptavidin mutants

### B.3.1 Bioconjugation of $[Ru(bpy)_2(phenNHCOCH_2Br)](PF_6)_2$ to the cysteine-containing streptavidin mutants

According to a modified protocol of Roelfes *et al.*[269]

The Sav mutants (1.2 µmol) were dissolved in $NaH_2PO_4$ buffer (6.0 ml, 50 mM, pH 7.6) and $[Ru(bpy)_2(phenNHCOCH_2Br)](PF_6)_2$ **1** (9.6 µmol, 9.8 mg) in 50 µl DMSO were added. The mixture was agitated in the dark at 4°C, 600 rpm for 24 h. The solution was then centrifuged and transferred to a Spectra/Por® 1 Dialysis Membrane Standard RC Tubing (MWCO: 6-8 kD) and dialyzed against MilliQ water in the dark for 5 days at 4°C, changing the water twice a day. After 5 days, the dialyzed water was colourless. The solution was filtered through a Filtropur S 0.2 µm and lyophilized for 2 days to yield a yellow fluorescent protein sample.

## B.3.2 Mass Spectrometry of the Ru-Sav adducts

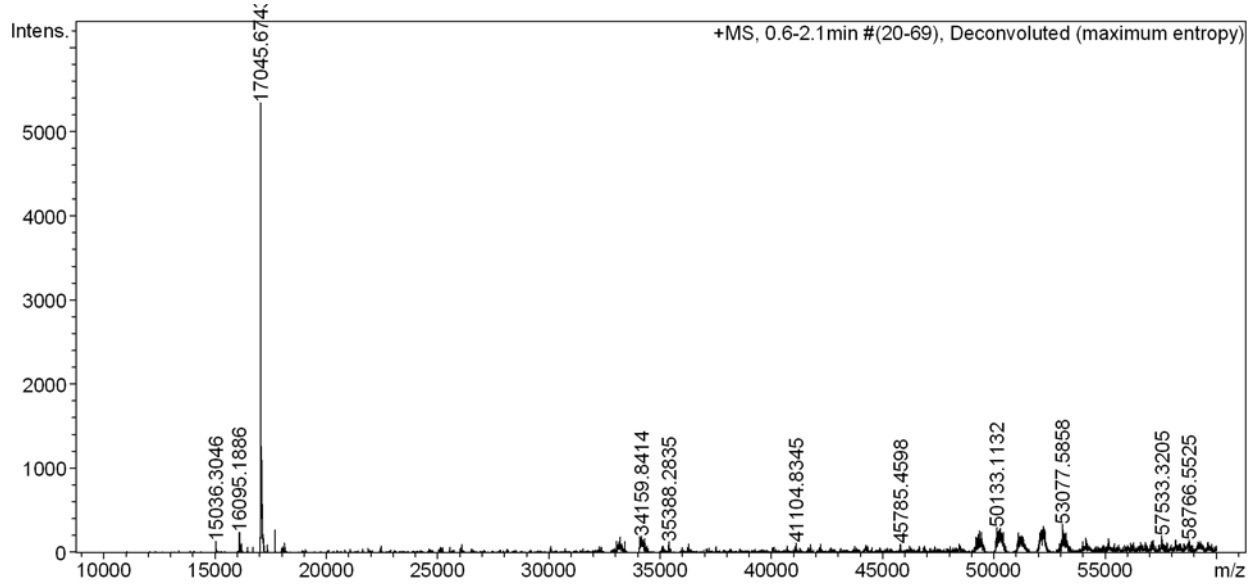


**Figure B.9:** Mass spectrum of K121C-Ru modified Sav mutant. K121C unmodified mass: 16400 Da, expected for bioconjugated with Ru complex 17049 Da , found 17046 Da.

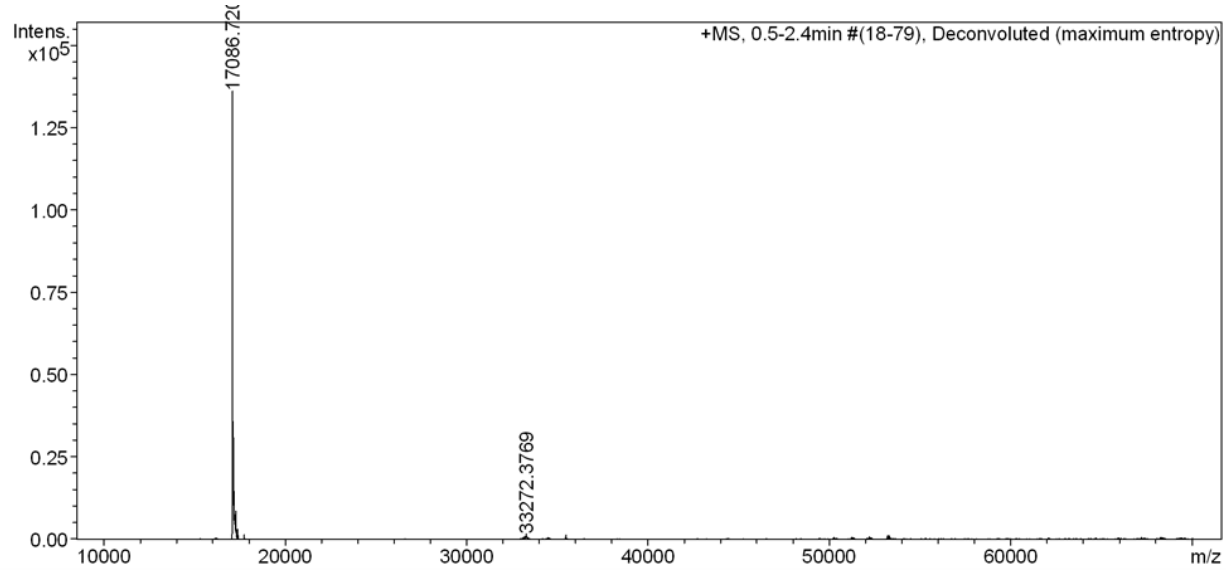


**Figure B.10:** Mass spectrum of S112C-Ru modified Sav mutant. S112C unmodified mass: 16441 Da, expected for bioconjugated with Ru complex 17090 Da , found 17087 Da.

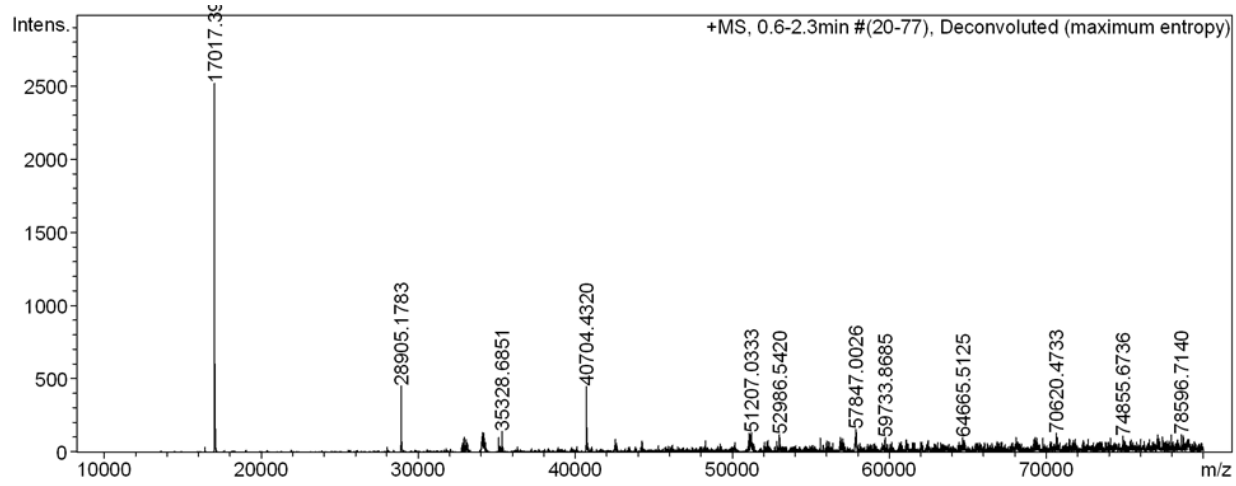


**Figure B.11:** Mass spectrum of R84C-Ru modified Sav mutant. R84C unmodified mass: 16372 Da, expected for bioconjugated with Ru complex 17021 Da , found 17017 Da.

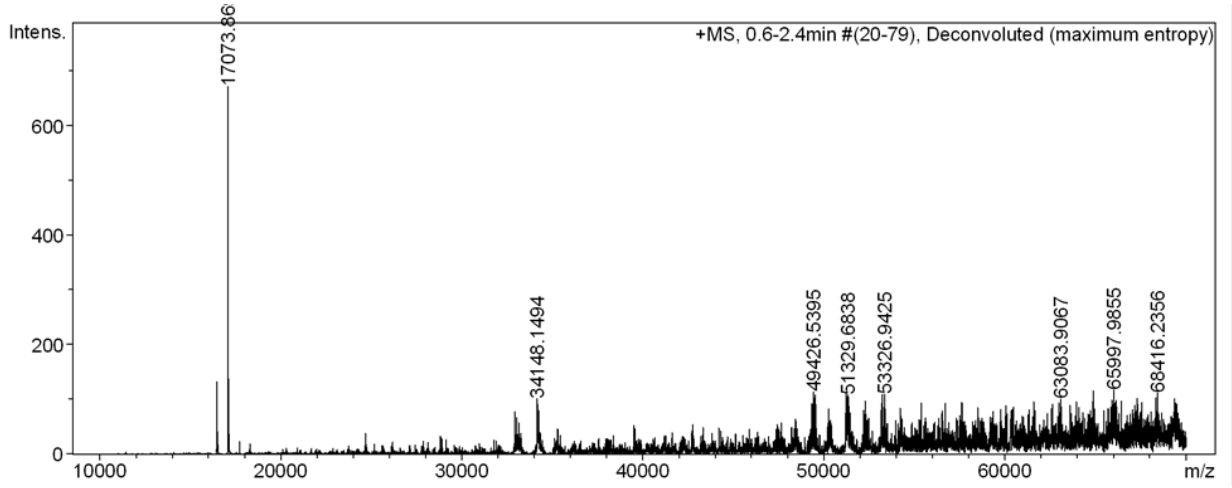


**Figure B.12:** Mass spectrum of T66C-Ru modified Sav mutant. T66C unmodified mass: 16427 Da, expected for bioconjugated with Ru complex 17076 Da , found 17074 Da.

## B.4 Photoexcitation experiments

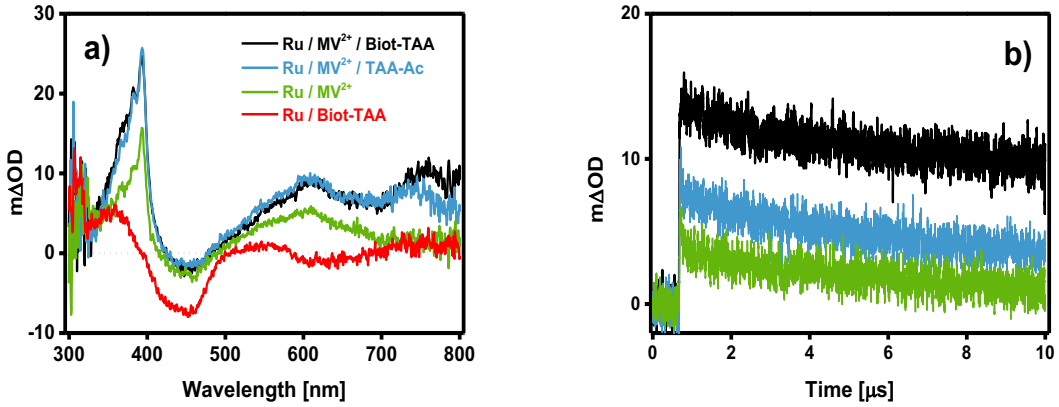


**Figure B.13:** (a) Transient absorption spectra of S112C-Ru measured after excitation at 532 nm with laser pulses of ~10 ns duration. The spectra were time-integrated over 200 ns immediately after excitation. Sample concentrations were: $5 \cdot 10^{-5}$ M Ru(II)-streptavidin, 120 mM $MV^{2+}$, $2.5 \cdot 10^{-5}$ M **Biot-TAA** or **TAA-Ac**, where applicable. The solvent was MilliQ water at 25 °C. (b) Temporal evolution of the transient absorption signal at 760 nm for 3 of the 4 samples from (a).

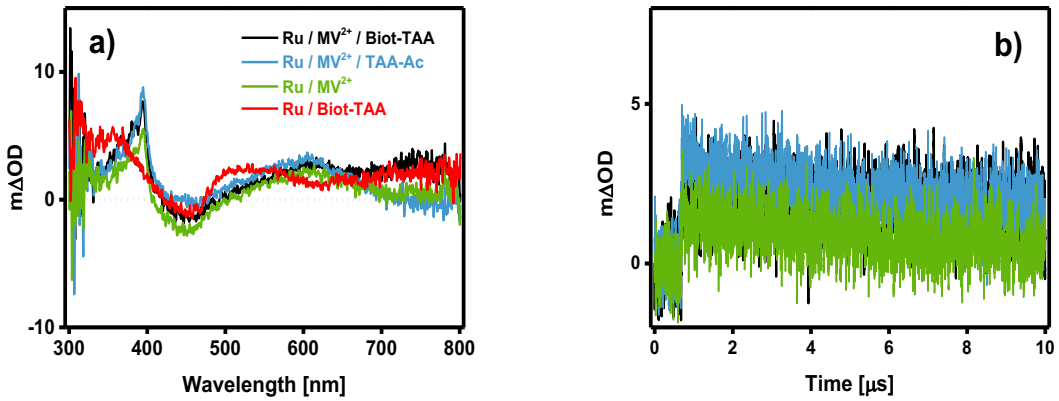


**Figure B.14:** (a) Transient absorption spectra of R84C-Ru measured after excitation at 532 nm with laser pulses of ~10 ns duration. The spectra were time-integrated over 200 ns immediately after excitation. Sample concentrations were: $5 \cdot 10^{-5}$ M Ru(II)-streptavidin, 120 mM $MV^{2+}$, $2.5 \cdot 10^{-5}$ M **Biot-TAA** or **TAA-Ac**, where applicable. The solvent was MilliQ water at 25 °C. (b) Temporal evolution of the transient absorption signal at 760 nm for 3 of the 4 samples from (a).

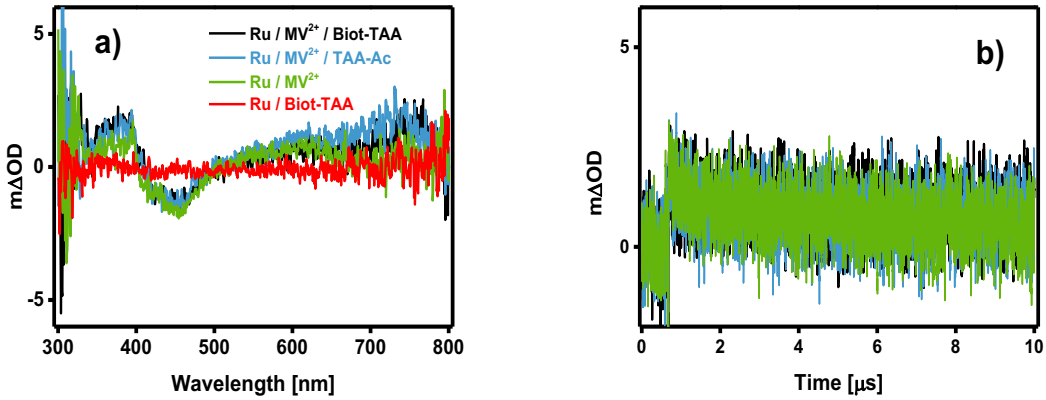


**Figure B.15:** (a) Transient absorption spectra of T66C-Ru measured after excitation at 532 nm with laser pulses of ~10 ns duration. The spectra were time-integrated over 200 ns immediately after excitation. Sample concentrations were: $5 \cdot 10^{-5}$ M Ru(II)-streptavidin, 120 mM $MV^{2+}$, $2.5 \cdot 10^{-5}$ M **Biot-TAA** or **TAA-Ac**, where applicable. The solvent was MilliQ water at 25 °C. (b) Temporal evolution of the transient absorption signal at 760 nm for 3 of the 4 samples from (a).

## B.5 Distance estimations

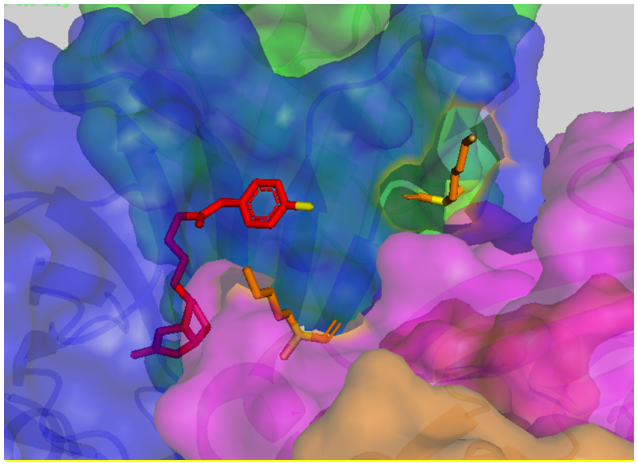

**Figure B.16:** Close-up view of the biotin binding vestibule bearing a single arylated biotin from pdb code: 3PK2. The distances were measured through space from the sulfur atom (yellow) of the cofactor (red) to the α-carbon atoms (yellow) of the amino acids of interest (here K121 displayed in orange). The iridium-Cp*-complex was omitted for clarity.

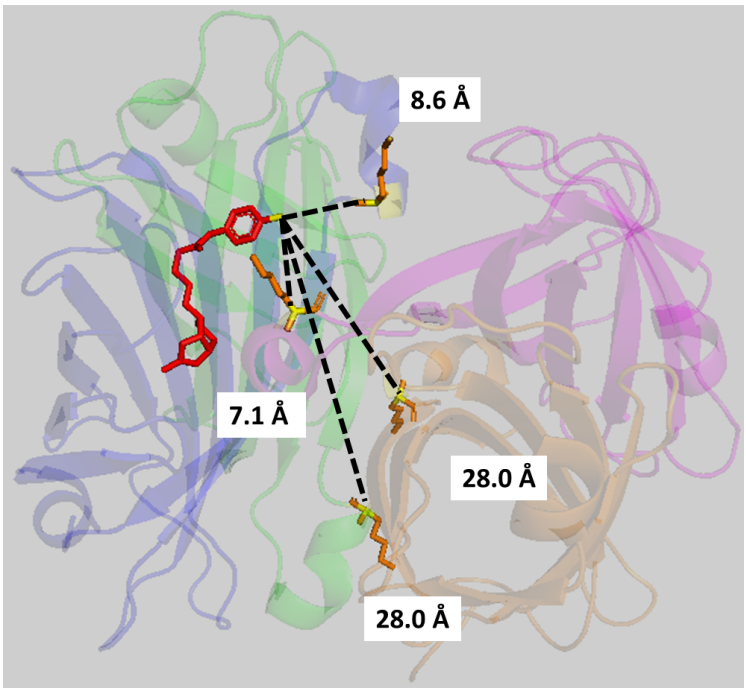


**Figure B.17:** Estimated through-space distances between the sulfur atom of a biotinylated cofactor (pdb code 3PK2) and the α-carbon atoms of the K121 residue of all four monomers of homotetrameric Sav.

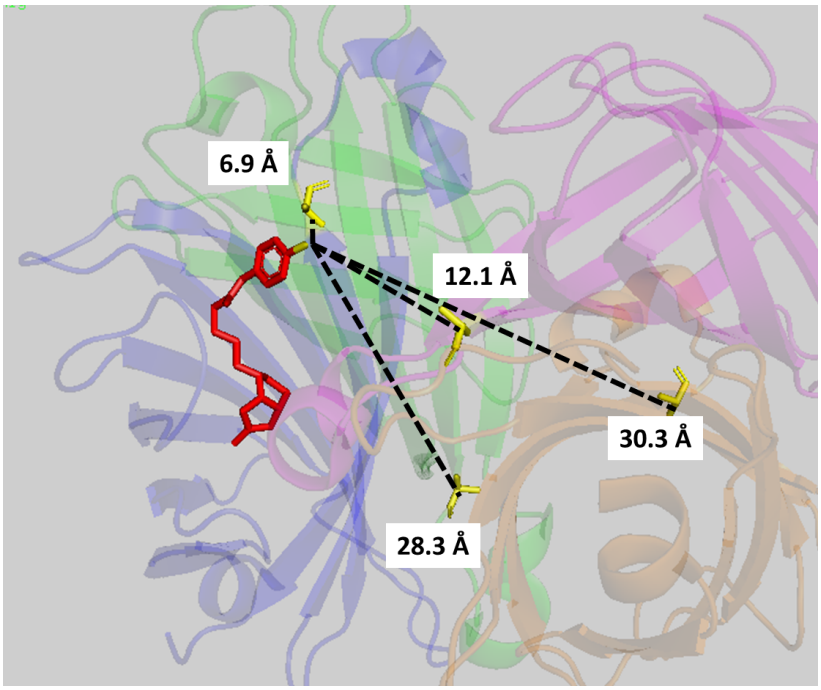


**Figure B.18:** Estimated through-space distances between the sulfur atom of a biotinylated cofactor (pdb code 3PK2) and the α-carbon atoms of the S112A residue of all four monomers of homotetrameric Sav.

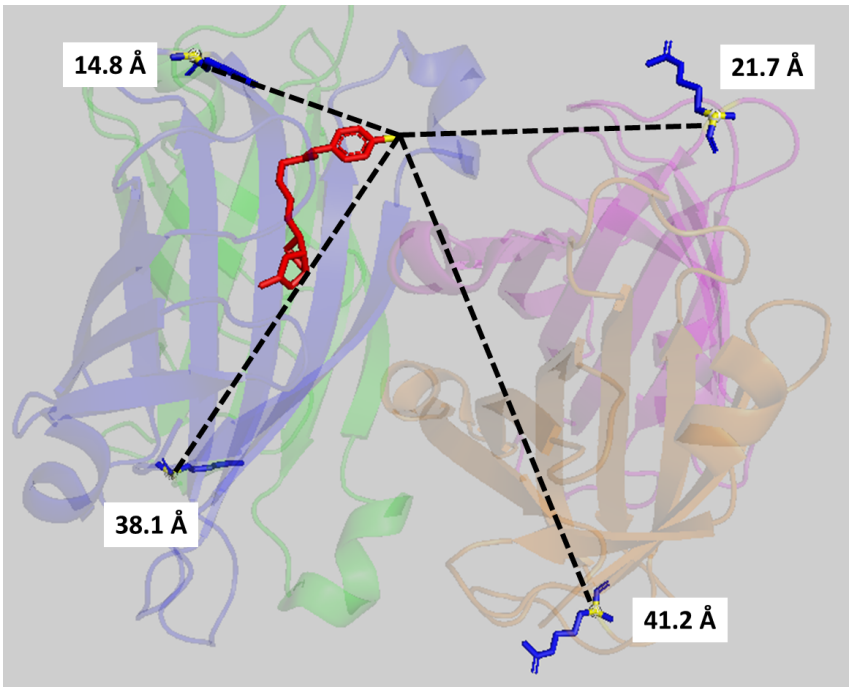


**Figure B.19:** Estimated through-space distances between the sulfur atom of a biotinylated cofactor (pdb code 3PK2) and the α-carbon atoms of the R84 residue of all four monomers of homotetrameric Sav.

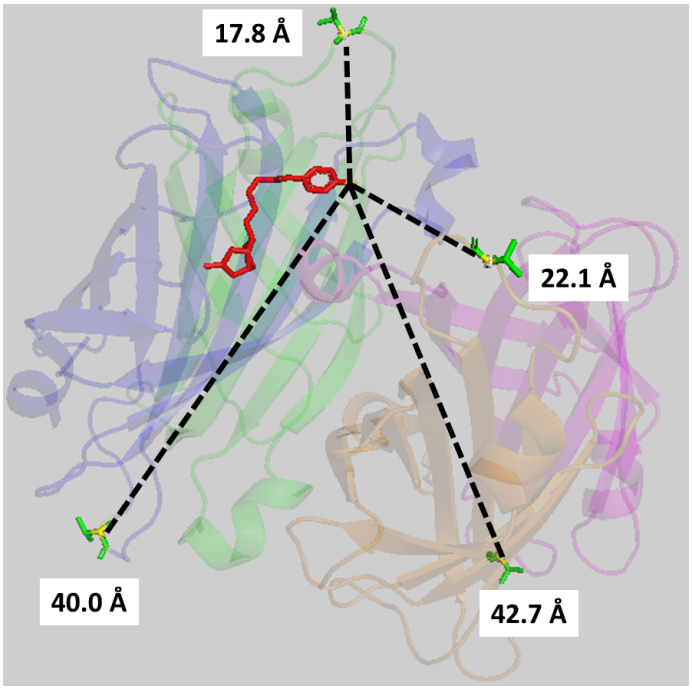


**Figure B.20.** Estimated through-space distances between the sulfur atom of a biotinylated cofactor (pdb code 3PK2) and the α-carbon atoms of the T66 residue of all four monomers of homotetrameric Sav.

## B.6 Biotin-binding site determination[187,242]

The Sav mutants (76.8 nmol) were dissolved in $NaH_2PO_4$ buffer (2.4 ml, 20 mM, pH 7.0). The solutions were treated with a 2-(4-hydroxyphenylazo)benzoic acid (HABA) solution (300 µl, 9.6 mM) in $NaH_2PO_4$ buffer (20 mM, pH 7.0) filled into a cuvette and left standing for 5 minutes. A blank of the buffer was measured at 506 nm in a Varian 50 Scan UV-Vis spectrophotometer. The resulting sample was analyzed and aliquots (5.0 µl) of a biotin (or **Biot-TAA**) solution (0.96 mM) in DMSO were added after each spectroscopic determination. The data points were plotted with Origin Pro 9.0.0 to determine the number of biotin-binding sites and the stoichiometry for the Sav embedded dyads.

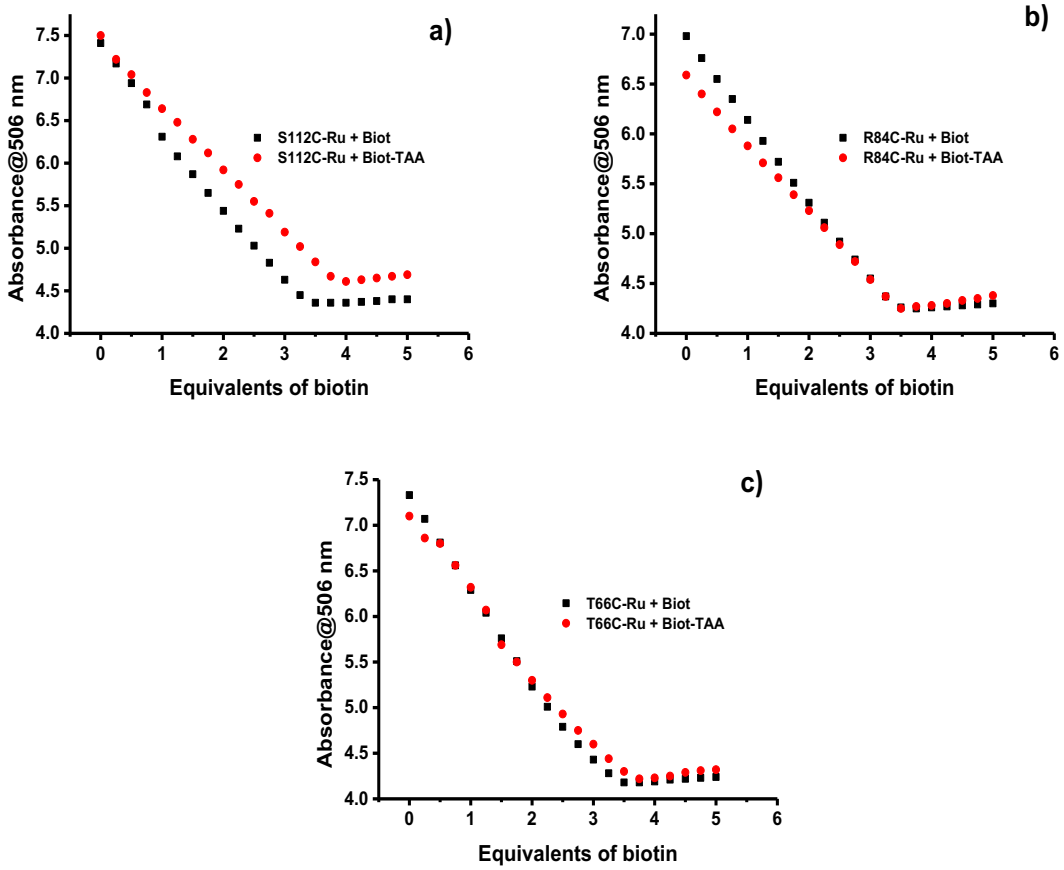


**Figure B.21:** HABA displacement titrations of biotin (black symbols) and the biotinylated triarylamine **Biot-TAA** (red symbols) of a) S112-Ru b) R84C-Ru c) T66C-Ru.

C

# Supplemental Information Chapter 5

## C.1 Materials and Instruments

Recombinant cysteine-containing streptavidin isoforms were engineered, expressed, purified and quantified as previously described.[270,375] Other reagents, substrates and materials were purchased from Sigma, Aldrich, TCI and Acros. $MV^{2+}$ was added as methyl viologen dichloride hydrate purchased from Sigma-Aldrich and used as is. NMR experiments were performed on a Bruker Avance III NMR spectrometer operating at 400 MHz proton frequency and 101 MHz carbon frequency. Chemical shifts were referenced to residual $d_6$-DMSO (2.50ppm) for $^1H$ spectra or $d_6$-DMSO (39.52 ppm) for $^{13}C$ spectra. Signals are quoted as s (singlet), d (doublet), t (triplet) and m (multiplet). Flash column purification was performed on a Biotage Isolera One. Mass spectra were acquired on Bruker Esquire 3000 plus and Bruker maxis 4GQTOF EDI spectrometers. An LP920-KS instrument from Edinburgh Instruments was used for transient absorption spectroscopy. The frequency-doubled output of a Quantel Brilliant b laser served as an excitation source. The laser pulse duration was 10 ns and the pulse frequency was 10 Hz. The typical pulse energy used for transient absorption studies was 10 mJ. The excitation wavelength was 450 nm in all experiments and the number of averages used to record all of the presented spectra was 20. Detection of transient absorption spectra occurred on an iCCD camera from Andor and the spectra were time-integrated over 4 µs. The data is presented as raw data without artificial baseline and emission corrections. The experimental uncertainty of the lifetime measurements is +/- 10%. All optical spectroscopic experiments were performed under deaerated conditions in milliQ water. $ESI^+$-MS spectra of proteins were recorded with a Waters SQ

Detector 2 on a Waters Acquity M-class UPLC (Acetonitrile / $H_2O$, both with 0.1 % formic acid) with a Aeris Widefore column from phenomenex (3.6 µm, C4, 50 x 2.1 mm) and deconvoluted with the software MassLynx.

## C.2 Synthesis

The compounds **Biot-TAA,**[322] **TAA-$NH_2$,**[376] **Ru(bpy)$_2$(phenNH$_2$COCH$_2$Br)](PF$_6$)$_2$**[377] and **MeMV$^+$I**[378] were synthesized as previously reported, Scheme S1

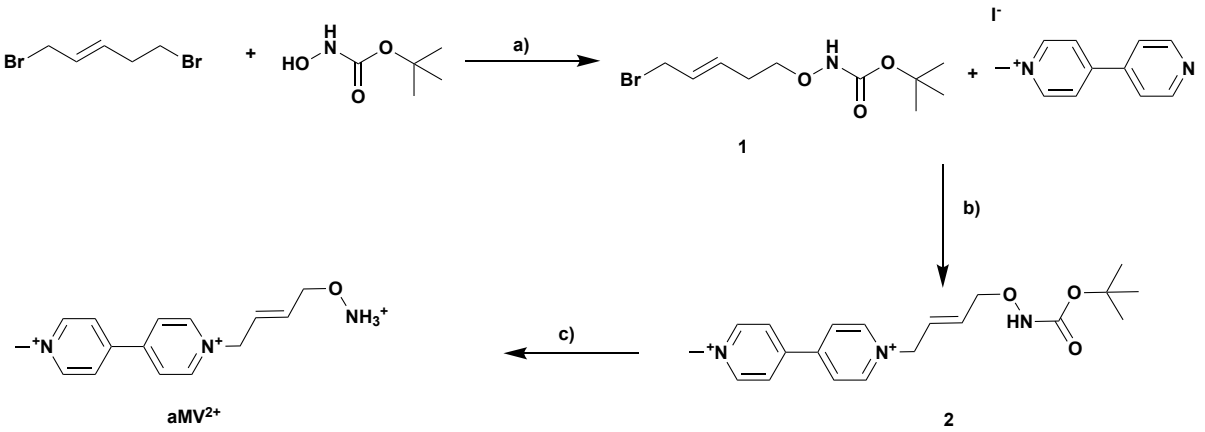


**Scheme C.1:** Synthesis of **aMV$^{2+}$**: a) DBU, DCM, r.t., overnight, b) $CH_3CN$, 75°C, overnight c) **2**, MeOH, 4 M HCl in Dioxane, r.t., 1 h.

### C.2.1 Synthesis of BrCH$_2$CHCHCH$_2$ONHBoc

To a solution of *trans*-1,4-dibromobut-2-ene (4.28 g, 20.0 mmol) and *N*-Boc-hydroxylamine (900 mg, 6.76 mmol) in dry DCM (10.0 ml) 1,8-Diazabicyclo[5.4.0]undec-7-en (DBU) (1.6 ml, 10.3 mmol) was added at 0°C. It was left stirring in the dark overnight at room temperature. The solvent was then removed *in vacuo* and the crude reaction mixture was purified via automated flash column chromatography (10% EtOAc/Cyclohexane, $R_f$ = 0.35). The product was obtained as a colourless oil (453 mg, 25%).

**$^1$H (400 MHz, CDCl$_3$):** 7.11 (s, 1H), 6.04-5.86 (m, 2H), 4.36 (dd, J = 6.0, 0.9 Hz, 2H), 3.95 (dd, J = 7.1, 0.7 Hz, 2H), 1.48 (s, 9H). **$^{13}$C (101 MHz, CDCl$_3$):** 156.92, 131.57, 129.35, 82.08, 75.94, 31.54, 28.35, **HRMS** (ESI+) calcd. for [M+Na$^+$] $C_9H_{16}BrNNaO_3$ 288.0206; found 288.0206.

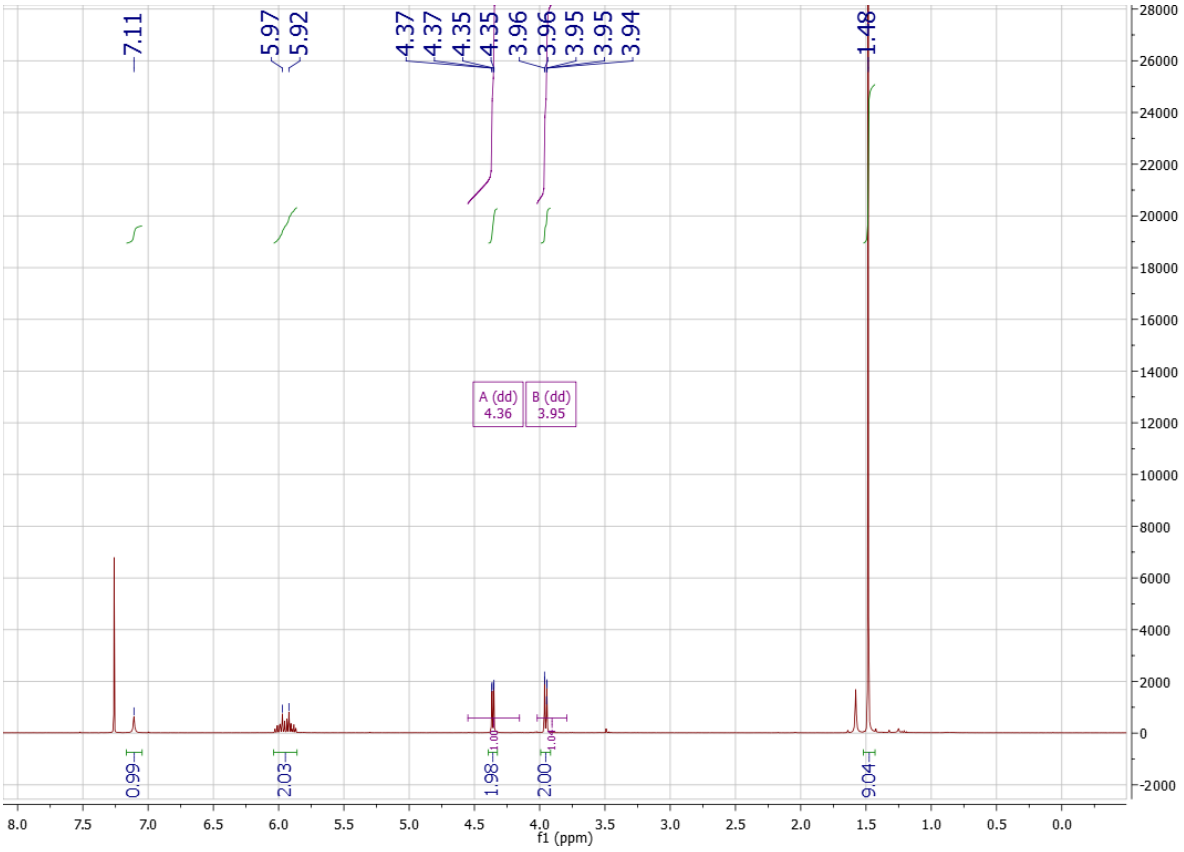


**Figure C.1:** $^{1}$H-NMR spectrum of **1** in $CDCl_3$.

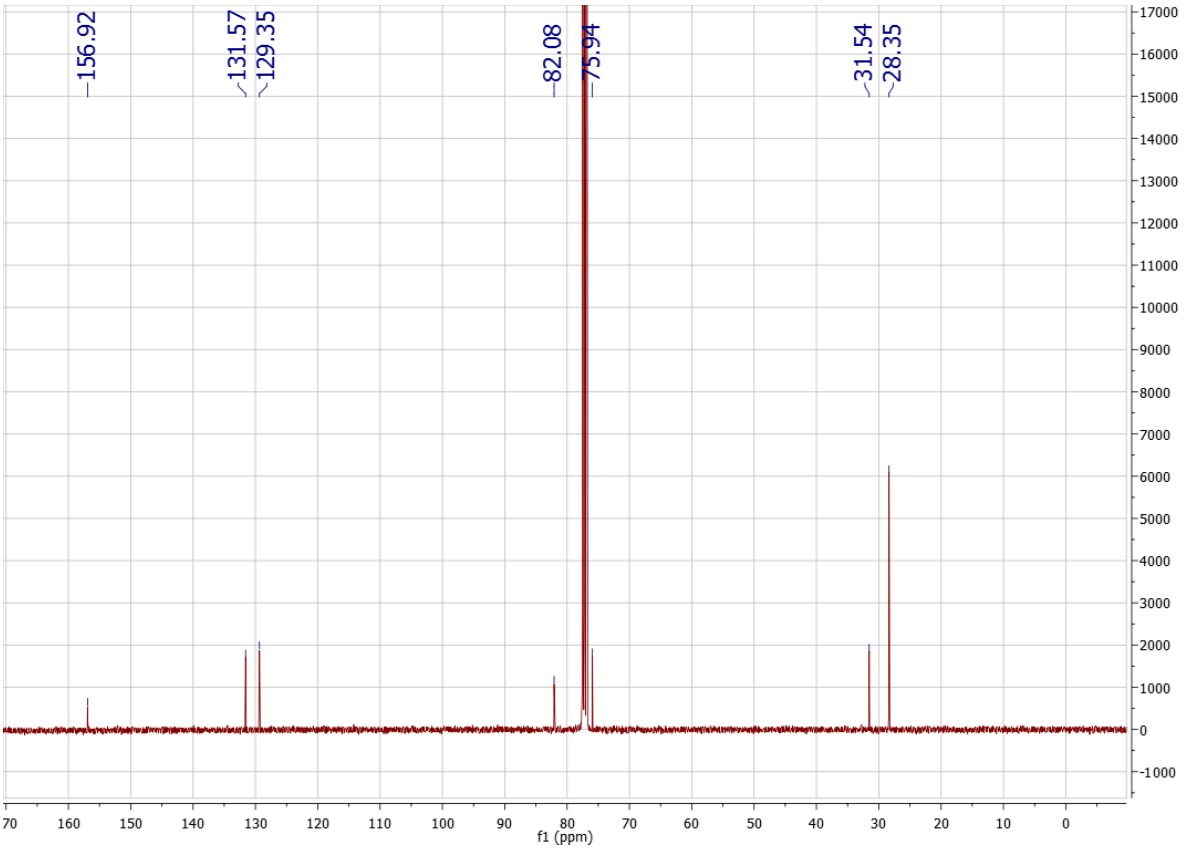


**Figure C.2:** $^{13}$C-NMR spectrum of **1** in $CDCl_3$.

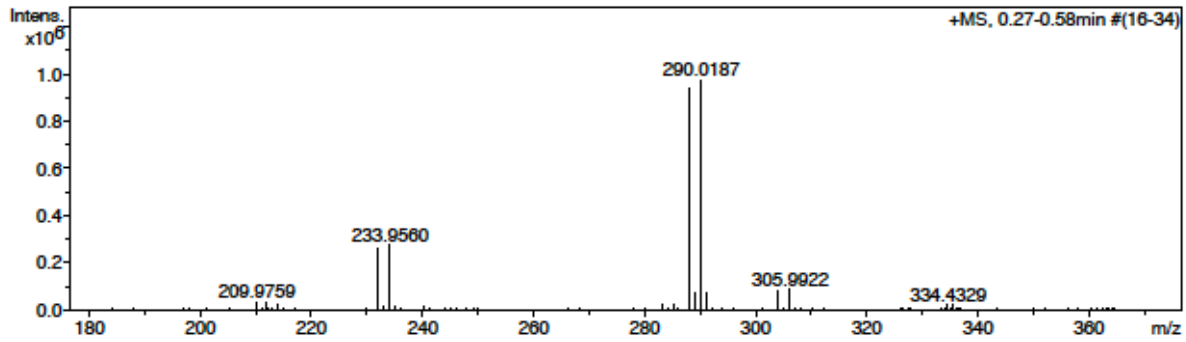


**Figure C.3: HRMS** (ESI+) spectrum of **1**; calcd. for [M+Na$^+$] $C_9H_{16}BrNNaO_3$ 288.0206; found 288.0206, calcd. for [M+K$^+$] $C_9H_{16}BrNKO_3$ 303.9945; found 303.9941; calcd. for [M-$C_4H_8$+Na$^+$] $C_5H_8BrNNaO_3$ 231.9580; found 231.9580; calcd. for [M-$C_4H_8$+H$^+$] $C_5H_9BrNO_3$ 209.9760; found 209.9759.

### C.2.2 Synthesis of MeMV$^{2+}$-$CH_2CHCH_2ONHBoc$I$^-$Br$^-$

Under $N_2$, BrONHBoc **1** (180 mg, 0.68 mmol) was added to a solution of **MeMV**$^+$I$^-$ (100 mg, 0.34 mmol) in dry acetonitrile (10.0 ml). The reaction mixture was heated to 75°C and stirred overnight. It was then left to cool to room temperature and centrifuged. The solid was dissolved in a minimal amount of MeOH. Then, $Et_2O$ was added to precipitate the product. After washing three times with $Et_2O$, the salt was dried *in vacuo* to yield a light brown/orange solid (66 mg, 35%).

**$^1$H (400 MHz, $d_6$-DMSO):** 10.08 (s, 1H), 9.35 (d, J = 7.0 Hz, 2H), 9.30 (d, J = 6.7 Hz, 2H), 8.81 (d, J = 6.9 Hz, 2H), 8.76 (d, J = 6.9 Hz, 2H), 6.17-6.01 (m, 2H), 5.38 (d, J = 5.6 Hz, 2H), 4.44 (s, 3H), 4.27 (d, J = 4.5 Hz, 2H), 1.39 (s, 9H). **$^{13}$C (101 MHz, $d_6$-DMSO):** 156.09, 148.94, 148.10, 146.63, 145.77, 133.08, 126.73, 126.25, 126.16, 79.78, 74.38, 61.42, 48.04, 28.03. **EA** $C_{20}H_{27}BrIN_3O_3$: calcd. C 42.57, H 4.82, N 7.45; found C 42.92, H 5.11, N 7.96.

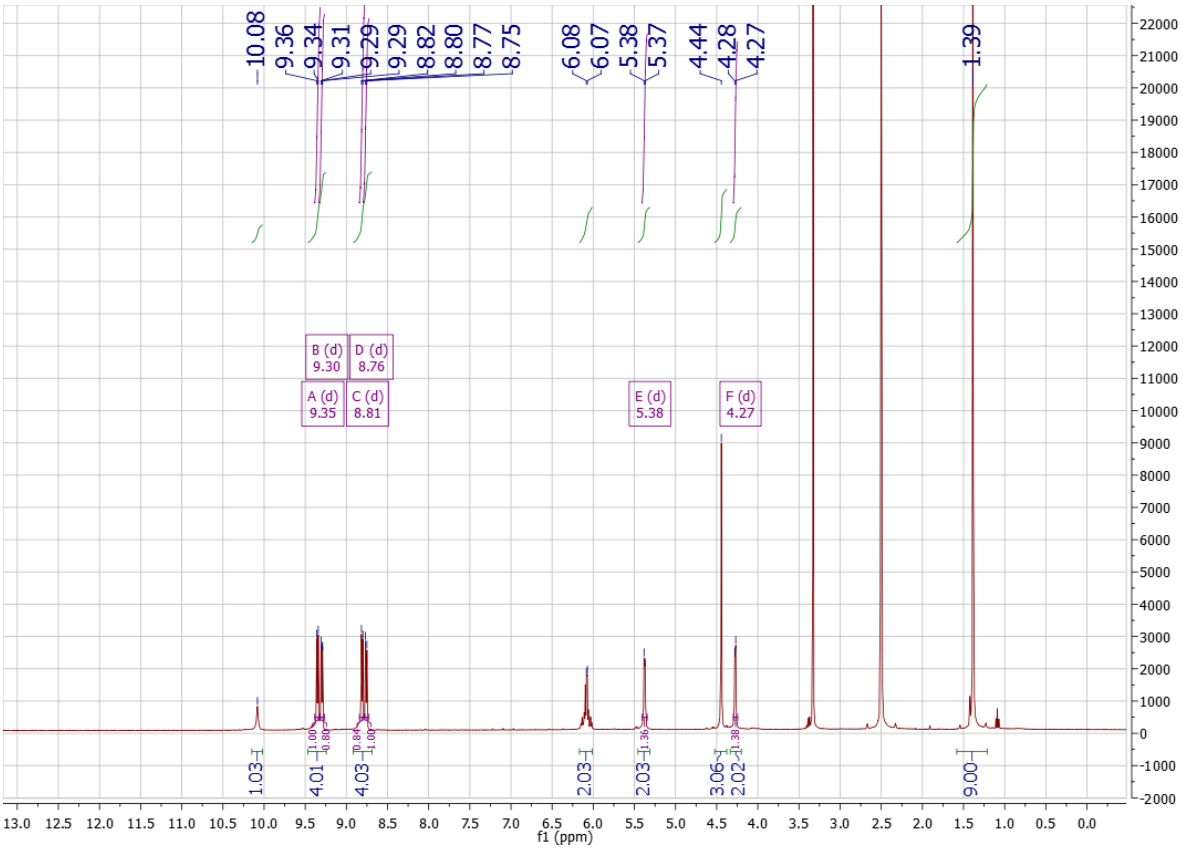


**Figure C.4:** $^{1}$H-NMR spectrum of **2** in $d_6$-DMSO.

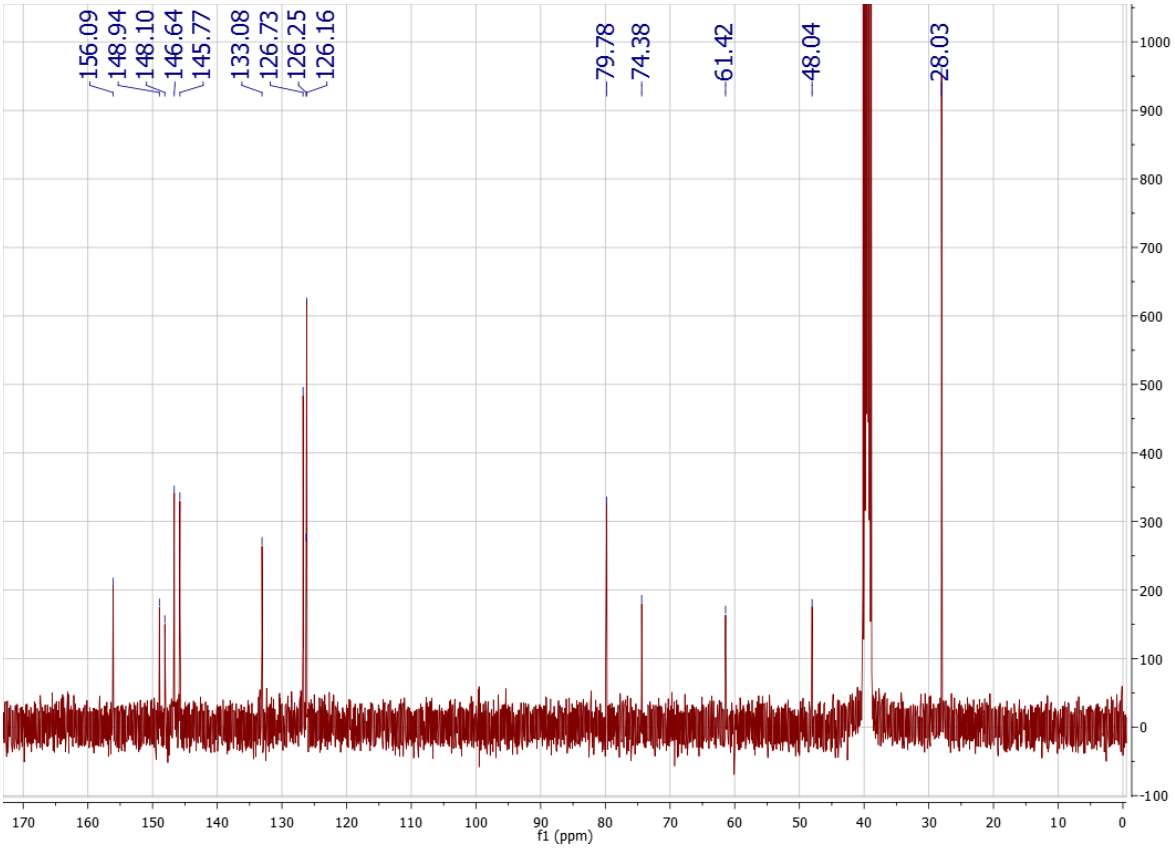


**Figure C.5:** $^{13}$C-NMR spectrum of **2** in $d_6$-DMSO.

### C.2.3 Synthesis of $MeMV^{2+}$-$CH_2CHCH_2ONH_3^+I^-Br^-Cl^-$ ($aMV^{2+}$)

The protected **$MeMV^{2+}$-$CH_2CHCHCH_2ONHBoc$ 2** (30 mg, 53.2 μmol) was dissolved in MeOH (2.0 ml) and 4 M HCl in Dioxane (2.0 ml) was added. It was left stirring for 2 h at room temperature. The solvent was removed *in vacuo* and it was dissolved in a minimal amount of MeOH. The final product was precipitated and washed three times with $Et_2O$. Yellow solid (23.3 mg, 88%).

**$^1$H (400 MHz, $d_6$-DMSO):** 11.01 (bs, 3H), 9.43 (d, J = 6.9 Hz, 2H), 9.32 (d, J = 7.0 Hz, 2H), 8.83 (d, J = 7.0 Hz, 2H), 8.79 (d, J = 7.0 Hz, 2H), 6.27-6.00 (m, 2H), 5.43 (d, J = 6.2 Hz, 2H), 4.60 (d, J = 5.0 Hz, 2H), 4.45 (s, 3H). **$^{13}$C (101 MHz, $d_6$-DMSO):** 148.95, 148.12, 146.64, 146.01, 130.17, 129.10, 126.66, 126.15, 72.89, 61.15, 48.00. **EA** $C_{15}H_{24}BrClIN_3O_3$: calcd. C 33.57, H 4.51, N 7.83; found C 33.52, H 4.25, N 7.83.

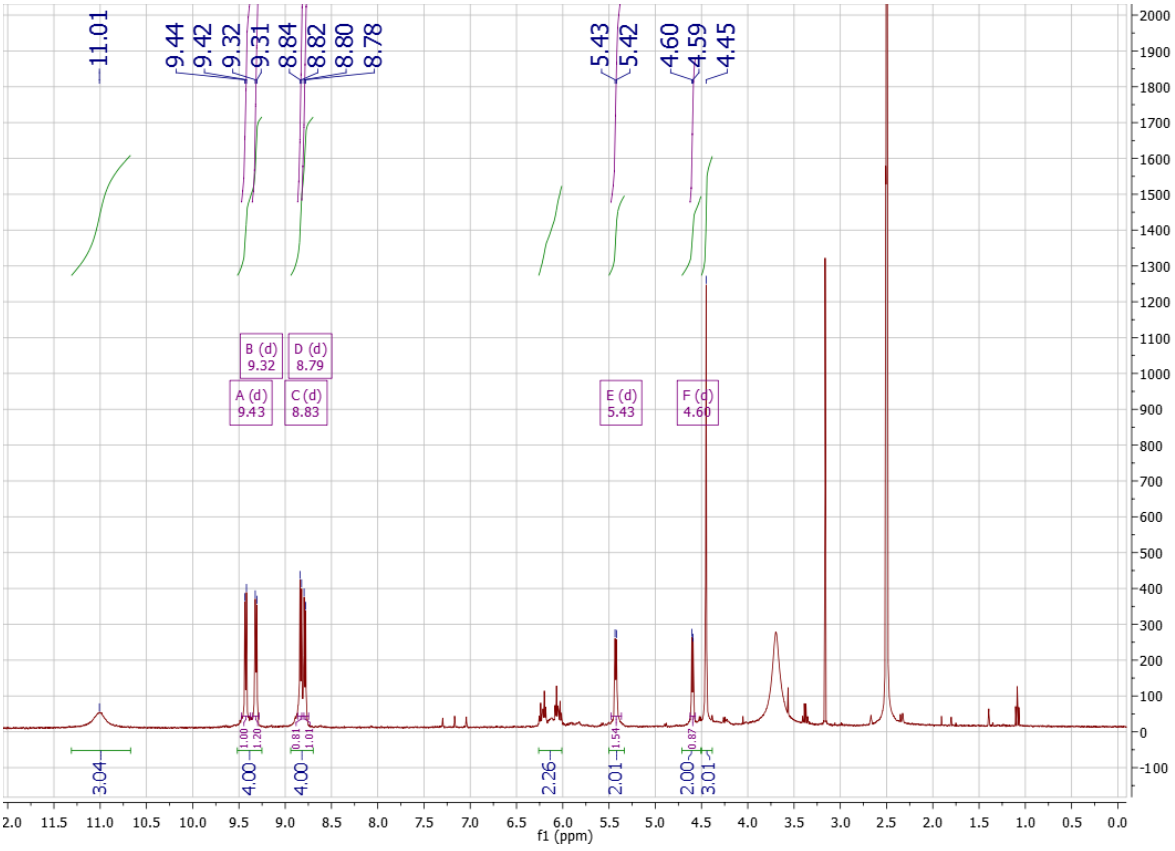


**Figure C.6:** $^1$H-NMR spectrum of **$aMV^{2+}$** in $d_6$-DMSO.

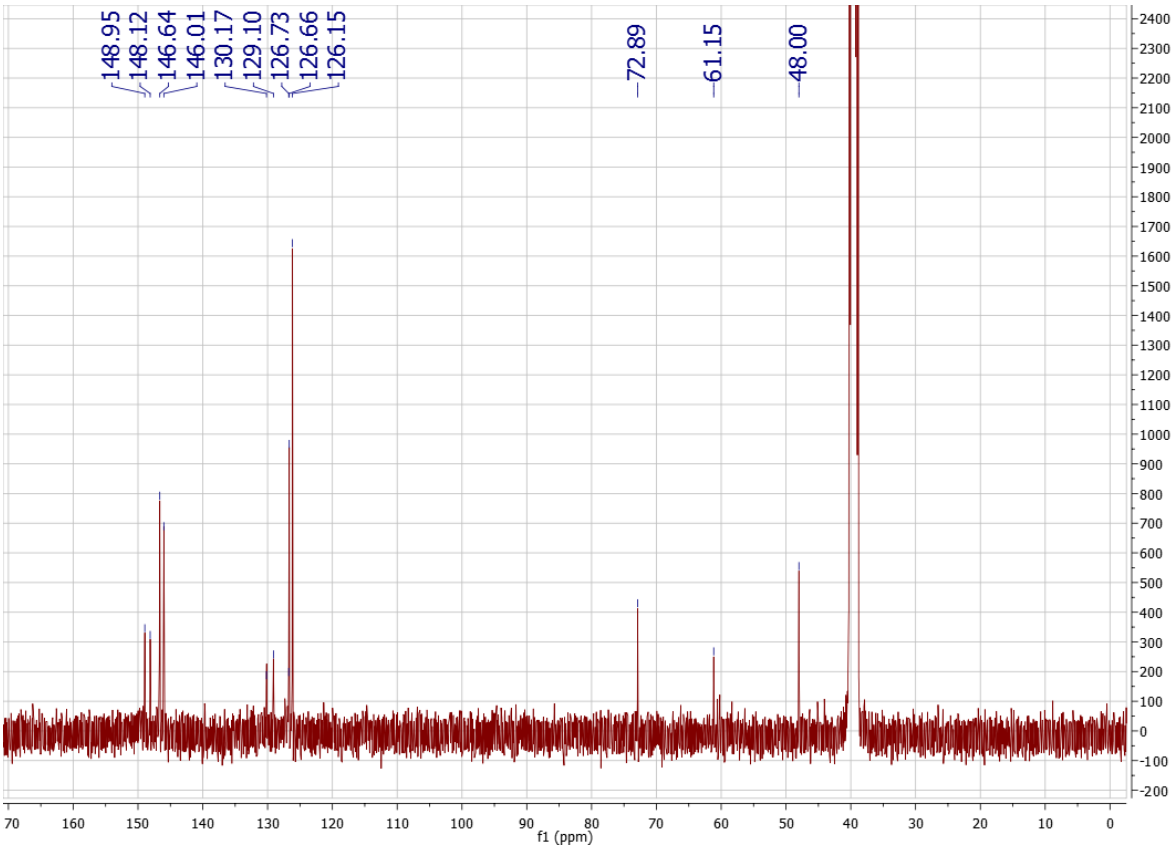


**Figure C.7:** $^{13}$C-NMR spectrum of **aMV$^{2+}$** in $d_6$-DMSO.

## C.3 Engineering a negative patch on the surface of Sav

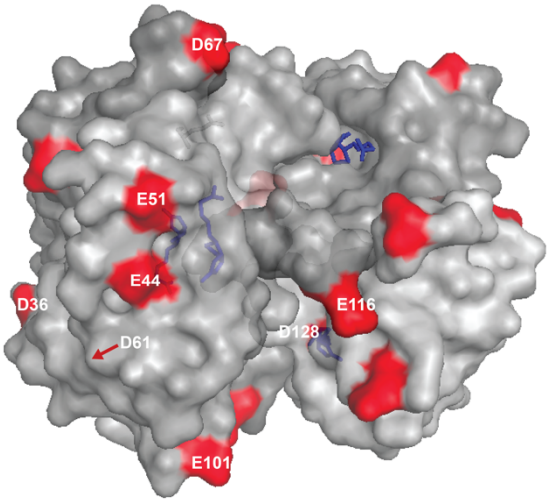


**Figure C.8:** Surface representation of S112A Sav highlighting its eight carboxylic amino acids, six of which are surface-exposed. The naturally occurring Glu and Asp residues are highlighted (red) as well as biotin (blue, stick representation; note: the organometallic cofactor bound to the biotin moiety in this crystal structure was removed due to clarity). The negative patch was engineered around E51. D61 is not visible as it is buried between two dimers of the protein (red arrow) (pdb: 3PK2).[185]

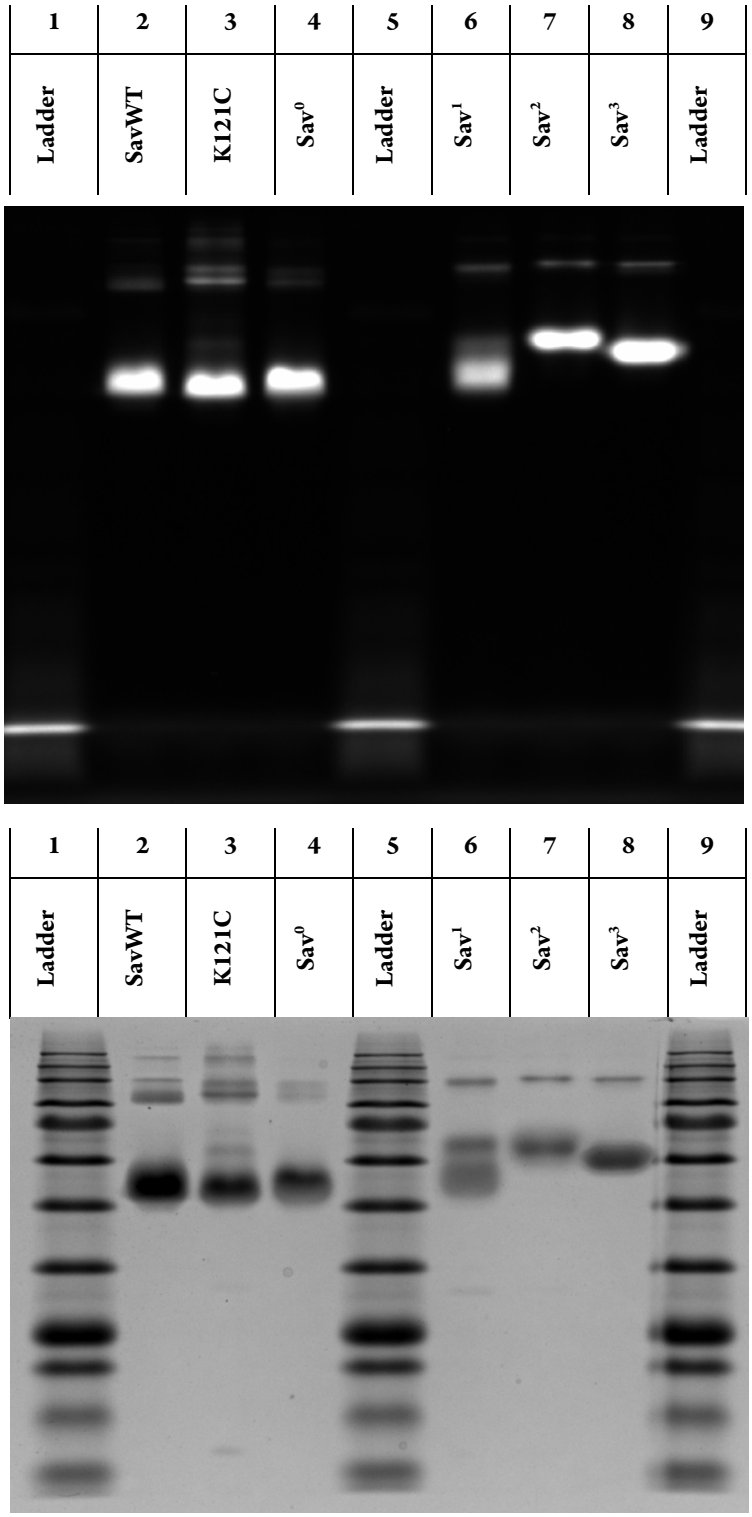


**Figure C.9**: SDS PAGE of Sav mutants with an engineered negative patch. Ladder (lines 1, 5, 9), SavWT (2), K121C (3), *N*-flex **Sav$^0$** (K121C with a flexible *N*-terminus) (4), *N*-flex **Sav$^1$** (additional R84E mutation) (6), *N*-flex **Sav$^2$** (additional N82D-R84E mutation) (7) and *N*-flex **Sav$^3$** (additional N82D-Y83E-R84E mutation) (8) with (top) B4F-fluorescence staining and (bottom) Coomassie staining.

## C.4 Bioconjugation of the MV2+ moiety at the N-terminus of the Sav mutants

The bioconjugation of the cysteine-containing streptavidin mutants with **[Ru(bpy)$_2$(phenNHCOCH$_2$Br)](PF$_6$)$_2$ (1)** was performed as previously described.[322]

The bioconjugation of the PS-containing mutants (**RuSav$^n$**, where n = 0 – 3) was performed according to a modified protocol of *Francis et al.*[328] First the protein (0.6 mol) were dissolved in 300 µl of phosphate buffer (pH 6.5, 20 mM). Then 300 µl of a **PLP** solution (pH 6.5, 0.2 M) was added and the combined solutions were agitated at 37°C for 1 h. Afterwards, the solution was filtered through a size exclusion centrifugation filter (10 kD cutoff) for 10 minutes at 14.8 G and washed with phosphate buffer until the eluate was colorless. The concentrated solution was then dissolved in buffer (total volume 150 µl). Then a **aMV$^{2+}$** solution (100 µl, pH 1.5, 60 mM, **aMV$^{2+}$** was dissolved in 50 µl $Na_2CO_3$ (sat. aq.) and the pH was subsequently adjusted to pH 1.5 with HCl) were added. The pH was adjusted to 2.2 with HCl (0.1 M) and it was agitated for 1.5 hours at 37°C. Then, the solution was diluted with phosphate buffer (pH 6.5, 20 mM to 6.0 ml and diafiltrated twice with a 10% NaCl solution and three times with milliQ water. After lyophilizing, the modified proteins (**RuSav$^n$-aMV$^{2+}$**, where n = 0 – 3) were obtained as a slight yellow powder.

## C.5 Mass spectra of the bioconjugated products

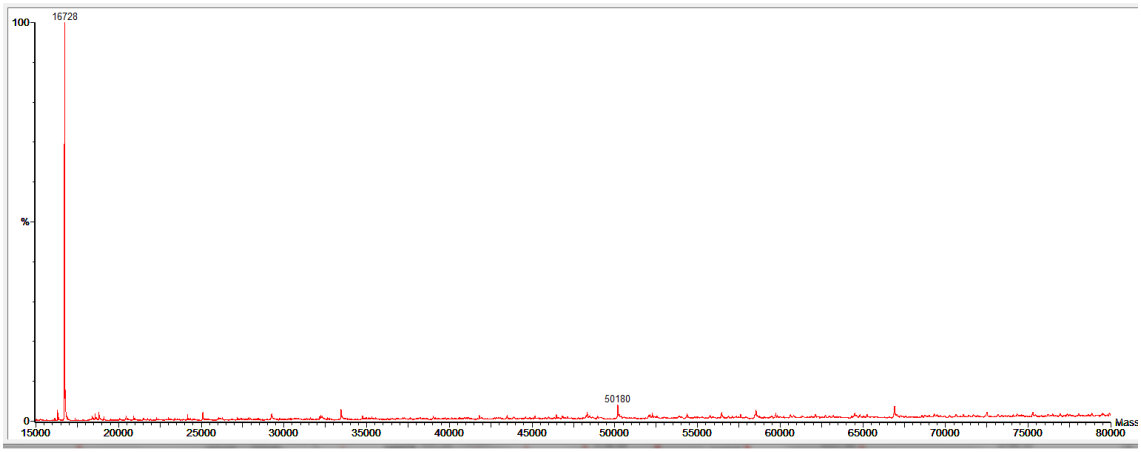


**Figure C.10:** ESI$^+$-MS spectrum of **RuSav$^0$**: expected for bioconjugated with **Ru(bpy)$_2$(phenNH$_2$COCH$_2$Br)](PF$_6$)$_2$** 16733 Da; found 16728 Da.

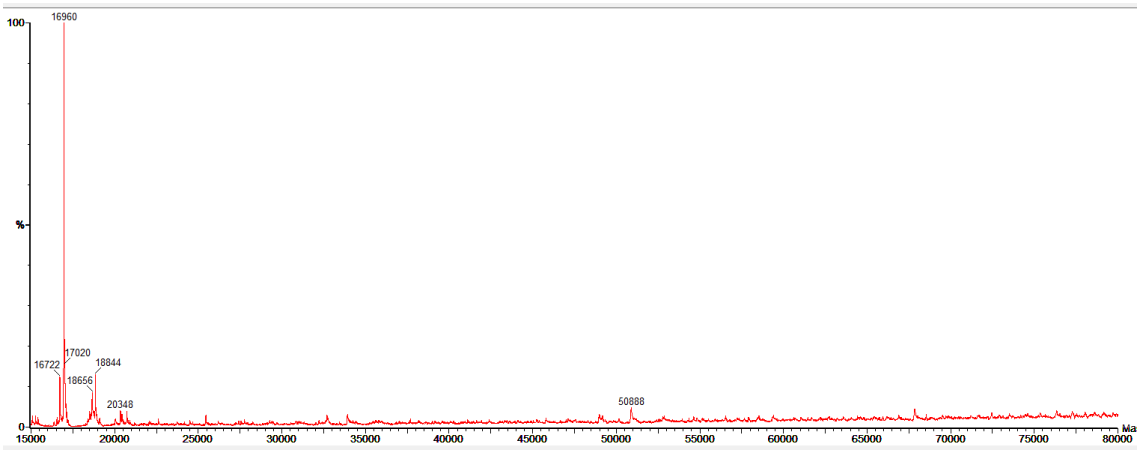


**Figure C.11:** ESI$^+$-MS spectrum of **RuSav$^0$—aMV$^{2+}$**: expected for bioconjugated with **Ru(bpy)$_2$(phenNH$_2$COCH$_2$Br)](PF$_6$)$_2$** and **aMV$^{2+}$** 16971 Da; found 16960 Da.

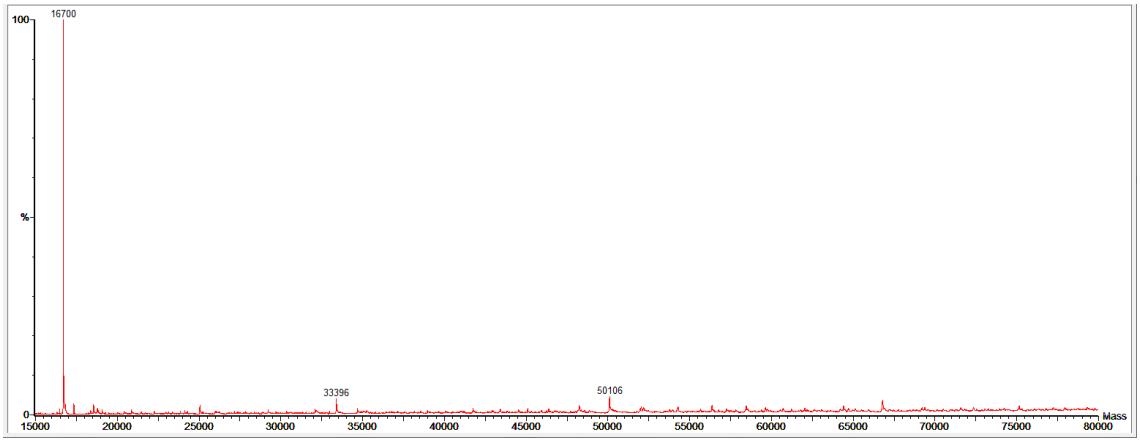


**Figure C.12:** ESI$^+$-MS spectrum of **RuSav$^1$**: expected for bioconjugated with **Ru(bpy)$_2$(phenNH$_2$COCH$_2$Br)](PF$_6$)$_2$** 16706 Da; found 16700 Da.

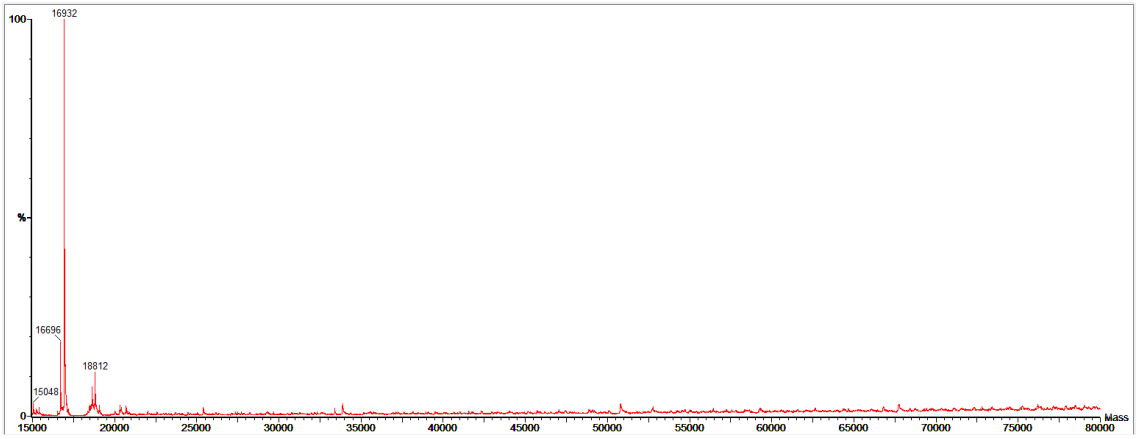


**Figure C.13:** ESI$^+$-MS spectrum of **RuSav$^1$—aMV$^{2+}$**: expected for bioconjugated with **Ru(bpy)$_2$(phenNH$_2$COCH$_2$Br)](PF$_6$)$_2$** and **aMV$^{2+}$** 16944 Da; found 16932 Da.

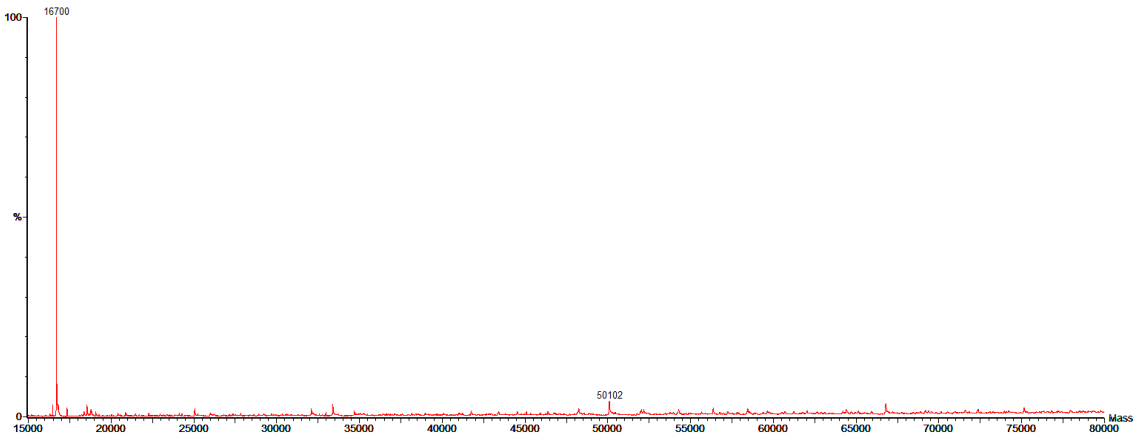


**Figure C.14:** ESI$^+$-MS spectrum of **RuSav$^2$:** expected for bioconjugated with **Ru(bpy)$_2$(phenNH$_2$COCH$_2$Br)](PF$_6$)$_2$** 16705 Da; found 16700 Da.

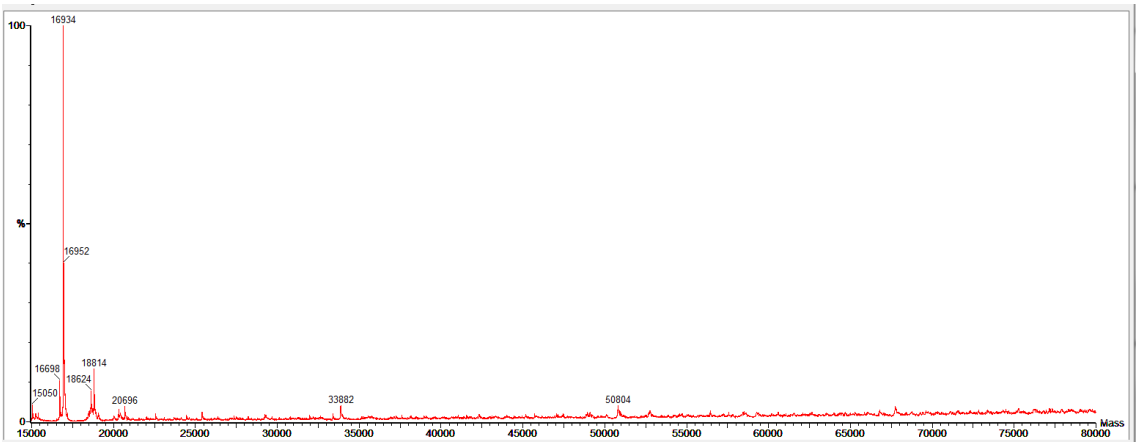


**Figure C.15:** ESI$^+$-MS spectrum of **RuSav$^2$—aMV$^{2+}$**: expected for bioconjugated with **Ru(bpy)$_2$(phenNH$_2$COCH$_2$Br)](PF$_6$)$_2$** and **aMV$^{2+}$** 16945 Da; found 16934 Da.

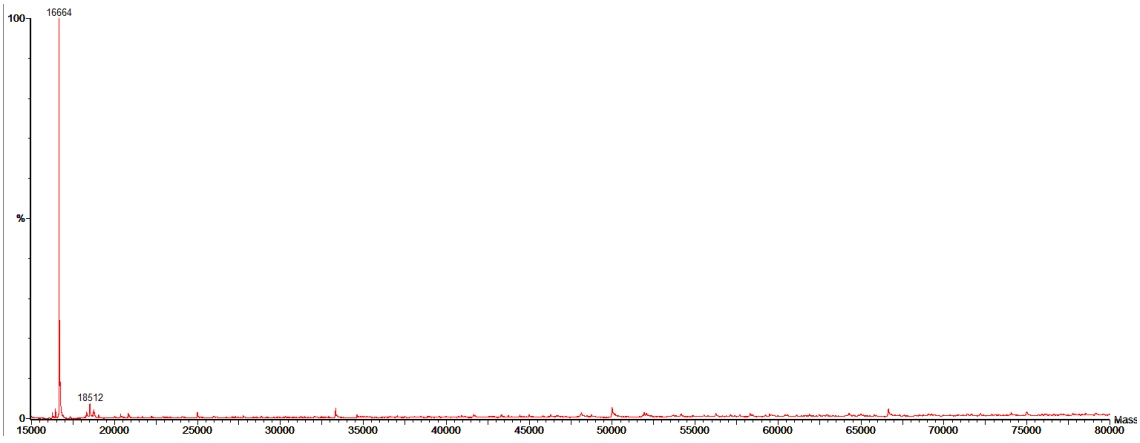


**Figure C.16:** ESI$^+$-MS spectrum of **RuSav$^3$**: expected for bioconjugated with **Ru(bpy)$_2$(phenNH$_2$COCH$_2$Br)](PF$_6$)$_2$** 16671 Da; found 16664 Da.


**Figure C.17:** ESI$^+$-MS spectrum of **RuSav$^3$—aMV$^{2+}$**: expected for bioconjugated with **Ru(bpy)$_2$(phenNH$_2$COCH$_2$Br)](PF$_6$)$_2$** and **aMV$^{2+}$** 16909 Da; found 16900 Da.

## C.6 Estimation of the distances

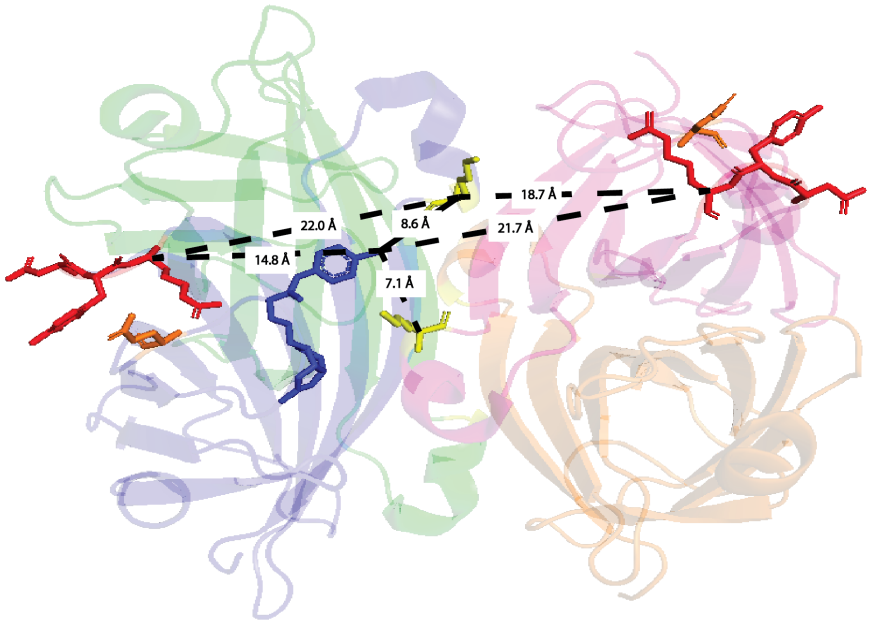


**Figure C.18:** Estimated through-space distances between the sulfur atom of a biotinylated cofactor (blue stick representation) and the α-carbon atoms of the K121 residues (yellow stick representation, here the position of the [**Ru(diimine)$_3$**]$^{2+}$ attachment) and the α-carbon atoms of the closest negatively charged amino acid R84E (red stick representation) of two monomers on the same face of homotetrameric Sav (These two monomers form the so-called biotin-binding vestibule that can accommodate up to two biotinylated probes). The naturally occurring negatively charged amino acid E51 is also highlighted (orange stick representation).[185]

**Table C.1:** Estimated through-space distances between α-carbon atoms of K121 and R84 positions and the sulfur atom of a biotinylated cofactor based on the crystal structure of streptavidin (pdb code: 3PK2).

| | **αC-K121** | ***N*-Biot-TAA** | **αC-R84** |
|---|---|---|---|
| **αC-K121** | - | **7.1 Å / 8.6 Å** | **18.7 Å / 22.0 Å** |
| ***N*-Biot-TAA** | **7.1 Å / 8.6 Å** | - | **14.8 Å / 21.7 Å** |
| **αC-R84** | **18.7 Å / 22.0 Å** | **14.8 Å / 21.7 Å** | - |

## C.7 Biotin-binding activity determination[296,302]

The Sav mutants (76.8 nmol) were dissolved in $NaH_2PO_4$ buffer (2.4 ml, 20 mM, pH 7.0). The solutions were treated with a 2-(4-hydroxyphenylazo)benzoic acid (HABA) solution (300 µl, 9.6 mM) in $NaH_2PO_4$ buffer (20 mM, pH 7.0) filled into a cuvette and incubated for 5 minutes. A blank of the buffer was measured at 506 nm using a Varian50 Scan UV-Vis spectrophotometer. The absorbance of the resulting sample was determined and aliquots of a biotin (or **Biot-TAA,** 5.0 µl) solution (0.96 mM) in DMSO were added sequentially. The data points were plotted with Origin Pro 9.0.0 to determine the number of biotin-binding sites and the number of **Biot-TAA** that can bind into the homotetrameric for the bioconjugated-Sav scaffolds.

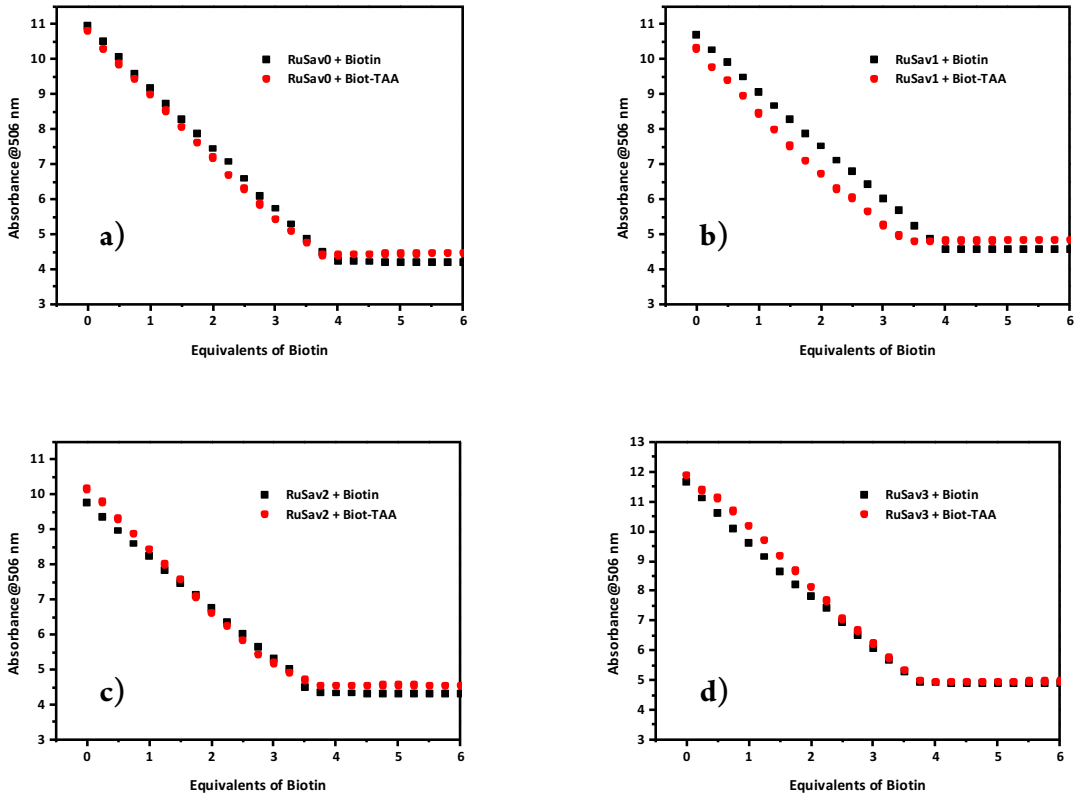


**Figure C.19:** HABA-displacement titration of biotin (black symbols) and the biotinylated triarylamine **Biot-TAA** (red symbols) of a) **RuSav$^0$** b) **RuSav$^1$** c) **RuSav$^2$** and d) **RuSav$^3$**.

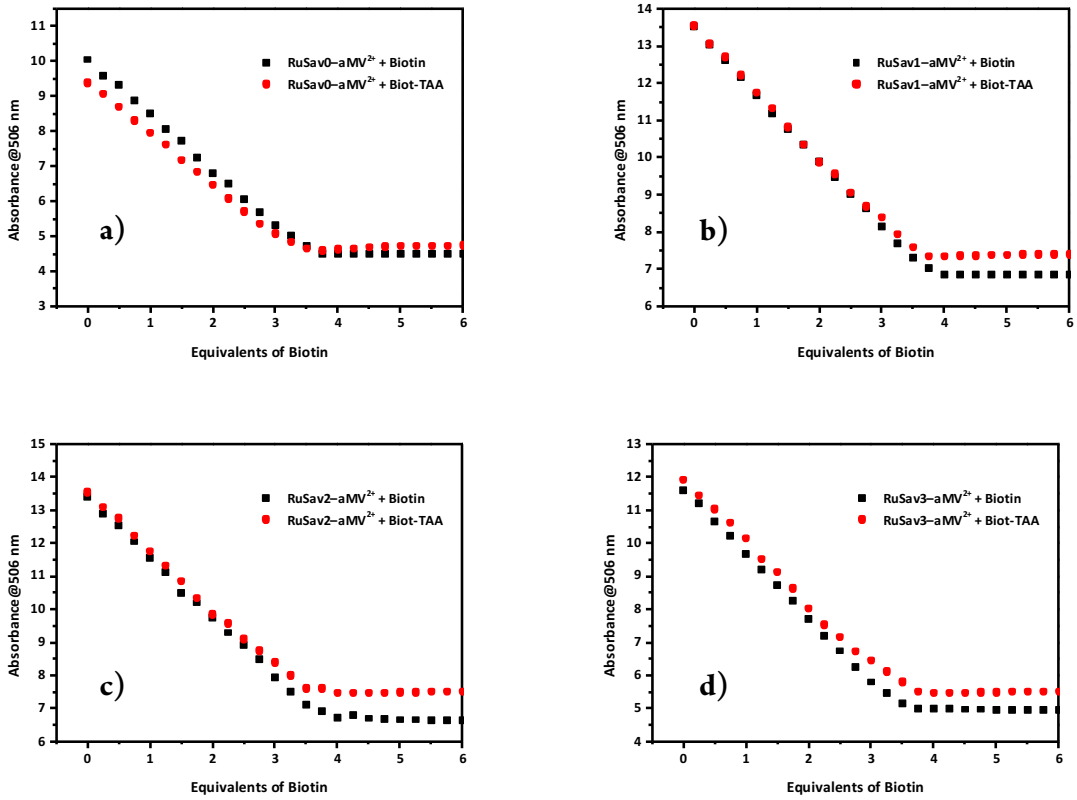


**Figure C.20:** HABA-displacement titration of biotin (black symbols) and the biotinylated triarylamine **Biot-TAA** (red symbols) of a) **RuSav$^0$—aMV$^{2+}$** b) **RuSav$^1$—aMV$^{2+}$** c) **RuSav$^2$—aMV$^{2+}$** and d) **RuSav$^3$—aMV$^{2+}$**.

## C.8 Photoexcitation experiments

The proteins **RuSav$^n$** or **RuSav$^n$—aMV$^{2+}$** (where n = 0 - 3) were dissolved in 1.5 ml milliQ water (50 µM final concentration) in an inert gas cuvette. The solution was then degassed using the freeze-pump-thaw method. After three cycles, the cuvette was filled with an argon atmosphere. After addition of **Biot-TAA**, **TAA-NH$_2$** or $MV^{2+}$, the cuvettes were again degassed using the same method. Stock solutions (7.5 µl) of the triarylamines **Biot-TAA** and **TAA-NH$_2$** as well as **MV$^{2+}$** were added to reach a final concentration of 50 µM.

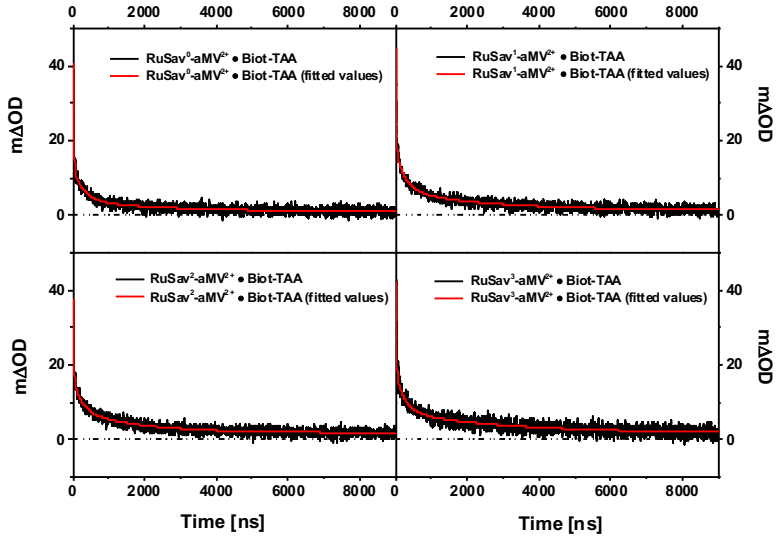


**Figure C.21:** Temporal evolution of the transient absorption signal at 750 nm of (a) **RuSav$^0$—aMV$^{2+}$**, (b) **RuSav$^1$—aMV$^{2+}$**, (c) **RuSav$^2$—aMV$^{2+}$** and (d) **RuSav$^3$—aMV$^{2+}$** with 1 equivalent of **Biot-TAA** (black traces) and the fitted functions (red traces).

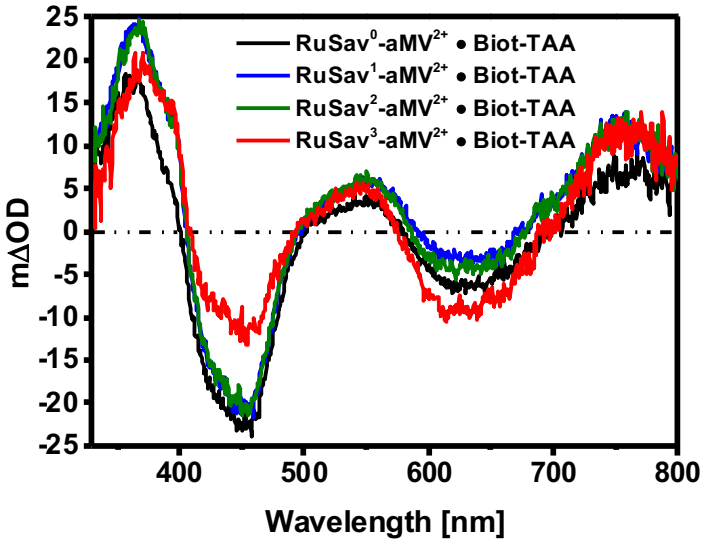


**Figure C.22:** Transient absorption spectra of 50 µM of **RuSav$^0$—aMV$^{2+}$** (black trace), **RuSav$^1$—aMV$^{2+}$** (blue trace), **RuSav$^2$—aMV$^{2+}$** (green trace) and **RuSav$^3$—aMV$^{2+}$** (red trace) in milliQ water at 25 °C, immediately after excitation at 450 nm in presence of 50 µM **Biot-TAA**.

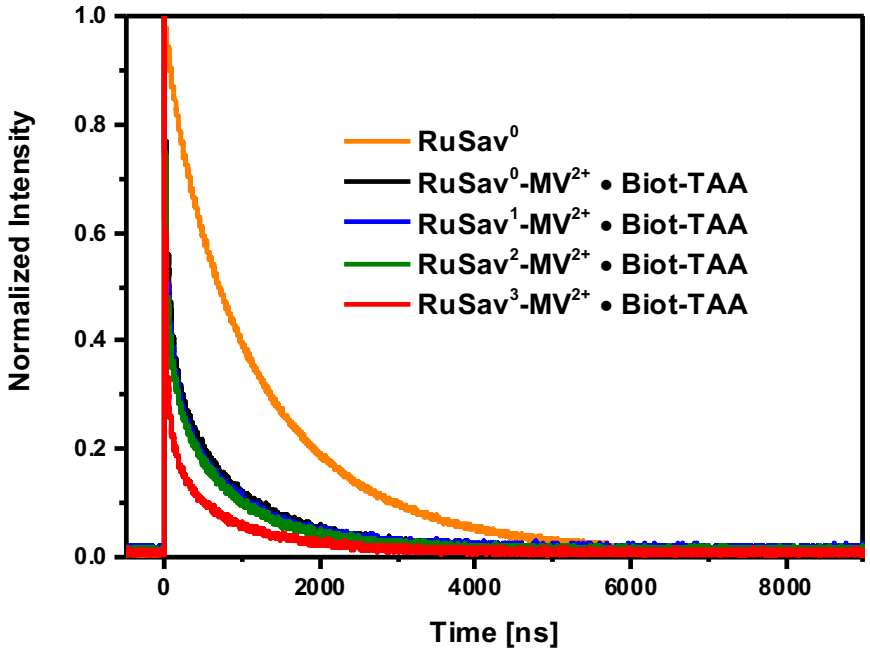


**Figure C.23:** Normalized luminescence decay detected at 630 nm following excitation of **RuSav$^0$** (orange trace) and **RuSav$^0$—aMV$^{2+}$ · Biot-TAA** (black trace), **RuSav$^1$—aMV$^{2+}$ · Biot-TAA** (blue trace), **RuSav$^2$—aMV$^{2+}$ · Biot-TAA** (green trace) and **RuSav$^3$—aMV$^{2+}$ · Biot-TAA** (red trace).

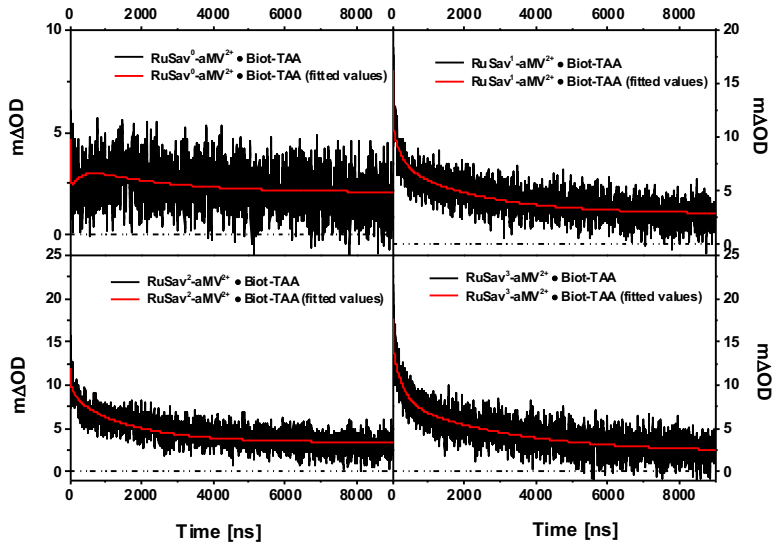


**Figure C.24:** Temporal evolution of the transient absorption signal at 400 nm of (a) **RuSav$^0$—aMV$^{2+}$**, (b) **RuSav$^1$—aMV$^{2+}$**, (c) **RuSav$^2$—aMV$^{2+}$** and (d) **RuSav$^3$—aMV$^{2+}$** with 1 equivalent of **Biot-TAA** (black traces) and the fitted functions (red traces).

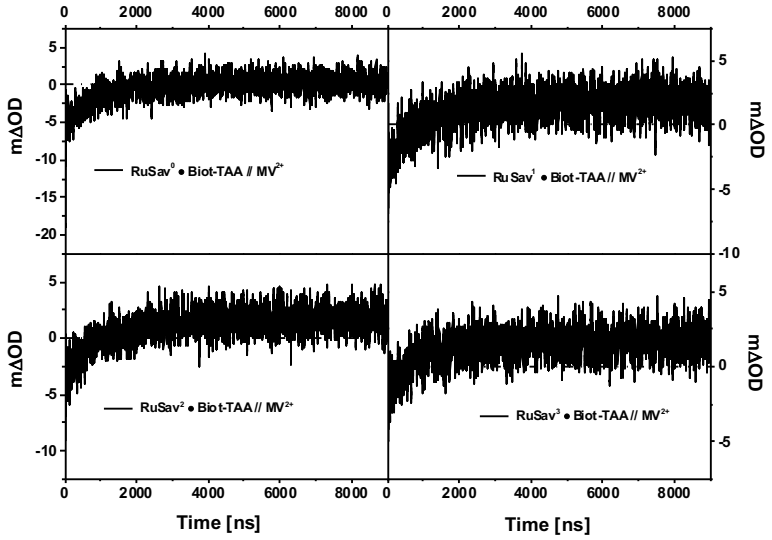


**Figure C.25:** Temporal evolution of the transient absorption signal at 400 nm of (a) **RuSav$^0$**, (b) **RuSav$^1$**, (c) **RuSav$^2$** and (d) **RuSav$^3$** with 1 equivalent of **Biot-TAA** and one equivalent of **MV$^{2+}$** in solution (// symbolizes that a compound was added in solution). The negative signal at early times is due to bleaching of the sensitizer MLCT absorption band.

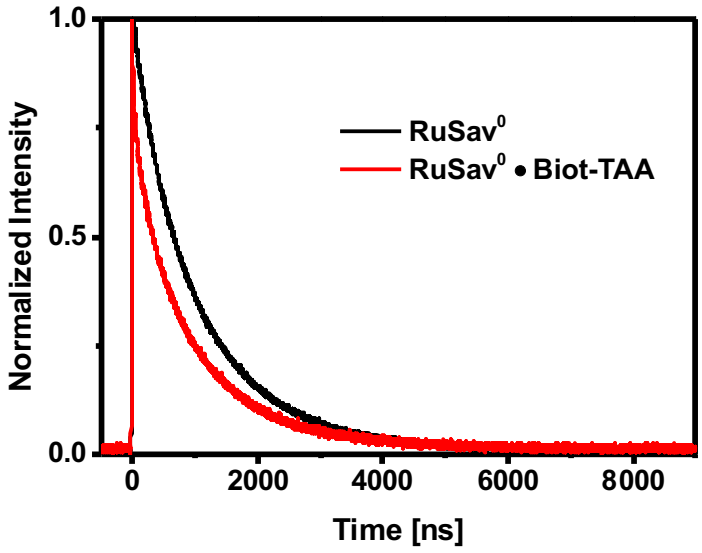


**Figure C.26:** Normalized luminescence decays detected at 630 nm following excitation of **RuSav$^0$** (black trace) and **RuSav$^0$** with 1 eq. **Biot-TAA** (red trace).

**Table C.2:** Decay time constants ($t_1$, $t_2$, $t_3$) of the photosensitizer luminescence extracted from Figure S23. After addition of **Biot-TAA** an initial rapid decay with a time constant ($t_1$) of ca. 27 ns can be detected. This is attributed to reductive quenching and fomration of Biot-TAA$^+$ to Ru(I), as discussed in the main paper.

| | $t_1$ [ns] | $t_2$ [ns] | $t_3$ [ns] |
|---|---|---|---|
| **RuSav$^0$** | | **444 (24 %)** | **1207 (74%)** |
| **RuSav$^0$ · Biot-TAA** | **27 (23%)** | **314 (22%)** | **1120 (55%)** |

The data in Figure C.26 displays that some quenching of the sensitizer's luminescence is caused by **Biot-TAA** in the absence of methyl viologen (initial rapid decay).

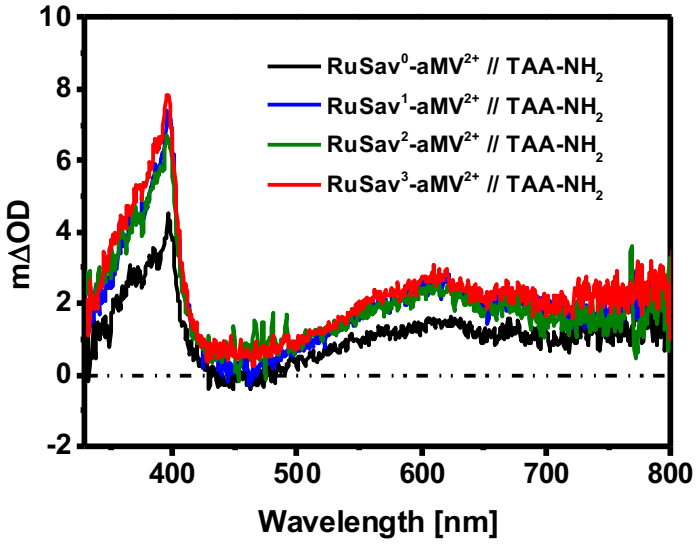


**Figure C.27:** Transient absorption spectra of 50 µM of **RuSav$^0$—aMV$^{2+}$**(black trace), **RuSav$^1$—aMV$^{2+}$** (blue trace), **RuSav$^2$—aMV$^{2+}$** (green trace) and **RuSav$^3$—aMV$^{2+}$** (red trace) in milliQ water at 25 °C, 10 µs after excitation at 450 nm in presence of 50 µM **TAA-NH$_2$** (// symbolizes that a compound was added in solution).

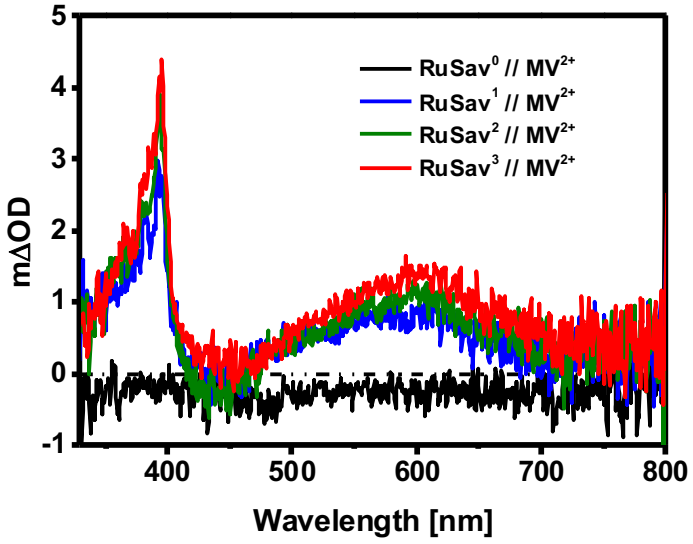


**Figure C.28:** Transient absorption spectra of 50 μM of **RuSav⁰** (black trace), **RuSav¹** (blue trace), **RuSav²** (green trace) and **RuSav³** (red trace) in milliQ water at 25 °C, 10 μs after excitation at 450 nm on presence of 50 μM **$MV^{2+}$** (// symbolizes that a compound was added in solution).

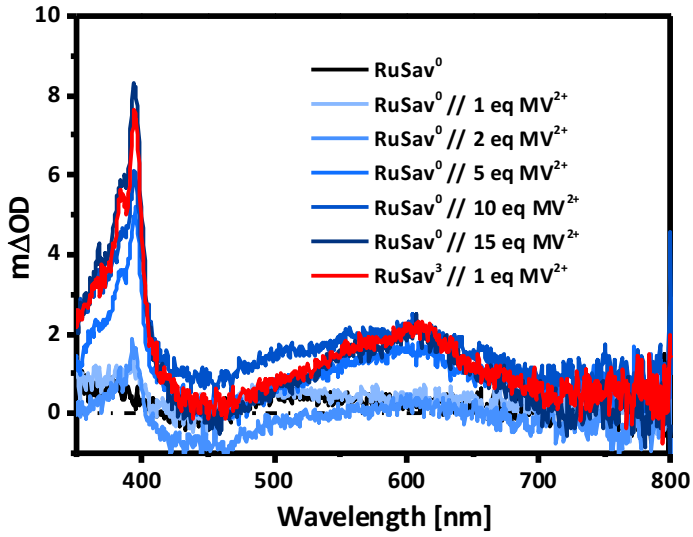


**Figure C.29:** Transient absorption spectra of 50 μM **RuSav⁰** (black trace) with 0, 50, 100, 250, 500, 750 μM **$MV^{2+}$** added in solution (blue traces) and 50 μM **RuSav³** (red trace) with 50 μM **$MV^{2+}$** added in milliQ water at 25 °C, 10 μs after excitation at 450 nm (// symbolizes that a compound was added in solution).

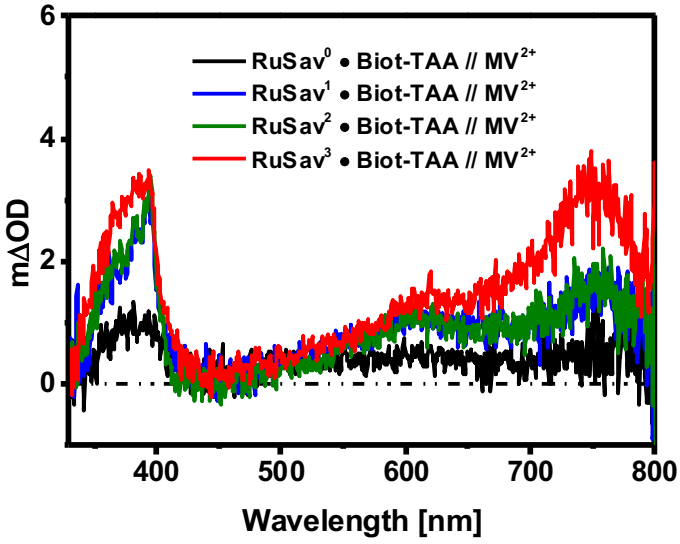


**Figure C.30:** Transient absorption spectra of 50 µM of **RuSav$^{0}$** (black trace), **RuSav$^{1}$** (blue trace), **RuSav$^{2}$** (green trace) and **RuSav$^{3}$** (red trace) with 50 µM **MV$^{2+}$** and 50 µM **Biot-TAA** added in milliQ water at 25 °C, 10 µs after excitation at 450 nm (// symbolizes that a compound was added in solution).

D

# Supplemental Information Chapter 6

## D.1 General Methods

Recombinant streptavidin isoforms were engineered, expressed, purified and quantified as previously described.[270,375] Other reagents, substrates and materials were purchased from Sigma, Aldrich, TCI and Acros. NMR experiments were performed on a Bruker Avance III NMR spectrometer operating at 400 MHz proton frequency and 101 MHz carbon frequency. Chemical shifts were referenced to residual Methanol-$d_6$ (3.31 ppm) for $^{1}H$ spectra or Methanol-$d_6$ (49.00 ppm) for $^{13}C$ spectra. Signals are quoted as s (singlet), d (doublet), t (triplet), q (quintet) and m (multiplet). Automated Flash column purification was performed on a Biotage Isolera One with a C18 silica column. Mass spectra were acquired on Bruker Esquire 3000 plus and Bruker maxis 4GQTOF EDI spectrometers. Hydrogen evolution was measured on a GC (Bruker GC-450 with TCD detector and automatic measurement) under a continuous argon flow with a 453 nm LED at 1100 Lux.

## D.2 Synthesis

The compounds **1**,[145] **2**,[379] **5**[373] and [**CoBr(appy)-OH**]**Br**[145] were synthesized as previously reported.

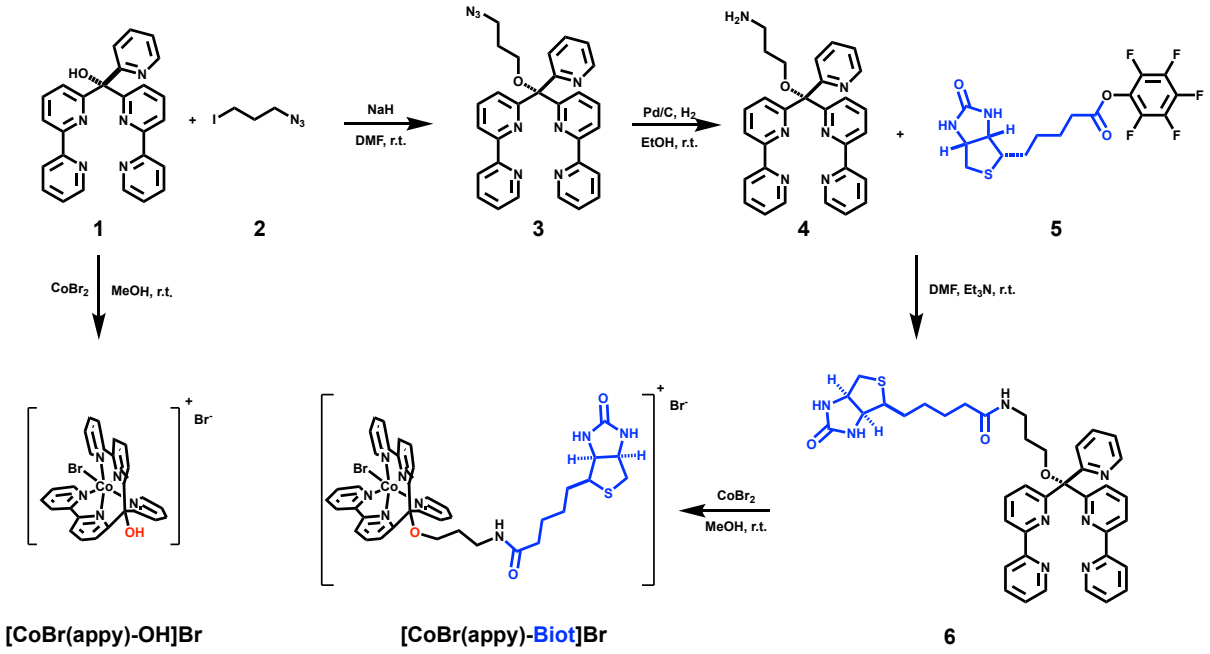


**Scheme D.1:** Reaction pathway for the synthesis of [CoBr(appy)-OH]Br and [CoBr(appy)-Biot]Br.

### D.2.1 Synthesis of (appy)-$N_3$

Di-2,2′-bipyridin-6-yl(pyridin-2-yl)methanol (**1**) (200 mg, 0.48 mmol, 1 eq.) was dissolved in dry DMF and NaH (60% in mineral oil; 55.1 mg, 1.44 mmol, 3 eq.) was added. The mixture was left stirring for 60 minutes at room temperature. Then 1-azido-3-iodopropane (**2**) (506 mg, 2.4 mmol, 5 eq.) was added and stirring continued for 24 h at room temperature. The reaction mixture was quenched with MeOH and HCl (2M) and $CH_2Cl_2$ were added and the phases separated. The organic phase was extracted with HCl (2M) three times. The combined aqueous phases were then neutralized with NaOH (2M) and extracted three times with $CH_2Cl_2$. The combined organic phases were dried over $MgSO_4$ and the solvent was removed. The crude product was purified by automated reverse column flash chromatography (Biotage, 12g C18-silica, $H_2O$/MeOH = 100:0 to 0:100 within 1 h, 12 mL/min). The combined fractions containing the product were reduced *in vacuo* to yield the desired product (**appy**)-$N_3$ (**3**) as an off-white solid (50.5 mg, 0.10 mmol, 21%).

**$^1$H-NMR (400 MHz, Methanol-** $d_4$**):** δ = 8.58 (ddd, *J* = 4.9, 1.8, 0.9 Hz, 2 H), 8.53-8.50 (m, 1H), 8.24 (dd, *J* = 7.8, 1.0 Hz, 2H), 8.13 (dt, *J* = 8.0, 1.1 Hz, 2H), 7.93 (t, *J* = 7.9 Hz, 2 H), 7.89-7.70 (m, 6H), 7.41-7.30 (m, 3H), 3.61 (t, *J* = 6.0 Hz, 2H), 3.46 (t, *J* = 6.7 Hz, 2H), 1.89 (p, *J* = 6.4 Hz, 2H); **$^{13}$C-NMR (101**

**Mhz, Methanol-$d_4$):** δ = 163.01, 162.40, 157.38, 155.43, 149.94, 148.83, 138.53, 138.33, 137.58, 126.30, 125.56, 125.15, 123.73, 122.64, 120.39, 89.74, 63.16, 49.69, 30.66; **HRMS** (ESI+) calcd. for [M + $H^+$] $C_{29}H_{25}N_8O$ 501.2146; found 501.2153.

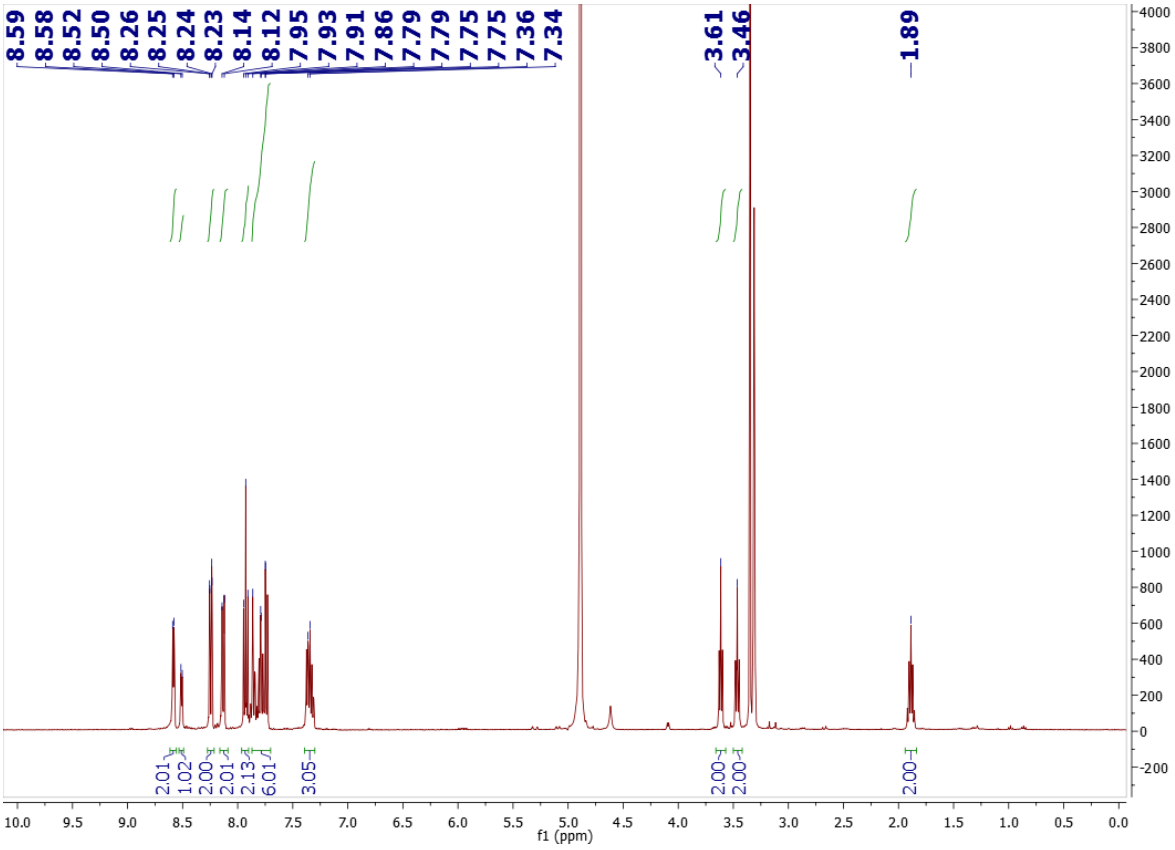


**Figure D.1:** $^1$H-NMR spectrum of **(appy)-$N_3$ (3)** in $d_4$-Methanol**.**

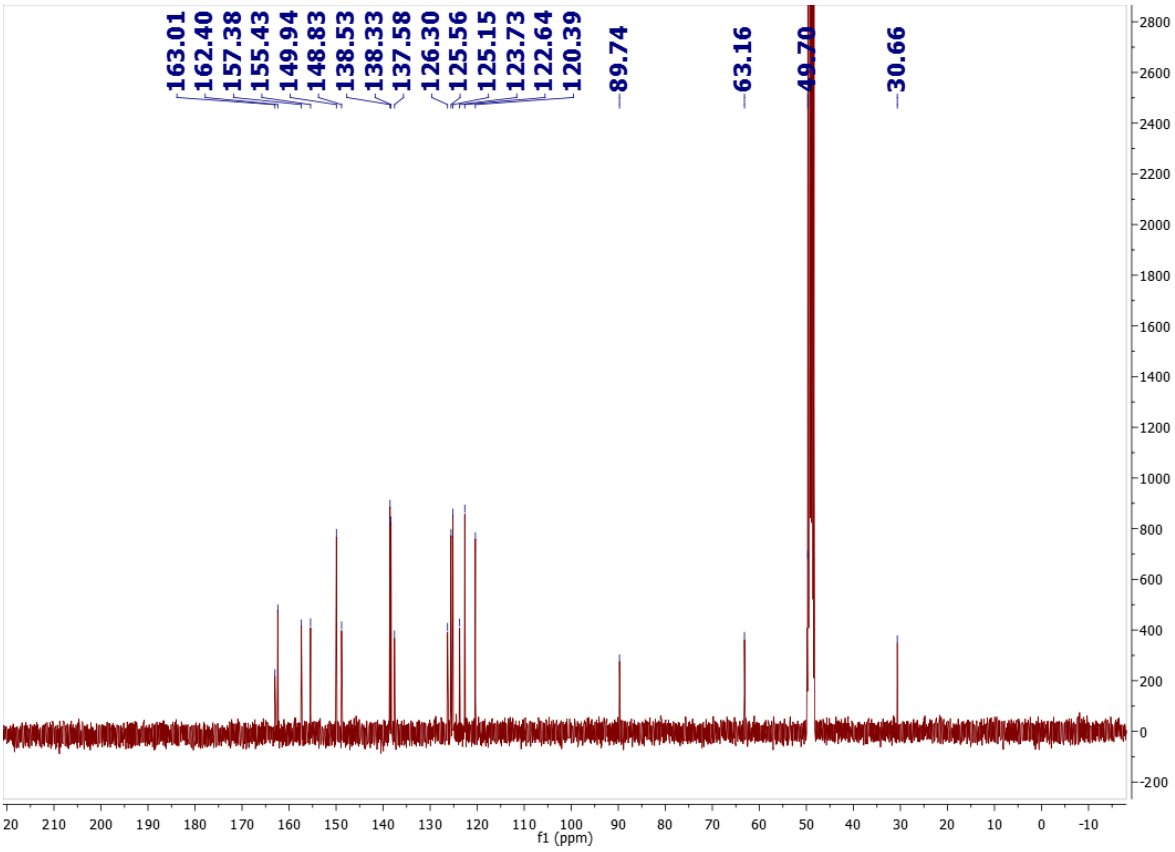


**Figure D.2:** $^{13}$C-NMR spectrum of **(appy)-N$_3$ (3)** in $d_4$-Methanol**.**

## D.2.2 Synthesis of (appy)-NH$_2$

The azide **(appy)-N$_3$ (3)** (30 mg, 0.06 mmol) was dissolved in dry MeOH under $N_2$. Then Pd/C (5 mg, 10% Pd) was added and a balloon filled with $H_2$ was attached. The solution was stirred vigorously for 24 h at room temperature. The mixture was filtered over Celite and the plug was washed with MeOH. The solvent was removed *in vacuo* to yield the reduced product **(appy)-NH$_2$ (4)** as an off-white solid (quantitative).

**$^1$H-NMR (400 MHz, Methanol-$d_4$):** δ = 8.62 (ddd, *J* = 4.9, 1.8, 0.9 Hz, 2 H), 8.56 (ddd, *J* = 5.0, 1.7, 0.9 Hz, 1 H), 8.27 (dd, *J* = 7.9, 1.0 Hz, 2H), 8.04-7.94 (m, 5H), 7.90 (ddd, *J* = 8.1, 7.3, 1.7 Hz, 1H), 7.80 (td, *J* = 7.7, 1.0 Hz, 2H), 7.69 (dd, *J* = 7.9, 1.0 Hz, 2H), 7.45-7.34 (m, 3H), 3.52 (t, *J* = 6.0 Hz, 2H), 3.28 (t, *J* = 6.7 Hz, 2H), 2.04 (p, *J* = 5.6 Hz, 2H); **$^{13}$C NMR (101 MHz, Methanol-$d_4$)**: δ = 162.07, 161.64. 157.08, 155.81, 150.20, 148.03, 138.96, 138.61, 137.60, 128.80, 125.33, 124.97, 124.25, 122.52, 121.04, 90.44, 66.19, 40.81, 28.07; **HRMS** (ESI+) calcd. for [M + H$^+$] $C_{29}H_{27}N_6O$ 475.2241; found 475.2246.

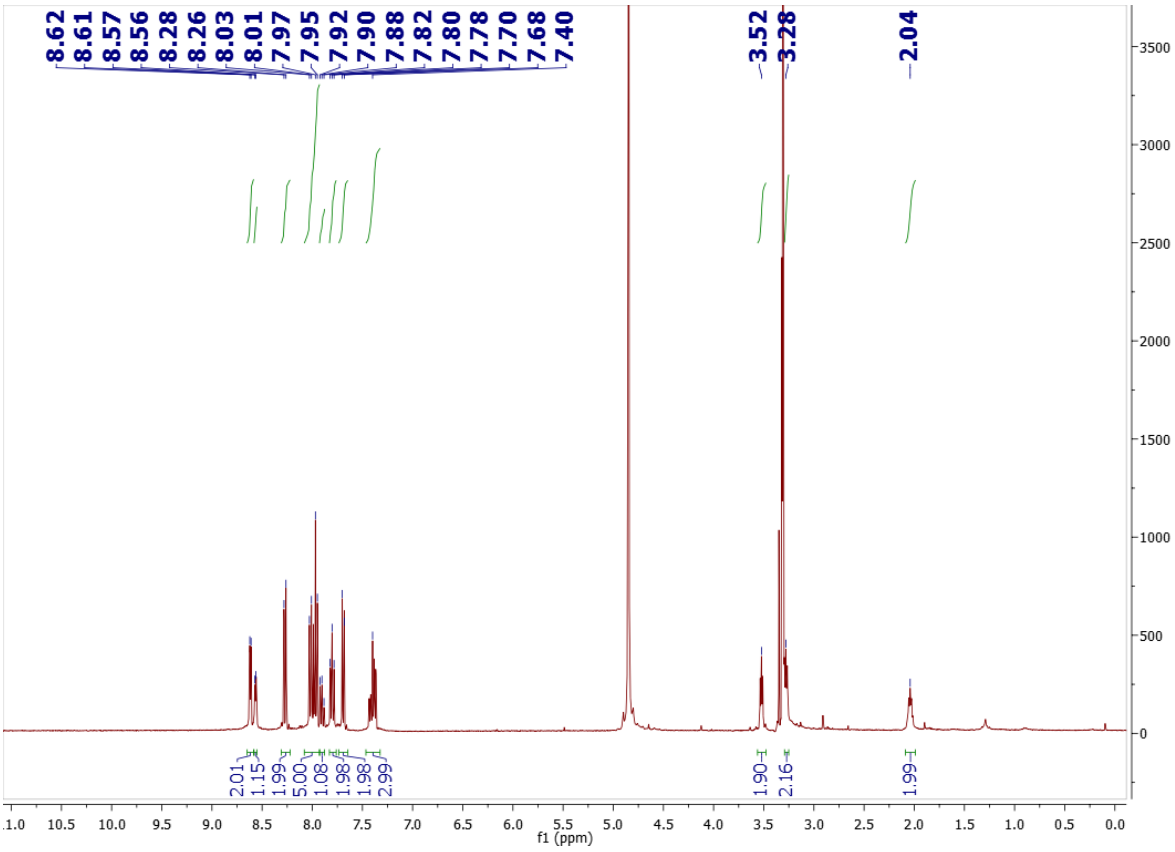


**Figure D.3:** $^{1}$H-NMR spectrum of **(appy)-NH$_2$ (4)** in $d_4$-Methanol**.**

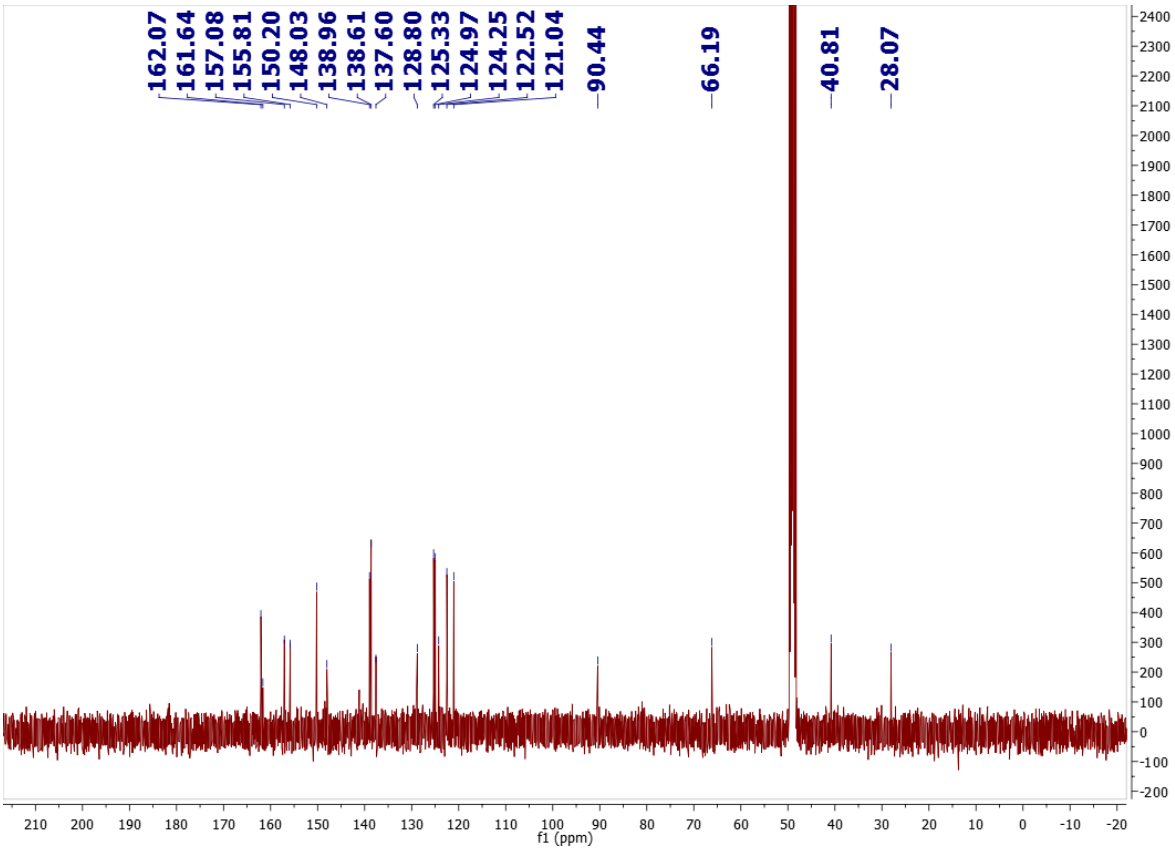


**Figure D.4:** $^{13}$C-NMR spectrum of **(appy)-NH$_2$ (4)** in $d_4$-Methanol**.**

### D.2.3 Synthesis of (appy)-Biot

The amine **(appy)-NH₂ (4)** (20 mg, 0.04 mmol, 1 eq.) was dissolved in dry DMF (1 ml) and it was cooled to 0°C. Then Biotin-pentafluorophenylester **(5)** (18.2 mg, 0.044 mmol, 1.05 eq.) and trimethylamine (4.45 mg, 6.1 µl, 0.044 mmol, 1.05 eq.) were added. The solution was allowed to come to room temperature und left stirring for 15 h. Then HCl (2M) and $CH_2Cl_2$ were added and the phases separated. The organic phase was extracted with HCl (2M) three times. The combined aqueous phases were then neutralized with NaOH (2M) and extracted three times with $CH_2Cl_2$. The combined organic phases were dried over $MgSO_4$ and the solvent was removed. The crude product was purified by automated reverse column flash chromatography (Biotage, 12g C18-silica, $H_2O$/MeOH = 100:0 to 0:100 within 1 h, 12 mL/min). The combined fractions containing the product were reduced *in vacuo* to yield the desired product **(appy)-Biot (6)** as an off-white solid (17.7 mg, 0.025 mmol, 63%).

**$^{13}$C-NMR (101 MHz, $d_4$-Methanol):** δ = 175.70, 166.07, 162.96, 162.48, 157.34, 155.48, 150.00, 148.81, 138.56, 138.40, 137.53, 126.59, 125.56, 125.19, 123.79, 122.64, 120.47, 89.80, 64.37, 63.31, 61.57, 56.90, 41.02, 38.19, 36.99, 30.74, 29.76, 29.41, 26.85; **HRMS** (ESI+) calcd. for [M + H$^+$] $C_{39}H_{41}N_8O_3S$ 701.3017; found 701.3007.

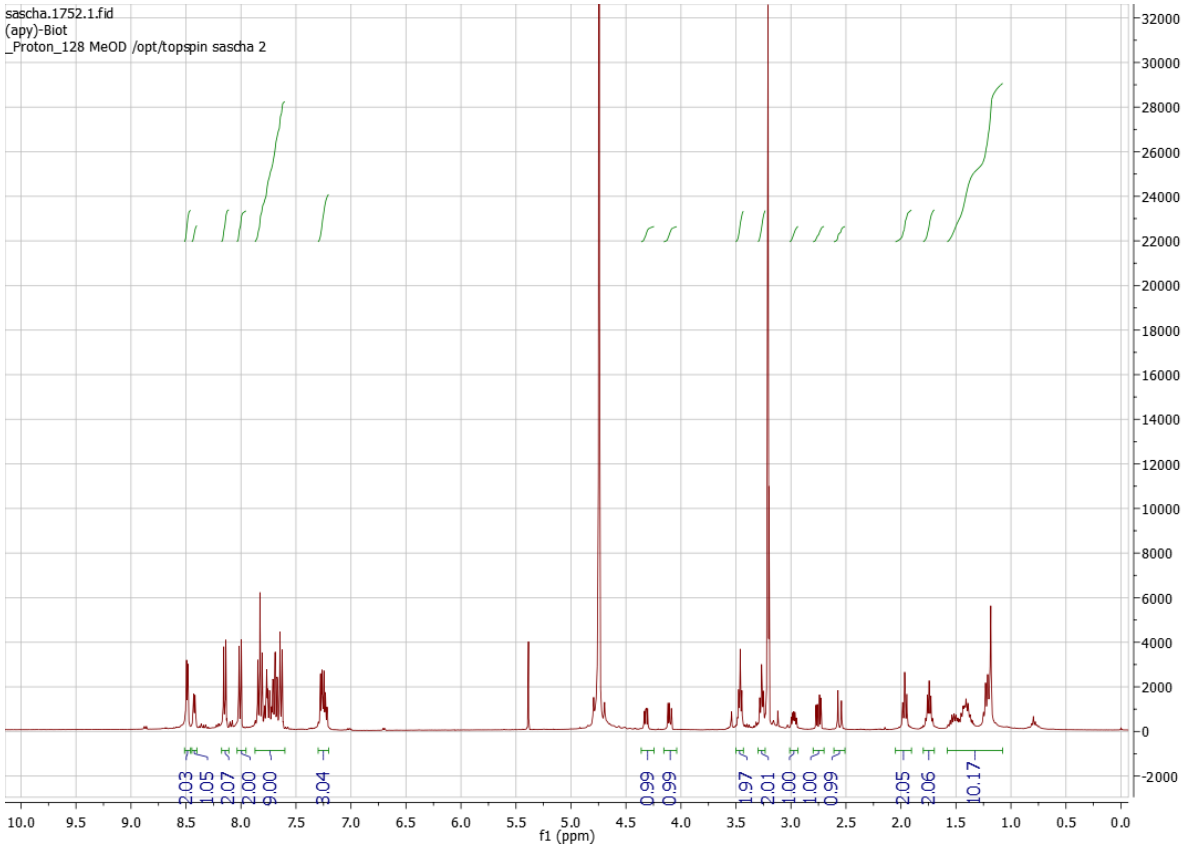


**Figure D.5:** $^1$H-NMR spectrum of **(appy)-Biot (5)** in $d_4$-Methanol.

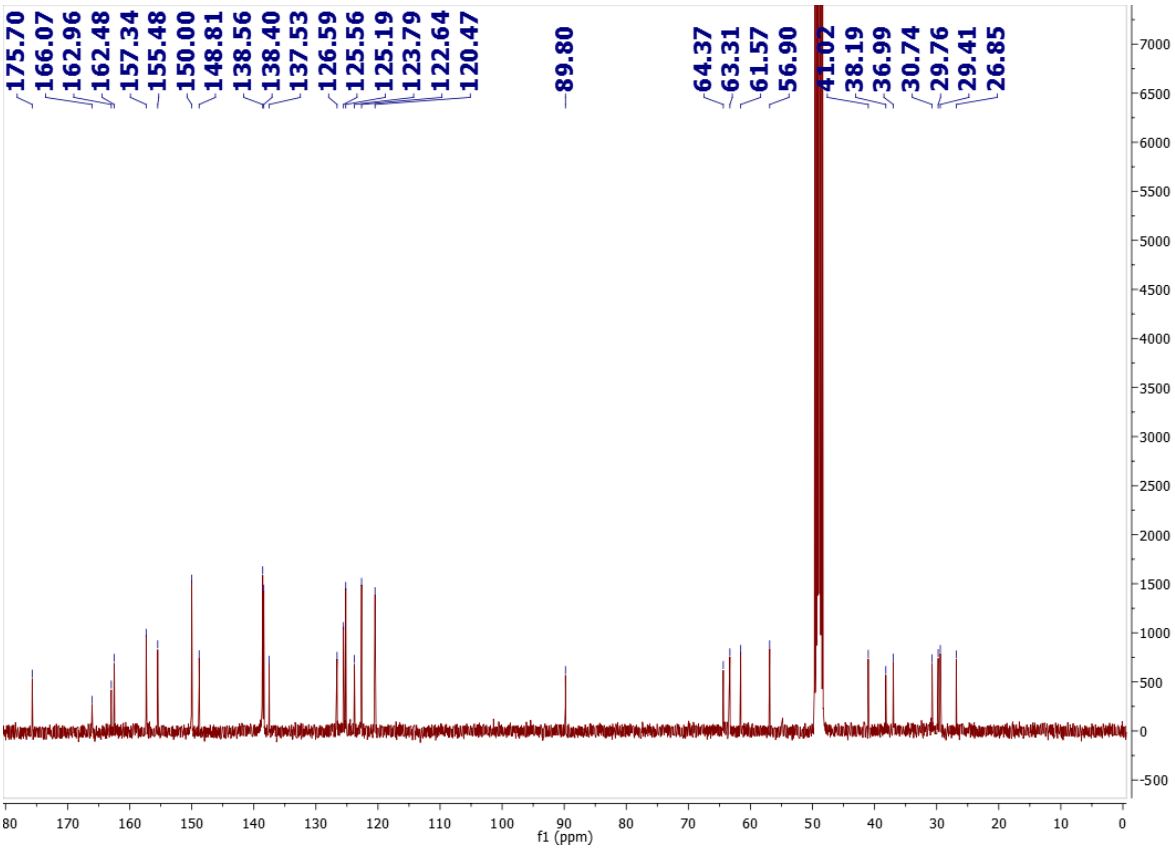


**Figure D.6:** $^{1}$H-NMR spectrum of **(appy)-Biot (5)** in $d_4$-Methanol**.**

### D.2.4 Synthesis of [CoBr(appy)-Biot]Br

The ligand **(appy)-Biot (5)** (10 mg, 0.014 mmol, 1 eq.) was dissolved in dry MeOH (2.0 ml). Then $CoBr_2 \cdot 6H_2O$ (4.66 mg, 0.014 mmol, 1 eq.) was added and left stirring for 3 h at room temperature. Afterwards, excess of $Et_2O$ was added to precipitate the product. The solid was filtered off, washed 3 times with $Et_2O$, recrystallized in MeOH and dried *in vacuo* to give [CoBr(appy)-OH]Br as light brown solid (10.6 mg, 0.011 mmol, 77%).

**HRMS** (ESI+) calcd. for $[M^+]$ $C_{39}H_{39}CoN_8O_3S$ 758.2192; found 758.2188.

## D.3 Biotin-binding activity determination[237,242]

The Sav mutants (76.8 nmol) were dissolved in $NaH_2PO_4$ buffer (2.4 ml, 20 mM, pH 7.0). The solutions were treated with a 2-(4-hydroxyphenylazo)benzoicacid (HABA) solution (300 µl, 9.6 mM) in $NaH_2PO_4$ buffer (20 mM, pH 7.0), filled into a cuvette and left standing for 5 minutes. A blank of the buffer was measured at 506 nm in a Varian50 Scan UV-Vis spectrophotometer. The resulting sample was analyzed and aliquots (5.0 µl) of a biotin (or **[CoBr(appy)-Biot]Br**) solution (0.96 mM) in $H_2O$ were added after each spectroscopic determination. The data points were plotted

with Origin Pro 9.0.0 to determine the number of biotin-binding sites and the stoichiometry for the Sav embedded triads.

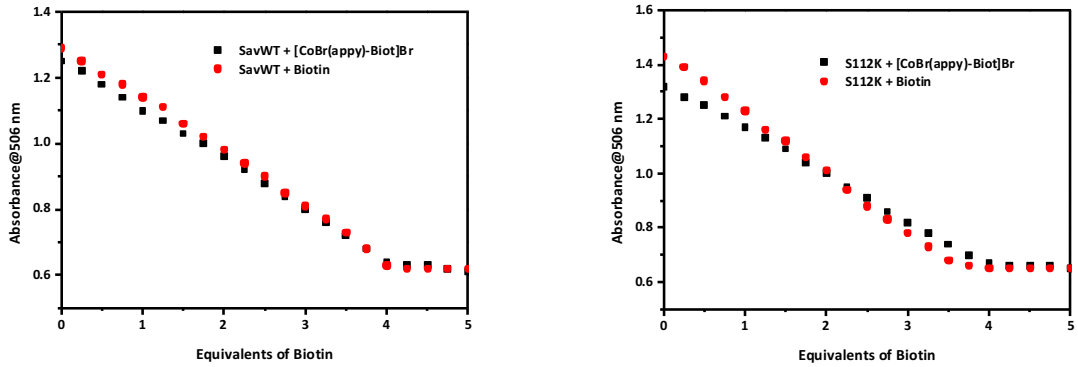


**Figure D.7:** HABA displacement titrations of [**CoBr(appy)-Biot**]**Br** (black symbols) and biotin (red symbols) with SavWT (left) and S112K (right). The biotinylated cofactors show a similar binding affinity as the native biotin.

## D.4 TON and rates

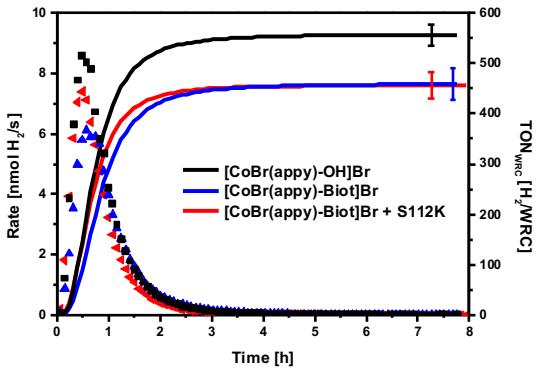


**Figure D.8:** Comparison of rates (dotted lines, left scale) and the TON of produced $H_2$ per WRC (solid lines, right scale) with 5 µM WRC, 1 M ascorbate buffer (pH 4) and 100 µM $Ru(bpy)_3^{2+}$ in each experiment and 10 µM free biotin binding sites, when protein was present. [**CoBr(appy)-OH**]**Br** (black trace), [**CoBr(appy)-Biot**]**Br** (blue trace) with additional S112K (red trace).

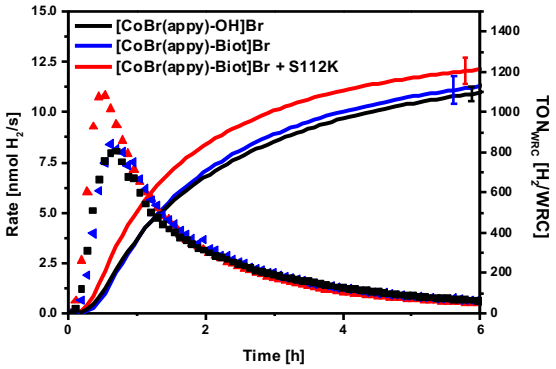


**Figure D.9:** Comparison of rates (dotted lines, left scale) and the TON of produced $H_2$ per WRC (solid lines, right scale) with 5 μM WRC, 1 M AcOH, 0.1 M AscOH (pH 5.7) and 100 μM $Ru(bpy)_3^{2+}$ in each experiment and 10 μM free biotin binding sites, when protein was present. [**CoBr(appy)-OH**]**Br** (black trace), [**CoBr(appy)-Biot**]**Br** (blue trace) with additional S112K (red trace).

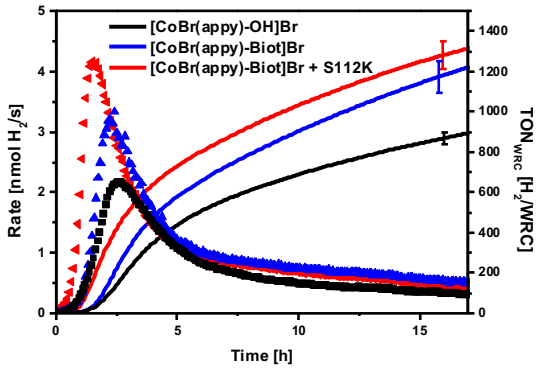


**Figure D.10:** Comparison of rates (dotted lines, left scale) and the TON of produced $H_2$ per WRC (solid lines, right scale) with 5 μM WRC, 1 M $NaHPO_4$, 0.1 M AscOH (pH 6) and 100 μM $Ru(bpy)_3^{2+}$ in each experiment and 10 μM free biotin binding sites, when protein was present. [**CoBr(appy)-OH**]**Br** (black trace), [**CoBr(appy)-Biot**]**Br** (blue trace) with additional S112K (red trace).

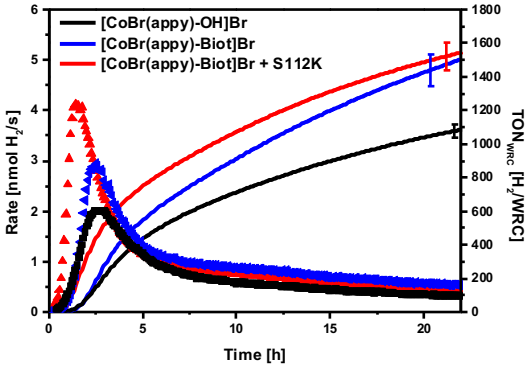


**Figure D.11:** Comparison of rates (dotted lines, left scale) and the TON of produced $H_2$ per WRC (solid lines, right scale) with 5 µM WRC, 1 M $NaHPO_4$, 0.1 M AscOH (pH 6.2) and 100 µM $Ru(bpy)_3^{2+}$ in each experiment and 10 µM free biotin binding sites, when protein was present. [**CoBr(appy)-OH**]**Br** (black trace), [**CoBr(appy)-Biot**]**Br** (blue trace) with additional S112K (red trace).

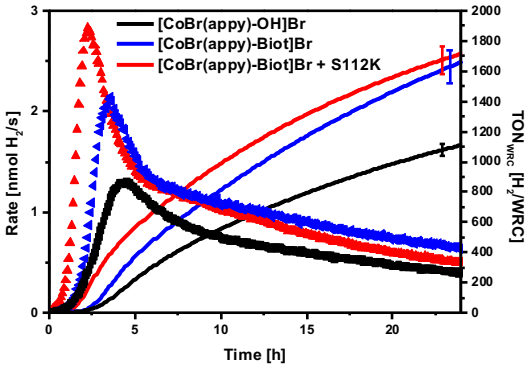


**Figure D.12:** Comparison of rates (dotted lines, left scale) and the TON of produced $H_2$ per WRC (solid lines, right scale) with 5 µM WRC, 1 M $NaHPO_4$, 0.1 M AscOH (pH 6.5) and 100 µM $Ru(bpy)_3^{2+}$ in each experiment and 10 µM free biotin binding sites, when protein was present. [**CoBr(appy)-OH**]**Br** (black trace), [**CoBr(appy)-Biot**]**Br** (blue trace) with additional S112K (red trace).

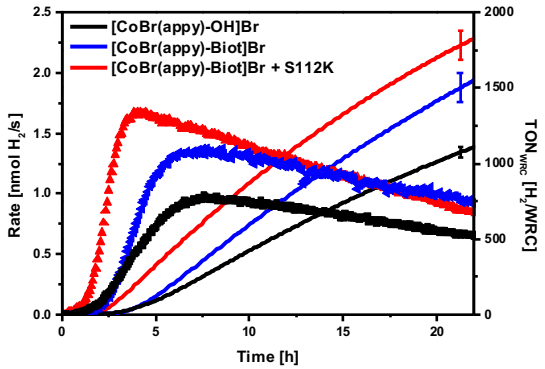


**Figure D.13:** Comparison of rates (dotted lines, left scale) and the TON of produced $H_2$ per WRC (solid lines, right scale) with 5 µM WRC, 1 M $NaHPO_4$, 0.1 M AscOH (pH 7) and 100 µM $Ru(bpy)_3^{2+}$ in each experiment and 10 µM free biotin

binding sites, when protein was present. [**CoBr(appy)-OH**]**Br** (black trace), [**CoBr(appy)-Biot**]**Br** (blue trace) with additional S112K (red trace).

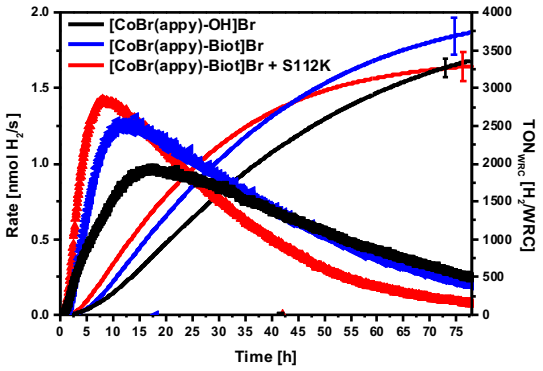


**Figure S14:** Comparison of rates (dotted lines, left scale) and the TON of produced $H_2$ per WRC (solid lines, right scale) with 5 μM WRC, 1 M $NaHPO_4$, 0.1 M AscOH (pH 7.5) and 100 μM $Ru(bpy)_3^{2+}$ in each experiment and 10 μM free biotin binding sites, when protein was present. [**CoBr(appy)-OH**]**Br** (black trace), [**CoBr(appy)-Biot**]**Br** (blue trace) with additional S112K (red trace).

**Table D.1:** Maximal rates measured, errors and the times when the maximal rates were achieved.

| pH | [**CoBr(appy)-OH**] | | [**CoBr(appy)-Biot**] | | [**CoBr(appy)-Biot**] + **SavWT** | | **CoBr(appy)-Biot**] + **K121W** | | **CoBr(appy)-Biot**] + **S112K** | |
|---|---|---|---|---|---|---|---|---|---|---|
| | Max. rate [nmol $H_2$/WRC] | t [min] | Max. rate [nmol $H_2$/WRC] | t [min] | Max. rate [nmol $H_2$/WRC] | t [min] | Max. rate [nmol $H_2$/WRC] | t [min] | Max. rate [nmol $H_2$/WRC] | t [min] |
| 4 | 8.6 ± 0.3 | 29.4 | 6.1 ± 0.4 | 34.4 | | | | | 7.4 ± 0.4 | 29.4 |
| 5 | 12.3 ± 0.7 | 39.7 | 8.6 ± 0.6 | 44.8 | 6.7 ± 0.2 | 34.6 | 4.2 ± 0.3 | 22.8 | 11.1 ± 0.6 | 40.8 |
| 5.7 | 8.0 ± 0.3 | 42.0 | 8.4 ± 0.5 | 37.0 | | | | | 10.8 ± 0.6 | 32.0 |
| 6 | 2.2 ± 0.1 | 154.0 | 3.3 ± 0.2 | 146.0 | | | | | 4.2 ± 0.2 | 89.7 |
| 6.2 | 2.0 ± 0.1 | 161.0 | 2.9 ± 0.2 | 151.0 | | | | | 4.1 ± 0.2 | 85.0 |
| 6.5 | 1.29 ± 0.04 | 246.0 | 2.1 ± 0.1 | 216.0 | | | | | 2.8 ± 0.2 | 135.0 |
| 7 | 0.98 ± 0.03 | 495.0 | 1.4 ± 0.1 | 513.0 | | | | | 1.6 ± 0.1 | 327.0 |
| 7.5 | 0.98 ± 0.03 | 1020.0 | 1.3 ± 0.1 | 645.0 | | | | | 1.4 ± 0.1 | 487.0 |

**Table D.2:** Table of maximal turnover numbers and its errors measured when the experiment was aborted (t in min).

| pH | t [min] | [**CoBr(appy)-OH**] | [**CoBr(appy)-Biot**] | [**CoBr(appy)-Biot**] + **SavWT** | **CoBr(appy)-Biot**] + **K121W** | **CoBr(appy)-Biot**] + **S112K** |
|---|---|---|---|---|---|---|
| 4 | 466 | 556 ± 21 | 458 ± 32 | | | 455 ± 27 |
| 5 | 385 | 1121 ± 61 | 1055 ± 68 | 818 ± 28 | 396 ± 26 | 1070 ± 58 |
| 5.7 | 377 | 1108 ± 38 | 1141 ± 74 | | | 1222 ± 66 |
| 6 | 1034 | 899 ± 32 | 1227 ± 80 | | | 1320 ±72 |
| 6.2 | 1324 | 1088 ± 39 | 1504 ± 98 | | | 1546 ± 84 |
| 6.5 | 1450 | 1117 ± 40 | 1668 ± 109 | | | 1722 ± 94 |
| 7 | 1332 | 1119 ± 40 | 1569 ± 103 | | | 1839 ± 100 |
| 7.5 | 4690 | 3364 ± 122 | 3742 ± 248 | | | 3294 ± 187 |

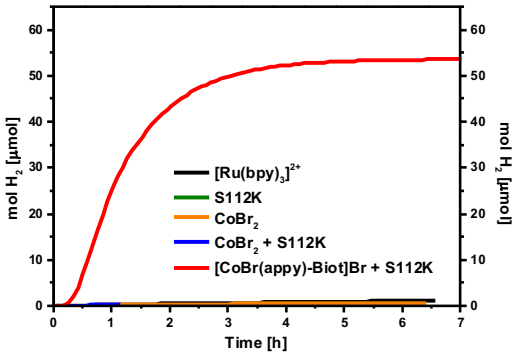


**Figure D.15:** Comparison of the produced amounts of $H_2$ in control experiments, with 1 M ascorbate buffer (pH 5) and 100 µM $Ru(bpy)_3^{2+}$ in each experiment and 5 µM Co and 10 µM free biotin binding sites, when applicable. $Ru(bpy)_3^{2+}$ only (black trace), additional S112K (green trace), $CoBr_2$ (orange trace), $CoBr_2$ and S112K (blue trace) and [**CoBr(appy)-Biot**]**Br** within S112K (red trace). No significant amounts of hydrogen were produced, when no catalyst was present.

## D.5 Crystal Structure Data

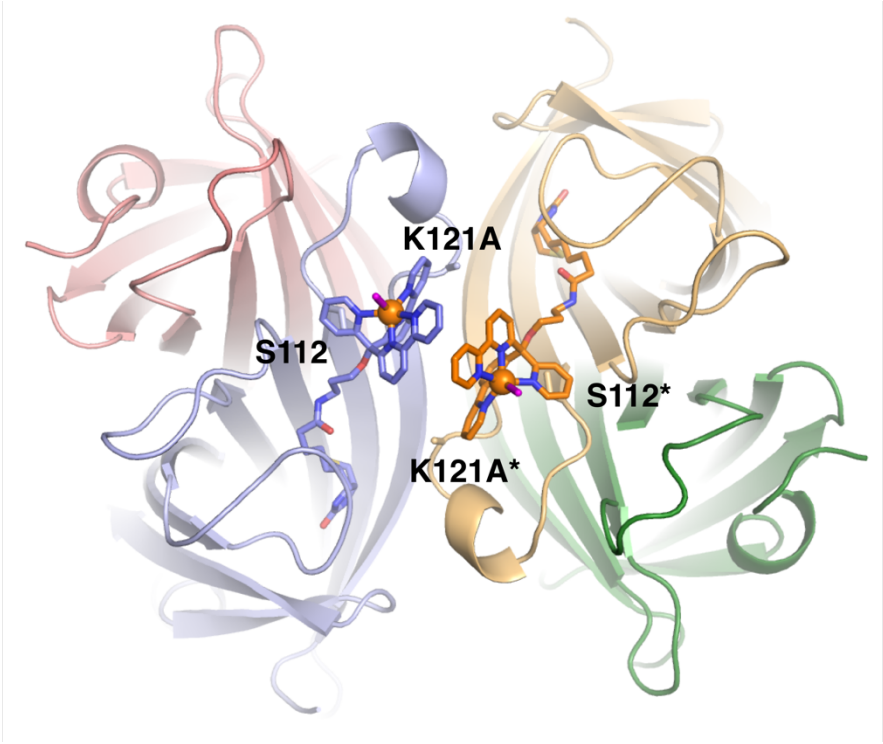


**Figure D.16:** Crystal structure of complex [**CoBr(appy)-Biot**] · **Sav-K121A**. The protein is displayed as cartoon and the cofactor as stick model. The orange sphere indicates a cobalt and the magenta stick a water molecule.

# Bibliography


[1] United Nations, *World Economic and Social Survey 2011: The Great Green Technological Transformation*, United Nations, New York, **2011**.

[2] T. R. Anderson, E. Hawkins, P. D. Jones, *Endeavour* **2016**, *40*, 178–187.

[3] H. Tian, C. Lu, P. Ciais, A. M. Michalak, J. G. Canadell, E. Saikawa, D. N. Huntzinger, K. R. Gurney, S. Sitch, B. Zhang, et al., *Nature* **2016**, *531*, 225–228.

[4] S. A. Montzka, E. J. Dlugokencky, J. H. Butler, *Nature* **2011**, *476*, 43–50.

[5] M. Perez, R. Perez, *Int. Energy Agency SHC Program. Sol. Updat.* **2015**, *62*, 4–6.

[6] T. M. I. Mahlia, T. J. Saktisahdan, A. Jannifar, M. H. Hasan, H. S. C. Matseelar, *Renew. Sustain. Energy Rev.* **2014**, *33*, 532–545.

[7] S. Rehman, L. M. Al-Hadhrami, M. M. Alam, *Renew. Sustain. Energy Rev.* **2015**, *44*, 586–598.

[8] D. Larcher, J.-M. Tarascon, *Nat. Chem.* **2014**, *7*, 19–29.

[9] United Nations, *Waste Manag. Res.* **2012**, *27*, 800–812.

[10] United Nations, *United Nations Publ.* **1999**, 1–11.

[11] C. MacFarling Meure, D. Etheridge, C. Trudinger, P. Steele, R. Langenfelds, T. van Ommen, A. Smith, J. Elkins, *Geophys. Res. Lett.* **2006**, *33*, L14810.

[12] W. Grochala, *Nat. Chem.* **2015**, *7*, 264–264.

[13] V. K. Ryabchuk, V. N. Kuznetsov, A. V. Emeline, Y. M. Artem'ev, G. V. Kataeva, S. Horikoshi, N. Serpone, *Molecules* **2016**, *21*, 1–20.

[14] V. Das, S. Padmanaban, K. Venkitusamy, R. Selvamuthukumaran, F. Blaabjerg, P. Siano, *Renew. Sustain. Energy Rev.* **2017**, *73*, 10–18.

[15] T. He, P. Pachfule, H. Wu, Q. Xu, P. Chen, *Nat. Rev. Mater.* **2016**, *1*, 16059.

[16] I. Dincer, C. Acar, *Int. J. Hydrogen Energy* **2015**, *40*, 11094–11111.

[17] D. G. Nocera, *Acc. Chem. Res.* **2017**, *50*, 616–619.

[18] S. Styring, *Faraday Discuss.* **2012**, *155*, 357–376.

[19] S. Berardi, S. Drouet, L. Francàs, C. Gimbert-Suriñach, M. Guttentag, C. Richmond, T. Stoll, A. Llobet, *Chem. Soc. Rev.* **2014**, *43*, 7501–7519.

[20] S. Fukuzumi, *Curr. Opin. Chem. Biol.* **2015**, *25*, 18–26.

[21] M. D. Kärkäs, O. Verho, E. V. Johnston, B. Åkermark, *Chem. Rev.* **2014**, *114*, 11863–12001.

[22] J. Barber, *Chem. Soc. Rev.* **2009**, *38*, 185–196.

[23] G. D. Considine, *Van Nostrand's Encyclopedia of Chemistry*, John Wiley & Sons, Inc., Hoboken, NJ, USA, **2005**.

[24] G. A. T. R. J. Press, K. S. V. Santhanam, M. J. Miri, A. V. Bailey, *Introduction to Hydrogen Technology*, John Wiley & Sons, Inc., Hoboken, NJ, USA, **2009**.

[25] S. M. M. Ehteshami, S. H. Chan, *Energy Policy* **2014**, *73*, 103–109.

[26] W. Peschka, *Liquid Hydrogen*, Springer Vienna, Vienna, Austria, **1992**.

[27] Office of Energy Efficiency & Renewable Energy, "Hydrogen Storage," can be found under https://www.energy.gov/eere/fuelcells/hydrogen-storage, **2017**.

[28] P. Parthasarathy, K. S. Narayanan, *Renew. Energy* **2014**, *66*, 570–579.

[29] T. L. LeValley, A. R. Richard, M. Fan, *Int. J. Hydrogen Energy* **2014**, *39*, 16983–17000.

[30] S. E. Hosseini, M. A. Wahid, *Renew. Sustain. Energy Rev.* **2016**, *57*, 850–866.

[31] C. Acar, I. Dincer, G. F. Naterer, *Int. J. Energy Res.* **2016**, *40*, 1449–1473.

[32] A. Iulianelli, S. Liguori, J. Wilcox, A. Basile, *Catal. Rev.* **2016**, *58*, 1–35.

[33] M. Carmo, D. L. Fritz, J. Mergel, D. Stolten, *Int. J. Hydrogen Energy* **2013**, *38*, 4901–4934.

[34] J. Barber, *Philos. Trans. R. Soc. A Math. Phys. Eng. Sci.* **2007**, *365*, 1007–1023.

[35] P. J. D. Janssen, M. D. Lambreva, N. PlumerÃ©, C. Bartolucci, A. Antonacci, K. Buonasera, R. N. Frese, V. Scognamiglio, G. Rea, *Front. Chem.* **2014**, *2*, 1–22.

[36] G. R. Fleming, G. S. Schlau-Cohen, K. Amarnath, J. Zaks, *Faraday Discuss.* **2012**, *155*, 27–41.

[37] M. A. Schöttler, S. Z. Tóth, A. Boulouis, S. Kahlau, *J. Exp. Bot.* **2015**, *66*, 2373–2400.

[38] J. Barber, *Q. Rev. Biophys.* **2003**, *36*, 71–89.

[39] M. R. Gunner, M. Amin, X. Zhu, J. Lu, *Biochim. Biophys. Acta* **2013**, *1827*, 892–913.

[40] B. B. Buchanan, *Photosynth. Res.* **2016**, *128*, 215–217.

[41] J. L. Dempsey, J. R. Winkler, H. B. Gray, *Chem. Rev.* **2010**, *110*, 7024–7039.

[42] A. R. Holzwarth, M. G. Muller, M. Reus, M. Nowaczyk, J. Sander, M. Rogner, *Proc. Natl. Acad. Sci.* **2006**, *103*, 6895–6900.

[43] D. R. Weinberg, C. J. Gagliardi, J. F. Hull, C. F. Murphy, C. A. Kent, B. C. Westlake, A. Paul,

D. H. Ess, D. G. McCafferty, T. J. Meyer, *Chem. Rev.* **2012**, *112*, 4016–4093.

[44] S. Chu, A. Majumdar, *Nature* **2012**, *488*, 294–303.

[45] G. F. Swiegers, D. R. MacFarlane, D. L. Officer, A. Ballantyne, D. Boskovic, J. Chen, G. C. Dismukes, G. P. Gardner, R. K. Hocking, P. F. Smith, et al., *Aust. J. Chem.* **2012**, *65*, 577.

[46] T. R. Cook, D. K. Dogutan, S. Y. Reece, Y. Surendranath, T. S. Teets, D. G. Nocera, *Chem. Rev.* **2010**, *110*, 6474–6502.

[47] V. Balzani, A. Credi, M. Venturi, *ChemSusChem* **2008**, *1*, 26–58.

[48] S. Y. Reece, J. A. Hamel, K. Sung, T. D. Jarvi, A. J. Esswein, J. J. H. Pijpers, D. G. Nocera, *Science* **2011**, *334*, 645–648.

[49] F. F. Abdi, L. Han, A. H. M. Smets, M. Zeman, B. Dam, R. van de Krol, *Nat. Commun.* **2013**, *4*, 1–7.

[50] A. J. Cowan, J. R. Durrant, *Chem. Soc. Rev.* **2013**, *42*, 2281–2293.

[51] J. Luo, J.-H. Im, M. T. Mayer, M. Schreier, M. K. Nazeeruddin, N.-G. Park, S. D. Tilley, H. J. Fan, M. Gratzel, *Science* **2014**, *345*, 1593–1596.

[52] M. G. Walter, E. L. Warren, J. R. McKone, S. W. Boettcher, Q. Mi, E. A. Santori, N. S. Lewis, *Chem. Rev.* **2010**, *110*, 6446–6473.

[53] E. A. Gibson, *Chem. Soc. Rev.* **2017**, *46*, 6194–6209.

[54] T. S. Teets, D. G. Nocera, *Chem. Commun.* **2011**, *47*, 9268.

[55] W. T. Eckenhoff, R. Eisenberg, *Dalt. Trans.* **2012**, *41*, 13004.

[56] D. G. H. Hetterscheid, J. N. H. Reek, *Angew. Chemie Int. Ed.* **2012**, *51*, 9740–9747.

[57] M. Nippe, R. S. Khnayzer, J. A. Panetier, D. Z. Zee, B. S. Olaiya, M. Head-Gordon, C. J. Chang, F. N. Castellano, J. R. Long, *Chem. Sci.* **2013**, *4*, 3934–3945.

[58] W. T. Eckenhoff, W. R. McNamara, P. Du, R. Eisenberg, *Biochim. Biophys. Acta - Bioenerg.* **2013**, *1827*, 958–973.

[59] V. Artero, M. Chavarot-Kerlidou, M. Fontecave, *Angew. Chemie Int. Ed.* **2011**, *50*, 7238–7266.

[60] B. Probst, A. Rodenberg, M. Guttentag, P. Hamm, R. Alberto, *Inorg. Chem.* **2010**, *49*, 6453–6460.

[61] J. D. Blakemore, R. H. Crabtree, G. W. Brudvig, *Chem. Rev.* **2015**, *115*, 12974–13005.

[62] Y. Pellegrin, F. Odobel, *Comptes Rendus Chim.* **2017**, *20*, 283–295.

[63] J. C. Deutsch, *J. Chromatogr. A* **2000**, *881*, 299–307.

[64] R. E. Hughes, *Nature* **1964**, *203*, 1068–1069.

[65] M. Guttentag, A. Rodenberg, R. Kopelent, B. Probst, C. Buchwalder, M. Brandstätter, P. Hamm, R. Alberto, *Eur. J. Inorg. Chem.* **2012**, *2012*, 59–64.

[66] V. Artero, J.-M. Saveant, *Energy Environ. Sci.* **2014**, *7*, 3808–3814.

[67] J. F. Yin, M. Velayudham, D. Bhattacharya, H. C. Lin, K. L. Lu, *Coord. Chem. Rev.* **2012**, *256*, 3008–3035.

[68] Y. Qin, Q. Peng, *Int. J. Photoenergy* **2012**, *2012*, 1–21.

[69] P. Chowdhury, G. Malekshoar, A. Ray, *Inorganics* **2017**, *5*, 34.

[70] V. Srivastava, P. P. Singh, *RSC Adv.* **2017**, *7*, 31377–31392.

[71] S. Garakyaraghi, P. Koutnik, F. N. Castellano, *Phys. Chem. Chem. Phys.* **2017**, *19*, 16662–16668.

[72] S.-P. Luo, E. Mejía, A. Friedrich, A. Pazidis, H. Junge, A.-E. Surkus, R. Jackstell, S. Denurra, S. Gladiali, S. Lochbrunner, et al., *Angew. Chemie Int. Ed.* **2013**, *52*, 419–423.

[73] M. Heberle, S. Tschierlei, N. Rockstroh, M. Ringenberg, W. Frey, H. Junge, M. Beller, S. Lochbrunner, M. Karnahl, *Chem. - A Eur. J.* **2017**, *23*, 312–319.

[74] S.-P. Luo, N.-Y. Chen, Y.-Y. Sun, L.-M. Xia, Z.-C. Wu, H. Junge, M. Beller, Q.-A. Wu, *Dye. Pigment.* **2016**, *134*, 580–585.

[75] J. Windisch, M. Orazietti, P. Hamm, R. Alberto, B. Probst, *ChemSusChem* **2016**, *9*, 1719–1726.

[76] A. Frei, R. Rubbiani, S. Tubafard, O. Blacque, P. Anstaett, A. Felgenträger, T. Maisch, L. Spiccia, G. Gasser, *J. Med. Chem.* **2014**, *57*, 7280–7292.

[77] K. Kalyanasundaram, *Coord. Chem. Rev.* **1982**, *46*, 159–244.

[78] J. H. M. Ortiz, N. Vega, D. Comedi, M. Tirado, I. Romero, X. Fontrodona, T. Parella, F. E. M. Vieyra, C. D. Borsarelli, N. E. Katz, *Inorg. Chem.* **2013**, *52*, 4950–4962.

[79] A. W. Adamson, J. N. Demas, *J. Am. Chem. Soc.* **1971**, *93*, 1800–1801.

[80] H. D. Gafney, A. W. Adamson, *J. Am. Chem. Soc.* **1972**, *94*, 8238–8239.

[81] C. B. Kelly, N. R. Patel, D. N. Primer, M. Jouffroy, J. C. Tellis, G. A. Molander, *Nat. Protoc.* **2017**, *12*, 472–492.

[82] J. M. R. Narayanam, C. R. J. Stephenson, *Chem. Soc. Rev.* **2011**, *40*, 102–113.

[83] J. Xuan, W.-J. Xiao, *Angew. Chemie Int. Ed.* **2012**, *51*, 6828–6838.

[84] C. K. Prier, D. A. Rankic, D. W. C. MacMillan, *Chem. Rev.* **2013**, *113*, 5322–5363.

[85] Y. Xi, H. Yi, A. Lei, *Org. Biomol. Chem.* **2013**, *11*, 2387.

[86] A. Juris, V. Balzani, F. Barigelletti, S. Campagna, P. Belser, A. von Zelewsky, *Coord. Chem. Rev.*

**1988**, *84*, 85–277.

[87] S. Campagna, F. Puntoriero, F. Nastasi, G. Bergamini, V. Balzani, in *Photochem. Photophysics Coord. Compd. I*, Springer Berlin Heidelberg, Berlin, Heidelberg, **2007**, pp. 117–214.

[88] J. P. Sauvage, J. P. Collin, J. C. Chambron, S. Guillerez, C. Coudret, V. Balzani, F. Barigelletti, L. De Cola, L. Flamigni, *Chem. Rev.* **1994**, *94*, 993–1019.

[89] D. W. Thompson, A. Ito, T. J. Meyer, *Pure Appl. Chem.* **2013**, *85*, 1257–1305.

[90] P. M. Vignais, B. Billoud, J. Meyer, *FEMS Microbiol. Rev.* **2001**, *25*, 455–501.

[91] P. M. Vignais, B. Billoud, *Chem. Rev.* **2007**, *107*, 4206–4272.

[92] W. Lubitz, H. Ogata, O. Rüdiger, E. Reijerse, *Chem. Rev.* **2014**, *114*, 4081–4148.

[93] A. I. Krasna, *Enzyme Microb. Technol.* **1979**, *1*, 165–172.

[94] R. K. Thauer, A.-K. Kaster, M. Goenrich, M. Schick, T. Hiromoto, S. Shima, *Annu. Rev. Biochem.* **2010**, *79*, 507–536.

[95] P. Tamagnini, E. Leitão, P. Oliveira, D. Ferreira, F. Pinto, D. J. Harris, T. Heidorn, P. Lindblad, *FEMS Microbiol. Rev.* **2007**, *31*, 692–720.

[96] P. Tamagnini, R. Axelsson, P. Lindberg, F. Oxelfelt, R. Wunschiers, P. Lindblad, *Microbiol. Mol. Biol. Rev.* **2002**, *66*, 1–20.

[97] J. C. Fontecilla-Camps, A. Volbeda, C. Cavazza, Y. Nicolet, *Chem. Rev.* **2007**, *107*, 4273–4303.

[98] J. C. Fontecilla-Camps, P. Amara, C. Cavazza, Y. Nicolet, A. Volbeda, *Nature* **2009**, *460*, 814–822.

[99] C. Afting, E. Kremmer, C. Brucker, A. Hochheimer, R. K. Thauer, *Arch. Microbiol.* **2000**, *174*, 225–232.

[100] R. K. Thauer, A. R. Klein, G. C. Hartmann, *Chem. Rev.* **1996**, *96*, 3031–3042.

[101] E. J. Lyon, S. Shima, R. Boecher, R. K. Thauer, F.-W. Grevels, E. Bill, W. Roseboom, S. P. J. Albracht, *J. Am. Chem. Soc.* **2004**, *126*, 14239–14248.

[102] M. Salomone-Stagni, F. Stellato, C. M. Whaley, S. Vogt, S. Morante, S. Shima, T. B. Rauchfuss, W. Meyer-Klaucke, *Dalt. Trans.* **2010**, *39*, 3057.

[103] Y. Nicolet, C. Cavazza, J. C. Fontecilla-Camps, *J. Inorg. Biochem.* **2002**, *91*, 1–8.

[104] T. Hiromoto, E. Warkentin, J. Moll, U. Ermler, S. Shima, *Angew. Chemie Int. Ed.* **2009**, *48*, 6457–6460.

[105] S. Vogt, E. J. Lyon, S. Shima, R. K. Thauer, *JBIC J. Biol. Inorg. Chem.* **2007**, *13*, 97–106.

[106] R. P. Happe, W. Roseboom, A. J. Plerlk, S. P. J. Albracht, K. A. Bagley, *Nature* **1997**, *385*, 126.

[107] M. Winkler, M. Senger, J. Duan, J. Esselborn, F. Wittkamp, E. Hofmann, U.-P. Apfel, S. T. Stripp, T. Happe, *Nat. Commun.* **2017**, *8*, 16115.

[108] A. Volbeda, E. Garcin, C. Piras, A. L. de Lacey, V. M. Fernandez, E. C. Hatchikian, M. Frey, J. C. Fontecilla-Camps, *J. Am. Chem. Soc.* **1996**, *118*, 12989–12996.

[109] Ö. F. Erdem, M. Stein, S. Kaur-Ghumaan, E. J. Reijerse, S. Ott, W. Lubitz, *Chem. - A Eur. J.* **2013**, *19*, 14566–14572.

[110] Ö. F. Erdem, L. Schwartz, M. Stein, A. Silakov, S. Kaur-Ghumaan, P. Huang, S. Ott, E. J. Reijerse, W. Lubitz, *Angew. Chemie Int. Ed.* **2011**, *50*, 1439–1443.

[111] G. Editor, D. Goldfarb, D. Sezer, M. J. Prandolini, T. F. Prisner, P. Chem, R. Z. Sagdeev, G. Klihm, E. Reijerse, W. Lubitz, et al., *Phys. Chem. Chem. Phys.* **2009**, *11*, 6553.

[112] J. Y. Yang, R. M. Bullock, M. R. DuBois, D. L. DuBois, *MRS Bull.* **2011**, *36*, 39–47.

[113] H. Ogata, S. Hirota, A. Nakahara, H. Komori, N. Shibata, T. Kato, K. Kano, Y. Higuchi, *Structure* **2005**, *13*, 1635–1642.

[114] Y. Nicolet, C. Piras, P. Legrand, C. E. Hatchikian, J. C. Fontecilla-Camps, *Structure* **1999**, *7*, 13–23.

[115] L.-F. Wu, M. A. Mandrand, *FEMS Microbiol. Lett.* **1993**, *104*, 243–269.

[116] T. R. Simmons, G. Berggren, M. Bacchi, M. Fontecave, V. Artero, *Coord. Chem. Rev.* **2014**, *270–271*, 127–150.

[117] R. Cammack, *Nature* **1999**, *397*, 214–215.

[118] C. Lambertz, N. Leidel, K. G. V Havelius, J. Noth, P. Chernev, M. Winkler, T. Happe, M. Haumann, *J. Biol. Chem.* **2011**, *286*, 40614–40623.

[119] S. T. Stripp, G. Goldet, C. Brandmayr, O. Sanganas, K. A. Vincent, M. Haumann, F. A. Armstrong, T. Happe, *Proc. Natl. Acad. Sci.* **2009**, *106*, 17331–17336.

[120] S. Shima, O. Pilak, S. Vogt, M. Schick, M. S. Stagni, W. Meyer-Klaucke, E. Warkentin, R. K. Thauer, U. Ermler, *Science* **2008**, *321*, 572–575.

[121] J. W. Peters, *Science* **1998**, *282*, 1853–1858.

[122] A. Volbeda, M.-H. Charon, C. Piras, E. C. Hatchikian, M. Frey, J. C. Fontecilla-Camps, *Nature* **1995**, *373*, 580–587.

[123] F. Gloaguen, T. B. Rauchfuss, *Chem. Soc. Rev.* **2009**, *38*, 100–108.

[124] C. Tard, C. J. Pickett, *Chem. Rev.* **2009**, *109*, 2245–2274.

[125] X. Liu, S. Ibrahim, C. Tard, C. Pickett, *Coord. Chem. Rev.* **2005**, *249*, 1641–1652.

[126] J. Capon, F. Gloaguen, P. Schollhammer, J. Talarmin, *Coord. Chem. Rev.* **2005**, *249*, 1664–

1676.

[127] F. Gloaguen, J. D. Lawrence, T. B. Rauchfuss, *J. Am. Chem. Soc.* **2001**, *123*, 9476–9477.

[128] J.-F. Capon, F. Gloaguen, F. Y. Pétillon, P. Schollhammer, J. Talarmin, *Coord. Chem. Rev.* **2009**, *253*, 1476–1494.

[129] M. Y. Darensbourg, E. J. Lyon, X. Zhao, I. P. Georgakaki, *Proc. Natl. Acad. Sci.* **2003**, *100*, 3683–3688.

[130] Q. Wang, J. E. Barclay, A. J. Blake, E. S. Davies, D. J. Evans, A. C. Marr, E. J. L. McInnes, J. McMaster, C. Wilson, M. Schröder, *Chem. - A Eur. J.* **2004**, *10*, 3384–3396.

[131] A. Perra, E. S. Davies, J. R. Hyde, Q. Wang, J. McMaster, M. Schröder, *Chem. Commun.* **2006**, *44*, 1103.

[132] S. Ogo, R. Kabe, K. Uehara, B. Kure, T. Nishimura, S. C. Menon, R. Harada, S. Fukuzumi, Y. Higuchi, T. Ohhara, et al., *Science* **2007**, *316*, 585–587.

[133] B. Kure, T. Matsumoto, K. Ichikawa, S. Fukuzumi, Y. Higuchi, T. Yagi, S. Ogo, *Dalt. Trans.* **2008**, *37*, 4747.

[134] S. Canaguier, L. Vaccaro, V. Artero, R. Ostermann, J. Pécaut, M. J. Field, M. Fontecave, *Chem. - A Eur. J.* **2009**, *15*, 9350–9364.

[135] Y. Oudart, V. Artero, L. Norel, C. Train, J. Pécaut, M. Fontecave, *J. Organomet. Chem.* **2009**, *694*, 2866–2869.

[136] Y. Oudart, V. Artero, J. Pécaut, M. Fontecave, *Inorg. Chem.* **2006**, *45*, 4334–4336.

[137] P. D. Tran, V. Artero, M. Fontecave, *Energy Environ. Sci.* **2010**, *3*, 727.

[138] S. Canaguier, V. Artero, M. Fontecave, *Dalt. Trans.* **2008**, 315–325.

[139] B. E. Barton, C. M. Whaley, T. B. Rauchfuss, D. L. Gray, *J. Am. Chem. Soc.* **2009**, *131*, 6942–6943.

[140] S. Canaguier, M. Field, Y. Oudart, J. Pécaut, M. Fontecave, V. Artero, *Chem. Commun.* **2010**, *46*, 5876.

[141] S. Losse, J. G. Vos, S. Rau, *Coord. Chem. Rev.* **2010**, *254*, 2492–2504.

[142] J. L. Dempsey, B. S. Brunschwig, J. R. Winkler, H. B. Gray, *Acc. Chem. Res.* **2009**, *42*, 1995–2004.

[143] P.-A. Jacques, V. Artero, J. Pecaut, M. Fontecave, *Proc. Natl. Acad. Sci.* **2009**, *106*, 20627–20632.

[144] N. Queyriaux, R. T. Jane, J. Massin, V. Artero, M. Chavarot-Kerlidou, *Coord. Chem. Rev.* **2015**, *304–305*, 3–19.

[145] C. Bachmann, M. Guttentag, B. Spingler, R. Alberto, *Inorg. Chem.* **2013**, *52*, 6055–6061.

[146] M. L. Helm, M. P. Stewart, R. M. Bullock, M. R. DuBois, D. L. DuBois, *Science* **2011**, *333*, 863–866.

[147] Z. Han, L. Shen, W. W. Brennessel, P. L. Holland, R. Eisenberg, *J. Am. Chem. Soc.* **2013**, *135*, 14659–14669.

[148] N. P. Boralugodage, R. J. Arachchige, A. Dutta, G. W. Buchko, W. J. Shaw, *Catal. Sci. Technol.* **2017**, *7*, 1108–1121.

[149] H. I. Karunadasa, C. J. Chang, J. R. Long, *Nature* **2010**, *464*, 1329–1333.

[150] W. T. Eckenhoff, W. W. Brennessel, R. Eisenberg, *Inorg. Chem.* **2014**, *53*, 9860–9869.

[151] A. D. Wilson, R. K. Shoemaker, A. Miedaner, J. T. Muckerman, D. L. DuBois, M. R. DuBois, *Proc. Natl. Acad. Sci.* **2007**, *104*, 6951–6956.

[152] K. Fraze, A. D. Wilson, A. M. Appel, M. Rakowski DuBois, D. L. DuBois, *Organometallics* **2007**, *26*, 3918–3924.

[153] A. D. Wilson, R. H. Newell, M. J. McNevin, J. T. Muckerman, M. Rakowski DuBois, D. L. DuBois, M. R. DuBois, D. L. DuBois, *J. Am. Chem. Soc.* **2006**, *128*, 358–366.

[154] J. Y. Yang, R. M. Bullock, W. J. Shaw, B. Twamley, K. Fraze, M. R. DuBois, D. L. DuBois, *J. Am. Chem. Soc.* **2009**, *131*, 5935–5945.

[155] N. Priyadarshani, A. Dutta, B. Ginovska, G. W. Buchko, M. O'Hagan, S. Raugei, W. J. Shaw, *ACS Catal.* **2016**, *6*, 6037–6049.

[156] T. K. Hyster, L. Knörr, T. R. Ward, T. Rovis, *Science* **2012**, *338*, 500–503.

[157] M.-H. Ho, M. O'Hagan, M. Dupuis, D. L. DuBois, R. M. Bullock, W. J. Shaw, S. Raugei, *Dalt. Trans.* **2015**, *44*, 10969–10979.

[158] C. Bachmann, B. Probst, M. Guttentag, R. Alberto, *Chem. Commun.* **2014**, *50*, 6737–6739.

[159] F. Schwizer, Y. Okamoto, T. Heinisch, Y. Gu, M. M. Pellizzoni, V. Lebrun, R. Reuter, V. Köhler, J. C. Lewis, T. R. Ward, *Chem. Rev.* **2018**, *118*, 142–231.

[160] M. E. Wilson, G. M. Whitesides, *J. Am. Chem. Soc.* **1978**, *100*, 306–307.

[161] K. Yamamura, E. T. Kaiser, *J. Chem. Soc. Chem. Commun.* **1976**, 830.

[162] T. Heinisch, T. R. Ward, *Eur. J. Inorg. Chem.* **2015**, *2015*, 3406–3418.

[163] K. A. Powell, S. W. Ramer, S. B. del Cardayré, W. P. C. Stemmer, M. B. Tobin, P. F. Longchamp, G. W. Huisman, *Angew. Chemie Int. Ed.* **2001**, *40*, 3948.

[164] J. D. Bloom, F. H. Arnold, *Proc. Natl. Acad. Sci.* **2009**, *106*, 9995–10000.

[165] M. T. Reetz, *J. Am. Chem. Soc.* **2013**, *135*, 12480–12496.

[166] C. K. Savile, J. M. Janey, E. C. Mundorff, J. C. Moore, S. Tam, W. R. Jarvis, J. C. Colbeck, A. Krebber, F. J. Fleitz, J. Brands, et al., *Science* **2010**, *329*, 305–309.

[167] N. Stephanopoulos, M. B. Francis, *Nat. Chem. Biol.* **2011**, *7*, 876–884.

[168] M. Raynal, P. Ballester, A. Vidal-Ferran, P. W. N. M. van Leeuwen, *Chem. Soc. Rev.* **2014**, *43*, 1734–1787.

[169] O. Boutureira, G. J. L. Bernardes, *Chem. Rev.* **2015**, *115*, 2174–2195.

[170] C. B. Rosen, M. B. Francis, *Nat. Chem. Biol.* **2017**, *13*, 697–705.

[171] J. M. Zimbron, T. Heinisch, M. Schmid, D. Hamels, E. S. Nogueira, T. Schirmer, T. R. Ward, *J. Am. Chem. Soc.* **2013**, *135*, 5384–5388.

[172] Q. Jing, K. Okrasa, R. J. Kazlauskas, in *Top Organomet Chem*, **2008**, pp. 11533–11542.

[173] P. S. Coelho, E. M. Brustad, A. Kannan, F. H. Arnold, *Science* **2013**, *339*, 307–310.

[174] H. Renata, Z. J. Wang, F. H. Arnold, *Angew. Chemie Int. Ed.* **2015**, *54*, 3351–3367.

[175] M. Bordeaux, V. Tyagi, R. Fasan, *Angew. Chemie Int. Ed.* **2015**, *54*, 1744–1748.

[176] P. Weber, D. Ohlendorf, J. Wendoloski, F. Salemme, *Science* **1989**, *243*, 85–88.

[177] N. M. Green, in *Adv. Protein Chem.*, **1975**, pp. 85–133.

[178] M. Wilchek, E. A. Bayer, *Avidin-Biotin Technology*, Academic Press, INC., San Diego, **1990**.

[179] A. Loosli, U. E. Rusbandi, J. Gradinaru, K. Bernauer, C. W. Schlaepfer, M. Meyer, S. Mazurek, M. Novic, T. R. Ward, *Inorg. Chem.* **2006**, *45*, 660–668.

[180] M. W. Pandori, *J. Biol. Chem.* **1995**, *270*, 28204–28209.

[181] M. González, L. A. Bagatolli, I. Echabe, J. L. R. Arrondo, C. E. Argaraña, C. R. Cantor, G. D. Fidelio, *J. Biol. Chem.* **1997**, *272*, 11288–11294.

[182] T. Sano, C. R. Cantor, *Proc. Natl. Acad. Sci.* **1990**, *87*, 142–146.

[183] M. Jeschek, M. O. Bahls, V. Schneider, P. Marlière, T. R. Ward, S. Panke, *Metab. Eng.* **2017**, *40*, 33–40.

[184] A. Zocchi, A. Marya Jobé, J.-M. Neuhaus, T. R. Ward, *Protein Expr. Purif.* **2003**, *32*, 167–174.

[185] M. Dürrenberger, T. Heinisch, Y. M. Wilson, T. Rossel, E. Nogueira, L. Knörr, A. Mutschler, K. Kersten, M. J. Zimbron, J. Pierron, et al., *Angew. Chemie Int. Ed.* **2011**, *50*, 3026–3029.

[186] Y. Eisenberg-Domovich, Y. Pazy, O. Nir, B. Raboy, E. a Bayer, M. Wilchek, O. Livnah, *Proc. Natl. Acad. Sci.* **2004**, *101*, 5916–5921.

[187] O. Livnah, E. a Bayer, M. Wilchek, J. L. Sussman, *Proc. Natl. Acad. Sci.* **1993**, *90*, 5076–5080.

[188] D. M. Mock, *J. Nutr.* **2017**, *147*, 1487–1492.

[189] W. Liu, S. K. Samanta, B. D. Smith, L. Isaacs, *Chem. Soc. Rev.* **2017**, *46*, 2391–2403.

[190] J. Steinreiber, T. R. Ward, in *Top. Organomet. Chem.*, **2009**, pp. 93–112.

[191] C. Lo, M. R. Ringenberg, D. Gnandt, Y. Wilson, T. R. Ward, *Chem. Commun.* **2011**, *47*, 12065.

[192] A. Pordea, M. Creus, J. Panek, C. Duboc, D. Mathis, M. Novic, T. R. Ward, *J. Am. Chem. Soc.* **2008**, *130*, 8085–8088.

[193] V. Köhler, J. Mao, T. Heinisch, A. Pordea, A. Sardo, Y. M. Wilson, L. Knörr, M. Creus, J.-C. Prost, T. Schirmer, et al., *Angew. Chemie Int. Ed.* **2011**, *50*, 10863–10866.

[194] J. Pierron, C. Malan, M. Creus, J. Gradinaru, I. Hafner, A. Ivanova, A. Sardo, T. R. Ward, *Angew. Chemie Int. Ed.* **2008**, *47*, 701–705.

[195] A. Chatterjee, H. Mallin, J. Klehr, J. Vallapurackal, A. D. Finke, L. Vera, M. Marsh, T. R. Ward, *Chem. Sci.* **2016**, *7*, 673–677.

[196] T. K. Hyster, L. Knörr, T. R. Ward, T. Rovis, *Science* **2012**, *338*, 500–503.

[197] C. Letondor, A. Pordea, N. Humbert, A. Ivanova, S. Mazurek, M. Novic, T. R. Ward, *J. Am. Chem. Soc.* **2006**, *128*, 8320–8328.

[198] J. W. Slater, H. S. Shafaat, *J. Phys. Chem. Lett.* **2015**, *6*, 3731–3736.

[199] A. Roy, I. Sarrou, M. D. Vaughn, A. V. Astashkin, G. Ghirlanda, *Biochemistry* **2013**, *52*, 7586–7594.

[200] V. Artero, G. Berggren, M. Atta, G. Caserta, S. Roy, L. Pecqueur, M. Fontecave, *Acc. Chem. Res.* **2015**, *48*, 2380–2387.

[201] L. M. Utschig, S. R. Soltau, D. M. Tiede, *Curr. Opin. Chem. Biol.* **2015**, *25*, 1–8.

[202] G. Caserta, S. Roy, M. Atta, V. Artero, M. Fontecave, *Curr. Opin. Chem. Biol.* **2015**, *25*, 36–47.

[203] Y. Sano, A. Onoda, T. Hayashi, *Chem. Commun.* **2011**, *47*, 8229.

[204] G. Berggren, A. Adamska, C. Lambertz, T. R. Simmons, J. Esselborn, M. Atta, S. Gambarelli, J.-M. Mouesca, E. Reijerse, W. Lubitz, et al., *Nature* **2013**, *499*, 66–69.

[205] G. Berggren, A. Adamska, C. Lambertz, T. R. Simmons, J. Esselborn, M. Atta, S. Gambarelli, J.-M. Mouesca, E. Reijerse, W. Lubitz, et al., *Nature* **2013**, *499*, 66–69.

[206] D. Chen, A. Ahrens-Botzong, V. Schünemann, R. Scopelliti, X. Hu, *Inorg. Chem.* **2011**, *50*, 5249–5257.

[207] J. F. Siebel, A. Adamska-Venkatesh, K. Weber, S. Rumpel, E. Reijerse, W. Lubitz, *Biochemistry* **2015**, *54*, 1474–1483.

[208] Y. Sano, A. Onoda, T. Hayashi, *J. Inorg. Biochem.* **2012**, *108*, 159–162.

[209] B. Kandemir, S. Chakraborty, Y. Guo, K. L. Bren, *Inorg. Chem.* **2016**, *55*, 467–477.

[210] M. Bacchi, G. Berggren, J. Niklas, E. Veinberg, M. W. Mara, M. L. Shelby, O. G. Poluektov, L. X. Chen, D. M. Tiede, C. Cavazza, et al., *Inorg. Chem.* **2014**, *53*, 8071–8082.

[211] L. M. Utschig, S. C. Silver, K. L. Mulfort, D. M. Tiede, *J. Am. Chem. Soc.* **2011**, *133*, 16334–16337.

[212] S. C. Silver, J. Niklas, P. Du, O. G. Poluektov, D. M. Tiede, L. M. Utschig, *J. Am. Chem. Soc.* **2013**, *135*, 13246–13249.

[213] N. M. Marshall, D. K. Garner, T. D. Wilson, Y.-G. Gao, H. Robinson, M. J. Nilges, Y. Lu, *Nature* **2009**, *462*, 113–116.

[214] R. Williams, R. S. Crandall, A. Bloom, R. Williams, R. S. Crandall, A. Bloom, *Appl. Phys. Lett.* **1978**, *381*, 33–36.

[215] G. Laurenczy, *Chim. Int. J. Chem.* **2011**, *65*, 663–666.

[216] M. Grasemann, G. Laurenczy, *Energy Environ. Sci.* **2012**, *5*, 8171.

[217] S. Enthaler, J. von Langermann, T. Schmidt, *Energy Environ. Sci.* **2010**, *3*, 1207.

[218] A. F. Dalebrook, W. Gan, M. Grasemann, S. Moret, G. Laurenczy, *Chem. Commun.* **2013**, *49*, 8735.

[219] A. Boddien, C. Federsel, P. Sponholz, D. Mellmann, R. Jackstell, H. Junge, G. Laurenczy, M. Beller, *Energy Environ. Sci.* **2012**, *5*, 8907.

[220] B. Loges, A. Boddien, H. Junge, M. Beller, *Angew. Chemie - Int. Ed.* **2008**, *47*, 3962–3965.

[221] J. F. Hull, Y. Himeda, W.-H. Wang, B. Hashiguchi, R. Periana, D. J. Szalda, J. T. Muckerman, E. Fujita, *Nat. Chem.* **2012**, *4*, 383–388.

[222] W.-H. Wang, J. F. Hull, J. T. Muckerman, E. Fujita, Y. Himeda, *Energy Environ. Sci.* **2012**, *5*, 7923.

[223] Y. M. Badiei, W. H. Wang, J. F. Hull, D. J. Szalda, J. T. Muckerman, Y. Himeda, E. Fujita, *Inorg. Chem.* **2013**, *52*, 12576–12586.

[224] J. H. Barnard, C. Wang, N. G. Berry, J. Xiao, *Chem. Sci.* **2013**, *4*, 1234.

[225] S. Fukuzumi, T. Kobayashi, T. Suenobu, *J. Am. Chem. Soc.* **2010**, *132*, 11866–11867.

[226] S. Fukuzumi, T. Suenobu, *Dalt. Trans.* **2013**, *42*, 18–28.

[227] Y. Himeda, *Eur. J. Inorg. Chem.* **2007**, *2007*, 3927–3941.

[228] W. Wang, J. T. Muckerman, E. Fujita, Y. Himeda, *ACS Catal.* **2013**, 856–860.

[229] Y. Himeda, *Green Chem.* **2009**, *11*, 2018.

[230] T. B. Causey, K. T. Shanmugam, L. P. Yomano, L. O. Ingram, *Proc. Natl. Acad. Sci.* **2004**, *101*, 2235–2240.

[231] J. Knappe, H. P. Blaschkowski, P. Grobner, T. Schmitt, *Eur. J. Biochem.* **1974**, *50*, 253–263.

[232] A. Becker, K. Fritz-Wolf, W. Kabsch, J. Knappe, S. Schultz, A. F. Volker Wagner, *Nat Struct Biol* **1999**, *6*, 969–975.

[233] V. Köhler, Y. M. Wilson, M. Dürrenberger, D. Ghislieri, E. Churakova, T. Quinto, L. Knörr, D. Häussinger, F. Hollmann, N. J. Turner, et al., *Nat. Chem.* **2012**, *5*, 93–99.

[234] D. W. Mulder, E. M. Shepard, J. E. Meuser, N. Joshi, P. W. King, M. C. Posewitz, J. B. Broderick, J. W. Peters, *Structure* **2011**, *19*, 1038–1052.

[235] F. Zheng, S. D. Rassat, D. J. Helderandt, D. D. Caldwell, C. L. Aardahl, T. Autrey, J. C. Linehan, K. G. Rappé, K. G. Rapṕ, *Rev. Sci. Instrum.* **2008**, *79*, 084103.

[236] Y. Manaka, W.-H. Wang, Y. Suna, H. Kambayashi, J. T. Muckerman, E. Fujita, Y. Himeda, *Catal. Sci. Technol.* **2014**, *4*, 34–37.

[237] M. Wilchek, E. A. Bayer, *Methods Enzymol.* **1990**, *184*, 5–13.

[238] C. M. Dundas, D. Demonte, S. Park, *Appl. Microbiol. Biotechnol.* **2013**, *97*, 9343–9353.

[239] T. R. Ward, *Acc. Chem. Res.* **2011**, *44*, 47–57.

[240] J. C. Lewis, *ACS Catal.* **2013**, *3*, 2954–2975.

[241] J. Bos, G. Roelfes, *Curr. Opin. Chem. Biol.* **2014**, *19*, 135–143.

[242] M. Skander, N. Humbert, J. Collot, J. Gradinaru, G. Klein, A. Loosli, J. Sauser, A. Zocchi, F. Gilardoni, T. R. Ward, *J. Am. Chem. Soc.* **2004**, *126*, 14411–14418.

[243] M. D. Levin, S. Kim, F. D. Toste, *ACS Cent. Sci.* **2016**, *2*, 293–301.

[244] K. K. W. Lo, W. K. Hui, C. K. Chung, K. H. K. Tsang, T. K. M. Lee, C. K. Li, J. S. Y. Lau, D. C. M. Ng, *Coord. Chem. Rev.* **2006**, *250*, 1724–1736.

[245] K. K. W. Lo, T. K. M. Lee, *Inorg. Chem.* **2004**, *43*, 5275–5282.

[246] T. Soller, M. Ringler, M. Wunderlich, T. A. Klar, J. Feldmann, H. P. Josel, J. Koci, Y. Markert, A. Nichtl, K. Kürzinger, *J. Phys. Chem. B* **2008**, *112*, 12824–12826.

[247] S. Delahaye, C. Loosli, S. X. Liu, S. Decurtins, G. Labat, A. Neels, A. Loosli, T. R. Ward, A. Hauser, *Adv. Funct. Mater.* **2006**, *16*, 286–295.

[248] K. K. W. Lo, W. K. Hui, C. K. Chung, K. H. K. Tsang, D. C. M. Ng, N. Zhu, K. K. Cheung, *Coord. Chem. Rev.* **2005**, *249*, 1434–1450.

[249] K. K. W. Lo, W. K. Hui, *Inorg. Chem.* **2005**, *44*, 1992–2002.

[250] K. K. W. Lo, K. H. K. Tsang, K. S. Sze, *Inorg. Chem.* **2006**, *45*, 1714–1722.

[251] K. K. W. Lo, M. W. Louie, K. S. Sze, J. S. Y. Lau, *Inorg. Chem.* **2008**, *47*, 602–611.

[252] K. K. W. Lo, W. K. Hui, D. C. M. Ng, *J. Am. Chem. Soc.* **2002**, *124*, 9344–9345.

[253] K. K. W. Lo, K. Y. Zhang, S. K. Leung, M. C. Tang, *Angew. Chemie - Int. Ed.* **2008**, *47*, 2213–2216.

[254] K. K. W. Lo, K. H. K. Tsang, K. S. Sze, C. K. Chung, T. K. M. Lee, K. Y. Zhang, W. K. Hui, C. K. Li, J. S. Y. Lau, D. C. M. Ng, et al., *Coord. Chem. Rev.* **2007**, *251*, 2292–2310.

[255] K. K. Lo, J. S. Lau, *Inorg. Chem.* **2007**, *46*, 700–709.

[256] K. Y. Zhang, K. K. W. Lo, *Inorg. Chem.* **2009**, *48*, 6011–6025.

[257] K. K. W. Lo, J. S. W. Chan, L. H. Lui, C. K. Chung, *Organometallics* **2004**, *23*, 3108–3116.

[258] K. K. W. Lo, C. K. Li, J. S. Y. Lau, *Organometallics* **2005**, *24*, 4594–4601.

[259] S. James, K. P. Maresca, J. W. Babich, J. F. Valliant, L. Doering, J. Zubieta, *Bioconjug. Chem.* **2006**, *17*, 590–596.

[260] V. Fernández-Moreira, F. L. Thorp-Greenwood, M. P. Coogan, *Chem. Commun.* **2010**, *46*, 186–202.

[261] O. S. Wenger, *Coord. Chem. Rev.* **2009**, *253*, 1439–1457.

[262] A. Fürstenberg, O. Kel, J. Gradinaru, T. R. Ward, D. Emery, G. Bollot, J. Mareda, E. Vauthey, *ChemPhysChem* **2009**, *10*, 1517–1532.

[263] J. N. Onuchic, D. N. Beratan, J. R. Winkler, H. B. Gray, *Annu. Rev. Biophys. Biomol. Struct.* **1992**, *21*, 349–377.

[264] H. B. Gray, J. R. Winkler, *Annu. Rev. Biochem.* **1996**, *65*, 537–561.

[265] D. S. Wuttke, M. J. Bjerrum, J. R. Winkler, H. B. Gray, *Science* **1992**, *256*, 1007–1009.

[266] B. R. Crane, A. J. Di Bilio, J. R. Winkler, H. B. Gray, *J. Am. Chem. Soc.* **2001**, *123*, 11623–11631.

[267] C. Fehl, B. G. Davis, *Proc. R. Soc. A Math. Phys. Eng. Sci.* **2016**, *472*, 20160078.

[268] J. R. Winkler, H. B. Gray, *J. Am. Chem. Soc.* **2014**, *136*, 2930–2939.

[269] J. Bos, F. Fusetti, A. J. M. Driessen, G. Roelfes, *Angew. Chemie - Int. Ed.* **2012**, *51*, 7472–7475.

[270] G. Klein, N. Humbert, J. Gradinaru, A. Ivanova, F. Gilardoni, U. E. Rusbandi, T. R. Ward, *Angew. Chemie Int. Ed.* **2005**, *44*, 7764–7767.

[271] M. J. Bjerrum, D. R. Casimiro, I. J. Chang, A. J. Di Bilio, H. B. Gray, M. G. Hill, R. Langen, G. A. Mines, L. K. Skov, J. R. Winkler, et al., *J. Bioenerg. Biomembr.* **1995**, *27*, 295–302.

[272] D. Hanss, O. S. Wenger, *Eur. J. Inorg. Chem.* **2009**, *2009*, 3778–3790.

[273] D. Hanss, O. S. Wenger, *Inorg. Chem.* **2009**, *48*, 671–680.

[274] P. S. Braterman, J. I. Song, *J. Org. Chem.* **1991**, *56*, 4678–4682.

[275] A. Pannwitz, O. S. Wenger, *Phys. Chem. Chem. Phys.* **2016**, *18*, 11374–11382.

[276] K. Sreenath, T. G. Thomas, K. R. Gopidas, *Org. Lett.* **2011**, *13*, 1134–1137.

[277] V. Coropceanu, N. E. Gruhn, S. Barlow, C. Lambert, J. C. Durivage, T. G. Bill, G. Nöll, S. R. Marder, J.-L. Brédas, *J. Am. Chem. Soc.* **2004**, *126*, 2727–2731.

[278] J. Hankache, O. S. Wenger, *Chem. Commun.* **2011**, *47*, 10145.

[279] J. Hankache, M. Niemi, H. Lemmetyinen, O. S. Wenger, *Inorg. Chem.* **2012**, *51*, 6333–6344.

[280] M. Kuss-Petermann, O. S. Wenger, *Angew. Chemie - Int. Ed.* **2016**, *55*, 815–819.

[281] M. Kuss-Petermann, O. S. Wenger, *J. Am. Chem. Soc.* **2016**, *138*, 1349–1358.

[282] M. Orazietti, M. Kuss-Petermann, P. Hamm, O. S. Wenger, *Angew. Chemie Int. Ed.* **2016**, *55*, 9407–9410.

[283] H. B. Gray, J. R. Winkler, *Proc. Natl. Acad. Sci.* **2005**, *102*, 3534–3539.

[284] N. Nelson, A. Ben-Shem, *Nat. Rev. Mol. Cell Biol.* **2004**, *5*, 971–982.

[285] D. Gust, T. A. Moore, A. L. Moore, *Acc. Chem. Res.* **2001**, *34*, 40–48.

[286] L. Hammarström, *Acc. Chem. Res.* **2015**, *48*, 840–850.

[287] A. Pannwitz, O. S. Wenger, *J. Am. Chem. Soc.* **2017**, *139*, 13308–13311.

[288] V. Balzani, *Electron Transfer in Chemistry*, Wiley-VCH Verlag GmbH, Weinheim, Germany, **2008**.

[289] M. R. Wasielewski, *Chem. Rev.* **1992**, *92*, 435–461.

[290] Y. W. Lin, *Coord. Chem. Rev.* **2017**, *336*, 1–27.

[291] A. Onoda, T. Hayashi, *Curr. Opin. Chem. Biol.* **2015**, *25*, 133–140.

[292] T. Matsuo, A. Asano, T. Ando, Y. Hisaeda, T. Hayashi, *Chem. Commun.* **2008**, 3684.

[293] V. Heleg-Shabtai, T. Gabriel, I. Willner, *J. Am. Chem. Soc.* **1999**, *121*, 3220–3221.

[294] L. Kubie, A. R. Amori, S. Chakraborty, K. L. Bren, T. D. Krauss, *Nanoscale Horiz.* **2017**, *2*, 163–166.

[295] M. Cordes, B. Giese, *Chem. Soc. Rev.* **2009**, *38*, 892.

[296] M. Wilchek, E. A. Bayer, *Methods Enzymol.* **1990**, *184*, 5–13.

[297] T. Heinisch, T. R. Ward, *Acc. Chem. Res.* **2016**, *49*, 1711–1721.

[298] N. Agrawal, J. A. E. Määttä, M. S. Kulomaa, V. P. Hytönen, M. S. Johnson, T. T. Airenne, *PLoS One* **2017**, *12*, e0176086.

[299] F. Schwizer, Y. Okamoto, T. Heinisch, Y. Gu, M. M. Pellizzoni, V. Lebrun, R. Reuter, V. Köhler, J. C. Lewis, T. R. Ward, *Chem. Rev.* **2017**, acs.chemrev.7b00014.

[300] J. C. Lewis, *ACS Catal.* **2013**, *3*, 2954–2975.

[301] J. Bos, G. Roelfes, *Curr. Opin. Chem. Biol.* **2014**, *19*, 135–143.

[302] M. Skander, N. Humbert, J. Collot, J. Gradinaru, G. Klein, A. Loosli, J. Sauser, A. Zocchi, F. Gilardoni, T. R. Ward, *J. Am. Chem. Soc.* **2004**, *126*, 14411–14418.

[303] M. T. Reetz, J. J.-P. Peyralans, A. Maichele, Y. Fu, M. Maywald, *Chem. Commun.* **2006**, 4318–4320.

[304] F. Yu, V. M. Cangelosi, M. L. Zastrow, M. Tegoni, J. S. Plegaria, A. G. Tebo, C. S. Mocny, L. Ruckthong, H. Qayyum, V. L. Pecoraro, *Chem. Rev.* **2014**, *114*, 3495–3578.

[305] O. Pàmies, M. Diéguez, J. E. Bäckvall, *Adv. Synth. Catal.* **2015**, *357*, 1567–1586.

[306] D. Gamenara, P. Domínguez de María, *Org. Biomol. Chem.* **2014**, *12*, 2989–2992.

[307] C.-C. Lin, C.-W. Lin, A. S. C. Chan, *Tetrahedron: Asymmetry* **1999**, *10*, 1887–1893.

[308] J. Collot, J. Gradinaru, N. Humbert, M. Skander, A. Zocchi, T. R. Ward, *J. Am. Chem. Soc.* **2003**, *125*, 9030–9031.

[309] T. K. Hyster, L. Knörr, T. R. Ward, T. Rovis, *Science* **2012**, *338*, 500–503.

[310] S. I. Mann, T. Heinisch, A. C. Weitz, M. P. Hendrich, T. R. Ward, A. S. Borovik, *J. Am. Chem. Soc.* **2016**, *138*, 9073–9076.

[311] M. E. Wilson, G. M. Whitesides, *J. Am. Chem. Soc.* **1978**, *100*, 306–307.

[312] K. K. W. Lo, W. K. Hui, C. K. Chung, K. H. K. Tsang, T. K. M. Lee, C. K. Li, J. S. Y. Lau, D. C. M. Ng, *Coord. Chem. Rev.* **2006**, *250*, 1724–1736.

[313] K. K. Lo, T. K. Lee, *Inorg. Chem.* **2004**, *43*, 5275–5282.

[314] T. Soller, M. Ringler, M. Wunderlich, T. A. Klar, J. Feldmann, H.-P. Josel, J. Koci, Y. Markert, A. Nichtl, K. Kürzinger, *J. Phys. Chem. B* **2008**, *112*, 12824–12826.

[315] K. K. W. Lo, W. K. Hui, C. K. Chung, K. H. K. Tsang, D. C. M. Ng, N. Zhu, K. K. Cheung, *Coord. Chem. Rev.* **2005**, *249*, 1434–1450.

[316] K. K. W. Lo, W. K. Hui, D. C. M. Ng, *J. Am. Chem. Soc.* **2002**, *124*, 9344–9345.

[317] K. K.-W. Lo, K. Y. Zhang, S.-K. Leung, M.-C. Tang, *Angew. Chemie Int. Ed.* **2008**, *47*, 2213–2216.

[318] K. Lo, K. Tsang, K. Sze, C. Chung, T. Lee, K. Hang, W. Hui, C. Li, J. Lau, D. Ng, *Coord. Chem. Rev.* **2007**, *251*, 2292–2310.

[319] K. K. Lo, J. S. Lau, *Inorg. Chem.* **2007**, *46*, 700–709.

[320] K. K. Lo, J. S. Chan, L. Lui, C. Chung, *Organometallics* **2004**, *23*, 3108–3116.

[321] O. S. Wenger, *Coord. Chem. Rev.* **2009**, *253*, 1439–1457.

[322] S. G. Keller, A. Pannwitz, F. Schwizer, J. Klehr, O. S. Wenger, T. R. Ward, *Org. Biomol. Chem.* **2016**, *14*, 7197–7201.

[323] B. H. Lee, T. Hibino, T. Takabe, P. J. Weisbeek, *J. Biochem.* **1995**, *117*, 1209–17.

[324] E. L. Gross, *Photosynth. Res.* **1993**, *37*, 103–116.

[325] M. R. Redinbo, T. O. Yeates, S. Merchant, *J. Bioenerg. Biomembr.* **1994**, *26*, 49–66.

[326] E. Krieger, G. Vriend, *Bioinformatics* **2014**, *30*, 2981–2982.

[327] H. Mallin, M. Hestericová, R. Reuter, T. R. Ward, *Nat. Protoc.* **2016**, *11*, 835–852.

[328] L. S. Witus, T. Moore, B. W. Thuronyi, A. P. Esser-Kahn, R. A. Scheck, A. T. Iavarone, M. B. Francis, *J. Am. Chem. Soc.* **2010**, *132*, 16812–16817.

[329] O. Livnah, E. a Bayer, M. Wilchek, J. L. Sussman, *FEBS Lett.* **1993**, *328*, 165–8.

[330] P. S. Braterman, J. I. Song, *J. Org. Chem.* **1991**, *56*, 4678–4682.

[331] R. Lomoth, T. Häupl, O. Johansson, L. Hammarström, *Chem. - A Eur. J.* **2002**, *8*, 102–110.

[332] J. Hankache, M. Niemi, H. Lemmetyinen, O. S. Wenger, *Inorg. Chem.* **2012**, *51*, 6333–6344.

[333] J. Hankache, O. S. Wenger, *Chem. Commun. (Camb).* **2011**, *47*, 10145–10147.

[334] M. E. El-Khouly, E. El-Mohsnawy, S. Fukuzumi, *J. Photochem. Photobiol. C Photochem. Rev.* **2017**, *31*, 36–83.

[335] E. S. Andreiadis, M. Chavarot-Kerlidou, M. Fontecave, V. Artero, *Photochem. Photobiol.* **2011**, *87*, 946–964.

[336] S. Soman, *Comments Inorg. Chem.* **2015**, *35*, 82–120.

[337] C. Liu, B. C. Colón, M. Ziesack, P. A. Silver, D. G. Nocera, *Science* **2016**, *352*, 1210–1213.

[338] P. A. Ash, R. Hidalgo, K. A. Vincent, *ACS Catal.* **2017**, *7*, 2471–2485.

[339] A. Roy, C. Madden, G. Ghirlanda, *Chem. Commun.* **2012**, *48*, 9816.

[340] M. Faiella, A. Roy, D. Sommer, G. Ghirlanda, *Biopolymers* **2013**, *100*, 558–571.

[341] S. R. Soltau, J. Niklas, P. D. Dahlberg, K. L. Mulfort, O. G. Poluektov, L. M. Utschig, *ACS Energy Lett.* **2017**, *2*, 230–237.

[342] S. R. Soltau, P. D. Dahlberg, J. Niklas, O. G. Poluektov, K. L. Mulfort, L. M. Utschig, *Chem. Sci.* **2016**, *7*, 7068–7078.

[343] A. Onoda, Y. Kihara, K. Fukumoto, Y. Sano, T. Hayashi, *ACS Catal.* **2014**, *4*, 2645–2648.

[344] T. Heinisch, T. R. Ward, *Acc. Chem. Res.* **2016**, *49*, 1711–1721.

[345] M. Pellizzoni, G. Facchetti, R. Gandolfi, M. Fusè, A. Contini, I. Rimoldi, *ChemCatChem* **2016**, *8*, 1665–1670.

[346] S. I. Mann, T. Heinisch, A. C. Weitz, M. P. Hendrich, T. R. Ward, A. S. Borovik, *J. Am. Chem. Soc.* **2016**, *138*, 9073–9076.

[347] Y. Okamoto, T. R. Ward, in *Compr. Supramol. Chem. II*, Elsevier, **2017**, pp. 459–510.

[348] C. Bachmann, B. Probst, M. Guttentag, R. Alberto, *Chem. Commun.* **2014**, *50*, 6737–6739.

[349] A. Rodenberg, M. Orazietti, B. Probst, C. Bachmann, R. Alberto, K. K. Baldridge, P. Hamm, *Inorg. Chem.* **2015**, *54*, 646–657.

[350] M. O'Hagan, W. J. Shaw, S. Raugei, S. Chen, J. Y. Yang, U. J. Kilgore, D. L. DuBois, R. M. Bullock, *J. Am. Chem. Soc.* **2011**, *133*, 14301–14312.

[351] L. E. Fernandez, S. Horvath, S. Hammes-Schiffer, *J. Phys. Chem. Lett.* **2013**, *4*, 542–546.

[352] A. Dutta, D. L. DuBois, J. A. S. Roberts, W. J. Shaw, *Proc. Natl. Acad. Sci.* **2014**, *111*, 16286–16291.

[353] A. Dutta, J. A. S. Roberts, W. J. Shaw, *Angew. Chemie - Int. Ed.* **2014**, *53*, 6487–6491.

[354] T. Shinagawa, K. Takanabe, *J. Phys. Chem. C* **2016**, *120*, 24187–24196.

[355] M. Natali, E. Badetti, E. Deponti, M. Gamberoni, F. A. Scaramuzzo, A. Sartorel, C. Zonta, *Dalt. Trans.* **2016**, *45*, 14764–14773.

[356] E. Deponti, A. Luisa, M. Natali, E. Iengo, F. Scandola, *Dalt. Trans.* **2014**, *43*, 16345–16353.

[357] S. Salzl, M. Ertl, G. Knör, *Phys. Chem. Chem. Phys.* **2017**, *19*, 8141–8147.

[358] S. C. Marinescu, J. R. Winkler, H. B. Gray, *Proc. Natl. Acad. Sci.* **2012**, *109*, 15127–15131.

[359] S. Mandal, S. Shikano, Y. Yamada, Y. M. Lee, W. Nam, A. Llobet, S. Fukuzumi, *J. Am. Chem. Soc.* **2013**, *135*, 15294–15297.

[360] H. Vázquez-Villa, S. Reber, M. A. Ariger, E. M. Carreira, *Angew. Chemie - Int. Ed.* **2011**, *50*, 8979–8981.

[361] T. Abura, S. Ogo, Y. Watanabe, S. Fukuzumi, *J. Am. Chem. Soc.* **2003**, *125*, 4149–4154.

[362] Y. K. Sau, X. Y. Yi, K. W. Chan, C. S. Lai, I. D. Williams, W. H. Leung, *J. Organomet. Chem.* **2010**, *695*, 1399–1404.

[363] K. I. Fujita, T. Yoshida, Y. Imori, R. Yamaguchi, *Org. Lett.* **2011**, *13*, 2278–2281.

[364] Y. Boutadla, D. L. Davies, R. C. Jones, K. Singh, *Chem. - A Eur. J.* **2011**, *17*, 3438–3448.

[365] Y. Maenaka, T. Suenobu, S. Fukuzumi, *Energy Environ. Sci.* **2012**, *5*, 7360.

[366] Z. M. Heiden, B. J. Gorecki, T. B. Rauchfuss, *Organometallics* **2008**, *27*, 1542–1549.

[367] T. Jerphagnon, A. J. A. Gayet, F. Berthiol, V. Ritleng, N. Mršić, A. Meetsma, M. Pfeffer, A. J. Minnaard, B. L. Feringa, J. G. De Vries, *Chem. - A Eur. J.* **2009**, *15*, 12780–12790.

[368] F. Feigl, *Spot Tests in Organic Analysis, 5th Ed.*, Elsevier, Amsterdam, **1956**.

[369] T. L. Hwang, A. J. Shaka, *J. Magn. Reson. Ser. A* **1995**, *112*, 275–279.

[370] K. Tahara, T. Nakakita, S. Katao, J. Kikuchi, *Chem. Commun. (Camb).* **2014**, *50*, 15071–4.

[371] E. Moulin, F. Niess, M. Maaloum, E. Buhler, I. Nyrkova, N. Giuseppone, *Angew. Chemie - Int.*

*Ed.* **2010**, *49*, 6974–6978.

[372] K. Lou, J. F. Lovell, *Chem. Commun.* **2014**, *50*, 3231–3233.

[373] D. Kessler, P. J. Roth, P. Theato, *Langmuir* **2009**, *25*, 10068–10076.

[374] A. Fedorova, M. Y. Ogawa, *Bioconjug. Chem.* **2002**, *13*, 150–154.

[375] T. Heinisch, T. R. Ward, *Acc. Chem. Res.* **2016**, *49*, 1711–1721.

[376] E. Moulin, F. Niess, M. Maaloum, E. Buhler, I. Nyrkova, N. Giuseppone, *Angew. Chemie Int. Ed.* **2010**, *49*, 6974–6978.

[377] K. Lou, J. F. Lovell, *Chem. Commun.* **2014**, *50*, 3231–3233.

[378] N. Asakura, T. Hiraishi, T. Kamachi, I. Okura, *J. Mol. Catal. A Chem.* **2001**, *174*, 1–5.

[379] P. Gobbo, P. Gunawardene, W. Luo, M. S. Workentin, *Synlett* **2015**, *26*, 1169–1174.

# Publications

## Peer-Reviewed Journal Publications

René Döpp, Christian Lothschütz, Thomas Wurm, Markus Pernpointner, Sascha G. Keller, Frank Rominger, A. Stephen K. Hashmi "*Gold Catalysis: Hydrolysis of Di(alkoxy)carbenium Ion Intermediates as a Sensor for the Electronic Properties of Gold(I) Complexes*", *Organometallics* **2011**, *30*, 5894–5903.

Sascha G. Keller, Mark R. Ringenberg, Daniel Häussinger, Thomas R. Ward "Evaluation of Formate Dehydrogenase Activity of Three-Legged Pianostool Complexes in Dilute Aqueous Solution", *Eur. J. Inorg. Chem.* **2014**, *34*, 5860-5864.

Sascha G. Keller, Andrea Pannwitz, Fabian Schwizer, Juliane Klehr, Oliver S. Wenger, Thomas R. Ward "*Light-driven electron injection from a biotinylated triarylamine donor to* $[Ru(diimine)_3]^{2+}$*-labeled streptavidin*", *Org. Biomol. Chem.* **2016**, *14*, 7197-7201.

Sascha G. Keller, Andrea Pannwitz, Hendrik Mallin, Oliver S. Wenger, Thomas R. Ward "*Streptavidin as a Scaffold for Light-Induced Long-Lived Charge Separation*", *Chem. Eur. J.*, **2017**, *23*, 18019-18024.

Sascha G. Keller, Benjamin Probst, Tillmann Heinisch, Roger Alberto, Thomas R. Ward "*Photo-Driven Hydrogen Evolution by an Artificial Hydrogenase Utilizing the Biotin-Streptavidin Technology*", *Helv. Chim. Acta.* **2018**, *101*, e1800036.

## Annual Reports

12.2013 *Molecular Nanofactories for Biohydrogen Production*
S. G. Keller, C. Tagwerker, S. Panke, T. R. Ward
SNI Annual Report 2013

12.2014 *Hydrogen production based on molecular nanofactories*
S. G. Keller, O. S. Wenger, S. Panke, W. Shaw, T. R. Ward
SNI Annual Report 2014

12.2015 *Hydrogen production based on molecular nanofactories*
S. G. Keller, A. Pannwitz, O. S. Wenger, S. Panke, T. R. Ward
SNI Annual Report 2015

12.2016 *Photo-driven hydrogen production based on molecular nanofactories*
S. G. Keller, A. Pannwitz, O. S. Wenger, S. Panke, R. Alberto, T. R. Ward
SNI Annual Report 2016

12.2017 *Photo-driven hydrogen production based on molecular nanofactories*
S. G. Keller, B. Probst, T. Heinisch, S. Panke, R. Alberto, T. R. Ward
SNI Annual Report 2017

## Oral Contributions

01.2014 *Hydrogen production from formic acid inside E. coli using an artificial metalloenzyme*
NIS Winter School, Kandersteg, Switzerland

04.2015 *Hydrogenase mimics using Biotin-Streptavidin technology*
Max-Planck Institute for chemical energy conversion, Mülheim a. d. Ruhr, Germany

03.2016 *Photo-driven Hydrogenase based on the Biotin-Streptavidin technology*
Schwarzenberg Symposium, Schwarzenberg, Austria

01.2017 *Towards a photo-driven artificial hydrogenase based on the biotin-streptavidin technology*
NIS Winter School, Zermatt, Switzerland

01.2017 *Towards a photo-driven artificial hydrogenase based on the biotin-streptavidin technology*
SCS Swiss Snow Symposium, Saas-Fee, Switzerland

## Poster Contributions

02.2016 *Photo-Driven Hydrogenase Based on the Biotin-Streptavidin Technology*
NIS Winter School, Zinal, Switzerland

07.2016 *Towards a Photo-Driven Artificial Hydrogenase Based on the Biotin-Streptavidin Technology*
11th Hydrogenase Conference, Marseille, France

09.2016 *Towards a Photo-Driven Artificial Hydrogenase Based on the Biotin-Streptavidin Technology*
SNI Annual Meeting, Lenzerheide, Switzerland

09.2016 *Towards a Photo-Driven Artificial Hydrogenase Based on the Biotin-Streptavidin Technology*
SNI Annual Meeting, Lenzerheide, Switzerland

01.2017 *Towards a photo-driven artificial hydrogenase based on the biotin-streptavidin technology*
SCS Swiss Snow Symposium, Saas-Fee, Switzerland

# Acknowledgements

I would like to express my greatest gratitude to **Professor Dr. Thomas R. Ward** for accepting me as a PhD candidate and for guiding me through that endeavour. Thank you for giving me the opportunity to work in different labs and collaborate extensively. It has been a really enjoyable and scientifically fruitful time.

I sincerely thank **Professor Dr. Oliver S. Wenger** for accepting the co-examination and for guiding me during my detour through photochemistry.

Special thanks is given to **Professor Dr. Dennis Gillingham** for chairing the PhD defence session.

Thank you **Dr. Andrea Pannwitz** for having a lot of patience with me and the unforgettable measuring times!

A big thank you to all the collaborators I worked with I would like to thank **Dr. Wendy Shaw** and **Dr. Arnab Dutta** from the PNNL institute in Richland, WA, U.S.A.; **Dr. Olaf Rüdiger** and **Dr. Patricia Rodríguez Maciá** from the Max-Planck-Institute for chemical energy conversion in Mülheim a. d. Ruhr, Germany and **Professor Dr. Roger Alberto**, **Dr. Benjamin Probst** and **Dr. Henrik Braband**

Much appreciation and gratitude also to my former students **Jonas Schätti**, **Isaak Nohara** and **Yanik Weber**! Things did not always work, but I hope you had as much fun as I had.

Special thanks to **all the students from the practicals**, that I had the honour to teach. You were tough sometimes, but I enjoyed every day!

I am also very grateful to **all actual and former members of the Ward group**. Thanks for the time and the nice lunch breaks! Also, big thanks to **Isa Worni** and **Esthi Stalder** for all the organizational things needed during a PhD.

Thanks to **Professor Dr. Peter Hauser**, **Dr. Joel Koenka**, **Michael Liebetanz** and the whole **Werkstatt-Team** (especially **Andreas Koller**) for our work on "PIPER".

I also want to thank all members of other groups of the department. Especially the **Seebeck group** and the **Gillingham group**!

Special thanks to **Dr. Roxana Lemnaru**, **Dr. Kristina Goncharenko**, **Dr. Srbo Vujovic, Dr. Tommaso Quinto, Dr. Marko Stojkovic, Dr. Daniel Gliesche, Dr. Michael Gerspach, Dr. Pascal Engi, Dr. Stefanie Geigle, Dr. Laëtitia Misson.** Thanks, guys, for being good friends also outside of university.

To **the INASCON crew**: I really enjoyed the organization of the conference and especially that we still stayed in contact afterwards. This furthermore brings me to my gratitude to the **Swiss nanoscience Institute**. Thanks for the **PhD school**, all students that I met there and at related meetings. Special thanks to **Claudia Wirth**, **Dr. Christel Möller, Sandra Hüni** and **Michèle Wegmann** for the organization, you are doing a really good job!

Big shouts to my local football club "**Lietsch FC**"! You guys are amazing! Thanks for the last few years of exquisite, quality football! Euer Hüti!

Thanks to my friends from home! The "**ü30-WG**", you make coming home always special! Not so much thank you for not visiting me ;)!

I want to deeply thank **my whole family**. **Steffen** and **Linda**, nice that you were here with me for the last few years. It was awesome having you around. Grossen Dank an meine **Mutter** und meinen **Vater**!

Ihr habt mich immer unterstützt und endlich geht die scheinbar unendliche Geschichte doch tatsächlich dem Ende entgegen!

Last, but most importantly I want to thank my girlfriend **Veronica**. Thank you for supporting me throughout the last year, especially during the time of writing and applying. Thanks for listening to my complaints and your patience, even though you are also having a stressful time! I hope now I can make up for it!

# Curriculum Vitae

## Sascha Georg Keller

### Personal Information

| | |
|---|---|
| Date of birth | December 8, 1984 |
| Place of birth | Heidelberg, Germany |
| Nationality | German |
| Hometown | Heddesheim, Germany |

### Education

| | |
|---|---|
| 02.2013 – 12.2017 | **PhD Researcher** University of Basel, Basel, Switzerland<br>**Topic:** *Towards a Photo-Driven Artificial Hydrogenase Using the Biotin-Streptavidin Technology*<br>Supervisor: Prof. Dr. Thomas R. Ward |
| 02.2012 - 10.2012 | **Diploma thesis** University of Heidelberg, Heidelberg, Germany<br>**Topic:** *Synthesis and test of new phospholeneoxide catalysts for carbodiimide formation from isocyanates*<br>Supervisor: Prof. Dr. A. Stephen K. Hashmi |
| 10.2005 - 11.2012 | **Diploma in Chemistry**<br>University of Heidelberg, Heidelberg, Germany |
| 10.2004 - 07.2005 | **Military Service** |
| 09.1995 - 07.2004 | **Abitur** (high school diploma)<br>Carl-Benz Gymnasium Ladenburg, Ladenburg, Germany |

## Professional Experience

| | |
|---|---|
| 04.2018 | **Postdoctoral stay**, Group of Prof. Dr. Yasuteru Urano<br>The University of Tokyo, Tokyo, Japan |
| 01.2017 | **Research stay**, Group of Prof. Dr. Roger Alberto<br>University of Zürich, Zürich, Switzerland |
| 06.2015 - 07.2015 | **Research stay,** Group of Dr. Olaf Rüdiger<br>Max-Planck-Institute for chemical energy conversion, Mülheim an der Ruhr, Germany |
| 01.2015 - 02.2015 | **Research stay**, Group of Dr. Wendy Shaw<br>Pacific Northwest National Laboratory, Richland, Washington State, U.S.A. |
| 02.2014 - 02.2016 | **Head of the practical laboratory course** "Basic Chemistry"<br>University of Basel, Basel, Switzerland |
| 08.2010 - 12.2010 | **Visiting scholar**, Group of Prof. Dr. Janet Blümel<br>Texas A&M University, College Station, Texas, U.S.A. |
| 06.2010 - 07.2010 | **Pharmacological practical**, Group of Prof. Dr. Günther Schütz<br>German Cancer Research Center (DKFZ), Heidelberg, Germany |
| 02.2011 - 12.2012 | **Research assistant,** Group of Prof. Dr. Klaus Blaum<br>Max-Planck-Institute for Nuclear Physics, Heidelberg, Germany |
| 04.2010 - 06.2010 | **Research assistant**, Group of Prof. Dr. A. Stephen K. Hashmi<br>Ruprecht-Karls-University, Heidelberg, Germany |

## Scholarships Awards

| | |
|---|---|
| 11.2017 | **SNF Early Postdoc.Mobility Scholarship** |
| 02.2016 | **Best Poster Award**, Nanoscience in the Snow 2016, Zinal, Switzerland |

## Extracurricular Activities

| | |
|---|---|
| 08. 2014 - 08.2015 | **Organizing Committee Member**, "International Nanoscience Student Conference" INASCON, Basel, Switzerland |